Université de Strasbourg
École Doctorale 182 – Physique et Chimie-Physique
Institut Pluridisciplinaire Hubert Curien

Doctoral Thesis in Physics

Precision measurements in the multi-strange baryon sector at the LHC with the ALICE experiment

October 2020 – September 2023

Candidate:
Romain Schotter

Thesis advisors:
Antonin Maire, Boris Hippolyte

January 2022

Résumé

Abstract

Acknowledgements

For Romain Schotter, this work of the Interdisciplinary Thematic Institute QMat, as part of the ITI 2021 2028 program of the University of Strasbourg, CNRS and Inserm, has been supported by IdEx Unistra (ANR 10 IDEX 0002), and by SFRI STRAT'US project (ANR 20 SFRI 0012) and EUR QMAT ANR-17-EURE-0024 under the framework of the French Investments for the Future Program.

Contents

Chapter 1 | Preface

All known phenomena observed in Nature can presently be described by four fundamental interactions: the gravitational, electromagnetic, strong and weak interactions. The comprehension of these forces was at the heart of research in Physics throughout the XIX$^{\text{th}}$ and XX$^{\text{th}}$ centuries. This endeavor led to the two pillars of modern physics: Einstein's theory of general relativity, in which gravity is a geometric effect of the topology – in particular, the curvature – of spacetime, and the Standard Model of particle physics. In the latter case, the three other forces are understood as an exchange of elementary particles (vector gauge bosons or quanta) of their underlying quantum field.

Within the framework of the Standard Model, the strong interaction is described by quantum chromodynamics (QCD). In this theory, the *quarks* — the elementary particles sensitive to this force — carry a *colour* charge[1], that allows the exchange of *gluons*, the vector gauge bosons of QCD. The pecularity of this theory resides in its non-Abelian structure, meaning that gluons themselves are colour-charged and thereby can self-interact. The direct consequence of such feature is the running of the QCD coupling constant with the energy scale. In processes involving large momentum transfers (or at short length scale), the coupling constant weakens and the partons – quarks and gluons – can be viewed as free particles, leading to asymptotic freedom. Conversely, for lower momentum exchange (or at larger distance, typically of the order of the proton size), the coupling increases forcing partons to be confined inside composite objects, named hadrons, made of two or three valence quarks: the *mesons* and *baryons* respectively. In this regime, QCD calculations can only be achieved via non-perturbative approaches. One of these reveals another compelling feature: Lattice QCD (lQCD) predicts a phase transition from hadronic to partonic matter at extremely high temperature and/or densities; since the partons are deconfined and – similarly to plasmas – interact weakly, this state of matter is called the *quark-gluon plasma* (QGP). It is believed to have been the state of the primordial Universe, during the first microseconds of its existence, and could be present nowadays on a large scale in the core of neutron stars.

[1]This is the analog of the electric charge in QCD.

This QGP is not only a concept, it is an experimental fact. Although the first studies date from the 1970's [1][2][3], research on the QGP took off in 2000 with the hint of its existence by the experiments of the CERN (European Organisation for Nuclear Research) heavy ion programme [4]. This was validated later, in 2005, by the experiments at the Relativistic Heavy Ion Collider (Brookhaven National Laboratory) [5][6][7][8][9].

Experimentally, the QGP is recreated in laboratory by colliding heavy nuclei (Xe, Au, Pb,...) at extremely high energies. Due to its fleeting existence of about $10^{-23}s$, the study of this exotic state of matter relies primarily on the observation of the footprints/signatures left after the collision. The exploration of the QGP also hinges on more elemental collisions, namely proton-nucleus and proton-proton (pp) collisions, where no QGP is foreseen and which are therefore used as a reference.

Among the various available probes of the QGP, the multi-strange baryons, Ξ and Ω containing two or three *strange* quarks, play a special role. Being between light and heavy particles from the flavour point of view, they constitute exotic hadrons abundantly produced in high energy collision, that provide effective constrains on statistical models. Furthermore, thanks to a characteristic decay topology (cascade), their identification is possible on a vast domain of transverse momentum, associated with different production mechanisms (eventually intertwined). Finally, one key signature of the QGP is the *strangeness enhancement*, which consists in the increased yields of strange quarks and thus, in the final state, of strange hadrons. In particular, this enhancement intensifies for hadrons with the largest strangeness content, namely the Ξ and Ω.

Nowadays, the experiment at CERN devoted to studying QCD- and QGP-physics is *A Large Ion Collider Experiment* (ALICE), installed on the ring of the *Large Hadron Collider* (LHC). After two campaigns of data taking in 2009-2013 (Run-1) and 2015-2018 (Run-2), the LHC accelerator has restarted on the 5^{th} of July 2022 for a four-year programme (Run-3) [10]. During the second long shutdown period of the collider (2018-2022), ALICE has been fully revamped and comes out now as a brand-new experiment: more precision Inner Tracking System with reduced material budget; improved readout for its Time Projection Chamber; installation of a Muon Forward Tracker; upgraded detectors joined with a new Online-Offline software to enable continuous readout of Pb-Pb collisions to interaction rate up to 50 kHz [11]. Thanks to these upgrades, the study of QCD- and QGP-physics at LHC enters into a new age, an era of "precision".

About precision, it is enlightening to wonder what it truly means; after all, no one performs unprecise measurements. In the present context, this encompasses two aspects: on one hand, a thorough exploration/characterisation of the object of study with new observables or previously impossible measurements now at reach; on the other hand, accurate measurements going well beyond the current statistical or systematic limitations. In this respect, looking back at the achievements from the previous rounds of data taking, namely LHC Run-1 and Run-2, they are – to a certain extent – plenty of measurements, especially in the light flavour sector. For instance, we can mention [12][13][14].

This thesis proposes pursuing this precision endeavor on multi-strange baryons thanks to the excellent tracking and identification capabilities (at mid-rapidity) of ALICE during the LHC Run-2. The focus is on pp collisions at a centre-of-mass energy of $\sqrt{s}$ = 13 TeV. During this three-year PhD spanning from 2020 to 2023, two analyses have been performed; each one being appropriately introduced and detailed in a dedicated chapter.

The manuscript opens with an introduction of particle physics in Chap. 2. The basic concepts of the Standard Model are presented, with a detailed description of the strong interaction. The notion of QGP is also explained, from its formation to its experimental signatures. Among these, the phenomenon of strangeness enhancement receives a more particular attention.

It is followed by the Chap. 3, that provides an overview of the ALICE collaboration. First, the direct surroundings of ALICE is depicted, that is the CERN, its accelerator complex and the main experiments installed on the ring of the LHC. Then, the internal structure of the collaboration is presented, shortly accompanied by the showcase of the main sub-detectors of ALICE and particularly the ones used in the analyses reported in this manuscript. The event, vertex and tracks reconstruction procedures are outlined.

The Chap. 4 lays emphasis on the technique employed for identifying and selecting the characteristic cascade decay of the multi-strange baryons Ξ and Ω. What makes ALICE unique, among the LHC experiments, for studying those particles in the context of this thesis is also presented.

The Chap. 5 provides a detailed description of the first analysis of multi-strange baryons. It consists in measuring the Ξ^-, $\overline{\Xi}^+$, Ω^- , $\overline{\Omega}^+$ masses and mass differences between particle and anti-particle in pp collisions at $\sqrt{s}$ = 13 TeV. The values of the latter offer the opportunity to test the validity of the CPT symmetry to an unprecedented level of precision in the multi-strange baryon sector. This chapter underlines the challenge and the difficulties that one faces with such a measurement.

A second analysis has been carried out based on the experience gained from the first one. It is detailed in Chap. 6. It aims at studying the correlated production of strange hadrons in order to shed more light on the origin of the strangeness enhancement in pp collisions. The physical interpretation of the results is based on the comparison of our measurement to various QCD-inspired Monte Carlo models. The primary focus is to correlate a multi-strange baryon (Ξ or Ω) with a $\phi(1020)$ resonance ($s\bar{s}$), but other kind of correlations are also considered.

The final chapter, Chap. 7, consists in a discussion on the results of both analysis. Different extensions of the present work are also proposed.

Chapter

2 | Particle physics

Particle physics can fairly be defined as the field of Physics dedicated to the study of fundamental particles and their interactions. The idea that matter is composed of elementary bricks is not contemporary, though; the philosophical foundations of this idea date back to the Hellenic epoch in the Ancient Greece (V$^{\text{th}}$ century BC)[1] [15]. With the advent of the scientific method, this concept resurface throughout the XIX$^{\text{th}}$ and XX$^{\text{th}}$ centuries with, among the most notables, John Dalton's atomic theory[2] and the discovery of the electron by Joseph J. Thomson [16]. Although the first known particle, the electron, was discovered in 1897, research on particle physics gained momentum in the 1950s, thanks to the development of the particle accelerators. These devices made possible to observe high-energy collisions of known particles under controlled laboratory conditions and revealed the existence of dozens of particles: discovery of the pion [17] and kaon in cosmic rays in 1947 [18], followed by the ones of the Λ in 1950 [19], the anti-proton in 1955 [20], the electron and muon neutrinos in 1956 [21] and 1962 [22] respectively, the Ξ in 1964 [23], etc. In total, more than 30 new particles were found by the early 1960s [24] and it was still increasing. This particle "zoo" confused physicists for a decade. It is not until the 1970s that, thanks to the interplay between theory and experiment, a model successfully provided a unified description of these hundreds of particles: they are, in fact, composite objects, made of smaller and fewer constituents. This model still represents the best description of the sub-atomic universe to this day, hence its well-deserved name: the Standard Model of particle physics.

Throughout this chapter, an effort will be made to provide a historical introduction of the modern particle physics, with a particular attention on the many architects that contributed to its construction. The first section, Sec. 2|I, presents the Standard Model starting with some mandatory theoretical aspects. This is followed by the description of the different fundamental particles and interactions, that will ultimately lead to the classification of the elementary particles of the Stan-

[1] The fathers of the Atomism from the Ancient Greece, Leucippus and Democritus, thought that matter was made of both void and elementary, indivisible corpuscules: atoms.

[2] Apart from the name, it does not share much with the philosophical reasoning from the Ancient Greece.

dard Model. The theory of the strong interaction — the quantum chromodynamics (QCD) — will profit of a dedicated sub-section, considering its central role in the present manuscript. The different aspects of this force will be discussed, particularly the QCD phase diagram. One of the fascinating phases of QCD matter consists in state of matter in which quarks and gluons are no longer confined within hadrons: the quark-gluon plasma. Such a state — supposedly corresponding to the primordial state of the Universe a few micro-seconds after the Big Bang — is the heart of the Sec. 2|II. The formation of the QGP in laboratory will be presented, as well as its experimental signatures. One of them, called the strangeness enhancement, stands out of the others, since it has a central role in the studies described in this manuscript. Finally, this chapter will close on a discussion on the different probes of the QGP in view of the "recent" results in elementary systems, namely pp and p-Pb collisions.

I The Standard Model of particle physics

I-A Quantum field theories and fundamental symmetries

Mathematically speaking, the Standard Model is a (relativistic) quantum field theory (QFT), whose dynamics and kinematics are typically described by a Lagrangian[3]. In this formalism, particles are expressed in terms of dynamical fields defined at all points of spacetime [26]. The construction of the Standard Model relies strongly on group theory and symmetries (or invariances). In essence, the procedure for building a QFT consists in i) specifying a set of symmetries and their associated symmetry group, and ii) writing down the most general Lagrangian that is renormalizable and satisfies the postulated symmetries [27].

There are different classes of symmetries. A transformation that keeps the Lagrangian invariant and applies simultaneously at all points is called a *global* symmetry. Conversely, a similar transformation that would be applied differently at each point is a *local* symmetry. Both global and local symmetries can also be *continuous* if the transformation consists in a sum of infinitemisal transformations – typically described by Lie groups – or *discrete* and represented by finite groups [26][4]. Continuous symmetries are particularly interesting because of the Noether's theorem [28] that fundamentally states: to every continuous symmetry, there corresponds a conserved physical quantity (and vice versa).

All QFTs assume global Poincaré invariance, that involves spacetime translations and global Lorentz transformations including rotations in space and boosts. All these symmetries are continuous, and result in the conservation of momentum, energy, angular momentum and the speed of light respectively. The key elements that defines the Standard Model stem, in fact, from a subset of continuous and local symmetries: the *gauge* invariances. Each of these internal symmetries is associated

[3]The choice of a Lagrangian formulation is motivated, at least partially, by the fact that symmetries in the Lagrangian lead directly to conserved quantities/currents [25].

[4]There is also an additionnal difference concerning the quantum numbers: for a continuous symmetry, quantum numbers are additives; for a discrete one, they are multiplicatives [27].

to a certain number of group generators, from which emerge (vector) fields – called the *gauge* fields – describing a fundamental interaction. Intuitively, a gauge symmetry corresponds to an invariance under a change of scale or, in other words, of *gauge* [29]. For example, the electrostatic field depends on the potential difference and not the potential itself. This means that the electrostatic field is invariant under a shift of the potential. Additionnally, the potential is defined within an additive constant, which corresponds to a *global gauge* [27].

Finally, the Standard Model also relies on discrete symmetries: parity (P), time reversal (T) and charge conjugation (C). Although, most of the interactions preserve these three transformations, this must not be taken for granted. In the current state of the Universe, they are all broken and only the combination of C, P and T still holds as an exact symmetry of Nature [30]. That is closely connected with the Lorentz invariance via the so-called CPT theorem [31], which states that any unitary, local, Lorentz-invariant quantum field theory in a flat Minkowski spacetime must also be CPT invariant and vice-versa [31][32]. This being said, one can easily imagine that CPT invariance stands as one of the most sacred symmetry in the Standard Model. One of the implication of the CPT theorem involves the properties of matter and antimatter: since the combination C, P and T consists in a mirror-image transformation of particles into antiparticles, the CPT symmetry imposes that they share the same invariant mass, energy spectra, lifetime, coupling constants, etc [31][13].

I-B Particles and fundamental interactions

The Standard Model provides a description of the fundamental constituents of the observable Universe, the *elementary particles*, and their interactions, the *forces*. This description encompasses three of the four known fundamental forces: electromagnetic, strong and weak interactions. Gravity is not included for two reasons: on the theoretical side, this force is governed by the laws of general relativity. Its description within an unified framework with the three other interactions turns out to be a difficult – if not impossible – task. Furthermore, the coupling strength of gravity is by far the weakest of all the known forces, making it impossible to study experimentally at microscopic scales. Tab. 2.1 compiles some properties of the different forces.

The strong interaction, as the name suggests, is the strongest of the four fundamental forces; it is responsible for the cohesion of protons, and neutrons inside the nuclei (also called the nuclear force), for more than 99% of the observable mass in the Universe and for the confinement of the quarks (explained later in this section and in 2|I-C.i). It has a limited range, though, of only a few fm. On the opposite side, the weakest of the non gravitational forces is the weak interaction, which also has the shortest effective range (about less than a fm). The radioactive decay – as well as the decay of the particles studied in this thesis – and the fusion of atoms in the Sun originate from this force. Finally, the electromagnetic interaction is certainly the one we are the most familiar with; its coupling strength is in between the strong and weak forces, its range is infinite.

Interaction (Force)	**Particles Acted on by Force**	**Relative Strength**	**Typical Lifetimes for Decays via a Given Interaction**	**Range of Force**
Strong	Quarks, hadrons	1	$\leq 10^{-20}$ s	1 fm
Electromagnetic	Charged particles	$\approx 10^{-2}$	$\approx 10^{-16}$ s	∞
Weak	Quarks, leptons	$\approx 10^{-6}$	$\geq 10^{-10}$ s	10^{-3} fm
Gravitational	All particles	$\approx 10^{-43}$	?	∞

Table 2.1: The four fundamental interactions, with their corresponding relative strengths, typical lifetime for a decay and range. The relative strenghts are indicative values; obviously, they depend on the distance and energy scale considered. Here, they have been calculated for two particles at a distance of 0.03 fm. Table taken from [24].

These forces act on the fundamental constituents of matter, the quarks[5] and leptons[6], which are point-like fermions of spin 1/2. They are twelve organised in three families or generations, each containing two quarks with fractional electric charges (one with $+2e/3$ and the other with $-1e/3$, where e corresponds to the electric charge of the positron), one charged lepton and a neutrino[7]. The first family (or generation I) consists of the up and down quarks, the electron and the electron neutrino. These are the elements that characterize our low-energy Universe: the quarks make up the nucleons, forming the atomic nuclei, and with the electrons, they constitute the basic building blocks of all earthly matter. The electron-neutrino also plays a role in our everyday Universe, although an indirect one. Without its existence, the primordial hydrogen could not have been transformed into a variety of light and vital elements [34] for the development of life. The particles belonging to the first family can be duplicated to form the second and third families. Higher-generation particles have the exact same physical properties as their first-generation cousins, except for the mass that increases with the generation. Because of this difference, fermions from second and third generations tend to go through a chain of decay processes in order to reach particles from the first family. This is why ordinary matter is generally constituted of first-generation particles. I say *generally* because there are two subtleties when it comes to neutrinos: i) since they only interact via weak interaction and gravity, they cannot aggregate to form ordinary matter[8] and ii) they can oscillate from one flavour to another, giving rise to the

[5]The term is apparently inspired from Joyce's book *Finnegans Wake*:"Three quarks for muster Mark..." [33].

[6]From the Greek *leptos* meaning "small" to designate particles of small mass. Nowadays, any fermion that is insensitive to the strong interaction is tagged as a lepton [33].

[7]From the Italian "neutro" for "neutral" and the suffix "ino" for "tiny one", so "neutrino" means the "tiny neutral one" [33].

[8]Because the weak interaction only acts at a short distance, and the intensity of the gravitational

phenomenon of neutrino oscillation.

A final aspect concerns the *chirality* of the fermions, that is traditionnally introduced by concept of the helicity or handedness. Both are equivalent in the ultra-relativistic limit. On one hand, a particle exists in two versions: *right-handed* if the direction of spin coincides with the direction of motion; *left-handed* if the directions of spin and motion are opposite [35]. On the other hand, the chirality also has its own *left-* and *right-handed* states but the concept is more abstract. The chirality determines under which representation of the Poincaré group the particle transforms [36].

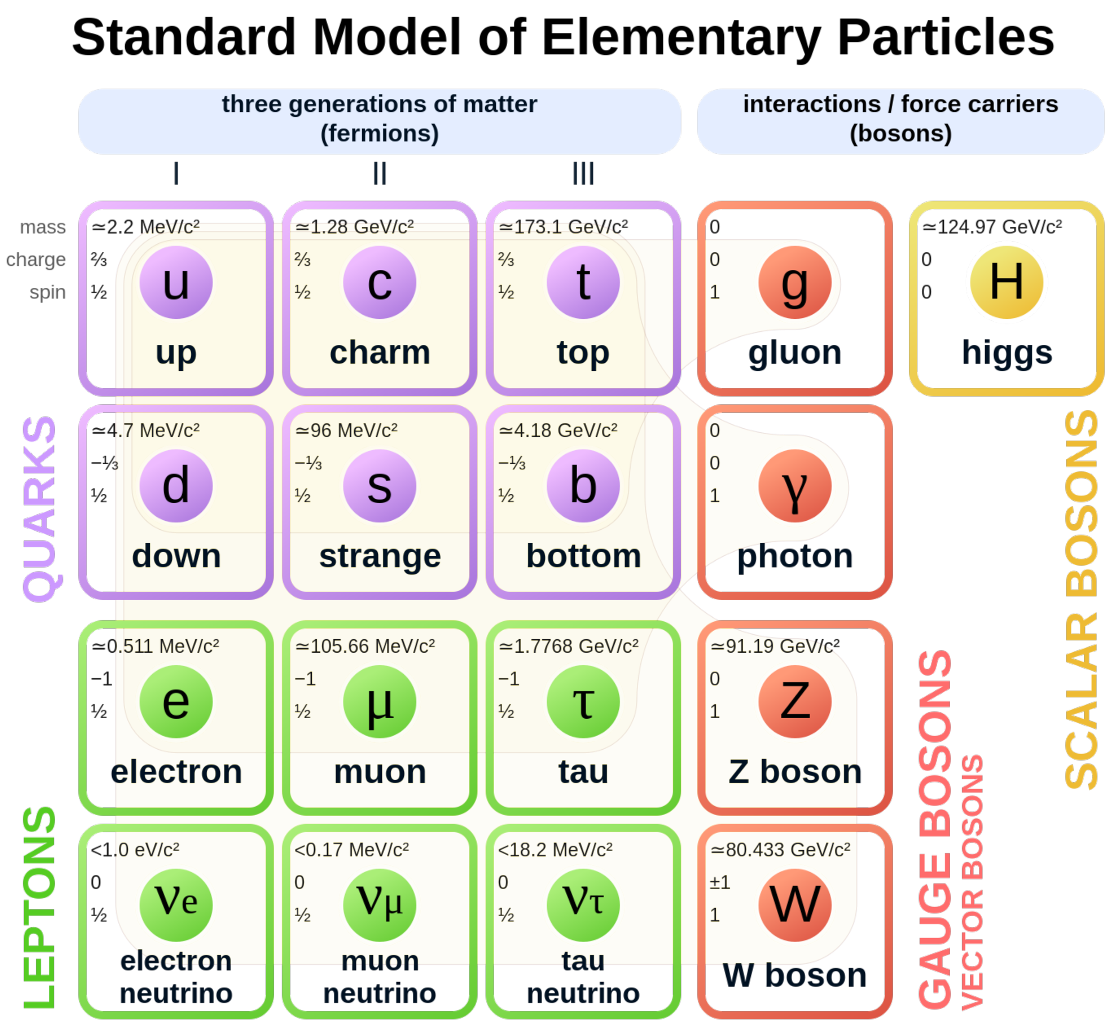

Fig. 2.1: Classification of the elementary particles of the Standard Model, with the fermions on the left and the gauge/scalar bosons on the right. Figure taken from [37].

Classically, a particle interacts with another via a field (for example, in electromagnetism, a positively charged particle generates an electric field that exerts an

force is minuscule considering the extremely small mass of neutrinos.

attractive/repulsive force on neighboring negative/positive charge). In QFT, fields are quantized, and the energy and momentum previously carried by the field are now conveyed by chunks, by quanta[9] [24]. So in particle physics, interactions are described as an exchange of quanta or force-carrying particles of spin 1, known as *(vector) gauge bosons*[10][27][35]. Following the remarks in Sec. 2|I-A, the term "(*vector*) *gauge*" emphasizes here the fact that the boson arises from a gauge vector field and therefore a gauge symmetry.

The most precise quantum field theory is the quantum electrodynamics (QED) that describes the interaction between charged particles and electromagnetic fields. It has been developped between 1947 and 1949 by Shin'-ichirō Tomonaga, Julian Schwinger, Richard P. Feynman and Freeman Dyson; only the first three received the 1965 Nobel Prize in Physics for their contributions[11]. It is based on a U(1) local gauge symmetry[12], that results into an interaction with charged particles mediated by massless photons. This continuous symmetry is associated to a conserved quantity, namely the electric charge. The dynamics of this interaction is given by the Lagrangian density of QED in Eq. 2.1.

$$\mathcal{L}_{QED} = \underbrace{i\bar{\psi}\gamma^{\mu}\partial_{\mu}\psi}_{\substack{\text{electron}\\ \text{kinetic term}}} + \underbrace{e\bar{\psi}\gamma^{\mu}A_{\mu}\psi}_{\substack{\text{electron-photon}\\ \text{interaction term}}} - \underbrace{m\bar{\psi}\psi}_{\substack{\text{electron}\\ \text{mass term}}} \underbrace{-\frac{1}{4}F_{\mu\nu}F^{\mu\nu}}_{\substack{\text{photon}\\ \text{kinetic term}}} \tag{2.1}$$

where

- γ^{μ} Dirac matrices that express the vectorial nature of the interaction and μ is the Lorentz vector index,
- A_{μ} the photon field,
- $F_{\mu\nu} = \partial_{\mu}A_{\nu} - \partial_{\nu}A_{\mu}$ the field-strength tensor,
- e the coupling constant of QED which coincides with the electric charge of the electron-positron field,
- m the electron/positron mass,
- ψ the electron-positron spinor field,

with the Einstein's notation $x^{\mu}x_{\mu} = \sum_{\mu=0}^{N} x^{\mu}x_{\mu}$ and the notations from [35].

Different terms appear in the expression of the Lagrangian density: the density of kinetic energy of the spinor field, the density of potential energy due to the

[9] Here, we present elementary particles as quanta of their underlying field as if the particles could be separated/reduced from their field, which corresponds to the usual experimentalist's picture of QFT. In fact, the relation between particles and fields is slightly more subtle [38].

[10] They are called *bosons* because, contrarly to the fermions, their intrinsic angular momentum (or spin) has an integer value.

[11] Unfortunately F. Dyson did not receive the Nobel Prize because i) his work was not considered as groundbreaking as the one of the three other laureates and ii) the Nobel Prize in a given field can only be awarded to organisation of maximum of three individuals [39].

[12] U(N) corresponds to the group of all unitary matrices to size $N \times N$. Thus, U(1) is a group containing all the continuous transformations of the phase of a complex number.

interaction between the spinor and gauge fields, the mass energy of the spinor field[13], the density of kinetic energy of the gauge boson (photon). The most interesting term is the second one, which describes the interaction between the charged particles and the photons. This interaction gives rise to different processes, usually pictured by Feynman diagrams. Fig. 2.2 shows the basic interaction vertex in QED.

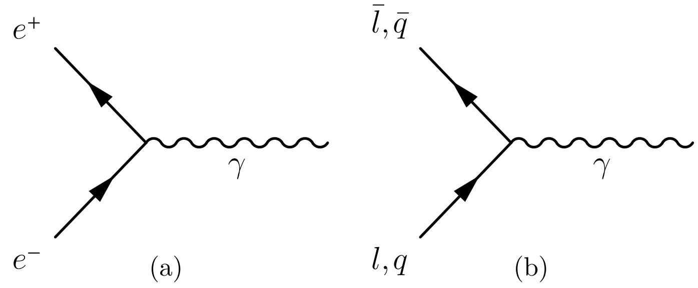

Fig. 2.2: Interaction vertex in QED: (a) involving an electron and a positron, (b) generalized to any charged particles.

Being the first quantum field theory developed, QED paved the way – and even served as a template – for all the subsequent quantum field theories. Therefore, it is not surprising that the form of Lagrangian density is the same for all the forces.

Following the success of QED, attempts to develop a quantum field theory for the weak interaction started in the 1950s; none of them could provide a satisfactory description. In the same decade, important discoveries have been made: the Wu's[14] (1956) and Goldhaber's (1957) experiments [40][41] showed that the P- and CP-symmetries are violated by the weak interaction. These led to conclude that this force has a vector-axial vector structure, meaning that only interacts with left-handed chiral particles and right-handed chiral anti-particles. Meanwhile, a few physicists – including Abdus Salam, Steven Weinberg, Schwinger and his PhD student Sheldon L. Glashow – foresaw that the weak and electromagnetic forces might be two aspects of the same phenomenon. Thanks to the work of Chen Ning Yang and Robert Mills on the development of a generalized gauge theory in 1954, Glashow delivered the electroweak interaction in 1961, which was consolidated later in 1967 and 1968 by Weinberg and Salam[15] respectively. In this quantum field theory, the electromagnetic and weak forces are described within an unified framework; the weak interaction is based on the SU(2) gauge group[16], three generators hence three gauge bosons: W^+, W^- and Z^0. These bosons exhibit two unique properties. First, contrarly to all other gauge bosons, these ones have an enormous mass ($m_{W^\pm} = 80.377$ GeV/c^2 and $m_{Z^0} = 91.1876$ GeV/c^2 [42]), which explains why the weak force is such a short-range interaction. Second, the $W^\pm$ bosons can change the flavour of quarks and leptons. The trend (or the probability) of the flavour-changing is given

[13] If the gauge boson is massive, there would be an extra mass term. Since the photon is massless, this term is null.

[14] Awarded of the 1957 Nobel Prize.

[15] For their contribution, Glashow, Salam and Weinberg receive the 1979 Nobel Prize.

[16] The S (for "special") refers to the group of all matrices whose determinant is equal to 1.

by the **C**abibbo-**K**obayashi-**M**askawa[17] (CKM) matrix [42][18] in Eq. 2.2.

$$V_{\text{CKM}} = \begin{pmatrix} V_{\text{ud}} & V_{\text{us}} & V_{\text{ub}} \\ V_{\text{cd}} & V_{\text{cs}} & V_{\text{cb}} \\ V_{\text{td}} & V_{\text{ts}} & V_{\text{tb}} \end{pmatrix} = \begin{pmatrix} 0.97425 \pm 0.00022 & 0.2253 \pm 0.0008 & 0.00413 \pm 0.00049 \\ 0.225 \pm 0.008 & 0.986 \pm 0.016 & 0.0411 \pm 0.0013 \\ 0.0084 \pm 0.0006 & 0.040 \pm 0.0027 & 1.021 \pm 0.032 \end{pmatrix} \tag{2.2}$$

Each matrix element provides the probability of transition from one flavour i to another j for quarks, but the same exists for the leptons and is called the **P**ontecorvo-**M**aki-**N**akagawa-**S**akata (PMNS) matrix. The elements of the PMNS matrix are slightly different from the CKM ones, though the structure and ordering are the same.

Finally, concerning the strong interaction, we will see later in its dedicated subsection, Sec. 2|I-C. Patience!

The overall picture of the Standard Model's elementary particles is presented in Fig. 2.1. To this figure should be added the antiparticles. Indeed, to each particle – fermion or boson – corresponds an antiparticle that has the same properties, because of the CPT invariance, but with oppositely sign quantum numbers. Consequently, this also means that both CKM and PMNS matrices are the same for particles and antiparticles.

There is, however, one element of the table in the Fig. 2.1 that has not been discussed yet, that is the Higgs boson. It originates from the electroweak unification, so let us retrace our footsteps. The principles of gauge invariance inevitably give rise to massless gauge bosons, like the photons but not the massive $W^{\pm}$, Z^0 bosons. At the time of Glashow's electroweak model in 1961, no one could imagine a mechanism to generate the enormous masses of the weak interaction force-carriers. In the same year, Jeffrey Goldstone showed that the process of spontaneous symmetry breaking[19] leads to the existence of massless gauge bosons, called Goldstone bosons. Three years later, in 1964, three independent groups (Robert Brout and François Englert; Peter Higgs; Gerald Guralnik, Carl Richard Hagen, and Tom Kibble) demonstrated the Goldstone bosons could be absorbed by the massless gauge bosons to acquire a mass: this is the Higgs mechanism. It is only in 1967-68, that Weinberg and Salam put to use this mechanism within Glashow's model to generate the masses of $W^{\pm}$ and Z^0 bosons. But this goes beyond the scope of the electroweak unification; with this

[17] The Universe is unfair: similarly to Dyson for the QED, Nicolas Cabibbo (the pioneer of the CKM matrix) was not awarded with the 2008 Nobel Prize, while Makoto Kobayashi and Toshihide Maskawa were.

[18] Mathematically speaking, this matrix relates the mass eigenstates to the weak eigentstates [35].

[19] This is the phenomenon in which a physical system perfectly symmetric breaks the symmetry without any external intervention. The most famous example of such process concerns the magnets. A material can be seen as an ensemble of microscopic magnets. If this material is ferromagnetic, all these magnets will tend to align with their neighbors. When the temperature increases, the thermal motions start to disrupt this alignement until the material is not magnetized anymore. Conversely, as the material cools down, neighboring magnets starts to align until a critical temperature, when all the magnets lines up in one macroscopic direction. All directions are equivalent but the magnet has to choose one. This choice breaks the symmetic situation when all the directions are equivalent; this is a *symmetry breaking*. Moreover, this choice is not influenced by any external agent, hence it is labelled as *spontaneous*.

mechanism, the mass of all elementary particles can be generated [33]. Incidentally, a new massive spinless particle, associated to a scalar field, emerges out of the Higgs mechanism: the Higgs boson. Its observation in laboratory was at the heart of Standard Model researches for decades until the 14th of March 2013 when the ATLAS and CMS experiments at the LHC at CERN announced the discovery of the Higgs boson [43][44]. The same year, Peter Higgs and François Englert receive the Nobel Prize for their contribution to the Standard Model.

I-C The strong force, a colourful interaction

Back in the 1960s, in the "glorious years" of particle physics, when physicists were submerged by the number of newly discovered "elementary" particles. Some of them were subject to the strong interaction, some were not; the former were referred as *hadrons*[20] and the latter as *leptons*, as discussed in Sec. 2|I-B. The hadrons were further sorted into two groups known as *mesons* and *baryons*[21]. But no one could draw out the underlying scheme between these particles and organise them into some kind of periodic table. There were some attempts though [45][46]; however the Mendeleev of particle physics is arguably Murray Gell-Mann.

In 1961, he (and independently Yuval Ne'eman) proposed a classification scheme called the *eightfold way* [47][48]. At that time, eight spinless mesons, eight vector mesons of spin 1 and eight spin 1/2 baryons were known. In each of these octets, a pattern emerges when the hadrons are organized into groups/multiplets of roughly the same mass, a hint of the underlying structure of strong interaction. A year later, the eightfold way is updated and completed with a decuplet formed of spin-$\frac{3}{2}$ baryons. However, one of the ten members of the decuplet was not yet discovered but this periodic table of elementary particles can predict its properties: a mass near the 1675 MeV/c^2, strangeness[22] of -3 and negatively charged, these are the characteristics of the Ω^- . Its existence is confirmed experimentally in 1964 by the Alternating Gradient Synchrotron at the Brookhaven National Laboratory (BNL)[23], validating the eightfold way once and for all.

Within the year of this discovery, Murray Gell-Mann (and independently Georges Zweig) unveiled the symmetry behind the eightfold way: there are no elementary hadrons; they are, in fact, all built out of more fundamental particles named *quarks*. A composite object made of bosons can only lead to a boson whereas, formed by fermions, the object is either a fermion or a boson depending on the number of constituents involved. Hence, the quarks must be fermions of spin one-half, mesons are

[20]The expression originates from the Greek *adros* meaning "thick and bulky".

[21]These terms originally refer to the mass of the particle: *meson* comes from the Greek root *meso* for "middle", that is in between the electron and proton masses; *baryon* stem from Greek *barys* for "heavy", suggesting any particle with a mass greater or similar to the one of the nucleons. Before the development of the quark model, the difference between the meson and the baryon was driven by their spin. The meson is a boson (integer spin values) where as the baryon is a fermion (half-integer spin values)[33].

[22]A quantum number introduced by Murray Gell-Mann in 1953 order to explain the *strange* behaviour of some particles, such as kaons [49]. Any particle with a non-zero strangeness value is dubbed *strange particle*.

composed of an even number of quarks, baryons of an odd number. The smallest odd number is one, but i) it does not make sense to say that a composite structure is made of one constituent and ii) we will see later in Sec. 2|I-C.i that a system of one quark is physically impossible. Thus, mesons must be made out of two quarks and baryons out of three; these are the simplest imaginable arrangements.

Originally, quarks exist in two flavours, *up* (u) and *down* (d), with fractional electric charges of $+2e/3$ and $-1e/3$ respectively. But an extra flavour was needed to explain the existence of strange hadrons: the strange quark, s, is born. It has the same properties as the d quark, except that it is much heavier and it has an assigned strangeness number of -1. Any strange hadrons actually contains one to three s quark, depending on their strangeness. Therefore, the predicted particle by the eightfold way, the Ω^- , corresponds actually to the strangest hadron possible, a baryon with three strange quarks.

With this particle comes the first difficulty of the quark model. Whatever the particle, it must obey the spin-statistics theorem. Quarks being fermions, the theorem states that two *identical* fermions can not occupy the same quantum states simultaneously. However, Ω^- is constituted of three exactly identical s-quark [50]. This problem was overcome by Oscar W. Greenberg [51], Moo-Young Han and Yoichiro Nambu [52] in 1964-65 that introduced a new quantum number, the colour. Each quark comes in three colours or variants labelled as red (r), green (g) and blue (b). In this way, the spin-statistics problem is solved but new questions arises. If quarks carry a colour, hadrons are a mixture of colours. This is assumed to be an equal mixture of all the colours, such that the hadrons are colourless. How come? Why are there no coloured hadrons?

Along the same line: in 1966, the main accelerator at the Stanford Linear Accelerator Center (SLAC) becomes operational and starts a program of deep inelastic scattering experiments in order to study the inner structure of nucleons. Based on James Bjorken's [53] and Richard Feynman's [54] calculations, the results of SLAC's experiments, in 1969, showed that the nucleons were made of point-like constituents of spin-$\frac{1}{2}$, dubbed *partons*, behaving as free particles [26]. The partons were nothing else than the quarks, and these observations established the validity the quark picture to the whole particle physics community. However, it is curious that the partons seem to behave as free particles but they can not escape the hadron.

These questions remain unanswered until 1973. This year had seen the development of Quantum Chromodynamics (QCD) – the quantum field theory of the strong force – and the discovery of two of its most salient properties, namely the colour confinement and the asymptotic freedom (discussed in Sec. 2|I-C.i). Fruit of the work of Harald Fritzsch, Heinrich Leutwyler and Murray Gell-Mann [55], the QCD describes the interaction between colour-charged objects, namely the partons. It is based on the gauge symmetry group SU(3), which has eight generators, giving rise to eight massless gauge bosons called *gluons*, and imposes the conservation of colour.

QCD is very similar to QED: the electric charge is replaced by a colour charge, antiparticles carry opposite colour charges, and the eight gluons take the role of the photon. The dynamics of QCD is given by the Lagrangian density in Eq. 2.3.

$$\mathcal{L}_{QCD} = \underbrace{i\bar{\psi}_q^i \gamma^\mu \delta_{ij} \partial_\mu \psi_q^j}_{\substack{\text{quark}\\\text{kinetic term}}} + \underbrace{g_s \bar{\psi}_q^i \gamma^\mu t_{ij}^a A_\mu^a \psi_q^j}_{\substack{\text{quark-gluon}\\\text{interaction term}}} - \underbrace{m_q \bar{\psi}_q^i \psi_{qi}}_{\substack{\text{quark}\\\text{mass term}}} - \underbrace{\frac{1}{4} F_{\mu\nu}^a F^{a\mu\nu}}_{\substack{\text{gluon}\\\text{kinetic term}}} \quad (2.3)$$

where, using the notations from [50],

- $g_s^2 = 4\pi\alpha_s$ with α_s the coupling constant of QCD,
- $F_{\mu\nu}^a = \underbrace{\partial_\mu A_\nu^a - \partial_\nu A_\mu^a}_{\text{Abelian part}} + \underbrace{g_s f^{abc} A_\mu^b A_\nu^c}_{\text{non-Abelian part}}$ the field-strength tensor,
- ψ_q^i the quark field spinor with colour index i such that $\psi_q = \left(\psi_{qR}, \psi_{qG}, \psi_{qB}\right)^\mathrm{T}$,
- m_q the quark *bare* mass induced by the Higgs mechanism,
- A_μ^a the gluon field with colour index a,
- $t_{ij}^a = \frac{1}{2}\lambda_{ij}^a$ and λ^a the fundamental[23] representation of the generator of SU(3) associated to the colour index a,
- f^{abc} the structure constants of SU(3).

As in QED, the Lagrangian density can be expressed with four terms; the quark-gluon interaction is described by the second one. However, the field-strength tensor $F_{\mu\nu}^a$ here admits an extra term because the generators of SU(3) do not commute. The non-Abelian property of the gauge group of QCD gives rise to gluon-self interactions, as shown in the Feynman's diagrams of Fig. 2.3.

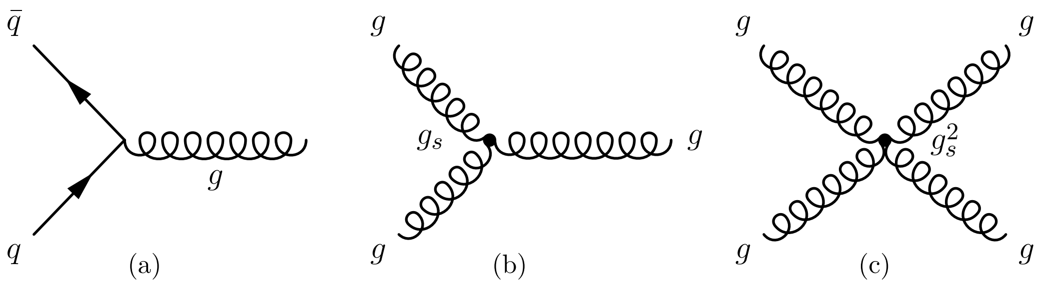

Fig. 2.3: The three possible interaction vertices within the framework of QCD: (a) quark-gluon, (b) triple-gluon and (c) four-gluon interactions.

Consequently to the self-interaction of QCD's force-carriers, gluons can not be colour neutral. To ensure colour conservation at the interaction vertex in Fig. 2.3(a), the gluon must carry a colour and an anti-colour charges. This calls for a revision of the term *partons*: it corresponds to any colour-charged elementary particle, that is the quarks *and* gluons.

[23] The representation of a group is *fundamental* when its generators are hermitian and traceless matrices.

Furthermore, quarks are bound together inside hadrons through the exchange of gluons, but because of their self-interaction feature, gluons can radiate other gluons (Fig. 2.3(b)); the latters can, in turn, split into a quark-antiquark pair (Fig. 2.3(a)) or emit gluons again, and so on. The static picture of hadrons with two or three quarks exchanging gluons turns out to be more complex, permeated in a *sea* of quarks (and antiquarks) and gluons[24]. However, the elements inside the sea do not determine the quantum numbers or properties of the hadron, as opposed to the "original" quarks; for this reason, the latter are often refered as *valence quarks*.

Finally, an incidental consequence of gluon's self-interaction is the running of the coupling constant. This can be understood by making a (anti)parallel with QED. Let us say we want to measure the coupling strength with a charged particle (an electron, for example). In QFT, the vacuum is not entirely empty, it contains pairs of particles and antiparticles that are constantly created and annihilated. Such a pair can also be formed by the cloud of *virtual*[25] photons surrounding the charged particle to be tested; in this case, it is said to *polarise the vacuum*. An example of this process can be found in Fig. 2.4(a). The positively charged particle from the vacuum is attracted to the initial electron, leading in a screening effect similar to the one found in a dielectric material (Fig. 2.4(b)). At large distance (or small energy), it is more difficult to penetrate inside the cloud of virtual particle-antiparticle pairs and to probe the initial charge, reducing the coupling strength. Conversely, at small distance (or large energy), the initial charge can be distinguished from the surrounding positively charged particles and the coupling strengthen. In QCD, the opposite happens. Because gluons carry a colour charge, the initial colour of the particle to be tested (a quark) gets spread out, as depicted in Fig. 2.4(c). Thus, an anti-screening effect occurs: the initial red-coloured quark spends most of its time coloured as blue or green, and the red colour charge is diluted in the surrounding cloud of partons. At large distance (or small energy), the initial quark r is overly apparent for an incoming gluon $\bar{r}g$ or $\bar{r}b$; conversely, at small distance (large energy), the initial red quark – likely converted into a green or blue quark – is invisible to such a gluon, resulting in a weakening of the coupling strength.

Before continuing, allow me to digress and finish with the different quarks within the QCD framework. The alert reader may have guessed that the story did not end with the strange quark. In 1964, James Bjorken and Sheldon Glashow introduced a new quark flavour: the charm quark. It is motivated by the idea of a quark-lepton symmetry[26] at that time, there was four known leptons (electron, muon and their associated neutrinos) and three quarks. But the charm quark definitely comes into play in 1970 by Sheldon Glashow (again), John Iliopoulos and Lucinao Maiani to

[24]An effect of the sea of quarks and gluons is the Bjorken scaling violation observed by the HERA experiment [27][35].

[25]Certainly the most vague concept in particle physics. It appears in perturbation theory (see later) and an attempt for a definition could be: it corresponds to a theoretical particle wich exhibits the same properties as ordinary particles but not necessarily (for example, they do not satisfy the energy-momentum relation), and with a lifetime so short that it could never be observed experimentally.

[26]The term *charm* is chosen for designating this fourth flavour because the definition found by Bjorken and Glashow in *American Heritage Dictionnary*: "an action or formula thought to have magical power", implying magical power to restore the quark-lepton symmetry [33].

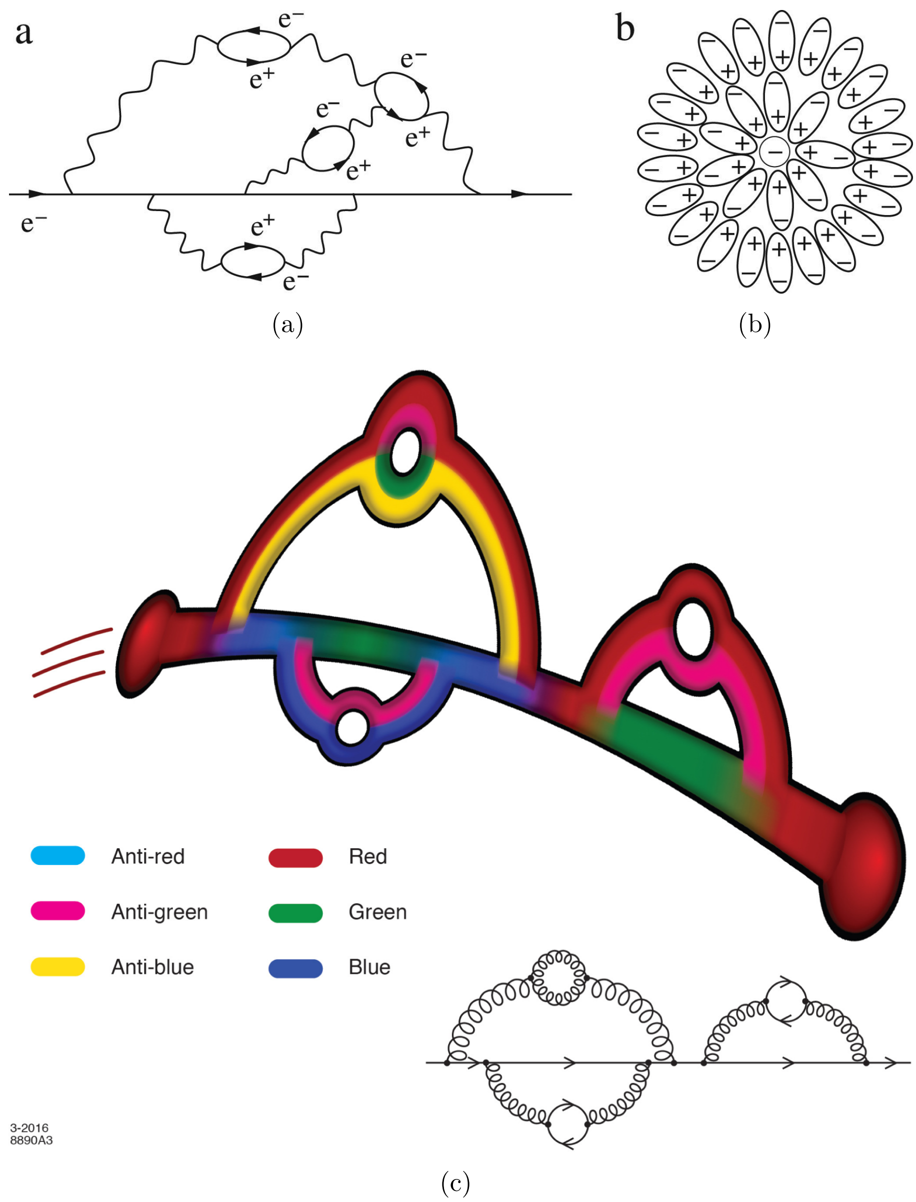

Fig. 2.4: (a) screening effect of an electron in QED, induced ;(b) analogy with the screening effect in a dielectric material; (c) pictural representation of the colour spread of an initially red coloured quark.

explain the strangeness-changing neutral currents[27]. Its existence is validated by the observation of the first charmed hadron in 1974 by Burton Richter (SLAC)[56] and Samuel Chao Chung Ting (BNL)[57]; both receive the 1976 Nobel Prize for that discovery. In parallel, a third generation of quark is introduced, in 1972 by

[27] This is typically the case of the decay of a negative kaon to a negative pion with a neutrino and an anti-neutrino ($K^- \to \pi^- \nu\bar{\nu}$). It is called a strangeness-changing neutral current because i) the strange particle (kaon) changed into an ordinary one (pion), and ii) there is no electric (or neutral) charge transfer between the hadrons to the leptons. This process was never observed in laboratory, as opposed to the strangeness-changing charged current: ($K^- \to \pi^0 e^- \bar{\nu}_e$). To eliminate the strangeness-changing neutral currents, a new quark flavour needed to be introduced [33].

Makoto Kobayashi and Toshihide Maskawa[28] to explain the observed CP violation. The particles composing this new family make their appearence in 1975, thanks to Haim Harari [58], under the name of *bottom* and *top* quarks[29]. Evidence of the bottom quark is found in 1977 by Leon M. Lederman at Fermilab [59]. Due to its large mass, the discovery of the top quark takes more time but ultimately occurs in 1995 by two groups at Fermilab [60][61].

I-c.i Running of α_s, colour confinement and asymptotic freedom

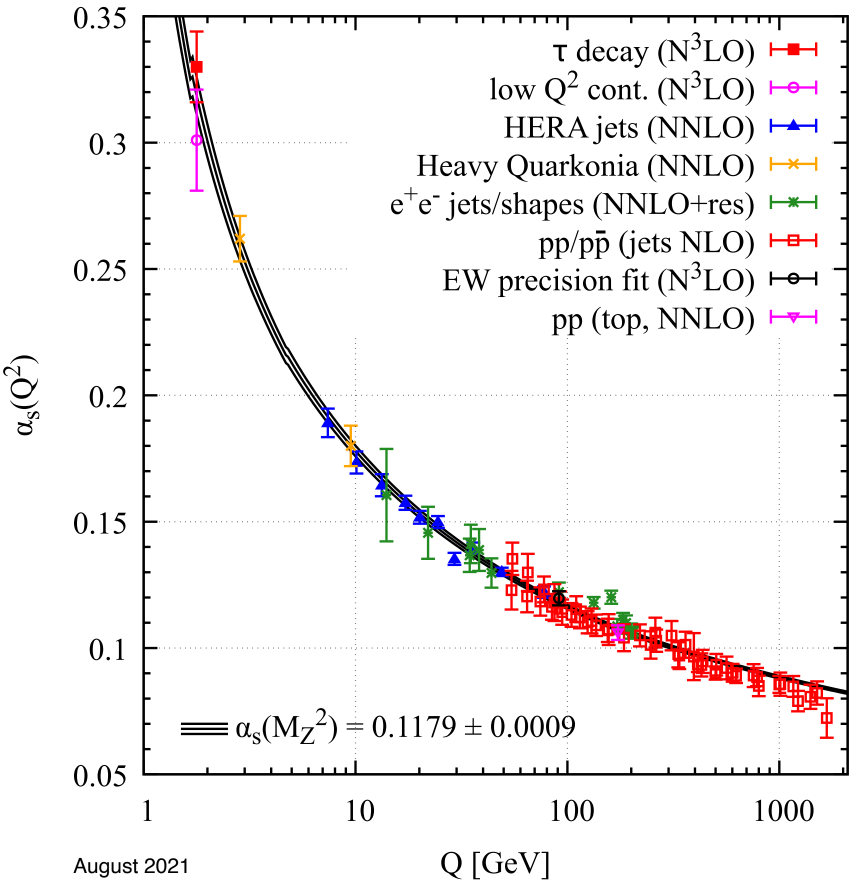

Fig. 2.5: Running of the coupling constant of the strong interaction, α_s, as a function of the energy transfer Q. The markers represent measurements based on perturbative calculation (the order of the perturbation development is indicated in parenthesis), the solid line corresponds to analytical prediction. Figure taken from [42].

Fig. 2.5 shows the running of the coupling constant α_s of QCD as a function of the energy transfer Q. The strength of the interaction varies considerably, such

[28]For the discovery of, at least, a third family of quarks, they both receive the 2008 Nobel Prize.
[29]Both belong to the same weak isospin doublet, as are the down and up quarks. To match the labelling of the first generation of quarks, the names *bottom* and *top* were chosen.

that two regimes can be discerned: one at large Q (or small distance) when the strong interaction is "weak" (α_s small), the other at small Q (or large distance) when the coupling constant gets "strong" (α_s large). Usually, these two regimes are delimited by defining an energy scale, denoted as Λ_{QCD}, at which $\alpha_s \sim 1$. This corresponds to $\Lambda_{QCD} \sim 200$ MeV[30]. Far above this value, the contribution of high-order diagrams decreases with their order such that most of them can be neglected, and QCD predictions can be calculated easily – or in the some cases, it simply renders the calculations possible – using perturbation theory. In this case, we talk about perturbative QCD (pQCD).

As the energy transfer decreases, the coupling constant increases and perturbative calculations starts to diverge until the point where it becomes infinite, at Λ_{QCD}. At this value or below, QCD is dominated by the contributions from high-order diagrams and can not be treated perturbatively anymore. The only way out is to perform analytical calculations, which is not possible due to the complexity of QCD. A more viable option is to resort to numerical calculations. A well-established technique is called *lattice QCD*, where to each (space-time) point of the lattice/-grid corresponds a spinor field representing the quarks possibly connected (or not) by links describing the gluon vector field. Although it provides some insights on non-perturbative physics aspects of QCD, it is extremely demanding in terms of computational power and time – these two factors being strongly dependent on the lattice size.

A phenomenological approach of QCD, supported by lattice calculations, can also be followed by considering that the interaction potential between two quarks separated by a distance r is approximated by[31]

$$V(r) \approx -\frac{\alpha_s(r)}{r} + \kappa r, \tag{2.4}$$

where the constant κ is typically about 1 GeV/fm [62]. The alert reader recognises the first term as the Coulombian-potential, similar to the one in QED; the second term corresponds to an elastic spring-type force. As illustrated in Fig. 2.6, they describe two specific behaviours of the QCD interaction potential.

At small distance ($r \lesssim 0.1$fm), the Coulomb-type term dominates, the interaction potential diminishes asymptotically as the distance decreases; it is not divergent though, as α_s also varies. The quarks interacts less and less, and becomes quasi-free. This phenomenon, known as *asymptotic freedom*, has been discovered by David Gross, Frank Wilczek in 1973 [64] and Hugh David Politzer in 1974 [65], and sets the groundwork for the development of a quantum field theory of strong interaction, that is the QCD[32]. Neither the electrostatic force between two charges nor the

---

[30] The definition of Λ_{QCD} is convenient because it allows to classify quarks as a function of their mass hierarchy with respect to Λ_{QCD}: u, d and s quarks belongs to the light-flavour sector ($\Lambda_{QCD} \ll m_s, m_u, m_d$), the others are heavy-flavour quarks ($m_t, m_b, m_c \gg \Lambda_{QCD}$).

[31] The expression of the potential is experimentally motivated by the ordering in the spectra of the charmonium ($c\bar{c}$) and bottomium ($b\bar{b}$) bound states [35] [62].

[32] In the early seventies, the common belief among the theoreticians was that quantum field theory fails to describe the strong interaction, and therefore it would be impossible to have a common mathematical framework for all the known forces (except gravity) [33].

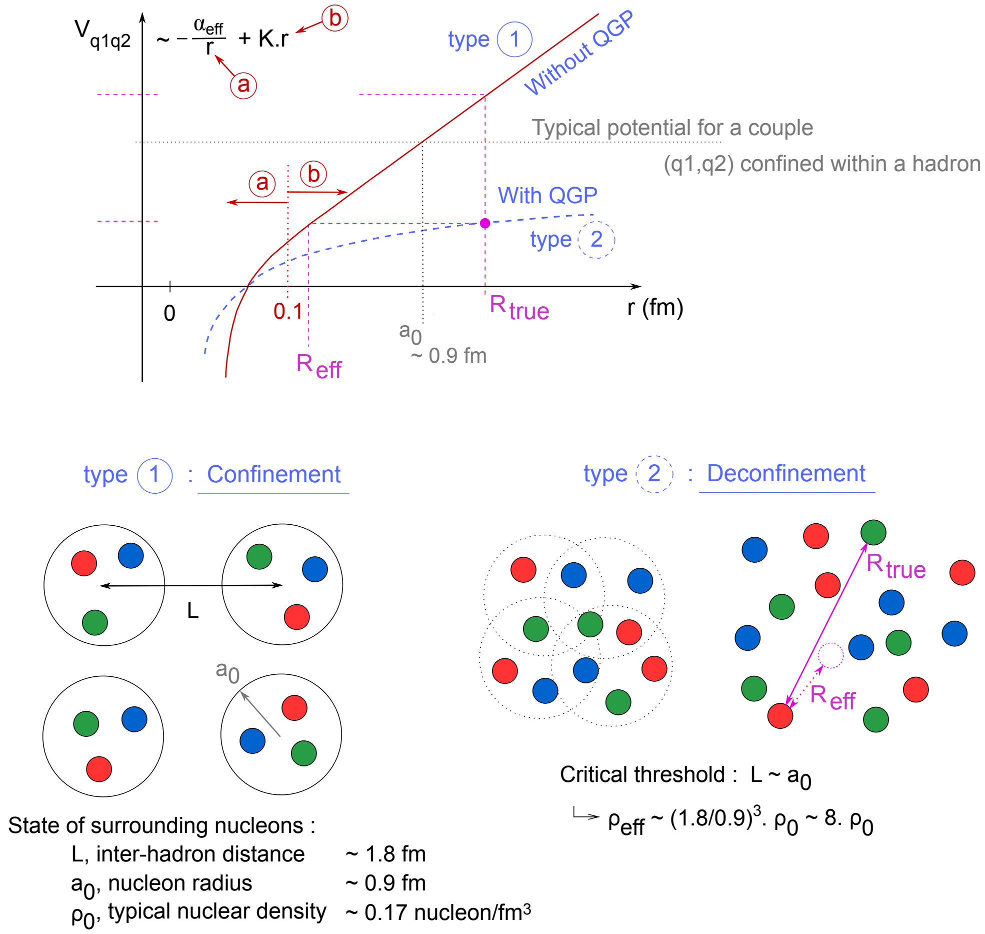

Fig. 2.6: QCD interaction potential between two coloured-objects (quark-quark or quark-antiquark) as a function of their separation r. Figure taken from [63].

gravitational force between two masses exhibit this property; in these cases, the interaction gets weaker as the distance increases between the two objects.

Conversely, the second term takes the upper hand at $r \geq 1$fm, the force increases linearly with the distance between the two quarks, as if they were connected by an elastic or spring made of gluons. As the quarks are pulled away, the energy stored in the spring of gluons accumulates until it reaches the threshold to create a quark-antiquark pair[33]. This description is shown on Fig. 2.7. The spring tying together the initial $q_i\bar{q}_i$ pair ruptures and the accumulated energy is expended on producing a $q_1\bar{q}_1$ pair: the freshly created quark, q_1, binds with $\bar{q}_i$, $\bar{q}_1$ with q_i. This process continues until all the $q\bar{q}$ pairs have a sufficiently low energy to combine into a hadron. Note that the initial quark-antiquark pair could be replaced by a pair of gluons and the process would still be the same. As a result, any colour-charged particle – quark or gluon – can not be found isolated; they must be confined in a colour-neutral object, such as meson and baryon[34]. This phenomenon is refered as

[33]There is an alternative scenario: the energy stored in the spring of gluons continues to increase until it reaches the threshold to create not one but two quark-antiquark pairs. Obviously, this path – which explains the production of one or several baryons from the vaccum – demands more energy and thus is less probable to occur.

[34]If there is (ordinarily...) no such thing as free parton, the same would be true for a colour-charged hadron. For this reason, baryons and mesons are colour-neutral structures.

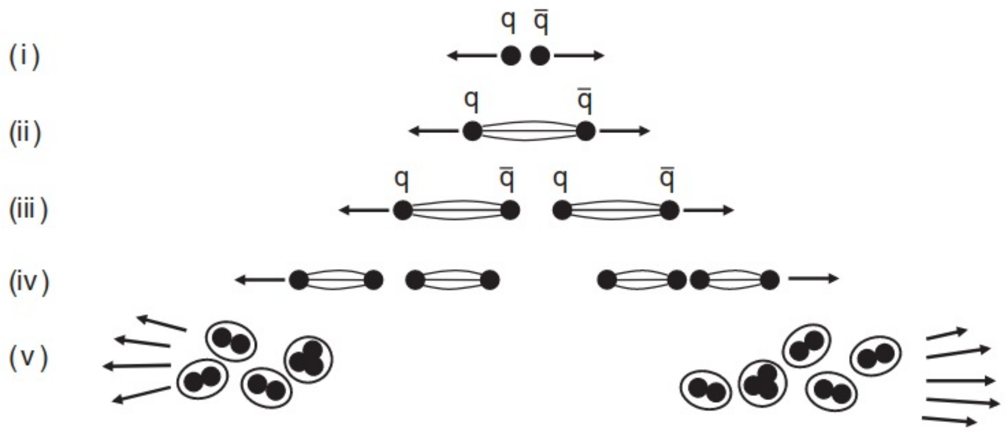

Fig. 2.7: Schematic of the quark confinement: (i) the quark and antiquark are pulled away from each other;(ii) as they separated, the string of force tying together the pair stretches; (iii) the energy stored in the string now exceeds the necessary energy for creating a new quark-antiquark pair, the string will break and the two initial quarks will form smaller strings with the newly created pair;(iv) this process continues;(v) until all the quarks and antiquarks have a sufficiently low energy to form hadrons. Figure taken from [35].

colour confinement.

Interestingly enough, the quark confinement is analogous to the behaviour of a magnet. The latter consists of a north and south poles. If one tries to isolate one of the poles, for example, by cutting the magnet in half, this would only yield into two small magnets. Like the quarks, no one has ever seen an isolated magnetic pole (magnetic monopole).

I-c.ii Chiral symmetry breaking

In Eq. 2.3, the Lagrangian density of QCD was presented and split into four different terms. The quark and gluon kinetic energy and the quark-gluon interaction terms preserve the chiral symmetry, meaning that they leave the chirality of the quarks unchanged. The mass term, though, mixes the left- and right-handed particles:

$$m_q \bar{\psi}_q^i \psi_{qi} = m_q \left(\bar{\psi}_q^{i,L} \psi_{qi}^R + \bar{\psi}_q^{i,R} \psi_{qi}^L \right). \tag{2.5}$$

The quark mass, m_q, controls whether the chiral symmetry is broken or preserved. For massless quarks, this term is null hence left- and right-handed particles do not interact together; they would live, somehow, in two separate worlds. Consequently, every hadron would have a twin, identical in every point apart from the handedness: one is left-handed, the other right-handed. In practice, the quarks have a finite mass but, for the light-flavour ones, it is sufficiently small to consider the chiral symmetry as an approximate symmetry. Therefore, chiral partners are expected to have slightly different masses. However, this is clearly not the case of the ρ ($m_\rho = 770\text{MeV}/c^2$) and a_1 ($m_{a_1} = 1260\text{MeV}/c^2$) mesons, meaning that the chiral symmetry is much more broken than expected [25].

To be exact, it is *spontaneously* broken[35]. This concept is visualised in Fig. 2.9. Returning to the example in the note 19, the continuous transition of the ferromagnet is characterised by an order parameter: the magnetisation. When the temperature is so high that the thermal motions disrupt the alignement of all the magnetic dipoles, the potential is symmetric and the minimum is centred at zero magnetisation (left Fig. 2.9). As the temperature decreases and the magnet cools down, the symmetry of the potential is preserved but there are now two minima. The system (the ball) has to choose one, acquiring a non-zero magnetisation in the process, and hence breaking the symmetry (right Figs. 2.9).

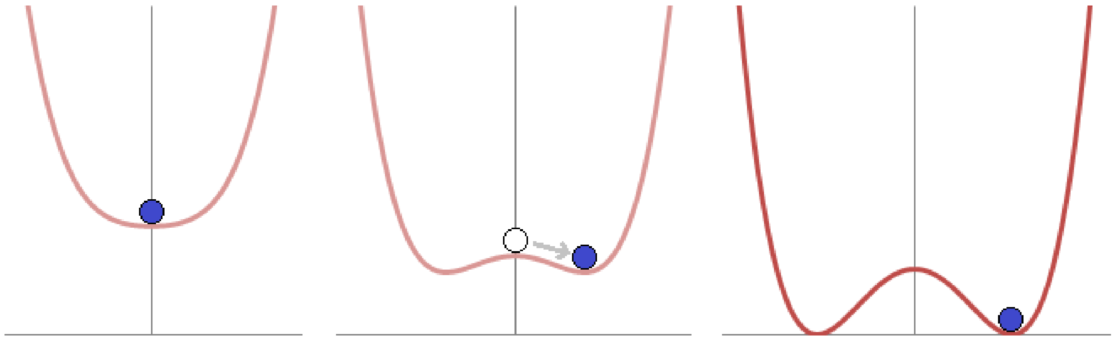

Fig. 2.8: The left figure represents the shape of the potential at high energy, there is one minimum and it is centred on zero. Right figures: as the energy decreases and below a certain critical temperature, the ground state is no longer centred on zero but some distance away from it. Both ground states are equivalent, the system chooses one of them; this is a spontaneous symmetry breaking. The x-axis here represents the order parameter. Figure taken from [66].

The same process occurs for the chiral symmetry but, in this case, the order parameter is the *chiral condensate*. This quantity, $<\psi_q\bar{\psi}_q>$ or $<q\bar{q}>$, measures the coupling between left- and right-handed particles in vacuum. It was mentioned earlier that, in QFT, the vacuum is not empty but is composed of fleeting particle-antiparticle pairs that pop in and out. It could be that the Lagrangian density of QCD have an approximate chiral symmetry, but the vacuum does not. This means that particles with different handedness in the vacuum may (or not) interact together, depending the vacuum expectation value of the chiral condensate. If the $<q\bar{q}>$ is null, the chiral symmetry is restored (left figure 2.9). Conversely, it is spontaneously violated when the chiral condensate is non-zero (right figures 2.9).

This symmetry was extensively studied by Yoichiro Nambu and Giovanni Jona-Lasinio in 1961 [67]. In their model, the chiral condensate emerges from the passage of particles in the vacuum[36]; for that reason, the chiral symmetry breaking is qualified as *dynamical*. Moreover, as the partons (inside a hadron) travel through the vacuum, they interact with the condensate and acquire an additionnal mass, the *dynamical mass*[37]. Predominant fraction of the hadron mass originates from this

[35]Well, it is also *explicitly* broken but we will pass on that detail.

[36]In fact, the chiral condensate, and hence the spontaneous chiral symmetry breaking, is a consequence of the colour confinement [26].

[37]As opposed to the *bare mass* stemming from the Higgs mechanism. It should be mentioned

extra mass: for example, the proton mass sits ~ 938 MeV/c^2 and the bare mass of its quark constituents represents almost 10 MeV/c^2, that is ~ 1% of proton mass.

On a side note, lattice QCD calculations predict that the chiral symmetry can be restored by heating or compressing matter. This is clear on Fig. 2.9 where the chiral condensate vanishes as the temperature and/or density increases. In such conditions, the ordinary hadronic matter undergoes a phase transition, in which hadrons are only clothed by the bare mass of its constituents.

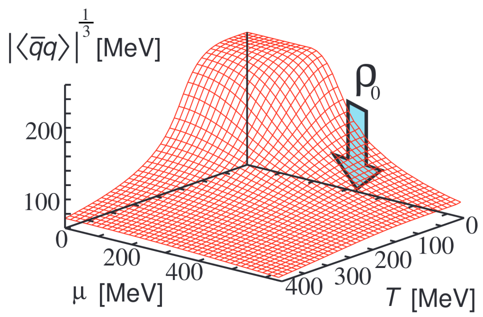

(a)

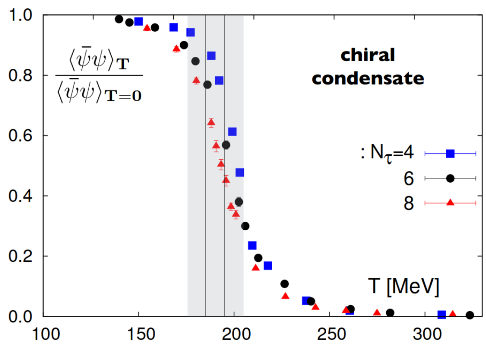

(b)

Fig. 2.9: Lattice QCD results on the evolution of the chiral condensate as a function of (a): the matter density (or the baryochemical potential μ) and the temperature (T) [68], (b): the temperature for different lattice points N_τ [69]. The arrow on the left figure indicates the value of μ corresponding the ordinar nuclear density, ρ_0. The grey bands on the right figure indicate a range for the transition temperature.

I-C.iii The QCD-phase diagram

In addition to the chiral phase transition, another one comes onto stage as the temperature increases. The Fig. 2.10 shows the predicted evolution of the pressure, energy density and entropy density for a hadron gas as a function of the temperature of the medium. The properties of the gas change rapidly when the temperature reaches $T_c = 154$ MeV, indicating the liberation of many degrees of freedom. In this case, these are the partons – ordinarly confined within hadrons – that now undergoes a *deconfinement* transition and becomes quasi-free.

I write *quasi*-free because even at $T \sim 400$ MeV, the energy density does not reach the ideal gas limit. As a consequence, the quarks and gluons are still interacting but weakly. Due to this shared similarity with the plasmas, this new state of hadronic matter is dubbed *quark-gluon plasma* (QGP). Note that, because the coupling between the partons decreases with the increasing momentum transfer and temperature (asymptotic freedom), the energy density will ultimately overlap with

that nothing prevents the gluons to acquire also a dynamical mass. In this case, there would not be massless anymore.

the ideal gas limit but at much larger temperature though.

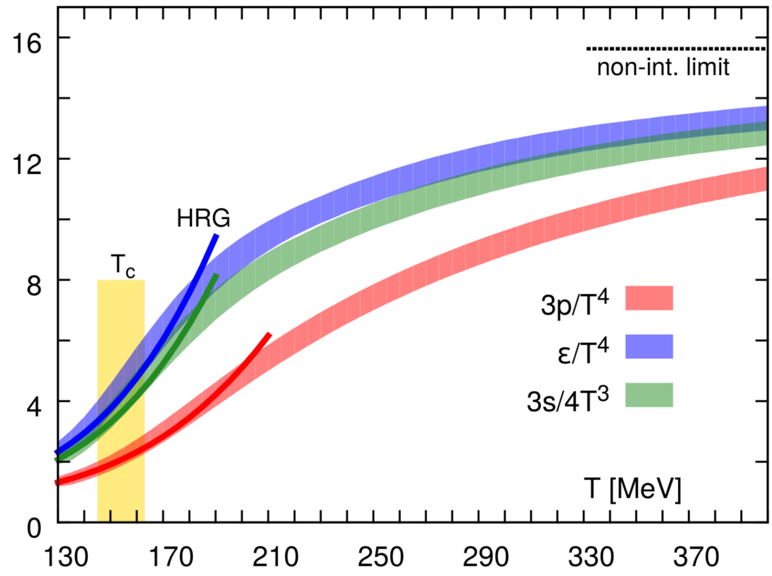

Fig. 2.10: Lattice QCD calculations of the pressure (p), energy density (ϵ) and entropy density (s) normalised to the fourth (third, for the last quantity) power of temperature. The solid lines represent the prediction of the hadron resonance gas (HRG) model, the black dashed line indicates the energy density in the limit of an ideal gas. The transition temperature T_c is equal to 154 ± 9 MeV. It should be emphasised that these predictions have been obtained assuming a zero net baryon density. Figure taken from [70].

The Fig. 2.11 provides the full QCD phase diagram. As it can be seen, there are two general ways to form a quark-gluon plasma: either one increases the temperature, or one increases the net baryonic density by compressing hadronic matter. The above phase transition corresponds to the former: by heating up the system at (almost) zero net baryon density, ordinary nuclear matter transforms first into a hadron gas and then undergoes a phase transition towards a QGP. This is what someone would see if he/she could rewind the videotape of the time-evolution of the Universe, from nowadays to a few μs after the Big Bang. In the latter, the ordinary nuclear matter at relatively low temperature acquires, by compression, a larger and larger baryon density until the system transforms into a QGP. This state of matter is supposed to be present in the core of neutron stars[71], with potentially a colour superconductor behaviour [72].

There is a profund difference in the nature of the phase transition between the one in the high-temperature region and the other with a high baryon density. Similarly to chiral transition on Fig. 2.9, the Fig. 2.10 shows a smooth evolution from one phase to another, indicating a second order — or at least, a crossover — phase transition [74]. In contrast, the high baryon density driven evolution is expected to be more abrupt, more sharp as when ice melts to turn into water. This corresponds to a first order transition. It follows that there must be a critical point somewhere in the middle of the phase diagram, joining the first and second (or crossover) phase transitions [75]. Its precise location is currently unknown, as no singularities have

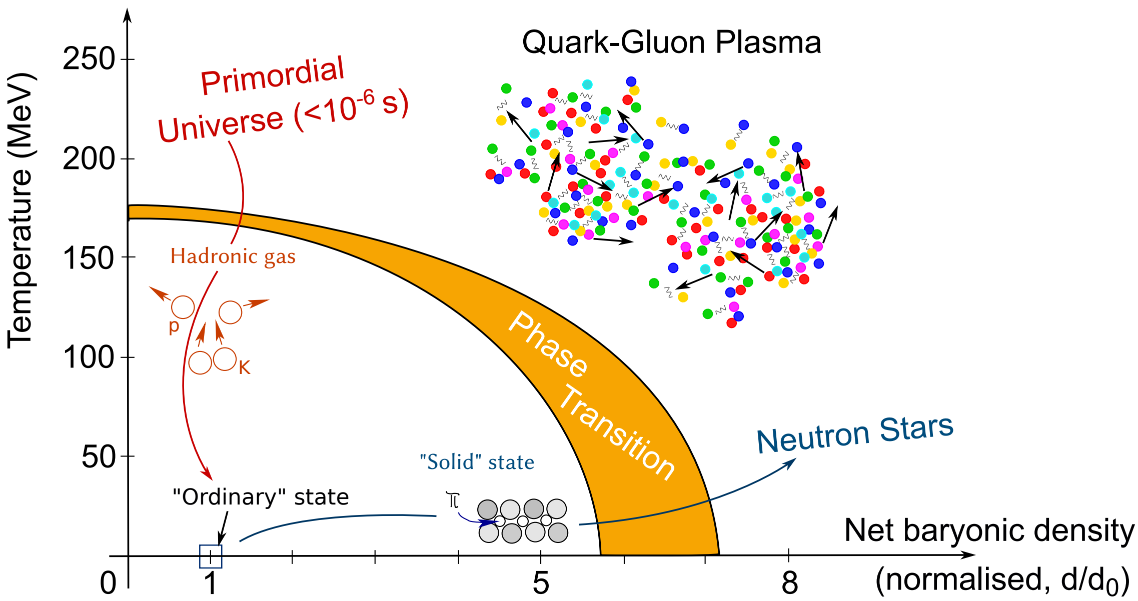

Fig. 2.11: Schematic representation of the QCD phase diagram as a function of the temperature and the net baryonic density. The latter is normalised to the net baryon density of ordinary nuclear matter. Figure taken from [73].

been observed yet.

II The Quark-Gluon Plasma

Each field of research has its pioneers and the study of the quark-gluon plasma is no exception. The first one was arguably Rolf Hagedorn, who approached the particle production making use of statistical physics. This endeavor led ultimately to the invention of the statistical bootstrap model (SBM) in 1964. At that time, a large number of massive resonances were observed, and this model provided a successful production mechanism for these particles[38]. However, this description was conceived before the development of the quark model. When the quarks were finally considered as the elementary building blocks of hadrons, an extension of SBM was called for [76].

The mutation of the statistical hadronisation model was achieved by the father of SBM and Johann Rafelski, between 1977 and 1980. This process led to a new paradigm. It was realised that, at a certain temperature, hadrons are melting to form a new phase composed of boiling quarks: the quark-gluon plasma. Although this concept was already intuited before by numerous physicists – including Peter Carruthers in 1974 [77] or George F. Chapline and Arthur K. Kerman in 1978 [78] –, it was only approached qualitatively.

[38] The statistical bootstrap model considers a gas of interacting hadrons, composed of all possible particles and their resonances, in a heat bath. If several light hadrons and/or resonances get compressed into a smaller volume, they could themselves be considered as a highly excited and massive resonance (also called fireball). Thus, the hadron gas rather corresponds to a gas of fireballs, that can also become a fireball in itself if compressed. This description provided an explanation for the mass spectrum of hadronic states.

Nevertheless, Chapline and Kerman were the first ones to make the connection between the QGP and (relativistic) heavy-ion collisions. The same year, this point is addressed quantitatively by Siu A. Chin[79] and later refined in a paper by James D. Bjorken in 1983 [80]. In this renowned publication, Bjorken presents an analytical solution for one-dimensional relativistic hydrodynamics in heavy-ion collisions, as well as the space-time evolution of the QGP at mid-rapidity (*Bjorken scenario*), laying down the foundations for the research programme at CERN.

Starting in 1986, a vast number of heavy ion experiments emerges at the CERN's Super Proton Synchrotron (SPS): WA85, NA36, NA35, Helios-2, NA38, WA80, and their future descendants [81]. At first, ^{16}O and ^{32}S nuclei were accelerated at 200 GeV (per nucleon) until 1995, when the SPS switched to ^{208}Pb beams with an energy per nucleon of 158 GeV. In a press conference held in February 2000, CERN reports to have "compelling evidence that a new state of matter has been created. The new state of matter found in heavy-ion collisions at the SPS features many of the characteristics of the theoretically predicted quark-gluon plasma" [4]. This announcement marks a turning point for QGP research: partonic matter is not a mere theoretical concept anymore; it becomes real, tangible and measurable.

The Relativistic heavy-ion Collider (RHIC) at BNL enters in operation in the next few months, with its four experiments – BRAHMS [6], PHOBOS [7], PHENIX [8], STAR [9] – dedicated to observe and characterise the QGP under different observables. In April 2005, BNL holds a press conference in order to present the results of the RHIC experiments, and by doing so, confirms the existence of "a new type of nuclear matter" [5].

Nowadays, the study of the QGP is mainly centred around two accelerators: the RHIC at BNL and, since 2009, the Large Hadron Collider (LHC) at CERN. Alike RHIC, the latter also has four experiments: ATLAS, CMS, LHCb and ALICE. Although, they all have a heavy-ion research programme, ALICE is specifically designed to analyse the QGP. Concretely, it pursues the exploration of the QCD phase diagram and the characterisation of this new state of matter initiated at the RHIC, but at much higher energies. For comparison, the LHC delivers Pb-Pb collisions at a centre-of-mass energy per nucleon $\sqrt{s_{\mathrm{NN}}}$= 2.76 and 5.02 TeV, and Xe-Xe collisions at $\sqrt{s_{\mathrm{NN}}}$= 5.44 TeV. This is, at least, twenty times more energetic than at the RHIC. The LHC accelerator, as well as the ALICE collaboration, are presented in the next chapter, Chap. 3.

II-A The time evolution of a heavy-ion collision

We timidly started above to raise the question of how a heavy-ion collision leads to the formation of the QGP? This point was addressed by Bjorken in his scenario of the same name. Although the current description turns out to be more complex than anticipated, the Bjorken scenario still provides the key steps of the QGP formation process. The following discussion is structured around the Figs. 2.12 and 2.13

A facility, such as the LHC or RHIC, accelerates heavy nuclei to ultra-relativistic speed. At the LHC energies, the Pb nuclei in each beam are accelerated to, at least, 1.38 TeV[39], which corresponds to a Lorentz factor γ of about 1500. Consequently, as Bjorken argued [80], even though the partons involved in the collision carry a tiny fraction of the incident beam energy, the nuclei are so extremely boosted that the space-time evolution of the system should be the same in all centre-of-mass frames near central rapidity, and thereby the particle yield should be flat as a function of rapidity, defining a central plateau structure for particle production. Moreover, at such energies, the nuclei are not stopped but rather continue to recede in opposite direction with respect to the collision point; this is the *Bjorken regime* or *transparency regime* and corresponds to net baryonic density close to zero[40]. Another implication is that, because of the length contraction, the nucleus looks like a highly-contracted pancake at mid-rapidity, as can be seen on Fig. 2.12.

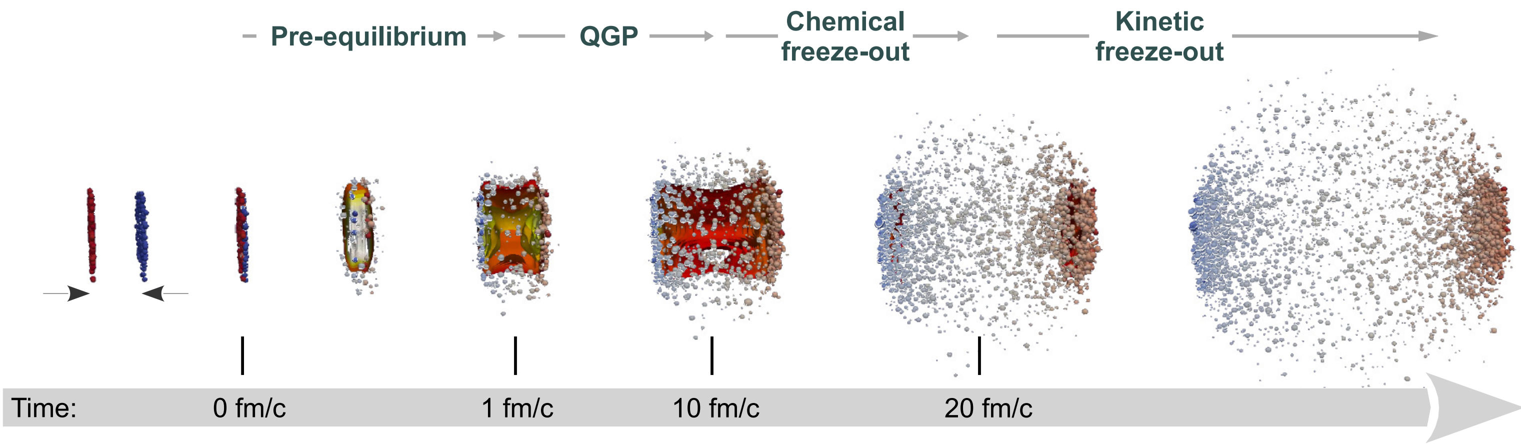

Fig. 2.12: Simulation of the time evolution of a heavy-ion collision, rendered in seven pictures. Figure originally created by Hannah Petersen, taken from [82] and modified by the present author.

The two extremely boosted nuclei approach each other and collide head-on[41]. At the same time, the clock associated to the centre-of-mass frame starts to run and indicates 0 fm/c.

The partons of each nuclei start interacting via either hard-processes – that involve large momentum transfers and lead to the creation of high momentum partons or massive quarks such as the charm, bottom or even top quarks – or soft-processes,

[39]The least energetic Pb-Pb collision available at the LHC being $\sqrt{s_{\mathrm{NN}}}$= 2.76 TeV, each beam carries 1.38 TeV per nucleon.

[40]As opposed to the *Landau regime* or *stopping regime*, where the nuclei are completely stopped in frontal collisions. It occurs only for collisions at centre-of-mass energies up to a dozen of GeV per nucleon pair. These two regimes actually relates to the two different QGP phase transition: either by heating the system (Bjorken scenario) or compressing it (Landau scenario).

[41]Note that this is not necessarily the case, the two nuclei can be slightly shifted. The *impact parameter* quantifies the offset usually in fm, or alternatively in percentage. In the latter case, we talk about *centrality*. Both parameters are accessible by making use of a *Glauber model*, that provides a semi-classical picture of a nucleus-nucleus collision as a function of the average number of nucleons and nucleon participants in the collision.

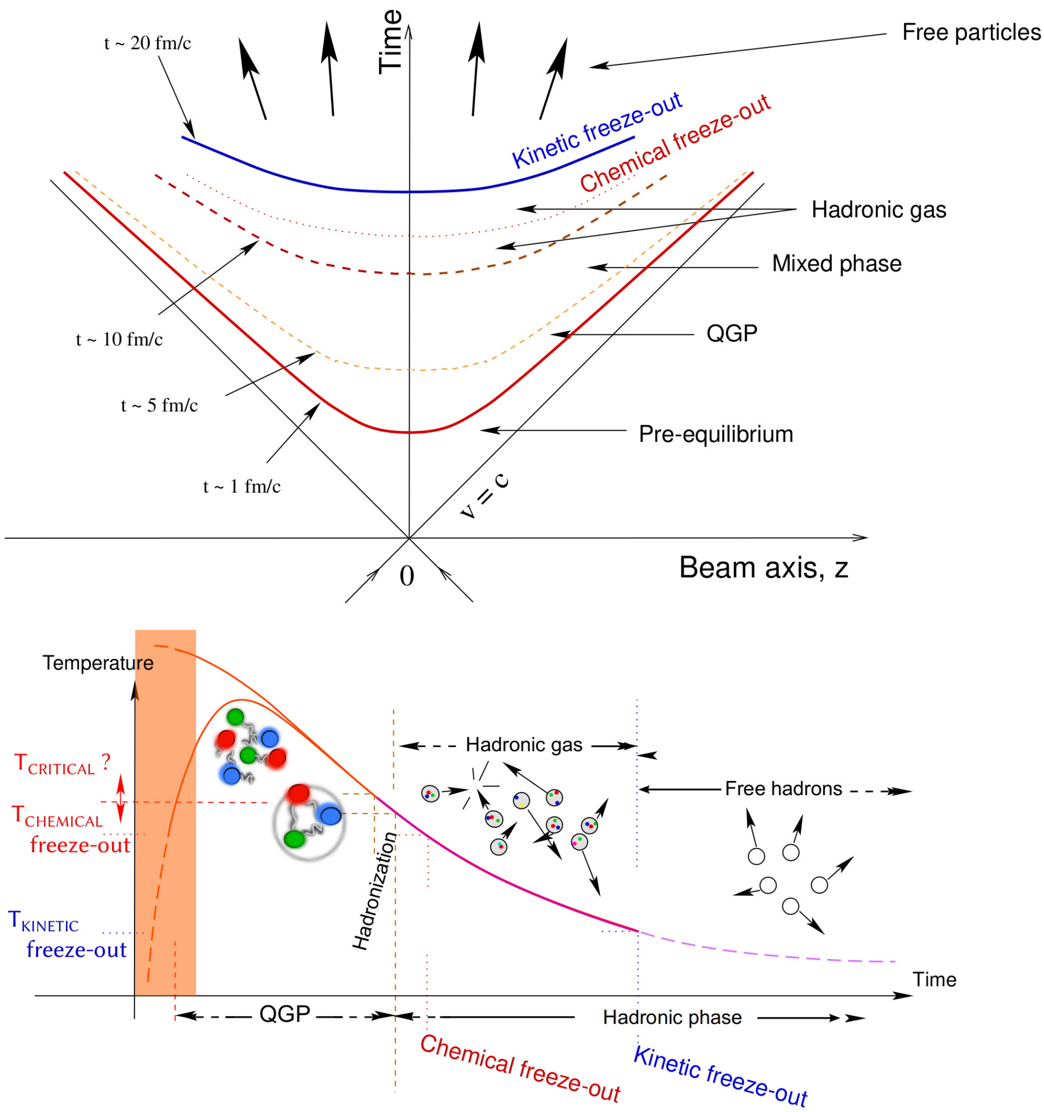

Fig. 2.13: The two views of the Bjorken scenario for ultra-relativistic heavy-ion collisions. Top panel: space-time evolution. Bottom panel: temperature-time evolution. Figure taken from [83].

characterised by small momentum transfer and representing most of the interactions in the initial stage of the collision. As the number of parton-parton interaction increases, the energy density of the system builds up enabling the creation of quarks and gluons out of the vacuum. Rapidly, a dense region of matter (dubbed "fireball") is formed, where partons are strongly coupled but not yet thermalised. This is the pre-equilibrium phase.

Here, the emphasis is on coloured particles, but other kind particles can be produced in the fireball, namely the leptons and photons. Because i) they carry no colour charge and ii) the typical interaction time of the weak ($\approx 10^{-10}$ sec) and electromagnetic forces ($\approx 10^{-16}$ sec) is too short compared to the timescale of a heavy-ion collision ($\approx 10^{-23}$ sec), they will simply escape the medium unaffected.

If the energy density is high enough (typically around 1 GeV/fm ^{3}), the initially produced matter undergoes, first, a phase transition towards the restoration of the chiral symmetry and, if possible, then towards the QGP. Due to multiple interaction between the medium constitutents, the energy gets distributed evenly among them leading the system to a thermal equilibrium around 1 fm/c ($\approx 10^{-23}$ sec) after the collision[42].

Once the QGP is formed, it experiences two expansions. Driven by the non-uniform geometrical energy distribution in the initial stage of the collision, a pressure gradient appears in the QGP, which results in a radial expansion of the system. Furthermore, the boost of the two incident nuclei causes the plasma of quarks and gluons to inflate in the longitudinal directions. Since the energy deposited initially in the system is fixed and its spatial size keeps extending, the energy density decreases and inevitably, the fireball cools down.

At some point, most of the parts of the system goes below the critical temperature, the deconfined partons start to recombine into hadrons. The QGP evaporates into a gas of hadrons. Note, that because the chiral transition – in this case, from a restored symmetry to a broken one – occurs below T_c, the mesons and baryons formed during this hadronisation process only carry the bare mass of their constituents. At least, until the system further cools down and undergoes a phase transition towards a breaking of the chiral symmetry, as explained in the Sec. 2|I-C.ii.

The energy density within the hadron gas remains significant, sufficiently to allow for inelastic collisions. Consequently, the chemical composition in terms of particle species is in constant evolution. Around 10 fm/c, as the energy density decreases, inelastic interactions become less and less frequent. They become impossible when the gas reaches the *chemical freeze-out* temperature. The particle composition is now fixed but hadrons can still interact elastically.

Although, the hadron content should be fixed, some resonances can still regenerate via pseudo-elastic scattering. This is, for example, the case of the K^{*0} that can be recreated through $\pi^{\pm}$-$\mathrm{K}^{\mp}$ interaction. On the other hand, elastic scatterings modify the momentum of one of its decay products. In such a case, the measured yield would decrease.

At 20 fm/c, the hadron gas fades into free hadrons. The momenta of the hadrons are now fixed. This is the *kinetic freeze-out*. These particles will fly towards the detectors and, for some of them, decay via weak or electromagnetic interactions. Either the particles originate directly from the collision or are decay products, once they have reached the detector, they will be detected and reconstructed, giving rise to an event such as the one displayed in the Fig. 2.14.

In total, the QGP only exists for about 10^{-22} sec, which is currently impossible to reach for the most advanced readout electronics. The study of this state of matter relies on the signatures that are printed in the detectors after the collision. Theoretical models provide predictions of what the QGP footprints look like. Nowadays, it is widely admitted that the following signatures are marks of the QGP.

- **Collective flow:** The QGP being an almost perfect liquid of constituents with small mean free path, the pressure gradient created by the collision leads

[42] Note that this is not a mandatory step for the QGP formation.

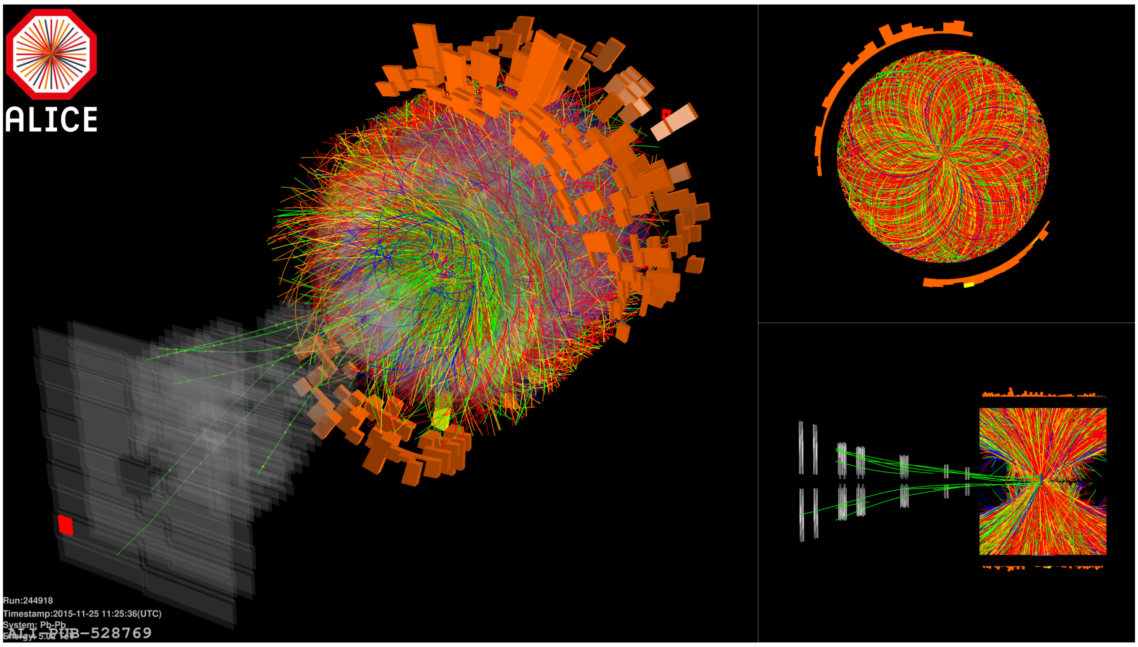

Fig. 2.14: Event display of the particles reconstructed with the ALICE detector and created in a Pb-Pb collision at $\sqrt{s_{\mathrm{NN}}}$= 5.02 TeV in 2015. Figure taken from [84].

to a collective flow, *i.e.* flow of partons, that can be described in the final state by ultra-relativistic hydrodynamic models. This aspect is addressed, in particular, by performing measurements sensitive to the radial/isotropic and anisotropic flow. The former is characterised by a boost of the low-p_{T} produced hadrons to higher p_{T}— the higher the mass, the higher the boost —; the latter is studied through a Fourier series decomposition of the azimuthal distribution of the emitted particle density. Moreover, the collective motion of partons can also be observed looking at long-range particle correlation.

- **Direct photons:** Photo-production occurs over the entire duration of the collisions, but it is strongly increased when the system is hot. Therefore, a significant excess of *direct*[43] photons is observed in heavy-ion collisions, suggesting that a QGP has been formed there. Moreover, since they leave the medium unaffected, they carry informations on its properties. In particular, the low-p_{T} photons are essentially produced out of the plasma heat, hence they are designated as *thermal photons*. Accounting for the blue-shift induced by radial expansion of the system (Doppler effect), the measurement of their yield provides an effective temperature of 304 ± 41 MeV in the most central Pb-Pb collisions [84].

- **Jet quenching:** The high-p_{T} or massive partons are produced in the early stage of the collision. As they interact with other soft partons of the QGP, a part of their energy is transferred to the medium, resulting in energy loss

[43] The term *direct* aims at designating only the photons originating from the different stage of the collisions (prompt), and not the ones from hadronic decays (non-prompt).

effects. They are of two kinds: collisional, which consists in elastic scattering *with* the medium constituents, and radiative that corresponds to an inelastic interaction and results in the emissions of gluons *within* the QGP. In the case of two jets, back-to-back, created close to the phase boundary, one will escape the fireball whereas the other will loose most of its energy in the medium. Thus, if one of the back-to-back jets is missing in the event, this would suggest the existence of a hot and dense medium, as observed in [85]

- **Heavy quarkonia suppression:** The heavy quarks, such as charm or beauty, can fragment and hadronise to form a quarkonia ($c\bar{c}$ or $b\bar{b}$ mesons). Because of the low binding energy of these states, they will start to melt and dissolve within the medium. On the other hand, this suppression can be counter-balanced by a regeneration of the quarkonia state: at the chemical freeze-out, it is possible for a heavy quark to recombine with a heavy anti-quark. Therefore, the quarkonia production is compared to theoretical models, and so far, the results are consistent with the formation of a QGP.

- **Hadron abundancy:** At chemical freeze-out, the hadron gas is supposed to be in thermal and chemical equilibrium. The hadron composition in the hadron can therefore be addressed in a statistical approach using the grand canonical formalism. The *statistical hadronisation model* (SHM) provides a prediction of the mesons and baryons abundancies, as a function of the gas volume and temperature, and the different chemical potentials (μ_B for the baryonic one, μ_S for the strangeness one,...). By fitting the measured yields of various hadron species with the SHM prediction, the chemical freeze-out temperature T_{ch} and volume V_{ch} can be estimated. The values $T_{\mathrm{ch}} = 155 \pm 2$ MeV and $V_{\mathrm{ch}} = 5924 \pm 543$ fm^3 are consistent with lattice QCD calculations.

About abundancy, the one of strange particles stands out of the other species. It is, in fact, one of the historical key signatures of the QGP and is called the *strangeness enhancement*.

II-B Strangeness enhancement

The concept of strangeness enhancement, that consists in the abundant production of strange hadrons in heavy-ion collisions, starts to take shape in the mind of Johann Rafelski in 1980. The original argument is based on the assumption that, in a melted vacuum such as the one that settles in the QGP pre-equilibrium stage, the chiral symmetry restoration results in strange quarks carrying only their bare mass (m_s), that is at least two times lower than QGP temperature ($2m_s < T_{\mathrm{QGP}}$) . Thus, this opens the way to a chemical equilibration/saturation of strangeness. When the fireball cools down, the numerous s and $\bar{s}$ tend to hadronise into strange baryons (qqs or $\bar{q}\bar{q}\bar{s}$,...) rather than mesons ($\bar{q}s$ or $q\bar{s}$).

Back then, gluons were still hypothetical objects. Strangeness production was mainly considered in the annihilation process of light quark pairs $q\bar{q} \to s\bar{s}$ (Fig. 2.16d).

In 1981, József Zimányi and Tamás Bíró estimated that, with this process, the chemical equilibrium of strangeness takes too much time to settle and is reached around eight times the natural lifespan of a QGP fireball. However, Zimányi and Bíró assumed that there were no gluons and were focused on the physical case of a hadron gas [86].

In parallel, it was realised that gluon fusion processes dominates the production rates. Together with Berndt Müller, Rafelski shows in 1982 that the chemical equilibration of strangeness is possible within the QGP lifespan thanks to the fusion of gluons created out of the vacuum heat [87]. The different $gg \rightarrow s\bar{s}$ processes are depicted in Fig. 2.16a,b,c.

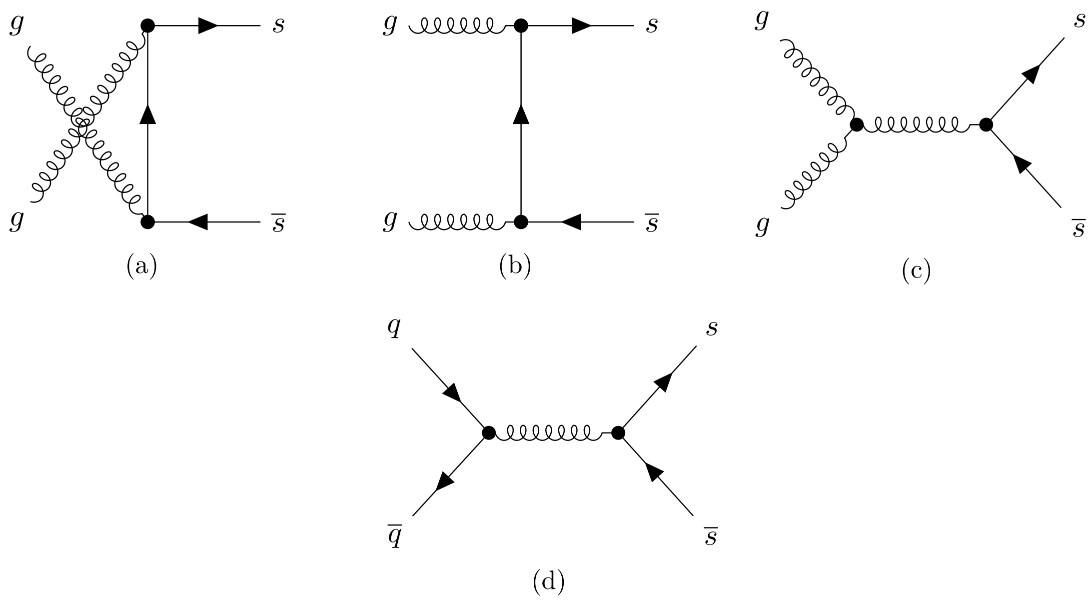

Fig. 2.15: The lowest-order QCD diagrams for $s\bar{s}$ production. (a)(b)(c) the different gluon fusion processes $gg \rightarrow s\bar{s}$; (d) quark-antiquark annihilation process $q\bar{q} \rightarrow s\bar{s}$. Figure taken from [63].

In summary, the strangeness enhancement was proposed by Rafelski and Müller in 1982 as a signature of a deconfined quark-gluon matter. They demonstrated that:

- the QGP begins to be saturated by strange quarks and anti-quarks when the temperature of the plasma reaches the 200 MeV after about 2×10^{-23} sec,

- this saturation is possible because strange quarks can pop in out of the QGP heat ($2m_s < T$) via gluon fusion processes (Fig. 2.15). These processes are favoured because i) they are more energy/time efficient and ii) the high density of gluons created out of the vacuum,

- at the hadronisation, the strangeness tends to be distributed on baryons rather than mesons. Consequently, this leads to an increased production of strange particles in the final state of the collision. In fact, the larger the strangeness content, the larger the enhancement of the hadron production.

Experimentally, the strangeness enhancement manifests itself through an increase of the *relative* yields of strange hadrons in heavy-ion collisions. Now comes two difficulties: so far, only the strangeness enhancement from the formation of a QGP was considered, however a similar phenomenon could occur in a hadron gas[44]. The difference between these two increases in strange particle abundancies resides in the hierarchy between hadrons with different strangeness content [63]:

$$\Omega(sss)\ /\ \Xi(dss)_{\text{QGP}} \quad \approx \quad \Xi(dss)\ /\ \Lambda(uds)_{\text{QGP}} \tag{2.6}$$
$$\Omega(sss)\ /\ \Xi(dss)_{\text{Hadron Gas}} \quad \ll \quad \Xi(dss)\ /\ \Lambda(uds)_{\text{Hadron Gas}} \tag{2.7}$$

$$\Omega(sss)\ /\ \Xi(dss)_{\text{QGP}} \quad > \quad \Omega(sss)\ /\ \Xi(dss)_{\text{Hadron Gas}} \tag{2.8}$$
$$\Xi(dss)\ /\ \Lambda(uds)_{\text{QGP}} \quad > \quad \Xi(dss)\ /\ \Lambda(uds)_{\text{Hadron Gas}} \tag{2.9}$$

Another issue arises from the definition of *relative* yields. In other words, this comes down to asking what normalisation to use? There are different possibilities, depending on the physics target. Most of the time, the yields of strange hadrons in heavy-ion collisions are compared to the ones in pp collisions. This is relevant in order to discriminate the strangeness enhancement originating from the QGP (heavy-ion collisions) from the one occuring in a hadron gas (as in pp collisions, assuming that there are enough interactions between the different produced hadrons). Alternatively, one could also look at the "continuous" evolution of the yields as a function of the collision system. In such a case, the relative yields correspond to the ratio of production rate between the particle of interest and the lighest known hadron, namely the π. Finally, the focus can also be on the difference of yields between hadrons with the same strangeness content but different mass, typically the yields ratio between a resonant and a non-resonant hadronic state. This could provide some information on the influence of the hadronic phase.

The Fig. 2.16 presents, on the left, the measurement of relative yields of strange hadrons with respect to the pions a function of the average charged multiplicity of the collision, and on the right, the yield ratios between resonant and non-resonant states are displayed. The lowest multiplicities correspond to pp collisions, and as it increases, we move on towards more and more central heavy-ion collisions.

The left panel of Fig. 2.16 shows that the yield of strange hadrons increases in Pb-Pb and Xe-Xe collisions with respect to pp and p-Pb collisions, and the enhancement factor gets bigger with the strangeness content. This is compatible with the strangeness enhancement picture and confirms the existence of a deconfined quark-gluon matter. Notice that the ratios do not change with the centre-of-mass energy, suggesting that the initial stage of the collision does not play an important role in the strangeness enhancement (at least, at the LHC energies).

On the right panel, the yield ratios between resonant and non-resonant hadronic states seems to decrease when going from elementary collision systems (pp and p-Pb) to the heavy-ion ones. This trend indicates that the temperature of the hadron

[44]Strange hadrons could be formed via inelastic collisions between light mesons and baryons. Because of the large dynamical mass of hadrons, the production of strange particles should be suppressed. This reduction gets more pronounced as the hadron mass is high.

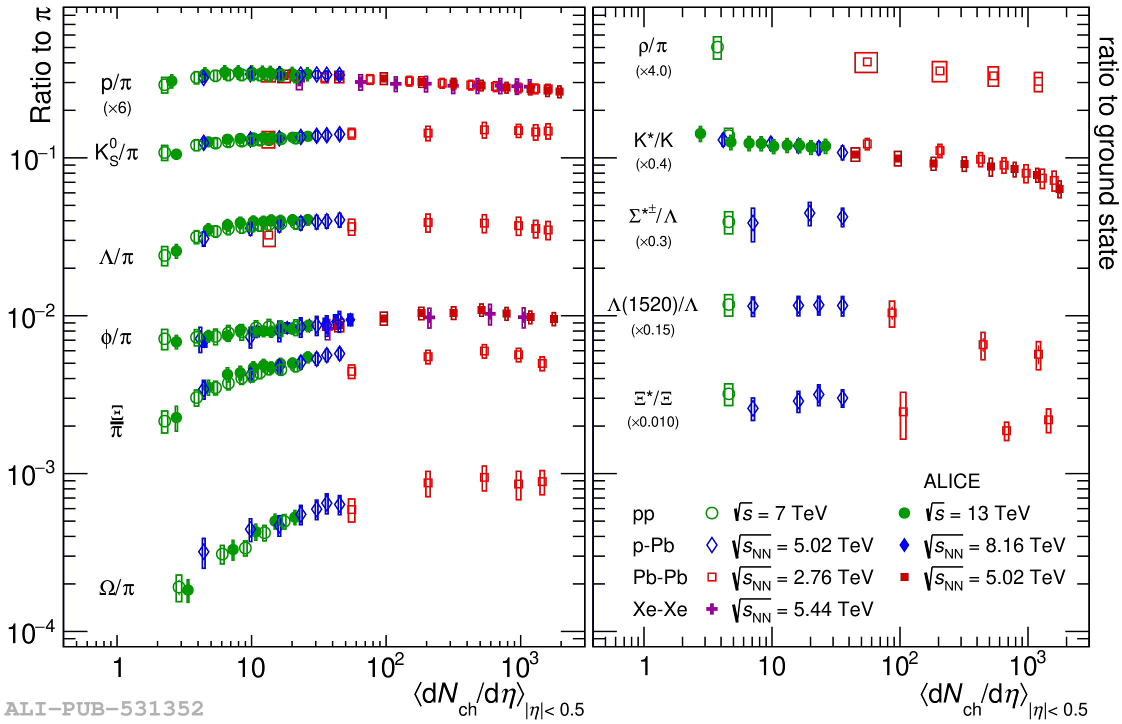

Fig. 2.16: (Left panel) Relative yields of strange hadrons with respect to the pions and (right panel) yield ratios between resonant and ground state hadrons as a function of the average charged particle multiplicities at midrapidity. Results from different collision systems are presented: pp at $\sqrt{s}$ = 7 and 13 TeV; p-Pb at $\sqrt{s_{\rm NN}}$= 5.02 and 8.16 TeV; Pb-Pb at $\sqrt{s_{\rm NN}}$= 2.76 and 5.02 TeV; Xe-Xe at $\sqrt{s_{\rm NN}}$= 5.44 TeV. The left panel considers the following strange hadrons: $\mathrm{K}^0(\bar{d}s)$, Λ (uds), ϕ $(s\bar{s})$, Ξ (dss) and Ω (sss). The error bars corresponds to the statistical uncertainty, whereas the boxes show the total systematic uncertainty. Figure taken from [84].

gas after the QGP is sufficiently high to suppress the resonance yields by elastic rescattering of the decay products.

II-C Comparison with elementary systems

Throughout this section, it was suggested that the formation of the QGP is exclusive to heavy-ion collisions, and it is not expected in more elementary systems – such as pp and p-Pb collisions – because the size of the colliding system is *a priori* too small. Looking more attentively at the Fig. 2.16, one notices that relative yields of strange hadrons increases smoothly from low to high multiplicity pp and p-Pb collisions. In other words, this means that strangeness enhancement seems to be present as well in small systems.

In fact, the aforementionned QGP manifestations, the heavy quarkonia suppression [88], the strangeness enhancement [84], the collective flow [14] have been observed in both heavy-ion collisions and small systems, suggesting the presence of a common collective behaviour. Some signatures are missing though; for example, there are so far no indication of jet quenching nor thermal photons in small systems.

As a consequence, the classical picture of a heavy-ion collision, forming a hot and dense matter where quarks and gluons are deconfined, needs to be revised. At least, the elementary colliding systems can no longer be considered as a valid reference point, for sufficiently high energies such as the LHC ones. This point will be further addressed in more details in Chap. 6.

Chapter 3 | ALICE: A Large Ion Collider Experiment

As it was already mentionned before, ALICE (*A Large Ion Collider Experiment*) aims at studying QCD bulk matter and, in particular, the quark-gluon plasma (QGP). It is situated in the CERN area, in the vicinity of Geneva, on the ring of the LHC (*Large Hadron Collider*). Being the spearhead of the QGP studies at CERN, it has been designed in order to access to a large variety of observables over a wide range of transverse momentum, thus offering the ability to study the evolution the heavy-ion collision from its initial stages to the hadronic phase.

The first section, Sec. 3|I provides a brief introduction of the immediate surroundings of the ALICE collaboration, the CERN. Different aspects are mentioned, from the organisation to the main experiments on the LHC rings, through the CERN accelerator complex. This brings to the description of the ALICE in Sec. 3|II, from the viewpoint of the collaboration and the experiment via the detector. The latter point allows to exhibit the strength of the ALICE detector, as well as presenting the event reconstruction procedure and the offline framework.

I The CERN

I-A The organisation

Located the border between France and Switzerland, the CERN is like a tiny country with its own culture, its own language (essentially composed of acronyms). It is mostly known for its expertise on particle accelerators and detectors for high energy physics, but it is also the birthplace of some of our everyday devices – such as the World Wide Web (1990), the touchscreen (1972) – or less daily tools, like the Worldwide LHC computing grid (2005) and the multi-wire proportionnal chamber

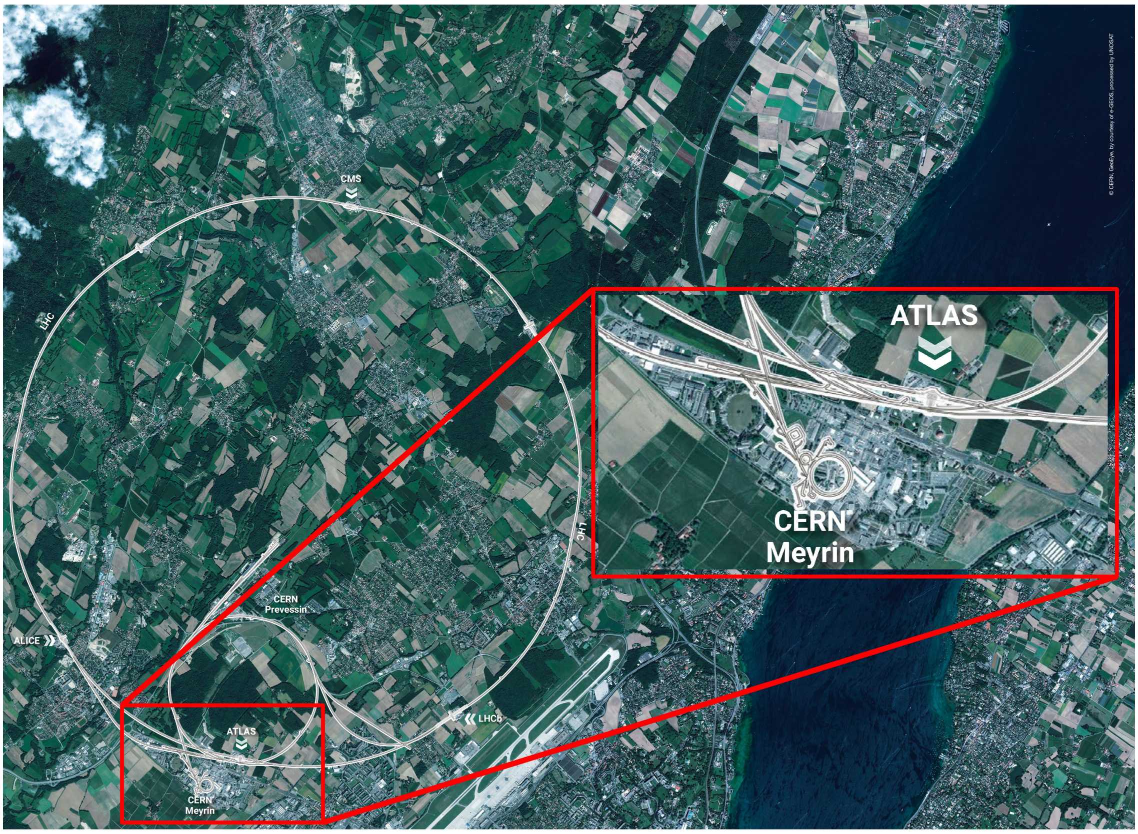

Fig. 3.1: Aerial view of the CERN accelerator complex (highlighted by the white curves), with an insert on the main site in Meyrin (Switzerland, canton of Geneva). Figure taken from [89] and modified by the present author.

(1968). The Fig. 3.1 provides an aerial view of the CERN sites, with an insert on its headquarters in Meyrin (Switzerland, canton of Geneva). A location that has been decided from the very beginning of the organisation, back in the 1950s.

At the end of the Second World War, Europe lays in ruins, most of the research facilities are destroyed and many physcists have left the continent to work on the other side of the Atlantic. Europe is no longer at the forefront of scientific progress. A situation from which the old continent might never recover, as the european nations do not have the resources to rebuild the basic infrastucture. Nevertheless, things begin to change in 1949 when, at the European Cultural Conference, Louis de Broglie – supported by Raoul Dautry, Pierre Auger, Lew Kowarsky, Edoardo Amaldi and Niels Bohr – proposes to create an European laboratory in order to promote collaboration between Europe's nations, and share the costs.

The project gains momentum such that, in late 1951, the United Nations Educational, Scientific and Cultural Organization (UNESCO) – pushed by the United States – organises a dedicated meeting on that matter. Some countries shows their skepticism: even though the infrastructure costs are mutualised, this kind of endeavor still demands an initial investement; a few years after the end of the war, many countries are still in a difficult financial position and are thus reluctant to participate. After two months of debate, the first resolution of the convention establishing the European Council for Nuclear Research ("Conseil Européen pour la

Recherche Nucléaire" in French or CERN) is ratified in 1952 by the twelve founding member states: Belgium, Denmark, France, Germany, Greece, Italy, Netherlands, Norway, Sweden, Switzerland, United-Kingdom and Yugoslavia [90].

Later that year, Geneva was chosen to host the laboratory. In 1953 the CERN convention is completed and signed by all the members. It defines, amongst others, the membership, the financial contributions, the decision protocols, its denomination[1] and its missions. In particular, the CERN aims not only for technological developments and scientific researches on high-energy physics but also for the "promotion of contacts between, and the interchange of, scientists, the dissemination of information [...]", and "collaborating with and advising other research institutions" [91].

Nowadays, the organisation includes 23 Member States and ten Associate Member States. There are also non-members States or institution with an Observer status, such as the United-States, Japan, European Union, UNESCO and previously the Russian Federation. In 2017, the CERN counted more than 17 500 people, all over the world, working together towards a common goal, including more than 12 200 scientists [92]. This makes it the largest scientific organisation in the World.

I-b The accelerator complex

As stated in the Article II of the Convention, the construction and operation of particle accelerators stand as one of the CERN's purposes. In particular, the organisation must immediately develop a 600 MeV synchro-cyclotron and a 28 GeV proton synchrotron (PS). The former, built in 1957, corresponds to the first accelerator of CERN; the latter starts accelerating protons in 1959.

The next step up in beam energies arrives in 1976 with the first underground accelerator, the Super Proton Synchroton (SPS). It consists in two rings, of seven kilometers circumference each, delivering beams of 300 GeV of protons and antiprotons. At least, on the paper because it is one of the rare cases in particle physics, when the final product performs better than expected in the technical design reports. Thanks to technological advances during its construction, the SPS could reach beam energies up to 400 GeV, and gradually of 450 GeV after some upgrades.

In 1989, a 27-kilometre circular accelerator enters in operation, namely the Large Electron-Positron (LEP) collider. It was tuned such that the colliding energy sits on the resonance mass peak of the Z^0 and $W^{\pm}$ bosons, but in the search of the Higgs boson, it was also operated with a centre-of-mass energy of 209 GeV on its last year, in 2000. This was – and still is – the largest electron-positron collider ever built.

As one World record calls for another, the LEP collider is decomissionned in order to be replaced in 2008[2] by the Large Hadron Collider (LHC), the World's largest and most energetic particle collider. The accelerator is currently operational

[1] The CERN Convention was the opportunity to rename the CERN as the "Organisation Européenne pour la Recherche Nucléaire" (or European Organisation for Nuclear Research in English), that would corresponds to the acronym OERN now. Because the initial abbreviation turns out to be more elegant, the name CERN remained.

[2] Technically, because of an incident on one of the dipole magnets, the accelerator undergoes

Collision type	pp	Pb-Pb	Xe-Xe
Energy per beam	6.5 TeV	2.56 TeV	2.72 TeV
Luminosity ($cm^{-2}s^{-1}$)	2.1×10^{34}	6.1×10^{27}	0.4×10^{27}
Velocity (in units of c)	0.99999998	0.99715693	0.99898973
Circumference		26 659 m	
Beam vacuum		10^{-13} atm	
Number of RF cavities		8 per beam	
Number of magnets		9593	
Number of dipole magnets		1232	
Dipole operating temperature		1.9 K (-271.3 C)	
Current flowing in the dipole		11 850 A	
Magnetic field of the dipole		8.33 T	

Table 3.1: A selection of design parameters for the LHC during the Run-2. Values taken from [95] and [42].

and should still be, at least, until 2038. Beyond this date, the CERN might start the construction of the Future Circular Collider, a particle accelerator with a circumference of 100 km[93][94].

The LHC is the collider of (almost) all superlatives. To put it into perspectives, the Tab. 3.1 lists some of its important characteristics.

As in any accelerator, particles circulate in a vacuum tube in order to avoid collisions with gas molecules. The beam is subject to ultra-high vacuum, corresponding to a pressure of 10^{-13} atm, applied over the approximately 9 000 m^3 covered by the LHC. In comparison, this is like pumping down the nave of a cathedrale to a pressure level similar to the one at the Moon's surface.

Various magnets control the particle trajectory: 1232 dipoles to bend the 6.5 TeV beams, 392 quadrupoles to squeeze and focus the beam down to the collision point, etc. If we hope to curve the particle's trajectory at the LHC energies, the dipoles must create an intense magnetic field of 8.33 T, demanding a current of 11 850 A. For comparison: at ambient temperature, the dissipated heat would melt down the magnet. Hence, 90 tonnes of superfluid helium are injected into the magnets bringing their temperature down to 1.9 K (-271.3 C), that is even lower than the temperature of outer space (2.7 K). At this level, the dipoles become superconducting and can now endure the flow of currents to develop the necessary magnetic field.

The particle acceleration is ensured by eight radiofrequency cavities (RF cavities)[3] per beam. Most often, they accelerate protons at 6.5 TeV, which corresponds to the typical kinetic energy of flying mosquito but distributed on the minuscule volume of a proton. At such energy, a proton travels at almost light-speed and makes 11 245 LHC turns per second. Furthermore, because of the RF cavities, each

some repairs that delay its operation by fourteen months.

[3]It consists in a cavity filled with an electromagnetic field oscillating at a specific frequency (in the radio wave's domain, hence the name of the radiofrequency cavities), and shaped in such a way that resonance occurs.

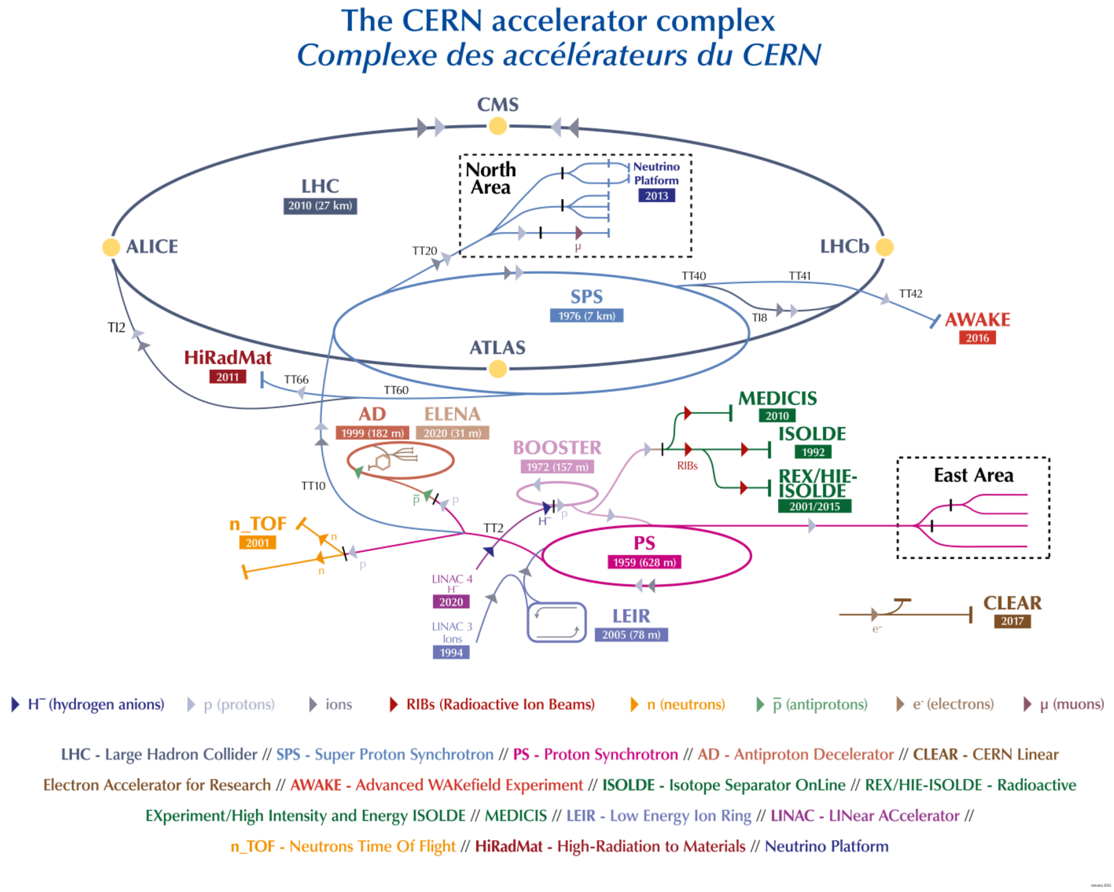

Fig. 3.2: Schematic representation of the CERN accelerator complex as in 2023. Figure taken from [96].

beam is divided into 2808 bunches separated by 7.5 m (or 25 ns[4]) and containing about 10^{11} protons.

It is noteworthy that the LHC is only the last element of the acceleration chain, as represented in the Fig. 3.2. The beam energy increases gradually using the past CERN's accelerators. Depending on the type of beams (pp or AA), the route to the LHC differs slightly. For a proton beam, negatively charged hydrogen ions are first accelerated by the Linear Accelerator 4 (LINAC 4)[5] to 160 MeV, and then they are injected in the Proton Synchroton Booster (BOOSTER) in order to reach an energy of 2 GeV. The electrons of the hydrogen ions are removed when leaving the LINAC 4. For a heavy-ion collision, the Linear Accelerator 3 (LINAC 3) provides a beam of heavy-ions – already stripped of their electrons – to the Low Energy Ion Ring (LEIR), which accelerates them to 72 MeV per nucleon. Whether it is a beam made of protons or heavy-ions, they are successively accelerated by the PS and SPS up to 450 GeV (or 177 GeV per nucleon for heavy-ions). The particles are finally injected

[4]This is the case for the LHC Run-2, but in the Run-1, the distance between two bunches was twice as big, that is 50 ns.

[5]Until 2020, the first acceleration stage was performed by the LINAC 2 that accelerated hydrogen atoms.

in the rings of the LHC in order to reach their top energy of 6.5 TeV (or 2.56 TeV per nucleon for Pb beams) and collide in the four collision points where sits the four main LHC's experiments: ATLAS, CMS, LHCb, and ALICE[97]. Tab. 3.2 presents a few of their characteristics.

Experiment	ATLAS	CMS	ALICE	LHCb
Participants	5 991	5 824	2 085	1 585
Height (m)	25	15	16	10
Length (m)	46	21	26	21
Width (m)	25	15	16	13
Weight (tonnes)	7 000	14 000	10 000	5 600

Table 3.2: A few characteristics of the four main LHC experiments, namely ATLAS, CMS, ALICE and LHCb. The participants include particle physicists, engineers, technicians and students; their number corresponds to the one as of March 2023[98]. The dimensions of each detector originate from [99][100][101][102].

A Toroidal LHC Apparatus (ATLAS) and a Compact Muon Solenoid (CMS) are the most colossal experiments at the LHC, as much in terms of the number of participants as in the dimension of their detectors. Both cover a wide range of physics and share the same goals, namely characterising the elementary particles of Standard Model – in particular, the Higgs boson – and searching for the new particles beyond the Standard Model, such as dark matter candidates or supersymmetric particles.

ALICE and LHCb (Large Hadron Collider beauty) are more specialised. ALICE aims at studying QCD matter, and particularly under extreme energy densities where a phase of deconfined quark-gluon matter forms, the QGP. On the other hand, LHCb focuses on heavy flavour physics. It is concerned about new physics in CP violation and rare decays, primarily of beauty but also charm hadrons.

In order to carry out their physics programme, the LHC must provide different types of beam. For instance, ATLAS and CMS are essentially interested in pp collisions with the highest interaction rate possible, whereas ALICE needs heavy-ion runs to study *directly*[6] the QGP. Therefore, the Run Coordination of each experiment gathers regularly with LHC Programme Coordination to discuss and negotiate the accelerator schedule, in order to define a programme which best meets everyone's needs.

I-c The accelerator programme

As shown in the Tab. 3.3, the LHC delivers his first collisions on the 23$^{\text{rd}}$ of November 2009; these are pp collisions at $\sqrt{s} = 900$ GeV. The centre-of-mass energy

[6]As discussed in Sec. 2|II-C, the QGP can also be investigated via the study of its signatures in pp collisions.

LHC Run	Year	Collision	Centre-of-mass energy (per nucleon)	Dates
Run 1	2009	pp	900 GeV	23$^{\text{rd}}$ Nov. to 14$^{\text{th}}$ Dec.
		pp	2.36 TeV	14$^{\text{th}}$ and 16$^{\text{th}}$ Dec.
	2010	pp	7 TeV	30$^{\text{th}}$ Mar. to 4$^{\text{th}}$ Nov.
		pp	900 GeV	2$^{\text{nd}}$, 3$^{\text{rd}}$ and 27$^{\text{th}}$ May
		Pb-Pb	2.76 TeV	9$^{\text{th}}$ Nov. to 6$^{\text{th}}$ Dec.
	2011	pp	7 TeV	21$^{\text{th}}$ Feb. to 4$^{\text{th}}$ Nov.
		pp	2.76 TeV	24$^{\text{th}}$ to 27$^{\text{th}}$ Mar.
		Pb-Pb	2.76 TeV	5$^{\text{th}}$ Nov. to 7$^{\text{th}}$ Dec.
	2012	pp	8 TeV	5$^{\text{th}}$ Apr. to 16$^{\text{th}}$ Dec.
	2013	p-Pb	5.02 TeV	20$^{\text{th}}$ Jan. to 10$^{\text{th}}$ Feb.
		pp	2.76 TeV	11$^{\text{th}}$ to 14$^{\text{th}}$ Feb.
Run 2	2015	pp	13 TeV	3$^{\text{rd}}$ Jun. to 19$^{\text{th}}$ Nov.
		pp	5.02 TeV	19$^{\text{th}}$ to 23$^{\text{rd}}$ Nov.
		Pb-Pb	5.02 TeV	24$^{\text{th}}$ Nov. to 13$^{\text{th}}$ Dec.
	2016	pp	13 TeV	23$^{\text{rd}}$ Apr. to 26$^{\text{th}}$ Oct.
		p-Pb	5.02 TeV	4$^{\text{th}}$ to 17$^{\text{th}}$ Nov.
				4$^{\text{th}}$ to 5$^{\text{th}}$ Dec.
		p-Pb	8.16 TeV	18$^{\text{th}}$ to 25$^{\text{th}}$ Nov.
		Pb-p	8.16 TeV	26$^{\text{th}}$ Nov. to 4$^{\text{th}}$ Dec.
	2017	pp	13 TeV	23$^{\text{rd}}$ May to 26$^{\text{th}}$ Nov.
		pp	5.02 TeV	11$^{\text{th}}$ to 21$^{\text{st}}$ Nov.
		Xe-Xe	5.44 TeV	12$^{\text{th}}$ Oct.
	2018	pp	13 TeV	12$^{\text{th}}$ Apr. to 23$^{\text{th}}$ Oct.
		Pb-Pb	5.02 TeV	7$^{\text{th}}$ Nov. to 2$^{\text{nd}}$ Dec.

Table 3.3: Summary of the LHC Run 1 and 2 physics programmes with the data taking periods in the rightmost column [103].

gradually increases over the years, from 0.9 TeV to 2.36 and then 7 TeV in 2011, and 8 TeV in 2012. The proton-proton programme is complemented by Pb-Pb collisions at $\sqrt{s_{\rm NN}}$= 2.76 TeV in November 2010 and 2011, followed in early 2013 by the first p-Pb run at a centre-of-mass energy per nucleon of 5.02 TeV. A few days later, the collider enters in a long shutdown (LS1), marking the end of the first campaign of data taking now called Run-1 (2009-2013). During this period, the LHC undergoes maintenance operations and preparations in view of an increase by a factor two of both energy (reaching $\sqrt{s}$ = 13 TeV in pp collisions) and luminosity[7] (bunches of protons are separated by 25 ns instead of 50 ns).

In spring 2015 begins the second campaign of data taking, the LHC Run-2. The latter opens with pp collisions at a record energy of 13 TeV, which will be the default collision energy in pp until the end of the Run-2. The same goes for heavy-ion collisions: the Pb-Pb and p-Pb data are now collected at $\sqrt{s_{\rm NN}}$= 5.02 TeV, and up to 8.16 TeV in the latter case. Note also the presence of a short Xe-Xe run at $\sqrt{s_{\rm NN}}$= 5.44 TeV in October 2017. The Run-2 comes to an end on December 2018; the LHC enters in its second long shutdown (LS2). As for the LS1, this is the opportunity for the collider and its experiments to be renovated and upgraded.

On the 5th of July 2022, the LHC restarts and delivers its first pp collisions – almost four years after the start of the LS2 – at the new record energy of 13.6 TeV, signalling the beginning of the Run-3.

II The ALICE collaboration

Amongst the different collaboration based at CERN, ALICE holds a particular place since the work presented in this manuscript has been realised within this experiment. As mentioned above, it aims at studying the properties of strongly interacting matter and particularly under extreme energy densities where the quark-gluon plasma is formed (Sec. 2|II).

II-A The collaboration

As of March 2023, the ALICE collaboration counts 2084 physicists, engineers, technicians and students from 174 institutes in 41 countries. Most of its members originate from Europe (France, Italy, Germany,...), but also from Asia (China, South Korea, Japan,...) and America (United States, Brazil, Mexico,...). In order to coordinate the efforts within the collaboration, ALICE is organised in different boards and committees, each covering a specific scope[8]:

- *The Collaboration Board (CB)* is the highest instance of the collaboration, it can examine and render a decision on any issues from the construction of the detector to the publication policy. It consists in a legislative assembly, mainly composed of the representatives of each member institute (one per member).

- *The Management Board (MB)* supervises the experiment in any matters (scientific, technical, organisational, operational and financial). It plays the role of the executive authority of the collaboration, and is represented by the Spokesperson and its deputies.

[7] This quantity corresponds to a measure of the number of collisions either per unit of time (*instantaneous luminosity*) or over a certain period of time (*integrated luminosity*). In the latter case, it is expressed in inverse barns (b^{-1}) or femtobarns (fb^{-1}).

[8] Only a subset of the ALICE management structure is mentioned. The complete picture is specified in the ALICE Constitution [104].

- *The Resource Board (RB)* deals with the financial aspect of ALICE. Each national funding agency has a seat within this committee.
- *The Physics Board (PB)* coordinates the analysis efforts in order to address the physics goals defined by the CB and MB. It consists in eight Physics Working Groups (PWG), each covering a specific theme, as presented in Tab. 3.4.

Physics Working Group	Topic
PWG-CF	Correlations and Flow
PWG-DQ	Dileptons and Quarkonia
PWG-EM	Electromagnetic probes
PWG-HF	Heavy Flavour
PWG-JE	Jets
PWG-LF	Light-Flavours
PWG-MM	Monte Carlo generators and Minimum bias analysis
PWG-UD	Ultra-peripheral collisions and Diffraction

Table 3.4: The eight working groups of the ALICE Physics Board, as of 2023.

Each PWG is also subdivided in Physics Analysis Group (PAG). For instance, the PWG-Light Flavours includes four PAGs: *Resonances*, *Spectra*, *Nuclei and Exotica*, and *Strangeness*. The present analyses on multi-strange baryons (Chap. 5 and 6) are part of the latter group.

- *The Run Coordination (RC)* is responsible for the operation of the ALICE detector. Amongst its duties, it must ensure efficient data taking, optimal data quality and must define the LHC schedule with the LHC Programme Coordination in order to meet the physics goals of the collaboration.
- *The Editorial Board (EB)* manages the publication process (publication, conference proceedings, internal and technical notes). It is complemented by the *Conference Committee (CC)* that oversees the oral presentations (talk or poster) outside of the collaboration.

This structure is quite common in high-energy experiments, most of the collaboration are being organised in this way. With different denominations perhaps, but the essence stays the same.

II-B The detector

The ALICE detector sits in a cavern 56 m below the ground, in the vicinity of Saint-Genis-Pouilly in France. It is located at the interaction point 2 of the LHC, where the L3 experiment at the former LEP collider was installed. From the latter only remains the gigantic red octogonal solenoid magnet, now symbol of the ALICE collaboration.

Being the only experiment dedicated to studying the QGP, ALICE has been designed as general-purpose detector capable of accessing a large number of observables. The physics targets impose several design constraints.

The apparatus must be able to operate in a high-multiplicity environment, considering that the charged particle density per unit of rapidity in the most violent Pb-Pb collisions may reach $\mathrm{d}N_{\mathrm{ch}}/\mathrm{d}\eta = 2035 \pm 52$ [105]. For that reason, high granularity detectors – such as the Inner Tracking System – are employed to ensure an excellent reconstruction of the primary and secondary vertices, especially close to the interaction point. In fact, the design of ALICE was optimized to endure values up to $\mathrm{d}N_{\mathrm{ch}}/\mathrm{d}\eta = 4000$, and twice as much in simulations.

To gain as much insights as possible on the QGP evolution, most of the measurements shall be achievable over a wide momentum range, spanning from very low transverse momentum (~100 MeV/c) – where most of the particle production is – up to large transverse momentum ($\geq$ 100 GeV/c). This requires reducing the multiple scattering at low p_{T}, and thus using extremely thin detectors. At central rapidity, the material budget amounts to 13% radiation length, X_0[9], up to Time Projection Chamber outter wall[10]. For comparison, it is about 47% and 40% X_0 in ATLAS and CMS at the end of their inner tracker [99][100], and 17.5% X_0 down to the VELO (VErtex LOcator) for LHCb [102]. At high p_{T}, the constraint lies in the need for a good resolution. The latter, described by the Gluckstern's formula[11] [106]

$$\frac{\Delta p_{\mathrm{T}}}{p_{\mathrm{T}}} = \frac{p_{\mathrm{T}} \cdot r\delta\varphi}{0.3 \cdot B \cdot L^2_{\mathrm{track}}} \sqrt{\frac{720}{N_{\mathrm{clusters}} + 4}}, \tag{3.1}$$

is mostly achieved by means of a large tracking lever arm extending up to 2.5 m, as well as an abundant number of data points, thanks to the Time Projection Chamber.

This brings an extra consideration. In order to avoid excessivily bending the low p_{T} charged particles and making them impossible to detect, the momentum measurement down to 100 MeV/c necessitates a moderate magnetic field of 0.5 T[12]. As a consequence, the high p_{T} charged particles are less curved resulting in a reduction of the momentum resolution – when they are still measurable – which, in turn, is compensated by their long track length.

Along the same line, many observables depend on the nature of the particle,

[9] This is the characteristic amount of matter over which a high-energy electron loses all its energy by bremsstrahlung (*i.e.* deceleration via the emission of photons) but $1/e$. It is expressed in g.cm^{-2} [42].

[10] Here, there are two antogonistic constraints: the detectors must be thin and radiation tolerant in order to function in a high-multiplicity environment, the latter requiring relatively thick materials. However, in ALICE, the interaction rate in heavy-ion collisions is low (about 10 kHz or 10 000 Pb-Pb collisions per second) such that the radiation doses are rather mild, compared with the levels in ATLAS and CMS (790 and 840 kGy respectively): the total dose over the period of a LHC-Run varies between tens of Gy for the furthest parts of the Inner Tracking System to 2.7 kGy close to the interaction point.

[11] A few words on the different terms in the formula. $r\delta\varphi$ corresponds to the resolution on a single space point, B refers to the magnetic field amplitude, L_{track} the track length and N_{clusters} the number of data points exploited for the momentum measurement.

[12] Among the four main LHC experiments, this is the most moderate magnetic field. For comparison, CMS uses a magnetic field of 4 T, the same as the LHCb dipole magnet, and ATLAS solenoid magnet delivers a 2 T field.

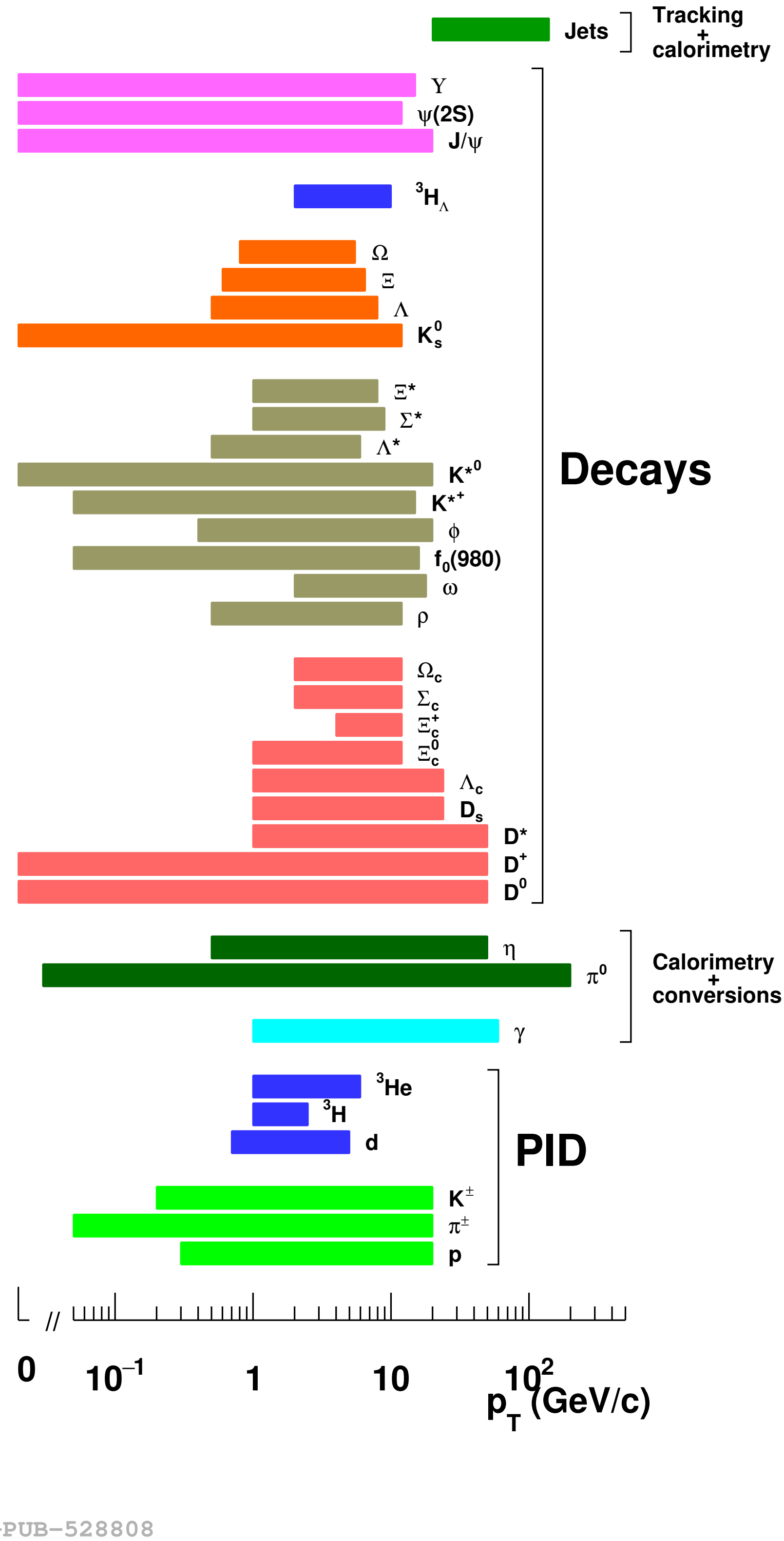

Fig. 3.3: ALICE particle identification and reconstruction as a function of p_T. Figure taken from [84].

and so it is essential to have a robust particle identification (PID) over a wide momentum range. To that end, ALICE exploits all the PID techniques on the

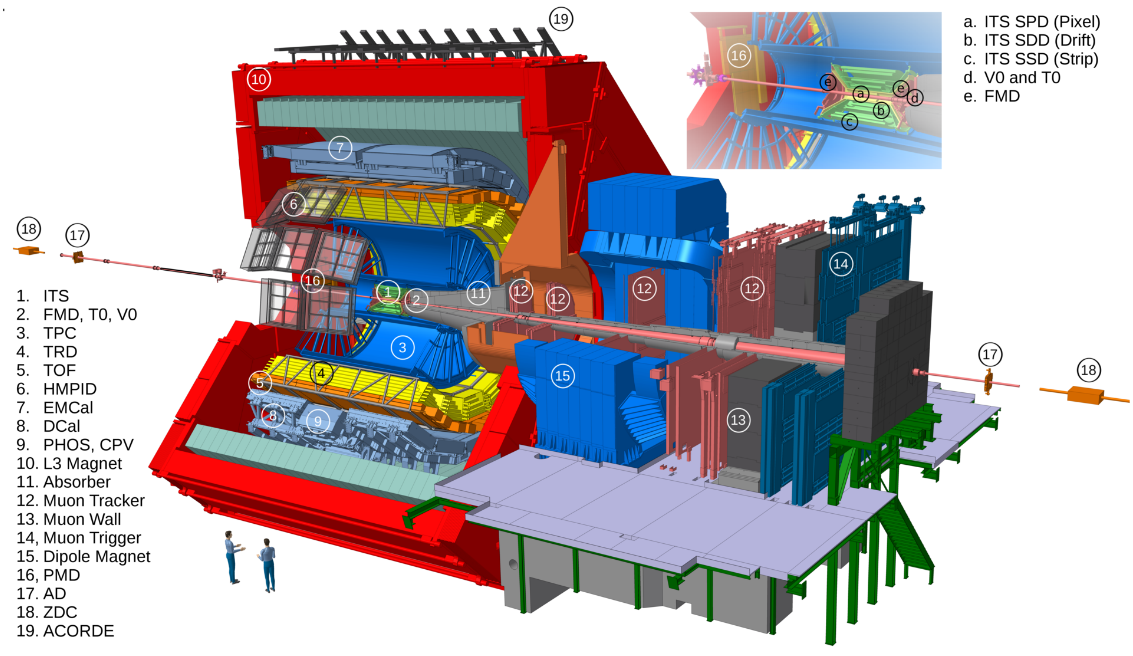

Fig. 3.4: Schematic representation of the ALICE apparatus, as it was operated in the LHC Run-2. Figure taken from [84].

market: ionization energy loss in the Time Projection Chamber, time-of-flight measurement with the Time-Of-Flight detector, Cerenkov and transition radiations in the High-Momentum Particle Identification Detector (HMPID) and Transition Radiation Detector (TRD) respectively, energy measurement with the Electromagnetic Calorimeters (EMCal) and the Photon Spectrometer (PHOS). The Fig. 3.3 provides an overview of the PID and reconstruction capabilities with the transverse momentum coverage.

Fig. 3.4 provides a overview of the different elements of the detector. It comprises 19 detection systems organised in two groups: the ones in the central barrel at mid-rapidity ($|\eta| < 0.9$), embedded in the L3 solenoid magnet that delivers a homogenous magnetic field up to 0.5 T; the others at forward rapidity ($-4 < \eta < -2.5$), dedicated to muon detection. An exhaustive description of the ALICE apparatus can be found in [101], as well as its physics performances in [107][108][109]. In the next paragraphs, we will concentrate on the main detectors employed in this thesis, namely the Inner Tracking System (Sec. 3|II-B.i), the Time Projection Chamber (Sec. 3|II-B.ii), the VZERO (Sec. 3|II-B.iii) and the Time-Of-Flight detector (Sec. 3|II-B.iv).

Before proceeding, a note on the location of the different parts of the apparatus: in the cartesian coordinate system of ALICE, the origin lies at the centre of the central barrel and the z-axis coincides with the beams. The elements located on positive z belongs to the A-side (beam circulating in Anti-clockwise direction, from ALICE to the ATLAS interaction point), the others with negative z are on the C-side (beam going in Clockwise direction, from ALICE to the CMS interaction point). The y-axis points towards the top of the detector and the x-axis is in the horizontal plane, going towards the centre of the LHC ring. Moreover, there exists

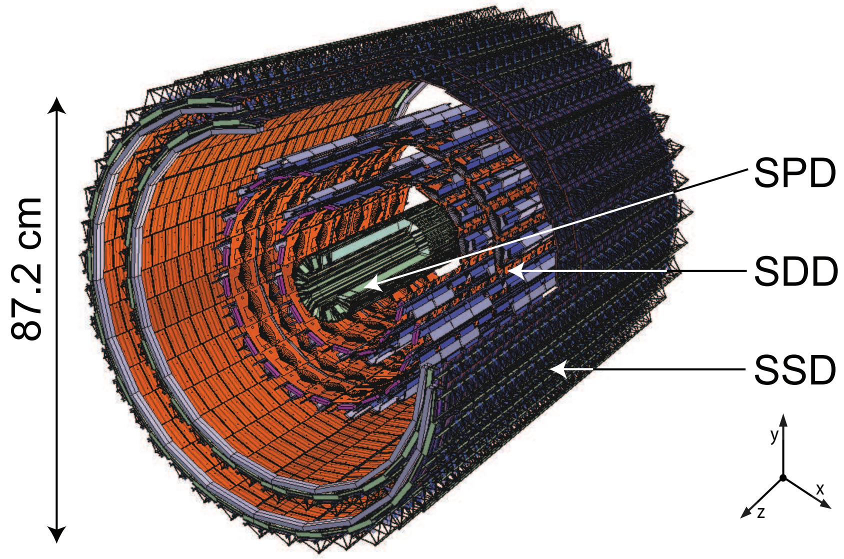

(a)

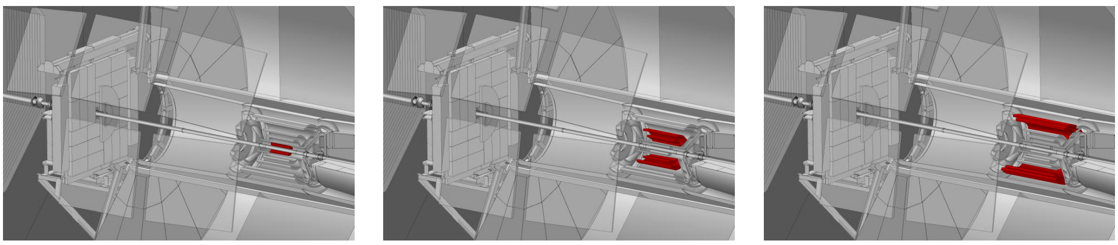

(b) (c) (d)

Fig. 3.5: Visualisation of the complete structure of the ITS detector (a), as well as a highlight on the SPD(b), SDD(c) and SSD(d) locations in the ALICE apparatus. Figures taken from [110][111].

a cylindrical coordinates system based on the distance from the origin r and the azimuthal angle φ in the transverse plane xy, as well as a spherical one with an additional angle, the zenithal angle denoted θ.

II-B.i Inner Tracking System

The Inner Tracking System (ITS) of ALICE is the closest detection system to the interaction point. It surrounds the beam pipe, a 800 μm-thick beryllium cylinder with an average radius of 2.9 cm. The ITS is designed in order to i) estimate the primary vertex position to a precision better than 100 μm, ii) reconstruct secondary decay vertices of relatively short lifetime particles such as hyperons, D or B mesons, iii) track and identify particles whose $p_{\mathrm{T}} \leq 200\mathrm{MeV}/c$, iv) bring constraints on the particles reconstructed by the Time Projection Chamber and, by so doing, improve the momentum and angle resolution, v) enhance PID capabilities of the ALICE apparatus, and finally vi) provide additionnal trigger information. As shown on the Fig. 3.5, the ITS is made of six coaxial cylindrical layers of silicon detectors

Layer	r (cm)	$\pm z$ (cm)	Area (m^2)	Active area per module (mm^2)	Resolution $r\varphi \times z$ (μm^2)	Material budget (%X_0)
1 - SPD	3.9	14.1	0.07	12.8 × 69.6	12 × 100	1.14
2 - SPD	7.6	14.1	0.14	12.8 × 69.6	12 × 100	1.14
3 - SDD	15.0	22.2	0.42	72.5 × 75.3	35 × 25	1.13
4 - SDD	23.9	29.7	0.89	72.5 × 75.3	35 × 25	1.26
5 - SSD	38.0	43.1	2.20	73 × 40	20 × 820	0.83
6 - SSD	43.0	48.9	2.80	73 × 40	20 × 820	0.86

Table 3.5: Details on the six layers of the ITS during the LHC Run-1 and Run-2. [101][107]. The radial distance r are, in fact, average positions. The rightmost column only includes the material budget of the sensor.

based on three different technologies. The two innermost layers are the Silicon Pixel Detectors (SPD), followed by the two layers of Silicon Drift Detector (SDD). The two outermost layers utilizes Silicon Strip Detectors (SSD). The number of detector, and their positionning, has been optimized in order to guarantee efficient track reconstruction and highly precise estimation of the impact parameter. The pseudo-rapidity coverage varies from a layer to another, but taken as a whole, the ITS covers a range of $|\eta| < 0.9$ for all interaction point within ± 5.3 cm along the beam direction. Its overall material budget of 7.18% X_0 (including the silicon detectors, thermal shields, electronics, support structure, cooling system) makes it the only device capable of detecting low-p_T particles, with a relative momentum resolution better than 2% for pions with momentum between 100 MeV/c and 3 GeV/c. Some important characteristics of the ITS are reported in Tab. 3.5.

The two innermost layers are positionned at 3.9 and 7.6 cm from the origin, covering a pseudo-rapidity range of $|\eta| < 2$ and $|\eta| < 1.4$ respectively. At this distance, the track density can reach values up to 80 tracks/cm^2. In order to cope with these high track densities, the layers are equipped with SPD employing hybrid[13] silicon pixels. It consists of a bi-dimensional matrix of 256 × 160 cells of dimension 50 μm ($r\varphi$) by 425 μm (z). Two matrices are mounted together along the z direction, forming a 141.6 mm long half-stave. Two of them are attached head to head along the beam direction on a carbon-fibre support with cooling tubes in order to forge a stave. The latter are arranged in ten sectors surrounding the beam pipe, each sector supporting two staves for the inner layer and four for the outer layer. While the high granularity of the SPD provides a spatial resolution of 12 μm in $r\varphi$ and 100 μm along z, its fast integration time of 100 ns– corresponding to four consecutive bunch-crossings in pp collisions or one in heavy-ions operation – offers additionnal trigger information.

[13] The term *hybrid* here refers to a type of pixel technology in which the silicon sensor and the readout chip are processed separatedly and connected together via a bump-bonding process. In this way, the detector (silicon sensor) and the electronics (readout chip) can be optimized individually. In LHC experiments, the optimisation is performed such that the detector has a good radiation tolerance and the readout is fast. In return, the assembly tends to be more complex and expensive, the readout chips dissipate a lot of power requiring an efficient cooling system and so more material budget.

The SDDs equip the two intermediate layers at an average distance of 15.0 and 23.9 cm, where the track density rises up to 7 tracks/cm^2. Both layers have a pseudo-rapidity acceptance of $|\eta| < 0.9$. The basic module consists in a sensitive area of 70.17 × 75.26 mm^2, split into two drift regions by a central cathode strip at high voltage such that the drift velocity is 8.1 μm/ns. At this speed, charges drift to one of the 256 collection anodes (with a 294 μm pitch) in a maximum time of 4.3 μs, making it the slowest ITS detector. The SSD modules are mounted on triangular support structure made of carbon-fibre called ladders. The third layer counts 14 ladders with six modules each, and 22 ladders with eight detectors each for the fourth layer. They yield to a spatial precision of 35 μm in the transverse plane and 25 μm along the beam axis. Because of the sensitivity of the SDD layers to temperature changes, two thermal shields surround them in order to avoid any radiation of heat.

The two outermost layers are constituted of double sided SSD of 73 × 40 mm^2, where each side has 768 parallel strips (with a pitch of 95 μm) and corresponds to a side of a p-n junction. The p-side (n-side) of the fifth layer (sixth layer) faces the inside of the ITS. The strips from one side are rotated by a stereo angle of 35 mrad with respect to the other, to reduce the overlapping between the strips and thus the number of ambiguities. The SSD modules are assembled on the same ladder design as those of the intermediate layers: 34 ladders, supporting 22 modules each, are installed on average at 38 cm from the beam pipe for the inner layer and 38 ladders, holding 25 modules each, at 43 cm for the outer layer. Both covers a pseudo-rapidity region of $|\eta| < 0.9$. The SSDs layers provide a spatial resolution of the track position of 20 μm in the $r\varphi$ direction and 820 μm along z, which is essential for the track matching from the Time Projection Chamber to the ITS. Similarly to the SDD layers, its analogue readout allows for the measurement of the charge deposited by the passage of a charged particle, and hence opens the door for PID of low-momentum particles.

II-B.ii Time Projection Chamber

The Time Projection Chamber (TPC) is main tracking device of the ALICE detector. It is responsible for measuring the momentum of charged particle above 150 MeV/c, as well as providing particle identification and primary vertex determination (addressed in more details in Sec. 3|II-D.iii). The TPC design is shown in Fig. 3.6(a). It consists in a cylindrical gaseous detector, surrounding the ITS, with an inner radius of about 85 cm, an outer radius of 250 cm and an overall length of 500 cm along the beam axis. The acceptance of the TPC covers pseudo-rapidities from $|\eta| < 0.9$ (for tracks traversing radially the entire ALICE detector) up to $|\eta| = 1.5$ and the full azimuth (except for the dead zones between sectors). Although it is the largest sub-detector of ALICE, its material budget remains quite low (about 3.5% X_0).

The detection volume corresponds to a field cage filled with gas and separated in two equal parts, along the beam axis, by a central electrode at -100 kV. At this high voltage, this central membrane generates an axial electrostatic field of 400 V/cm. When a charged particle traverses the 88 m^3 of TPC's active volume, it

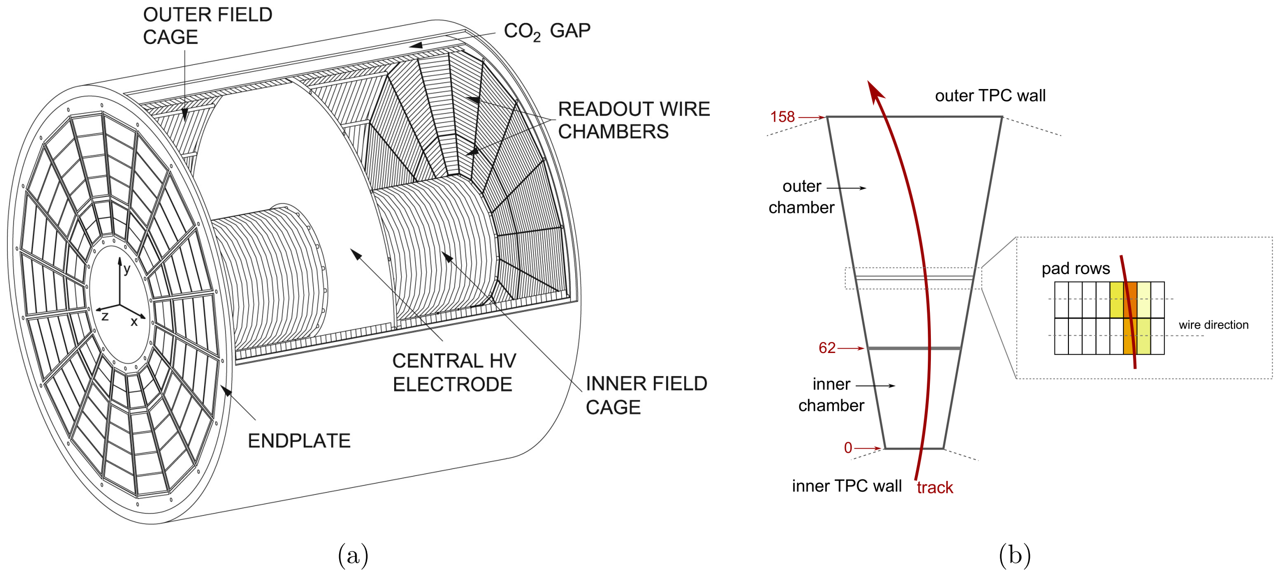

Fig. 3.6: (Left panel) Scheme of the TPC field cage, taken from [112]. (Right panel) Passage of a charged particle through a sector of the TPC. Figure taken from [113].

creates electron-hole pairs along its path by ionisation of the gas. The electrostatic field forces the electrons to drift from the central electrode to the end plates, where they are collected, in a maximum time of 92 μs at a speed of 2.7 cm/μs (depending on the gas composition).

Each end plate is segmented into 18 trapezoidal sectors (as represented in Fig. 3.6(b)), being themselves instrumented with two multi-wire proportionnal chambers (MWPC) with cathode pad readout: one stretches from $R = 84.8$ cm to 132 cm (inner chamber), the other from 134.6 cm to 246.6 cm (outer chamber). This is motivated by the variation of the track density with the radial distance (from the primary vertex), that requires MWPCs with different wire geometry and pad sizes (granularities). Together, the two chambers count a total of 159 readout pad rows: 63 of 4 × 7.5 mm^2 for the inner chamber, 64 of 6 × 10 mm^2 and 32 of 6 × 15 mm^2 for the outer chamber. They measure the deposited charge, as well as the radial position and the drift time. The longitudinal coordinate is inferred from the latter, provided that the drift speed is uniform over the whole volume[14]. In fact, the gas composition has been optimised for high and stable drift velocity, as well as low diffusion and small radiation length. At the start of the LHC Run-2, a mixture of Ne/CO_2/N_2 (90/10/5%) was employed. For the data taking campaign of 2017, it was replaced for Ar/CO_2 (90/10%) before switching back to the initial gas composition in 2018, as it turns out that the latter yields to a reduced space-charge distortion.

The spatial resolution varies from 1100 to 800 μm in the transverse plane, and 1250 to 1100 μm along the beam axis. Although the TPC can not compete with the degree of precision of the ITS, it stands as the main tracking detector in ALICE thanks to its almost continuous sampling of the particle trajectory over large distances.

[14]The longitudinal position is given by the product of the drift velocity and the drift time, $v_{\rm drift} \cdot t_{\rm drift}$.

Moreover, the pad rows provides an analogue readout of the charge deposition, which is used to measure the energy loss of charged particles per unit of length ($\mathrm{d}E/\mathrm{d}x$) with a resolution (σ_{TPC}) ranging from 5.2% in pp events to 6.5% in the most central Pb-Pb collisions. As the energy deposition is stochastic phenomenon by nature, only the moments of its underlying distribution can be predicted. For instance, the Bethe-Bloch formula describes the mean $\mathrm{d}E/\mathrm{d}x$:

$$\begin{aligned} \langle -\frac{dE}{dx} \rangle &= Kz^2 \frac{Z}{A}\frac{1}{\beta^2}\left[\frac{1}{2}\ln\frac{2m_e c^2\beta^2\gamma^2 T_{\max}}{I} - \beta^2 - \frac{\delta(\beta\gamma)}{2}\right], \\ \beta\gamma &= \frac{p}{Mc} \end{aligned} \tag{3.2}$$

with

- Z, the atomic number of the absorber (the TPC gas in this case),
- A, the atomic mass of the absorber (g.mol^{-1}),
- m_e, the electron mass,
- z, charge number of the incident ionising particle,
- M, mass of the incident ionising particle,
- p, momentum of the incident ionising particle,
- β, velocity of the incident ionising particle in units of c,
- γ, Lorentz factor of the incident ionising particle,
- I, mean excitation energy of the absorber,
- $\delta(\beta\gamma)$, density effect correction due to the polarisation of the absorber,
- $T_{\max} = \frac{2m_e c^2\beta^2\gamma^2}{1+2\gamma m_e/M+(m_e/M)^2}$, the maximum energy transfer to an electron in a single collision,
- K, an independent constant of the ionising incident particle or the absorber.

As a matter of fact, the energy deposition follows a Landau distribution. Its broad tail on the high-energy-loss side leads the mean energy loss to be significantly greater than the most probable value. However, the most probable energy loss is much easier to evaluate than the mean that requires large samples to converge. Thereby, the Landau distribution is usually truncated to keep only the 50 to 70% smallest values, and by so doing, the truncated mean coincides with the most probable energy loss [42].

Fig. 3.7 shows clearly the characteristic $\mathrm{d}E/\mathrm{d}x$ bands associated to e, π, p, d, t, ^{3}He and ^{4}He. The measurements distribute around dashed lines, that correspond to the expected mean value given by the Bethe-Bloch formula (Eq. 3.2). By comparing

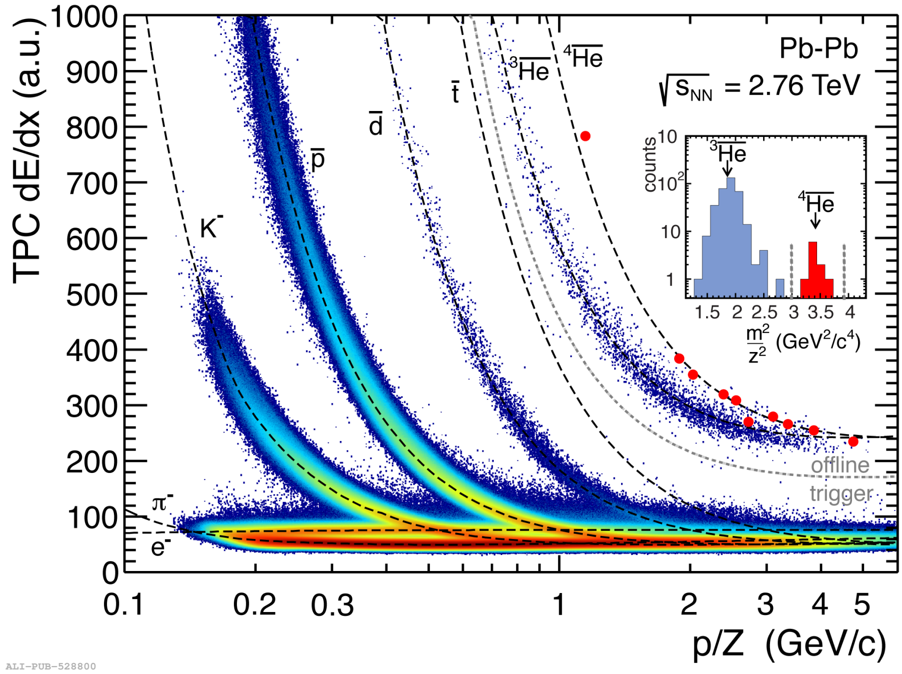

Fig. 3.7: Energy deposition of various charged particles (electron, pion, kaon, anti-proton, anti-deuteron, anti-tritium, and two anti-helium isotopes) in the ALICE TPC in arbitrary units as a function of the magnetic rigidity (momentum over charge number). The dashed lines correspond to the theoretical expectations for each particle species. Figure taken from [84].

the measured value to the expected energy loss for various particle species, the nature of the incident particle can be determined. The PID estimator,

$$n_\sigma = \frac{\langle \mathrm{d}E/\mathrm{d}x\rangle_{\mathrm{meas}} - \langle \mathrm{d}E/\mathrm{d}x\rangle_{\mathrm{exp,i}}}{\sigma_{\mathrm{TPC}}}, \tag{3.3}$$

gives the distance between measured dE/dx and the expected one under the particle mass hypothesis m_i (i = e, π, p, d, t, ^{3}He, ^{4}He), in units of relative resolution σ_{TPC}. Therefore, the TPC is able to distinguish a pion/electron from a kaon with a separation power better than 3σ below ~ 300 MeV/c, and a kaon from a proton up to 1 GeV/c.

II-B.iii VZERO

The VZERO system consists in two scintillator arrays, VZERO-A and VZERO-C, covering the pseudo-rapidity ranges $2.8 < \eta < 5.1$ and $-3.7 < \eta < -1.7$ respectively (Fig. 3.8(a)). It plays a crucial role in the data taking of ALICE as it provides minimum-bias triggers for the experiment, measures the charged particle multiplicity and centrality, and participates in the beam luminosity determination.

Each array is segmented in four rings, themselves being divided in eight sections, for a total of 32 cells made of 45° wide plastic scintillators, as sketched in the Fig. 3.8(b). Because of the integration constraints (mainly coming from the muon absorber), the arrays come in two different designs. The 2.5 cm thick VZERO-A

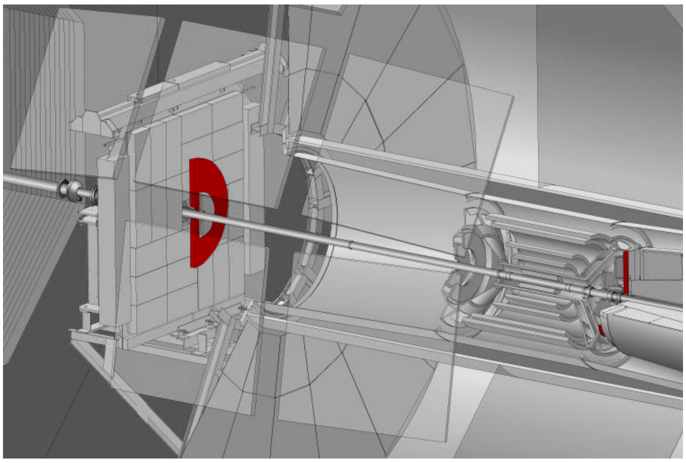

(a)

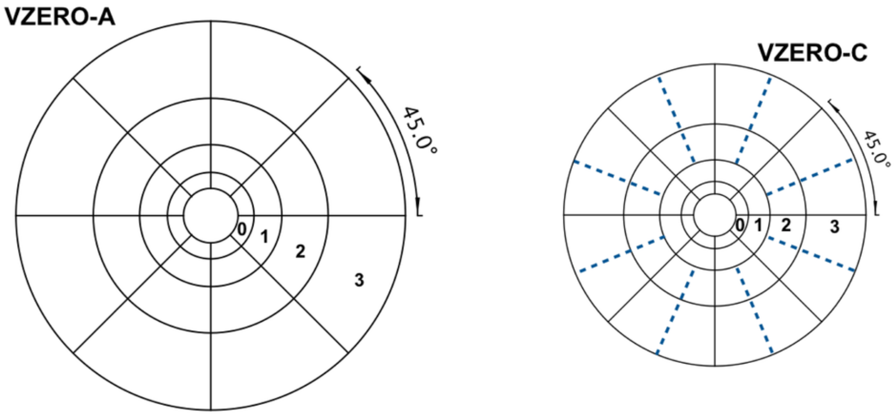

(b)

Fig. 3.8: (Top panel) View of the VZERO scintillator arrays inside the ALICE apparatus: VZERO-A on the left, and VZERO-C on the right. (Bottom panel) Sketches of the VZERO-A (left) and VZERO-C (right) with their segmentation. The dashed lines delimit segments connected to the same photomultiplier tube. Figures taken from [84][114].

sits at $z = 329$ cm from the origin of the detector ($z = 0$). Since the VZERO-C stands in front of the muon absorber, the scintillator thickness has been reduced to 2 cm and its rings are positionned between -86 and -88 cm along the beam axis.

The passage of a charged particle in the scintillator generates light, that is guided to photomultiplier tubes via 1 mm in diameter Wave-Length Shifting and optical fibers. For each of the 32 elementary cells, the photomultiplier tube outputs two analogue signals. The first measures the integrated charge, the second – amplified by a factor 10 – determines the pulse/arrival time relative to the LHC bunch clock with a resolution better than 1 ns. Each signal gives rise to a specific type of trigger algorithm.

Based on the coincidence between the time signals from the arrays, beam-induced background events[15] can be rejected. Fig. 3.9 shows an example of such rejection. A particle coming from the interaction point takes about 11 ns and 3

[15]They typically correspond to beam-gas collisions, that is a collision between a bunch from the beam and a residual gas molecule in the beam pipe

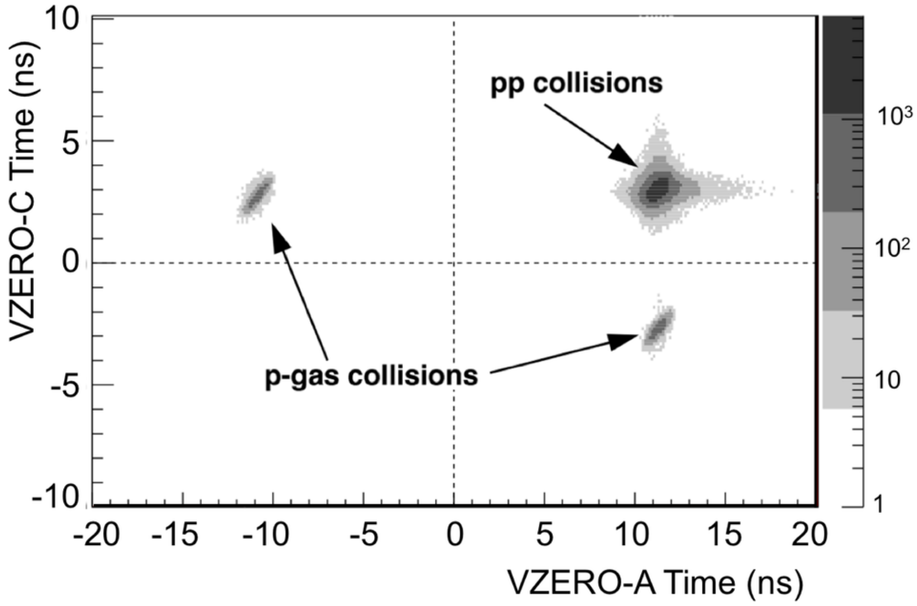

Fig. 3.9: Time of flight of the particles detected in the VZERO-C versus VZERO-A. Figure taken from [114].

ns to reach the VZERO-A and the VZERO-C respectively. If the signals mesured in the both scintillator arrays matches these values — as in the top right corner of Fig. 3.9 —, this indicates that a beam-beam collision have occured. However, the signals arriving in coincidence at -12 ns (VZERO-A) and 3 ns (VZERO-C), and 11 ns (VZERO-A) and -3 ns (VZERO-C) are not the signatures of a beam-beam event. They correspond to beam-gas collisions coming from the A-side and C-side respectively. This is the first type of trigger algorithm.

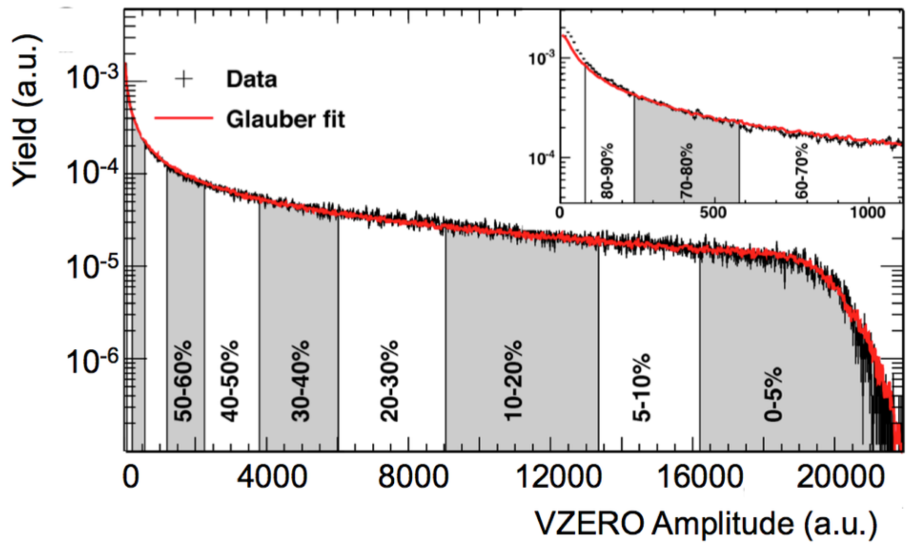

Fig. 3.10: Total yield as a function of the signal amplitudes in the two VZERO arrays in Pb-Pb collisions at $\sqrt{s_{\rm NN}}$= 2.76 TeV, fitted with a Glauber model in red. The shaded areas correspond to different centrality classes. Figure taken from [114].

The energy deposited in the scintillators provides a measurement of the charged particle multiplicity. Based on a simulation of the VZERO detectors, the total charge collected can be related to the number of primary charged particles, as shown in Fig. 3.10. The second type of trigger algorithm consists in dividing the distribution of the V0 amplitudes in different multiplicity/centrality[16] classes from the 5%-highest multiplicity to the 10%-lowest multiplicity events, as represented in shaded areas.

II-B.iv Time-Of-Flight detector

The Time-Of-Flight (TOF) detector is a large cylindrical array with an inner radius of 370 cm and an outer one of 399 cm. It covers the central pseudo-rapidity region, that is $|\eta| < 0.9$, and the full azimuth. While the separation power of TPC only goes up to 1 GeV/c, the TOF detector aims at providing particle identification at intermediate momentum from 0.2 to 2.5 GeV/c. To instrument this large volume (17.5 m^3), a gaseous detector is employed, as its manufacture turns out to be relatively simple and thus quite inexpensive. The best solution, with respect to the design considerations of the experiment, is the Multi-gap Resistive-Plate Chamber (MRPC) [115].

The basic constituent of the TOF system is a pair of MRPC strips, 122 cm in length and 12 cm in width, stacked together with an active area of 120 × 7.4 cm^2. As shown in Fig. 3.11(a), it consists in two cathodes and a central anode in a gas volume, and spaced by five 0.4 mm thin glass plates (with a 250 μm gap) for each strip. The full volume is filled with a gas mixture composed of $C_2H_2F_4$(90%), C_4H_{10}(5%), SF_6(5%), as it shows no ageing effects and has a rate capability much higher than the expected rate in ALICE [116].

To cover the full cylinder along the beam direction and minimise the cumulative dead areas from the innermost to outermost detectors in ALICE, five modules of different lengths are combined. The central element utilizes 117 cm long module, the intermediate ones 137 cm, the external ones 177 cm made of 15 MRPC strips for the central module and 19 for the others. Altogether, they form a supermodule of total length 930 cm with an overall active region of 741 × 7.4 cm^2, as shown on Fig. 3.11(b). Each of the 18 azimuthal sectors of the TOF system has a supermodule.

When a charged particle traverses the active volume, it ionises the gas along its path and produces electrons that drift to one of the cathodes. The key aspect of the MRPC resides in the high voltage of the anode (-13 kV), which delivers a high and uniform electrostatic field. The latter is sufficiently strong to start an avalanche process[17], and thereby to give rise to a detectable signal. The avalanche stops when

[16] In heavy-ion collisions, the impact parameter – and, *a fortiori*, its percentage value, the centrality – cannot be measured directly, but the number of charged particle is measurable using – among others – the VZERO detectors. Since the centrality and the charged particle multiplicity in the event are correlated, the latter allows to recover the centrality (as confirmed by the Glauber fit in Fig. 3.10, that also gives access to the centrality). Hence, for heavy-ion collisions, the different intervals in multiplicity in Fig. 3.10 are referred as *centrality classes*.

[17] Let us consider a medium containing free electrons and in which a strong electrostatic field exists. If the latter is strong enough, it accelerates the electrons such that they will collide with other atoms in the medium, thus ionising them and releasing additionnal electrons. These ones also get accelerated and collide with other atoms, releasing more electrons, and so on. This chain

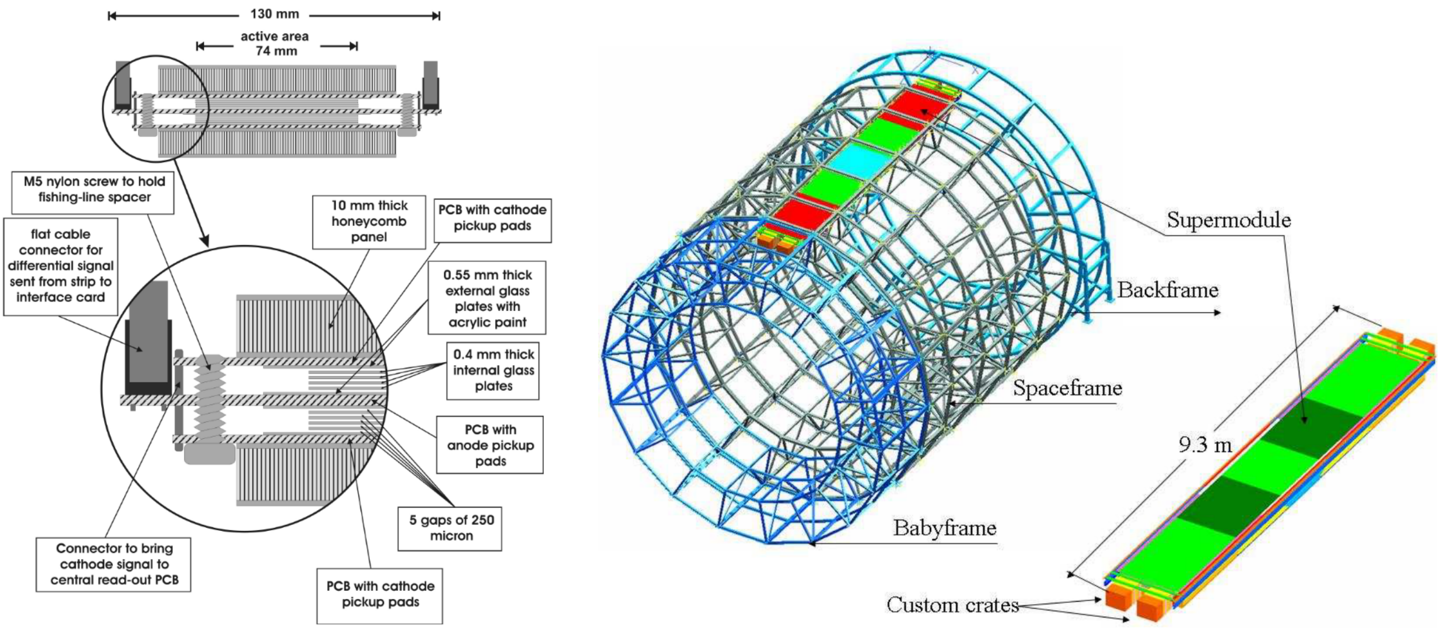

(a) (b)

Fig. 3.11: (Left panel) Drawing of the cross section of a 10-gap double-stack MRPC. (Right panel) Schematic view of the TOF barrel with one supermodule, consisting of five modules. Figure taken from [101].

it reaches a glass plate, but the produced electrons continue to drift – and to create avalanches in the gaseous medium along the way – until they are collected by the 48 cathode pad readouts of 3.5 × 2.5 cm^2 from each strip.

Their output signals carry informations on the deposited charge via the Time-Over-Threshold and the hit times relative to the collision time, t_{ev} , with an intrinsic resolution of 56 ps during the LHC Run-2. Due to the finite size of the colliding bunches, t_{ev} has to be measured on an event-by-event basis. To that end, different options are available.

The most precise measurement of the collision time is provided by the T0 detector. It consists in two arrays, each made of twelve Cerenkov counters, placed at $z = 375$ cm (T0-A) and -72.7 cm (T0-C). They respectively cover the pseudo-rapidity range $4.61 < \eta < 4.92$ and $-3.28 < \eta < -2.97$. Each counter is a quartz radiator of 20 mm in diameter and 20 mm thick, connected optically to a PMT. The readout electronics is quite similar to the one used for the TOF detector, with a dead time below 25 ns. The T0 system gives two time measurements, one for each array, $t_{\mathrm{T0-A}}$ and $t_{\mathrm{T0-C}}$. When both values are available, the average is taken as the start time of the event, $t_{\mathrm{ev}}^{\mathrm{T0}} = (t_{\mathrm{T0-A}} + t_{\mathrm{T0-C}})/2$, with a resolution of 50 and 25 ps in pp and Pb-Pb collisions. If only one of the two counters produces a signal, the collision time is given by either the $t_{\mathrm{T0-A}}$ or $t_{\mathrm{T0-C}}$ taking into account the longitudinal position of the primary vertex (provided by the ITS). Consequently, the resolution deteriorates to 100 and 60 ps in pp collisions for the T0-A and T0-C respectively, and 50 and 30 ps in heavy-ion collisions. Due to its limited acceptance, the triggering efficiency of

reaction is called an avalanche process.

the detector in coincidence is about 48%, and reaches 60% and 67% for the T0-A and -C individually in pp collisions[18].

The TOF system itself can also determine t_{ev}. Based on a sample of particles matching a hit in the detector, a χ^2-minimisation procedure is performed in order to extract the set of mass hypotheses that minimises their combined time-of-flights. From this set derives the event collision time, denoted $t_{\mathrm{ev}}^{\mathrm{TOF}}$. By construction, this procedure only applies for a minimum number of two tracks, and the resolution improves with the track multiplicity (scaling as $\sim 1/\sqrt{N_{\mathrm{tracks}}}$). It allows to reach time resolution from 80 ps for the low multiplicity events to 20 ps for the high multiplicity events, with efficiencies ranging from 20% to 100% respectively.

Considering the above efficiencies, the collision start time can be obtained from the T0 or TOF measurement ($t_{\mathrm{ev}}^{\mathrm{T0}}$ or $t_{\mathrm{ev}}^{\mathrm{TOF}}$), or even their combination if both are available. In the latter case, the final t_{ev} corresponds to their weighted average, with the inverse of their resolution squared as weighting factors. If none of the preceding procedures is usable, the start time of the event is set on the LHC clock[19] which has a resolution of 200 ps [117].

In any case, the difference between the arrival time t_{TOF} and the moment of the collision t_{ev} gives the *measured time-of-flight* of the charged particle from the primary vertex to the TOF detector. Based on the latter and the flight path length, the velocity of the particle – or rather the ratio of the velocity to the speed of light, $\beta = v/c$ – can be evaluated. The Fig. 3.12 shows the distribution of β for charged particles measured by the TOF detector as a function of their momentum in Pb-Pb events at $\sqrt{s_{\mathrm{NN}}}$= 5.02 TeV. A clear separation of the electron, pion, kaon, proton and deuteron bands is visible. This stems from the relation between the particle mass m, its momentum p and its velocity β:

$$m = \frac{p}{\beta\gamma} = p\sqrt{\frac{1}{\beta^2} - 1} \qquad \text{with} \quad \beta = \frac{v}{c} = \frac{L}{ct_{\mathrm{exp}}}, \tag{3.4}$$

$$\Rightarrow t_{\mathrm{exp}} = L\,\frac{\sqrt{p^2 + m^2}}{cp}. \tag{3.5}$$

In Eq. 3.5, t_{exp} corresponds to the *expected time-of-flight*, *i.e.* the time it would take for a particle of mass m, with a momentum p, to go from the interaction point to the TOF detector following a path of length L. To this quantity is attached an uncertainty coming from the track reconstruction, as it will be detailed in Sec. 3|II-D. By comparing the measured time-of-flight t_{TOF} and the expected one $t_{\mathrm{exp,i}}$ for different mass hypothesis m_{i} (i = e, μ, π, K, p, d, ^{3}He, ^{4}He), particle identification can be performed. The PID estimator n_σ is constructed in the following way:

$$n_\sigma = \frac{t_{\mathrm{TOF}} - t_{\mathrm{ev}} - t_{\mathrm{exp,i}}}{\sigma_{\mathrm{PID,i}}}, \qquad \text{with} \quad \sigma^2_{\mathrm{PID,i}} = \sigma^2_{t_{\mathrm{TOF}}} + \sigma^2_{t_{\mathrm{ev}}} + \sigma^2_{t_{\mathrm{exp,i}}}. \tag{3.6}$$

Therefore, the TOF detector is capable of identifying charged particles in the

[18] The triggering efficiency is close to 100% in heavy-ion collisions, due to their inherently high multiplicities.

[19] In fact, it is set on zero as, after alignement and calibration of the TOF detector, the LHC clock phase has been shifted to coincide with the nominal starting time.

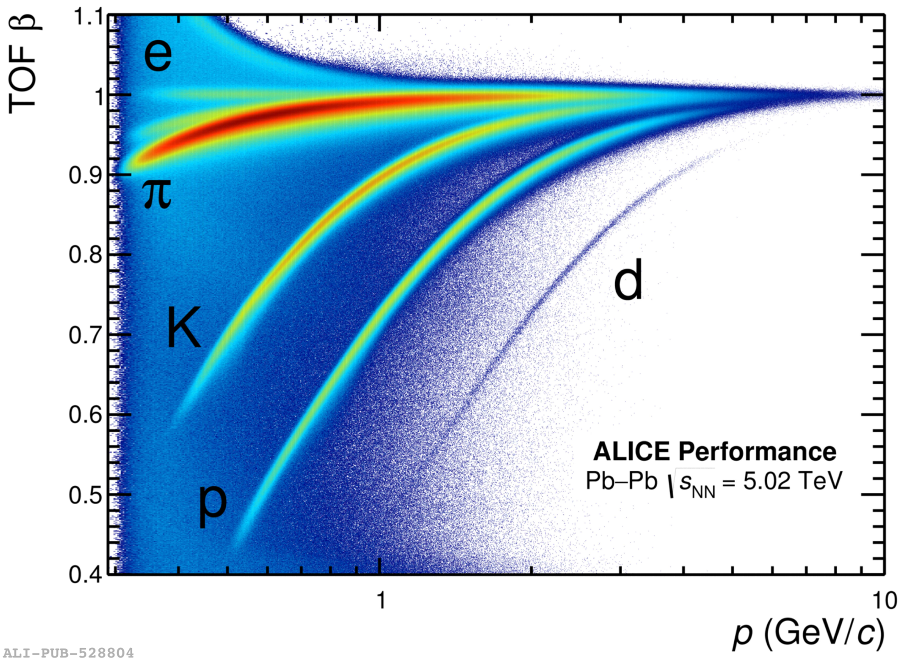

Fig. 3.12: Velocity ($\beta = v/c$) of electrons, pions, kaons, protons and deuterons as a function of their momentum (provided by the TPC), measured by the TOF detector, in Pb-Pb collisions at $\sqrt{s_{\rm NN}}$= 5.02 TeV. Figure taken from [84].

intermediate momentum range, with a separation power better than 3σ between pions and kaons below 2.5 GeV/c, and up to 4 GeV/c between kaons and protons.

II-c Trigger system and data acquisition

In contrast with its current LHC Run-3 version, ALICE only records triggered data in the Run-1 and Run-2, *i.e.* events are selected and stored based on a variety of different features. The Central Trigger Processor (CTP) is in charge of optimising the trigger system in order to make the best use of i) the various detector components, that are busy for different period of time (~88 μs for the TPC versus the T0 with <25 ns) when a valid trigger signal is received, and ii) the different running modes (pp, pPb, PbPb with specific interaction rates).

The latter is achieved by ensuring that the data collection is not ruined by the pile-up. Here, we refer primarily to event pile-up between different bunch crossings, that is treated differently depending on the expected multiplicity and luminosity. The one occuring between two central or semi-central heavy-ion collisions must be avoided as the density of tracks is so high that they become unreconstructable. However, the pile-up level between a (semi-)central and up to two peripheral Pb-Pb collisions is tolerable in some detectors – such as the TPC – and not in others – the ITS for example. The same applies for pp collisions where pile-up is unavoidable but tracks are reconstructable due to much lower track densities than in Pb-Pb. To that end, a *past-future* protection has been implemented, which basically verifies that the level of pile-up in the sensitive time windows of each detector[20] remains tolerable as defined in the above requirements.

To ensure efficient data taking, the ALICE detector is not entirely readout for every event. Instead, it is divided into groups of sub-systems named detector *clusters*. For instance, the data from the forward muon arm do not need the TPC to be exploitable, only the trigger detectors (in particular the V0 and SPD for determining the centrality/multiplicity class and primary vertex location) are required. By grouping these detectors into the same cluster, they can be read out separately from the other devices. Thereby, the number of detector clusters amounts to three: one for the full detector, another comprising only the central detectors, and a last one including the forward muon detectors and the trigger detectors.

In addition, the hardware trigger system divides into three levels – dubbed L0, L1 and L2 – with different latencies [118][119]. At each LHC clock cycle (that is every 25 ns in pp and 100 ns in heavy-ion mode), the CTP checks for the inputs from detectors with fast trigger capabilities (essentially the T0, V0, SPD and TOF) up to 800 ns after the collision (time needed for the SPD to transmit its trigger signal to the CTP). When the inputs coincide with the requirements of one (or more) *trigger class*[21], the trigger system issues a Level 0 (L0) decision in less than 100 ns, that reaches the detectors 1.2 μs after the interaction. Upon reception of the L0 signal, detectors move into a busy-state in which they stop taking new data until they have been fully read out. Since all the detector inputs can not be transmitted under 800 ns, the CTP collects all the signals that can be delivered under 6.1 μs, checks the conditions for all trigger classes and – in the absence of a veto from the past-future protection circuit – generates a Level 1 (L1) trigger arriving at the detectors 6.5 μs after the collision. Together, the L0 and L1 signals represent the fast response of the trigger system. The last signals arrives 87.6 μs after the collision, due to the drift period of the TPC. A level 2 (L2) trigger decision is sent with a latency of 100 ns and reaches the detectors at 88 μs, to finally conclude on whether the event is accepted or rejected. At this stage, a rejection most often comes from excessive pile-up.

ok!

Among the different trigger classes, two configurations play an important role in ALICE and in the present work: the minimum-bias (MB) and the high-multiplicity (HM) classes. As its name suggests, the former refers to the least biasing conditions for the data acquisition in ALICE over the full multiplicity distribution. Its requirements have evolved over the years, though. Because of the low interaction rate in pp in 2009 and 2010 data takings, the minimum-bias trigger selections were kept loose: it required a hit in either VZERO counters or in one of the two SPD layers (MB_{OR}). In this way, the collected event would have at least one charged particle in eight units of pseudo-rapidity. As the luminosity and the amount of beam-gas

(+)

[20]For instance, the past-future protection circuit checks on the TPC that the pile-up occuring between -88 μs (past) and +88 μs (future) relative to the collision time stays managable. The same logic applies to the rest of the ALICE devices. In fact, three categories of detectors can be drawn out: the ones that can provide a signal at each bunch crossing and thus do not not need a protection, the others requiring the application of the past-future condition under 10 μs, and the TPC demanding a protection under 88 μs.

[21]This is the set of detector signals that defines a trigger selection. ALICE counts 50 trigger classes [101].

background increase, the conditions were tightened up and the high selection efficiency MB trigger is traded off for a high purity one. Hence, to be recorded, an event necessitates a coincidence between the two VZERO detectors ($\mathrm{MB}_{\mathrm{AND}}$). This is equivalent of asking for, at least, two charged particles separated by 4.5 units of pseudo-rapidity: one in the A-side, the other in the C-side[22] [120][121].

The HM trigger corresponds to 0.1% highest multiplicity events from the MB sample; it has been implemented in order to study efficiently rare signals, most particularly in small systems. Throughout the LHC Run-1, it was based the number of hits in the outer layer of the SPD for the multiplicity estimation. The threshold was typically set between 80 to 100 hits which represent about 60 to 80 pairs of matching clusters between the two SPD layers, also refered as SPD tracklets ($\mathrm{HM}_{\mathrm{SPD}}$) [121]. However, in the Run-2, the default HM trigger configuration changes and now relies on the signal amplitude of the VZERO counters, that is correlated with the event multiplicity ($\mathrm{HM}_{\mathrm{VZERO}}$) as explained in Sec. 3|II-B.iii.

1 "The online HM trigger"

"in the Run-2, 2 if $\mathrm{HM}_{\mathrm{SPD}}$ still exists, the default HM trigger..."

As a side note, because the SDD is the slowest ITS detector (4.3 μs) compared to the others (300 ns for the SPD and 1.4 to 2.2 μs for the SSD), it acts as a bottleneck and limits significantly the triggering rate. For that reason, the trigger system operates in two modes: the default option, called "CENT", corresponds to the one where events are recorded with the informations of the SDD. In the case when this detector is still in busy-state at the reception of the L0 signal, the "FAST" configuration allows nevertheless to record the event without reading out the SSD. In this way, by combining these two trigger configurations (CENT and FAST), one can double the amount of data available but at the price of a lower track reconstruction efficiency (Sec. 3|II-D.ii).

The reception of a successful L2 trigger signal initiates the detectors readout. Each one produces *event fragments* that are transmitted to Data AcQuisition (DAQ) readout receiver cards, being themselves linked to Local Data Concentrators (LDCs). The latter gathers the event fragments from its associated cards and assembles them into sub-events. In parallel, a copy of the readout data is transfered to the High-Level Trigger (HLT) farm computer, that performs an online processing in order to filter out interesting physics events with more sophisticated and precise selections (jet identification, sharp p_{T} cut, etc) than the lower layer triggers (L0, L1, L2). It can also reduce the output size by selecting relevant parts of the event. The triggered event or the regions of interests are compressed, transfered back to the LDCs. The DAQ system treats the output of HLT system as the one of any other sub-detector.

A single machine of the Global Data Collector (GDC) farm[23] receives the sub-events from sub-detectors' LDCs — including the ones from the HLT computers –

[22] In fact, there exists still a few variants of the minimum-bias trigger such as at least a one hit in the SPD, or one hit in either VZERO scintillator arrays, or even both simultaneously.

[23] The Event-Destination Manager (EDM) supervises the distribution of LDC's sub-events from the same event to single GDC machines, and balances the data stream in order to avoid event loss by overloading the GDC farm (the so-called back-pressure). The latter point is critical for the reconstruction of rare events, as more frequent events take up most of the GDC load. Hence, the EDM monitors their GDC occupancy and, in case it is too high, they are blocked in favour of the rare events. With the past-future protections, these are the two cases that may lead to a rejection at the L2 trigger stage.

and proceeds to the event reconstruction. The Transient Data Storage archives the output data over the storage network before their final recording into the Permanent Data Storage.

II-D The event reconstruction

The event reconstruction starts at the DAQ-LDC level, where the digitised signals of each detector, that have been likely generated by the same particle, are grouped into a *cluster* based on their space and/or time proximities. Its centre of gravity is often taken as an estimate for the crossing point of a particle in the sensitive volume of the detector.

II-D.i Preliminary determination of the primary vertex

From these clusters in the two innermost layers of the ITS, a preliminary estimation of the primary vertex position is realised [122]. The pairing of SPD clusters between the inner and outer layers (within an azimuthal window of $\Delta\phi = 0.01$ rad) allows to form tiny track segments[24] called *tracklets*. The space point towards which the maximum number of tracklets converges gives a first estimate of the primary vertex location.

Concretely, the reconstruction algorithm attempts to minimise the quantity

$$D^2 = \sum_i^N \left(\frac{x_i - x_0}{\sigma_{xi}}\right)^2 + \left(\frac{y_i - y_0}{\sigma_{yi}}\right)^2 + \left(\frac{z_i - z_0}{\sigma_{zi}}\right)^2, \tag{3.7}$$

with N the number of considered tracklets, and each term of the sum corresponds to weighted distance along x, y or z between the tracklet i (x_i, y_i, z_i)[25] and the interaction point (x_0, y_0, z_0). The minimisation procedure is repeated several times; at each iteration, the tracklets contributing to the previously found vertex are discarded from the sample. Hence, by construction, the first reconstructed vertex takes up the majority of tracklets and is designated as the primary vertex. Since the spatial resolution scales as $1/\sqrt{N_{\text{tracklets}}}$, the latter also turns out to be the most accurate.

In cases where no convergence point is found (as it happens in low-multiplicity events), the algorithm searches for a vertex along the beam axis, with the constraint that it coincides with the beam position in the transverse plane. It is calculated as the weighted mean of the intersection points with the beam axis over all the tracklet candidates.

If no pair of clusters can be formed in the SPD, the primary vertex and thus the event are not reconstructed.

[24] The track curling being supposedly small between the radii of the two SPD layers (3.9 and 7.6 cm), it can be approximated as a straight line, most particularly in the case of high-momentum particles [107].

[25] Here, this is the tracklet's position at the point of minimum distance with respect to the primary vertex. At the start of the minimisation procedure, the initial location of the vertex is taken as the mean position of the intersection point of all selected tracklets [107].

II-D.ii Track reconstruction

The determination of the trajectory — or *tracking* in the particle physicist's jargon — of a charged particle breaks down into two major phases: the *track finding* and *track fitting*. The former aims at associating a set of clusters to the same track, and from this, the latter tries to estimate the track parameters such as the charge or momentum. Both can be performed using global or local methods.

Broadly speaking, the global approach treats all the measurements simultaneously, once all the informations have been collected. It has the advantages of being stable with respect to noise and directly applicable on raw data, but it does a require a precise knowledge of the model that may be unknown or do not exist because of random perturbations or non-uniformity of the magnetic field for instance. The online event reconstruction on the HLT computer farm typically uses such techniques (Cluster Finder and Track Follower methods, fast Hough transform), primarily because they are fast but also a high precision is not required at this stage (mostly interested in the reconstruction of high-momentum particles).

In contrast, the local methods proceed to a progressive estimation of the parameters from one measurement to the next, each step improving the knowledge about the trajectory. Thereby, they do not require to know the global model, as any local effect (stochastic processes, etc) can be naturally accounted for at each data point. However, they are sensitive to the noise, wrong measurement or misassociation, and rely on complex reconstruction algorithms. Among all the local approaches, the most advanced one is the Kalman filter technique, which is the one adopted for the offline reconstruction in ALICE.

Within the framework of the Kalman filter, the five track parameters at a given time (or equivalently, at the position of a given hit) are contained inside the *system state vector*. The latter evolves according to an iterative procedure in two steps.

- **Prediction:** The track parameters are extrapolated to the next detection plane as the sum of a deterministic term – depending only on the current knowledge of the state vector – and a noise term accounting for stochatistic processes such as multiple scattering or energy loss.

- **Filtering:** If a cluster at the extrapolated position is found in the vicinity of the predicted measurement, it is added to the prediction, thus improving/updating the state vector. In this way, cluster association with a track (track finding) appears naturally and simulatenously with the track fitting.

These steps repeat as many times as there are measurement points. There also exists a third (optional) phase, called **smoothing**, available once the full state vector has been extracted: the prediction and filtering steps are replayed in the opposite direction, starting from the last filtered point. These can be reiterated as much as required; each pass refining the track parameters such that the reconstructed track reproduces more and more the real particle trajectory.

Note that the two aforementionned random perturbations of the particle trajectory are in fact treated differently[26]. On one hand, the multiple scattering introduces an angular uncertainty on the position of the next measurement, which

[26] This originates from the different stochastic nature of these processes. The multiple scattering follows a Gaussian distribution with a zero mean value and a variance given by the Molière theory

translates into an increase of the covariance matrix elements of the state vector. On the other hand, the energy loss affects the momentum of track parameters, but can be estimated on average knowing the amount of crossed material and using the Bethe-Bloch formula in Eq. 3.2 under the assumption of a certain particle mass. Hence, a $\mathrm{d}E/\mathrm{d}x$ correction of the track parameters can be applied at each prediction step.

In ALICE, the Kalman-filtering track reconstruction uses three passes, as illustrated in Fig. 3.13.

The first inward stage (first path on Fig. 3.13) starts by looking for the first clusters of a track candidate, dubbed *track seed*, in order to initate the Kalman-filter procedure. This search commences in the best tracking device of the experiment, *i.e.* the TPC, and particularly at its outer radius where the low track density limits the number of ambiguous cluster association. At first, the seeds consist of two TPC clusters and the preliminary vertex point. This initial guess relies on the fact that the track originates from the interaction point. This process is reiterated later without such constraint, which would correspond to secondary tracks coming from a decay. In such case, the seeds are formed out of three clusters.

Once the seeds have been built, they are propagated inwards to the TPC inner radius. As described above, at each step, the seeds are updated with the nearest space point whenever one passes a proximity cut, taking into account multiple scatterings and energy losses[27]. At the end, only the tracks with at least 20 (out of 159) attached clusters and with a minimum of 50% of the predicted measurement points matching an associated hit, are selected.

During this propagation, a preliminary particle identification based on the energy deposit in the TPC gas (see Sec. 3|II-B.ii) allows to determine the most probable mass of the track candidate among eight hypothesis: $\mathrm{e}^{\pm}$, $\mu^{\pm}$, $\pi^{\pm}$, $\mathrm{K}^{\pm}$, $\mathrm{p}^{\pm}$, $\mathrm{d}^{\pm}$, $\mathrm{t}^{\pm}$, $^{3}\mathrm{He}^{2\pm}$ or $^{4}\mathrm{He}^{2\pm}$. In cases where there is an ambiguity, the pion mass is assigned by default. From this and the amount of crossed material at each step, energy losses can be corrected on average using the Bethe-Bloch formula (Eq. 3.2). It should be emphasised that all the parameters related to the TPC corresponds, in fact, to those of Ne. This approximation is justified by i) the fact that the TPC gas consists mainly of this element, and ii) the effect is relatively small.

When all the seeds have reached the inner wall of the TPC, the tracking in the ITS takes over. The reconstructed TPC tracks are extrapolated from the TPC inner wall (~ 85 cm) to the outermost layers of the ITS (SSDs at 38 and 43 cm) that serve as seeds for the track finding in the ITS. Similarly as in the TPC, the

---

[42]. In other words, the associated noise term should be unbiased ($\langle \epsilon \rangle = 0$) with a known covariance matrix. In contrast, the energy loss leads to a biased noise term ($\langle \epsilon \rangle \neq 0$), given by the Bethe-Bloch formula. However, it should be dominant for small particle energies where the covariance matrix is driven by the multiple scattering dominates. Hence no error term, associated to energy losses, is added to the covariance matrix [123].

[27] To keep in mind: for an outward propgation (for instance, from the primary vertex to the TPC), taking into account energy losses means subtracting energy to the track parameters, as this corresponds to the actual direction of flight of the charged particle and in which it looses energy while traversing material. Conversely, for an inward propagation (from TPC to the primary vertex, for example), energy needs to be added to the track parameters, since the particle travels in the counter-flight direction.

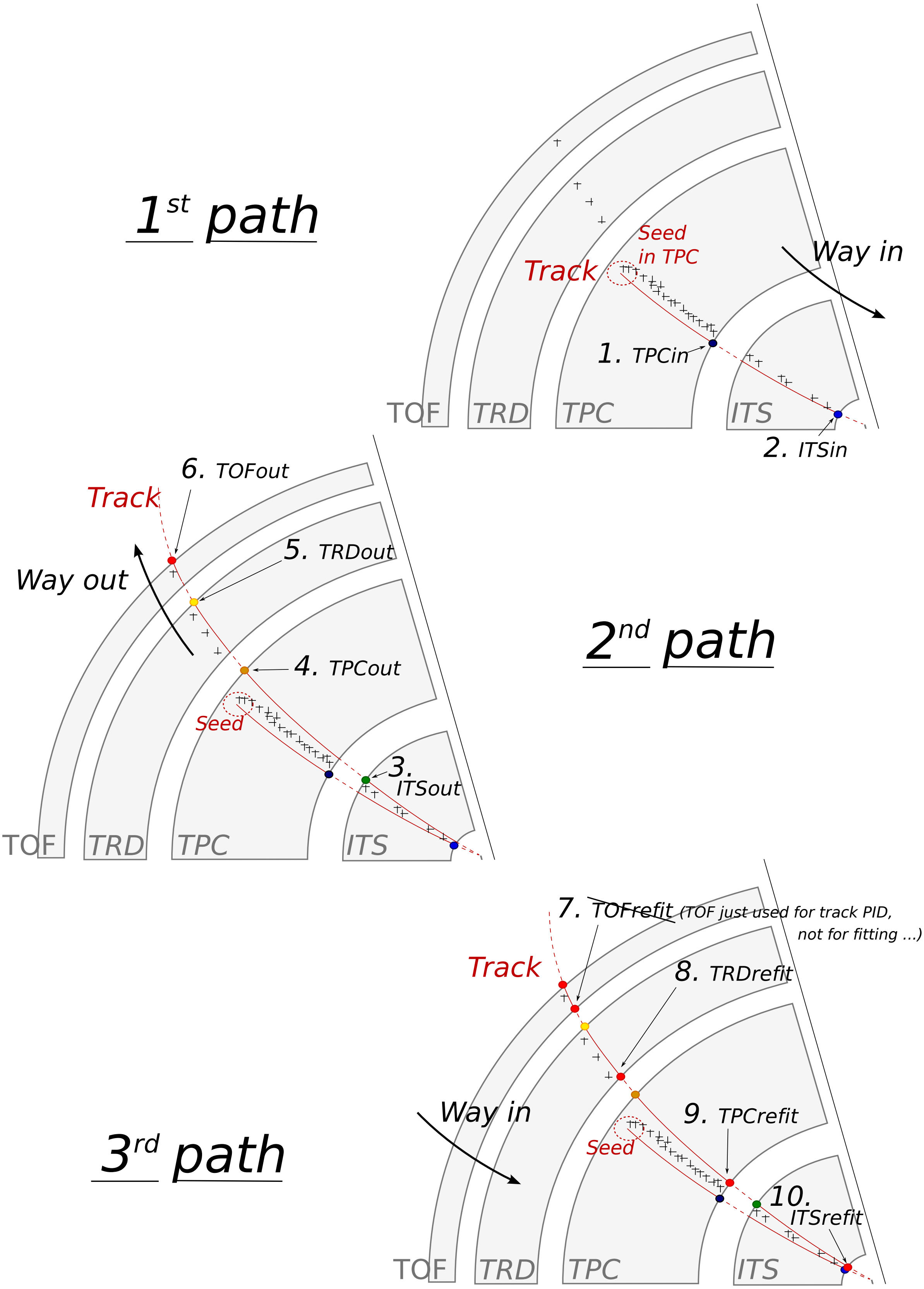

Fig. 3.13: Overview, at each pass of the Kalman filter, of the different elements related to the track reconstruction in ALICE. Figure taken from [124].

seeding procedure produces two kinds of seed: first, one with a vertex constraint, then the other without it. Whatever the hypothesis, they are all propagated as close as possible to the primary vertex, and updated along the way by any cluster passing a proximity cut. Only the highest quality candidates in the ITS from each TPC track are selected. A further check on cluster sharing among each other is performed. In such a case, the tracking algorithm tries to find another candidate and if this fails, the worst of the two tracks receives a special flag for containing a shared cluster that is potentially an incorrectly assigned cluster.

Once all the ITS-TPC tracks have been formed, the ITS standalone tracking procedure comes into play and uses the remaining clusters to recover unfound tracks in the TPC because of i) their very low momentum or ii) the deadzones between sectors, or iii) decays before reaching the TPC. Formed out of two clusters from the three innermost layers and the preliminary vertex point, the seeds are propagated to the other layers, and updated with clusters passing a proximity cut. Only the track hypothesis with the smallest reduced χ^2 is kept, and its assigned clusters are removed from further track finding. The procedure repeats until there are no more track to search.

Upon completion of the track reconstruction in the ITS, the first stage of the tracking ends with the extrapolation of all tracks to their point of closest approach to the preliminary primary vertex. As in the TPC, energy loss corrections are applied at each propagation step in the ITS, considering the same mass hypothesis as one used previously and assuming that all the materials in the ITS volume (including the beam pipe) are made of Si[28].

The second stage starts with the outward refitting of the track parameters by the Kalman filter using the previously associated clusters. It is also during this second pass that the track length integral, as well as the expected time of flight for the eight particle mass hypothesis, are calculated; both quantities are updated at each step. The propagation procedure goes first from the primary interaction point to the outermost layers of the ITS, and then towards the TPC outer wall (second path on Fig. 3.13). When reaching the outer edge of the TPC, the Kalman filter stops updating the track parameters but the propagation continues in an attempt to match the track with a hit in a further detector (TRD, TOF, EMCal, PHOS, HMPID). The track length integration and time-of-flight calculation finish upon arriving at the TOF detector.

At the final stage (third path on Fig. 3.13), starting from the TPC outer wall, all tracks are propagated inwards to their distance of closest approach (DCA) to the preliminary primary vertex. Along the way, their parameters are improved one last time with the previously associated clusters in the ITS and TPC.

The reconstruction efficiency of TPC standalone tracks saturates around 80-85% for transverse momentum above 0.5 GeV/c, due to the loss of clusters in dead-zones between sectors. At lower p_{T}, it drops rapidly due to the preeminence of

[28]This relies on the same arguments as those mentioned in the case of the TPC. The Chap. 5 addresses the limits of this approximation.

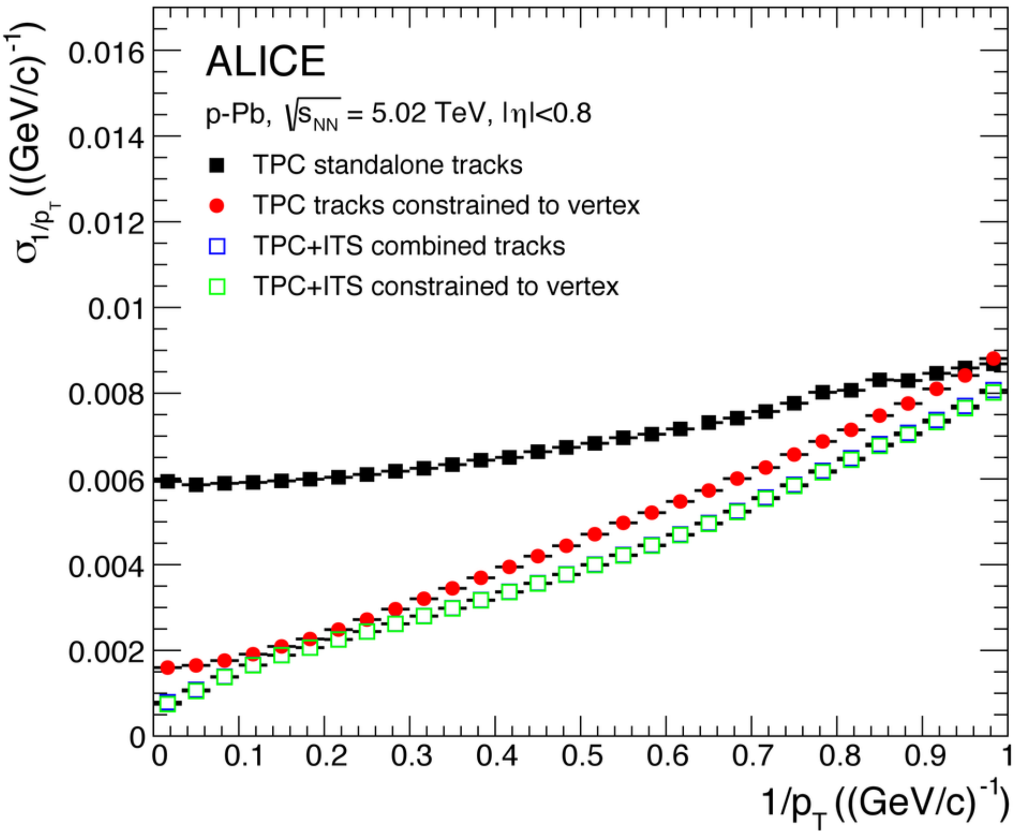

Fig. 3.14: Transverse momentum resolution for TPC standalone and ITS-TPC combined tracks, with and without vertex constraint, as a function of $1/p_T$ in p-Pb collisions at $\sqrt{s_{NN}}$= 5.02 TeV. The blue squares can not be seen as they overlap with the green ones. Figure taken from [109].

multiple scattering and energy loss in the detector material. Whatever the detector occupancy, the contamination of wrongly associated clusters in the TPC remains low; it does not exceed 3% for tracks with more than 10% of fake clusters, even in the most violent heavy-ion collisions.

The TPC track prolongation efficiency to the ITS depends mildly on transverse momentum. It reaches ~ 95% for tracks with at least two associated hits in the ITS, and decreases to about 80% in pp collisions at $\sqrt{s}$ = 7 TeV (75% in Pb-Pb collisions at $\sqrt{s_{NN}}$= 2.76 TeV) when they have a minimum of one hit over two SPD layers, the furthest detectors relative to the TPC. The contamination of wrongly associated ITS clusters, though, can be quite high: ~ 30% of tracks with at least one fake cluster below $p_T < 0.2$ GeV/c, ~ 7% at 1 GeV/c, and below 2 % at 10 GeV/c in the most central Pb-Pb collisions.

The Fig. 3.14 shows the resolution on the inverse transverse momentum for TPC standalone and ITS-TPC combined tracks, extracted from their covariance matrix. This quantity is related to the relative transverse momentum resolution, σ_{p_T}/p_T, via

$$\sigma_{1/p_T} = \frac{\sigma_{p_T}}{p_T}\frac{1}{p_T} \quad \Rightarrow \quad \frac{\sigma_{1/p_T}}{1/p_T} = \frac{\sigma_{p_T}}{p_T}. \tag{3.8}$$

The transverse momentum resolution varies as a function of the transverse momentum; typically, it is at least as good as 0.9% at $p_T = 1$ GeV/c and 6% at $p_T = 10$ GeV/c.

Note that the global ITS-TPC tracks always yields to a better relative p_{T} resolution than those reconstructed only with the TPC. In the latter case, the vertex constraint on the seeding strongly improves the resolution but the effect is negligible with a matching to the ITS detectors.

II-D.iii Final determination of the primary vertex

The end of tracking stage opens the way towards a new determination of the primary vertex, based on the ITS-TPC combined tracks. Unlike the tracklets, their curvature is known, which allows to find the interaction point with a much higher precision.

All the global tracks are extrapolated as close as possible to the nominal beam position (or luminous region[29]). After rejection of far outliers, the approximate point of closest approach of all selected tracks provides a first estimation of the interaction vertex. From here, in the near vicinity of its true position, a highly precise vertex fit can be performed [125]. It basically consists in finding the space point that minimises the weighted[30] distance of closest of approach to this same point over all the tracks, as in Eq. 3.7.

The precision on the vertex position increases with the number of tracks employed in the fitting algorithm. Therefore, in low-multiplicity events, the fit also includes the nominal beam position as an additional constraint/contribution with an uncertainty corresponding to the transverse size of the luminous region [125]. Although high-multiplicity events have plenty of tracks available, the high pile-up rate requires a different approach. In order to reduce the contamination from collisions, only tracks coming from the same bunch crossings (identified thanks to the timing information from the TOF detectors) can contribute to the same vertex. To further suppress the contribution of outliers, the vertex fitting relies on a more robust technique based on Tukey bisquare weights [109].

The Fig. 3.15 shows the transverse resolution on the primary vertex position as a function of the particle multiplicity per unit pseudo-rapidity in pp at $\sqrt{s} = 7$ TeV. As mentioned above, the accuracy on the interaction point position sharply improves with the track multiplicity in the event, reaching ~ 50 μm for $\mathrm{d}N/\mathrm{d}\eta > 15$. With respect to the preliminary vertices found with the SPD tracklets, the final ones determined with global tracks are better by at least a factor of two. Note that both resolutions scale as the square root of the number of contributing tracks/tracklets [122].

[29] When two beams collide, it gives rise to one or multiple collisions. Their interaction point *a priori* lies anywhere within the region defined by the convolution of the particle distribution – in other words, the beam size – of the two incoming beams. Also called *interaction region*, its transverse size is given by $\sigma_D = \sigma^{\mathrm{beam}}/\sqrt{2}$, with σ^{beam} the bunch size spread. [107].

[30] The track weighting has the effect of suppressing the contribution of any remaining outliers.

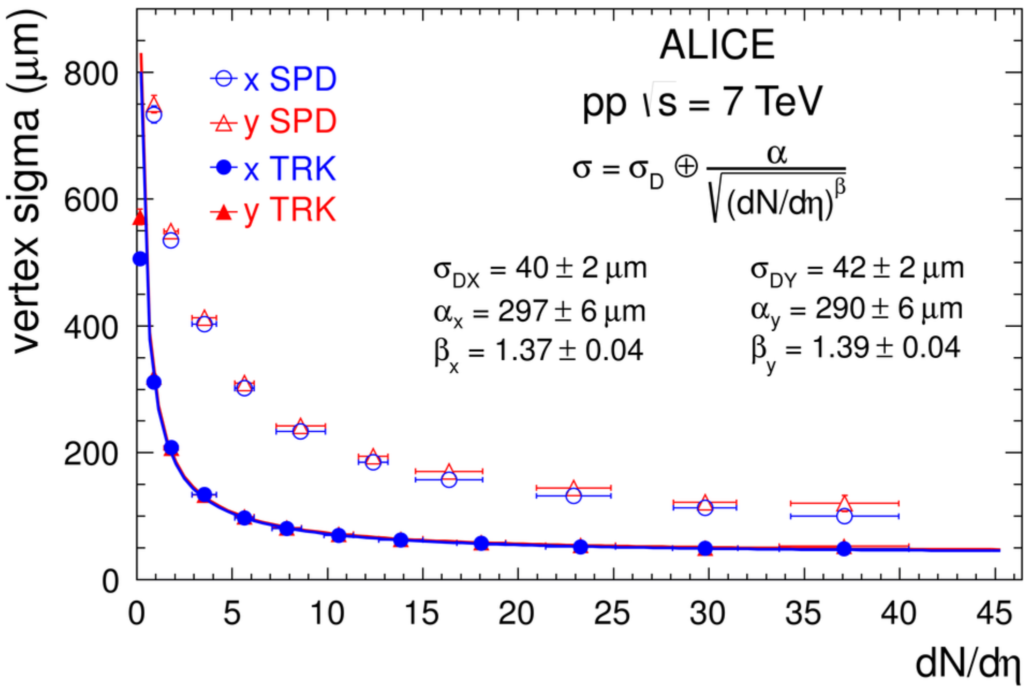

Fig. 3.15: Transverse width of the final vertex distribution, in solid markers, in pp collisions at $\sqrt{s} = 7$ TeV. Two contributions are separated: the transverse size of the nominal beam position $\sigma_{\rm D}$, and the transverse resolution on the vertex $\alpha/\sqrt{(\mathrm{d}N/\mathrm{d}\eta)^{\beta}}$. For comparison, the open markers show the same quantity determined making use of SPD tracklets. Figure taken from [109].

II-E The ALICE offline framework

II-E.i The computing model

Over the whole LHC Run-2, more than 160 PB of raw data have been collected by the ALICE experiment. Their treatment requires a robust framework, capable of processing them in a reliable and timely fashion.

To be processed, this volume of data requires an amount of computing resources that can not be concentrated in one place[31]. Instead, it is spread over different computing centres around the world. In particular, ALICE uses the Worlwide LHC Computing Grid (WLCG), a worldwide computer network infrastructure coordinated by the CERN and shared among all LHC experiments, that includes over 170 computing centres in 42 countries. The WLCG stands as the world's largest computing grid, that provides near real-time access to the LHC data regardless of their physical location [126].

The WLCG computing sites follows a hierarchical structure in layers or *Tiers* as shown in Fig. 3.16, that provides different levels of data storage and processing. The Tier-0 corresponds to the CERN Data Centre located in Geneva, that directly receives all the raw data from the LHC experiments, keeps one replica (on mag-

[31] There are various reasons. Although the funding agencies invest in the computing equipment of their scientific projects, they focus their investments in their own countries. Even if all computing resources could be put in one place – let us say, at CERN –, the manpower would be insufficient to ensure the upkeep of such a system.

netic tapes) and performs the first reconstruction pass. It also distributes the raw data and the reconstruction output to the thirteen Tier-1 computer centres around the world via high-speed connections between 10 and 100 GB/s. They share the same roles with CERN, namely safe-keeping the data, finishing their reconstruction and distributing them to the next layer. The Tier-2 regroups about 160 sites, corresponding typically to universities and scientific institutes, that store the data produced by the closest Tier-1 site. Beyond their mass-storage capabilities, they are used to run the physics analysis tasks, produce Monte Carlo simulations, and reprocess the data. A copy of the simulated data is stored in the Tier-1 centres.

Each site relies on four components: networking, hardware, middleware and physics analysis software. The networking – the backbone of any distributed computing infrastructure – allows to link together the hundreds of WLCG centres and exchange data with an excellent connectivity thanks to the CERN Internet Exchange Point, the high-bandwidth LHC optical-fibres and the Grid File Transfer Service. Each site can be seen as a computer farm that needs tending to; the hardware component refers to this aspect. It includes maintaining disk and tape servers, providing tools to access the data whatever the storage medium — via the **C**ERN **A**dvanced **STOR**age system (CASTOR) or CERN EOS — as well as upgrading regularly the necessary software to operate the Grid system — from the operating system to the physics analysis software libraries. The middleware corresponds to

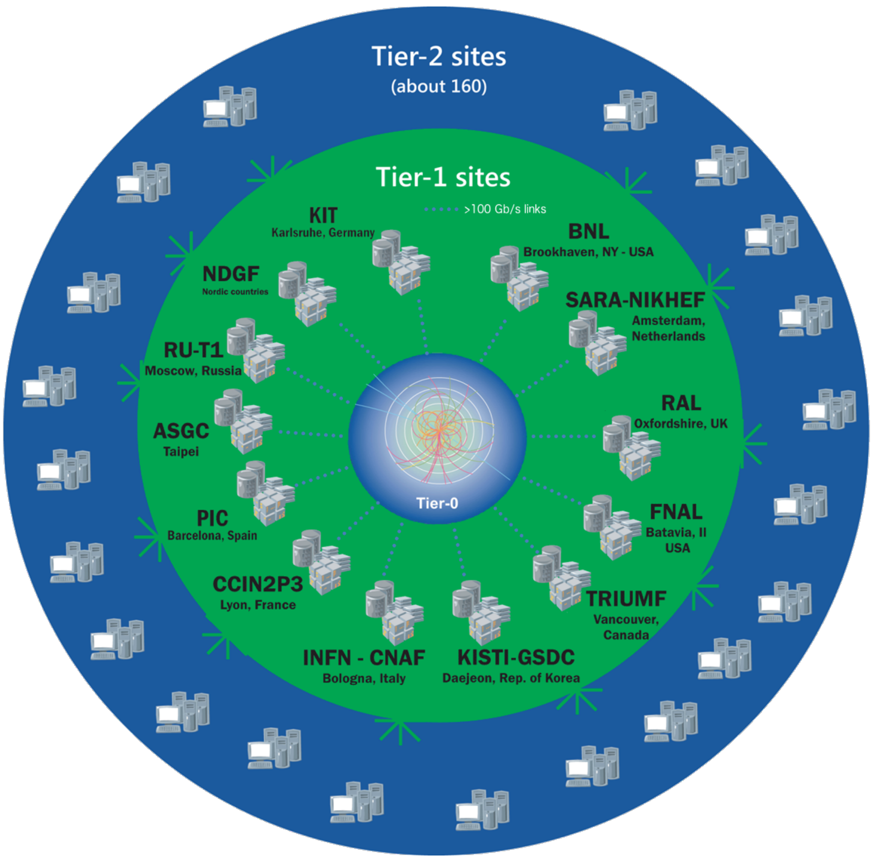

Fig. 3.16: The three Tiers of the Worlwide LHC Computing Grid as of 2023, with the list of the thirteen Tier-1 computing centres, with their geographic location. Figure taken from [126].

the software architecture that comes between the operating systems and the physics analysis software; it provides numerous services (interfacing, workload management, monitoring, job submission and execution, etc) in order to access at the titanic CPU power and storage ressources of the Grid. In ALICE, the AliEn system fills in this task. Last but not least, the physics analysis software provides the tools to analyse the data.

II-E.ii The analysis framework, AliRoot

As most of the current high-energy experiments – if not all –, the ALICE offline analysis framework is built upon ROOT, an high-performance object-oriented software developed by the CERN and implemented almost entirely in the C++ programming language. Created in 1994 by René Brun and Fons Rademakers, it provides the mathematical and statistical tools to manipulate large amounts of data and analyse them [127]. ROOT sets the foundations for the ALICE offline framework, that divides into two parts during the LHC Run-1 and Run-2:

AliRoot [128] contains the codes that are common to the whole collaboration. In particular, it includes:

- an interface for running Monte Carlo simulations (from the event generation to the detector response), event visualisation, etc,
- a description of the detector geometry as well as the material budget,
- the alignement and calibration of the detectors,
- the real and simulated data reconstruction,
- and the management of the data formats;

AliPhysics [129] regroups all the physics analysis tasks to process the collected and simulated events. Each PWG in Tab. 3.4 has a dedicated repository.

II-E.iii Data formats

Depending on the processing stage, the ALICE data come in three distinct formats with different levels of abstraction. At the output of the detectors (Sec. 3|II-B), they take the form of *Raw Data*, that regroups all the cluster informations recorded during a collision. They are collected by the DAQ system before being transmitted at a rate of 200 MB/s to the Tier-0 site for storage and distribution to Tier-1 data centres.

In parallel, the raw data undergo their first reconstruction pass at CERN. For pp collisions, it typically takes two minutes per event in pp collisions, mainly in input/output streaming. This first pass yields to an Event Summary Data (ESD) format, that contains most of the informations related to the reconstruction such as the reconstructed tracks with their associated hits. While a pp event from raw data occupies about 1 MB of disk space, it reduces to ~ 100 kB in ESD format.

At the analysis level, the ESD file presents the advantage of having the full knowledge of the tracking and event building, with the possibility of replaying some part of the reconstruction like the V0 and cascade vertexings (see next chapter, Chap. 4). However, they are still considered as too heavy and too expensive in terms of CPU time. For that reason, the first pass also produces a file in Analysis Object Data (AOD) format, a lighter version than the ESD counterpart, keeping only the relevant information to extract the physics content from the data. It covers 5 to 10 times less disk space than an ESD file, thereby reducing significatively the processing time by the analysis tasks.

Note that the first reconstruction pass only serves to calibrate the TPC, SDD, TOF, T0, luminous region and centrality. The second pass applies the derived calibration, and is then used to improve the calibrations and perform a first data quality assurance. These two reconstruction passes, using only a fraction of the data from each run, provides the input for a more complete and fine-tuned calibration, that is stored in the Offline Conditions DataBase[32] (OCDB) and is applied in the third pass. At each stage of the processing, a set of ESD and AOD files is produced.

II-E.iv Monte Carlo data

As mentionned in Sec. 3|II-E.ii, the AliRoot framework has the capability to run Monte Carlo (MC) simulations, that try to reproduce as accurately as possible the stochastic processes observed in the detector by sampling a given set of probability density distributions. Such a simulation consists in two consecutive steps.

It starts with the generation of the event, that simulates a collision as well as the associated physics processes ultimately leading to the creation of primary particles. This first step relies on different models called *event generators*, each having its own paradigm, its own production mechanisms, tuned to mimic the topology the collision (multiplicity, momentum distribution, etc). Among the most commonly used, there are Pythia [131] and Herwig [132] for pp collisions, Epos [133] for both pp and heavy-ion collisions, Hijing [134] exclusively for heavy-ion collisions.

After the generation of the event comes the propagation of the primary particles through the ALICE detector. This requires a modelisation of the apparatus in its entirety, from the various elements composing the sub-detectors to their geometric shape and their positioning. It also has to account for noisy or dead channels, detector defects, intensity of the magnetic field, etc. These informations available run by run on OCDB are used to *anchor* the simulation on the actual data taking conditions. The transport and interaction with the detector material typically rely on dedicated softwares, such as Geant3 [135], Geant4 [136] and Fluka [137].

Taking into account the detector response, the energy deposited by the passage of charged particles are converted into digits and then stored in raw data format. From this point, the reconstruction of the event can start. It follows the same procedure as the one applied for real data (Sec. 3|II-D), yielding to files in ESD and AOD formats.

In order to minimise the disk space usage and the computing time, only a

[32]In fact, OCDB stores the ideal geometry of the detector, the alignement objects (*i.e.* corrections on the ideal geometry derived using Millepede algorithm [130]) and the calibration parameters for each data taking period.

fraction of the total number of events in real data is simulated. The proportion of triggers remains unchanged between real and simulated data, though. For instance, if a run in its entirety has 10% of high-multiplicity events, its simulated twin will comprise the same fraction of such events.

The key point of MC data resides in the presence of the full information about the event. This is often referred as *MC truth*. Each element of the simulation is perfectly known: the number of generated particles, their type, charge, momenta, whether they are primary or secondary, where they deposit energy in the detector giving rise to hits – the so-called track references –, etc. This copious amount of additional informations opens the way towards specific kinds of investigations.

1 (+)

When designing a new experiment, it allows to anticipate the results and, if needed, to correct or optimise the current design. It gives also the opportunity to estimate the performances of a detector (typically, the efficiency) and to study its systematic features. Finally, the comparison between the measurements (real data) and the predictions from a given MC model (simulated data) helps to improve our understanding of the underlying physics.

It should be mentionned that there exists two classes of MC simulations in high-energy physics. Reproducing as accurately as possible a collision requires tuning the parameters of the simulation such that they correspond to the ones observed in real data, including the decay channels, the branching ratios, etc. This is the standard type of simulations, the *general-purpose* MC production. A limitation arises when dealing with rare signals: for them to be observed, an unrealistic amount of events would need to be generated.

Instead, one could resort to an *enriched* MC simulations, in which the abundancy of rare signals is increased. This can be achieved by artificially injecting the particles of interest in the simulation, according to a flat distribution in p_T or rapidity, etc. However, in this case, the production of such particles does not take account of the physics of the collision. Alternatively, the enrichment can also be accomplished by filtering out 3 the events that contain the particles of interest; that approach is the one followed by the enriched simulations in this thesis. A last option consists in embedding a pure sample of rare signals into a background event, coming from either a simulation or real data. This is particularly used in p-Pb or Pb-Pb simulations, where PYTHIA– a generator dedicated to pp collisions – produces an event with an enhanced abundancy in rare signals. However, the topology of the simulated event does not coincide with the one in p-Pb or Pb-Pb collisions. Therefore, the injected event is incorporated into a HIJING event, that plays the role of a background event[33].

2 (+) "enrichment" à la ALICE

3 "... the generated events that contain ... of interest and only for those peculiar events perform the transport stage of the simulation"

[33]Note that the background event can *a priori* be re-used several times.

Chapter 4 | Identification of V0 particles and cascades

The Chap. 2 and 3 have set the scene, it is time for the main actors to come onto stage, that are the (multi-)strange baryons or more precisely, the *hyperons*. These consist of any baryon containing at least one strange quark, but no heavier quarks such as charm, bottom or top. By describing their identification and the physics interests surrounding their reconstruction, this short chapter lays the foundations for the analysis performed throughout this thesis.

The first section, Sec. 4|I, underlines the appealing features of strangeness and, particularly, (multi-)strange particles. The hyperons of interest in the present analyses are specified in the following section, Sec. 4|II, as well as the motivations for this choice. This part also presents the principles for multi-strange baryon identification via topological reconstruction. Finally, in connection with Chap. 3, this short chapter closes on what makes ALICE an unique experiment for studying strange hadrons.

I The appealing features of strangeness

I-A The strange quark with respect to the other flavours

Similarly as for the charm, bottom and top quarks, there is no strangeness among the valence quarks of the nucleons from the collision beams. These only consist in up and down quarks; other flavours can still be found inside the sea of quarks and gluons, but in a moderate amount with respect to those produced during a collision at the LHC energies. From this, there arises an interesting and straightforward aspect of strangeness: all the strange quarks observed in the final state hadrons must have been produced in the processes that have occured during the collision.

Another property regards the mass of the strange quark. One way of classifying quarks is based on whether they preserve (at least, approximatively) or break the chiral symmetry (Sec. 2|I-C.ii): the up and down quarks belongs to the first kind and makes part of the light flavour sector. Those breaking the chiral symmetry – the charm, bottom and top quarks – constitute the heavy flavour sector. For comparison, the bare mass of the up quark sits at $2.16^{+0.49}_{-0.26}$ MeV/c^2, the down quark at $4.67^{+0.48}_{-0.17}$ MeV/c^2. In contrast, the one of the charm, bottom and top quarks lie around 1.27 ± 0.02 GeV/c^2, $4.18^{+0.03}_{-0.02}$ GeV/c^2 and 172.69 ± 0.30 GeV/c^2 respectively [42]. From this perspective, the strange quark with its bare mass of $93.4^{+8.6}_{-3.4}$ MeV holds an unique position: its lightweight makes it relatively inexpensive (in terms of energy) to produce; being still much heavier than the up and down quarks (by one order of magnitude), this also qualifies it as non-ordinary matter. Thus viewed as both light and heavy, the strange quark gives access to an abundant source of non-ordinary matter.

I-B The specificity of strange hadrons

Most of strange hadrons decays into charged particles in their dominant channel. In addition, they also have a relatively long lifetime, allowing them to fly over several centimeters before the decay. From these two elements stem the distinctive decay topology of strange particles known as V0 or cascade (Sec. 4|II-A), that can be used in their reconstruction by associating the different daughter tracks to reform the decay vertex (topological reconstruction, detailed later in Sec. 4|II-B) [138]. This characteristic turns to be particularly interesting as the latter provides a robust identification of strange hadrons over a wide momentum range, from low to high p_{T}.

Consequently, this offers the possibility for a continuous study of strange hadrons over different production regimes, involving soft, intermediary and hard processes such as multi-parton interactions, quark coalescence and jet fragmentation respectively. For that reason, strange particles represents prime choice probes to investigate and thus improve our understanding on the evolution of the hadronisation mechanisms[1] with momentum.

II The multi-strange baryon identification

Among all the strange hadrons, this work focuses on the strangest baryons, containing two or three strange quarks, the so-called multi-strange baryons. Excluding the associated resonances, this leaves five particles: three containing two strange quarks – the $\Xi^0(uss)$, Ξ^- (dss) and $\overline{\Xi}^+$ $(\bar{d}\bar{s}\bar{s})$ –, and two triple-strange hadrons namely the Ω^- (sss) and $\overline{\Omega}^+$ $(\bar{s}\bar{s}\bar{s})$.

[1] To be exact, it is not the hadronisation mechanisms that evolves with the transverse momentum but rather their relative weight. For instance, soft processes dominates at low p_{T}, and hard ones at high p_{T}. However, *a priori*, there are also soft processes at high momentum – conversely hard processes at low momentum –, although they represent only a small fraction.

Particle	Strangeness	Mass (MeV/c^2)	Lifetime (cm)	Decay channel	B.R.
Λ $[uds]$	+1	1115.683	7.89	p $[uud]$ $\pi^-[\bar{u}d]$	63.9 %
$\overline{\Lambda}$ $[\bar{u}\bar{d}\bar{s}]$	−1	1115.683	7.89	$\bar{\text{p}}$ $[\bar{u}\bar{u}\bar{d}]$ $\pi^+[u\bar{d}]$	63.9 %
$\Xi^0[uss]$	+2	1314.86	8.71	Λ $[uds]$ $\pi^0[u\bar{u}]$	99.6 %
Ξ^- $[dss]$	+2	1321.71	4.91	Λ $[uds]$ $\pi^-[\bar{u}d]$	99.9 %
$\overline{\Xi}^+$ $[\bar{d}\bar{s}\bar{s}]$	−2	1321.71	4.91	$\overline{\Lambda}$ $[\bar{u}\bar{d}\bar{s}]$ $\pi^+[u\bar{d}]$	99.9 %
Ω^- $[sss]$	+3	1672.45	2.461	Λ $[uds]$ K$^-$ $[\bar{d}s]$	67.8 %
$\overline{\Omega}^+$ $[\bar{s}\bar{s}\bar{s}]$	−3	1672.45	2.461	$\overline{\Lambda}$ $[\bar{u}\bar{d}\bar{s}]$ K$^+$ $[u\bar{s}]$	67.8 %

Table 4.1: Main characteristics of the Λ and the charged multi-strange baryons: quark content, strangeness, tabulated mass and lifetime ($c.\tau$), dominant decay channel with the associated branching ratio (B.R.) [42].

The Tab. 4.1 shows some characteristics of these five baryons, including their dominant decay channel, as well as the mono-strange baryon Λ since it appears in all decay channels. Unlike the Ξ^0, the four charged multi-strange baryons share a common feature and a particularly appealing one: in their dominant decay channel, they follow a cascade decay topology as detailed in the next section, Sec. 4|II-A. For that reason, the present work concentrates on the study of charged multi-strange baryons.

From now on, the following notation will be used. The $\overset{(-)}{\Xi}{}^{\pm}$ (or $\overset{(-)}{\Omega}{}^{\pm}$) refers to Ξ^- or $\overline{\Xi}^+$ (or Ω^- or $\overline{\Omega}^+$). Conversely, Ξ (or Ω) means Ξ^- and $\overline{\Xi}^+$ (or Ω^- and $\overline{\Omega}^+$). The same goes for other particles. Moreover, unless indicated otherwise, the term multi-strange baryon now designates only the Ξ^-, $\overline{\Xi}^+$, Ω^- or $\overline{\Omega}^+$.

II-A The V0 and cascade decays

The Fig. 4.1 depicts the full cascade decay chain of Ξ and Ω. After flying over a few centimeters, the multi-strange baryon decays weakly into a charged pion (or kaon for the Ω) and a Λ. The latter being electrically neutral, only the charged meson deposits energy in the different sensitive layers and thus can be detected at this stage; the meson plays the role of a *bachelor* particle.

The two decay products continue to travel through the detector, until the baryon daughter decays[2] at 63.9% via weak interaction into two oppositely charged particles: a proton and a pion. Depending on their electric charge, one is called the *positive* particle and the other the *negative* particle. This decay topology is known as V0[3]. Furthermore, the term "cascade" refers to the two-steps decay process un-

[2]The bachelor daughter being either a $\pi^{\pm}$or K$^{\pm}$, in most cases it does not decay in the detector due to their long lifetime ($c.\tau_{\pi}$ = 7.8045 m and $c.\tau_{\text{K}}$ = 3.711 m). For those that actually decays in the detector, they are characterised by *kink* topology due to their decay into a charged particle and a neutral particle.

[3]The term "V0" comes from the V-shape decay topology formed by the two oppositely charged

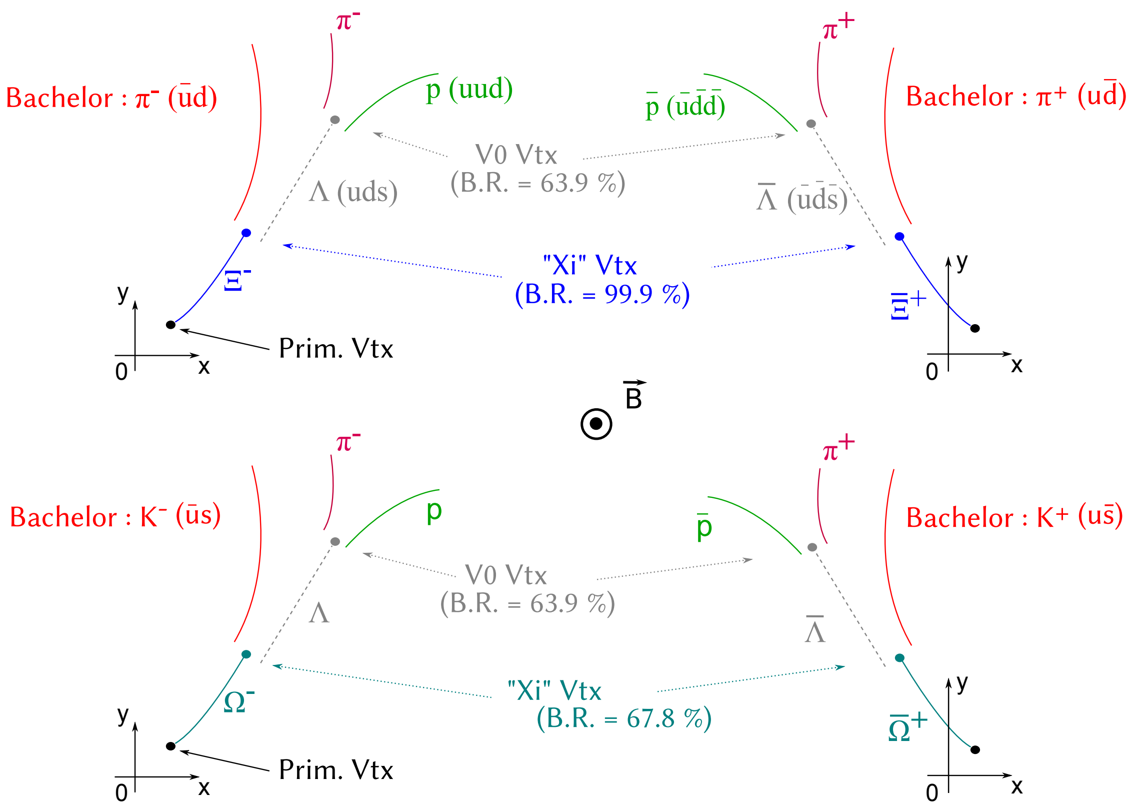

Fig. 4.1: Depiction of the full cascade decay chain of the Ξ^- (top left), $\overline{\Xi}^+$ (top right), Ω^- (bottom left) and $\overline{\Omega}^+$ (bottom right). Figure taken from [139].

dergone by the multi-strange baryons. Hence, in the following, the usage of the term *cascade* may be used to mention either the Ξ or Ω, and similarly the term *V0* for the Λ.

Note that the four cascades on Fig. 4.1 differ only in the nature of the particles involved. On one hand, from the left to right side, the particles are swapped to anti-particles. On the other hand, the larger strangeness content of the Ω imposes the presence of a bachelor particle containing a strange quark (kaon) while, in the Ξ case, it consists in an light unflavoured meson (pion).

It should also be mentioned that although the $\overset{(-)}{\Xi}{}^{\pm}$ decays into this channel quasi-systematically (99.9%), this is only the case for 67.8% of the $\overset{(-)}{\Omega}{}^{\pm}$.

The Fig. 4.2 shows the cascade decay of a Ξ^- within the ALICE detector. To make it more apparent, the surrounding tracks have been removed in the bottom left part. The $\overset{(-)}{\Xi}{}^{\pm}$ or $\overset{(-)}{\Omega}{}^{\pm}$ being electrically charged, they may loose energy in the detectors and can *a priori* be detected as any other charged particle. Although they can fly over relatively long distance compared to the vast majority of unstable particles, their $c.\tau$ remain too short to *systematically* reach the innermost detectors at about 3.9 cm and 7.6 cm (to be compared to $c.\tau_{\Xi}$ = 4.91 cm and $c.\tau_{\Omega}$ = 2.461 cm)[4]. Moreover, the Λ is a neutral particle, hence it can not deposit energy in the

decay daughters.

[4]Note that the detection and tracking of these two multi-strange baryons become possible with the upgraded version of the ITS in the LHC Run-3; the innermost silicon pixel detectors being positioned at a radius of 2.2 cm and 3.9 cm in the LHC, the Ξ and Ω have significantly more

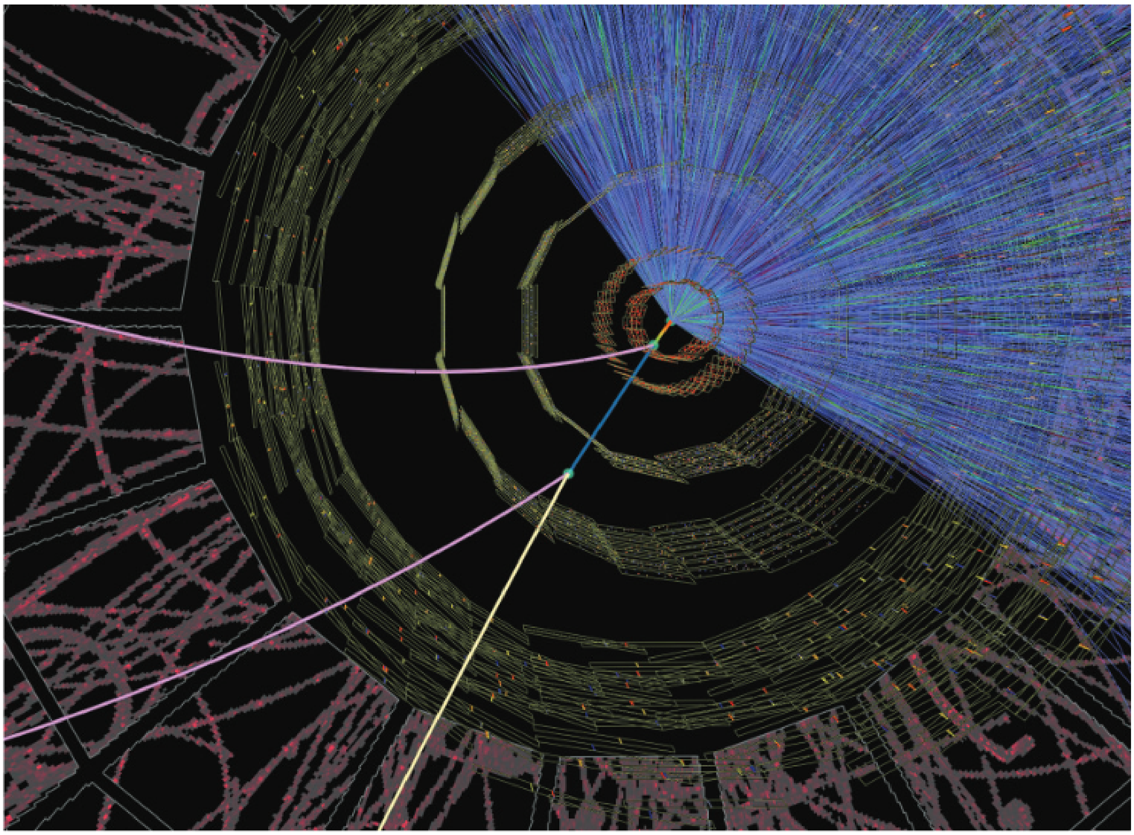

Fig. 4.2: Event display of a simulated Pb-Pb collision in the ALICE detector, with a close up on the ITS. The top part illustrates the typical density of tracks in such environment. The bottom part highlights the cascade decay of a Ξ^-. Figure taken from [108].

sensitive layers. In summary, only the bachelor, the positive and negative particles can be detected[5]. Therefore, it follows that the V0 and cascade have to be identified indirectly via their decay topology.

The top right part of Fig. 4.2 puts into perspective the difficulty of the reconstructing such a cascade topology. While the bottom part of the figure shows clearly the Ξ^- decay chain, it actually is immersed in a dense environment. In order to identify the multi-strange baryons in the event, the strategy followed in the present work consists in using topological reconstruction.

II-B The principles of the topological reconstruction

The cascade reconstruction is achieved by combining three tracks in the event. The association of two tracks allows to build a Λ (or $\overline{\Lambda}$) candidate, that may in turn be associated to another track (the bachelor) to form a cascade candidate. In a pp collision, the charged particle density[6] can vary from a few particles up to fifty, and more than a thousands in the most central heavy-ion collisions. The

chances to leave hits in this detection layers, and therefore to be detected [140].

[5]Due to their long lifetime, the detection of the $\pi^{\pm}$, $K^{\pm}$, p and $\overline{p}$ relies on the reconstruction and identification of their associated tracks in the ITS and TPC.

[6]per unit of pseudo-rapidity

mere association of three tracks leads inexorably to the formation of erroneous candidates, thus constituting a source of *combinatorial* background. In order to suppress the latter, geometric selections – aimed at singling out the candidates spatially compatible with the expected decay topology – are introduced; this is the general principle behind topological reconstruction.

II-B.i Formation of the V0 candidates

The reconstruction starts with the formation a V0 candidate. The first step consists in identifying *secondary* tracks, that do not originate from the interaction point. They are tagged as such, if the distance of closest approach (DCA) between the considered track and the primary vertex exceeds a critical value[7] (Fig. 4.3, V0.a).

The second step aims at forming pairs of secondary tracks of opposite charge – characterised by different curvatures –; by imposing that the DCA between the two tracks is small, only the pairs originating potentially from the same decay point are retained. The secondary vertex is then positioned on the segment defined by the previous DCA, weighted by the quality of the tracks (Fig. 4.3, V0.b).

The two daughter tracks are then propagated from their initial position (the point of closest approach to the primary vertex, Sec. 3|II-D.ii) to the secondary decay point[8]. This allows to calculate all the kinematic quantities of the V0, among which its momentum; the latter being equal to the momentum sum of the positive and negative particles at the secondary vertex, due to momentum conservation.

II-B.ii The reconstruction of cascade candidates

From the sample of V0 candidates (Sec. 4|II-B.i), only those compatible with a $\overset{(-)}{\Xi}{}^{\pm}$ or $\overset{(-)}{\Omega}{}^{\pm}$ decay are considered. In other words, the reconstruction of a cascade candidate must necessarily go through a secondary V0 that corresponds to either a Λ or $\overline{\Lambda}$.

Primary and secondary V0s are separated resorting to the pointing direction in the lab frame, given by the momentum at the decay vertex. This direction coincides with the straight-line trajectory of the candidate[9] and allows to estimate its DCA to the interaction point (Fig. 4.3, V0.c). The latter being close to zero for primary V0s, a lower cut on this variable enables their rejection to retain only those tagged as secondary.

The identification of the V0 goes through the calculation of the invariant mass under the Λ or $\overline{\Lambda}$ hypothesis. This boils down to making an assumption on the mass of each decay daughter. In the case of a Λ, the positive track corresponds to

[7]While one expects for a primary track to have a DCA to the primary vertex equal (or close) to zero, this is the opposite for a secondary track: since it does not originate from the collision point, its DCA to the interaction vertex must necessarily be different from zero.

[8]Most importantly, here the propagation is performed without taking the energy losses into account. This point will be addressed in Chap. 5

[9]If the candidate corresponds to an actual Λ or $\overline{\Lambda}$ (electrically neutral), its trajectory, not being curved under the influence of the magnetic field, must necessarily follow a straight line.

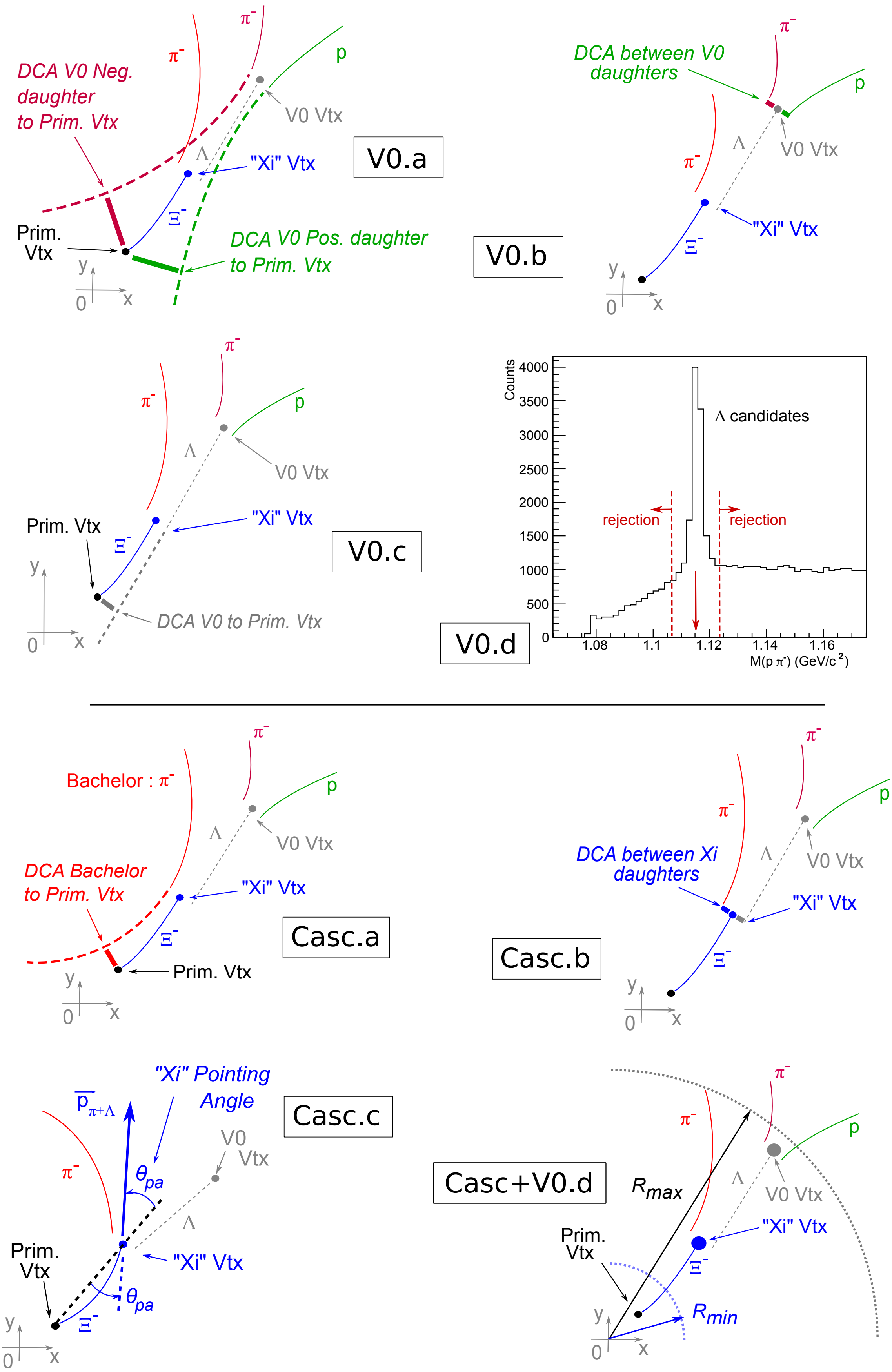

Fig. 4.3: Schematic representation of the different topological selections applied in order to first reconstruct V0s (top part), and then cascades (bottom part). Figure taken from [141].

a proton, the negative to a π^-(Eq. 4.3); conversely, for a $\overline{\Lambda}$, they are considered as a $\pi^+$and an anti-proton respectively. If it turns out that the candidate is, in fact, a true Λ or $\overline{\Lambda}$, the reconstructed mass should lie within a window of typically a few MeV/c^2[10] (Fig. 4.3, V0.d), centred around the nominal mass of the Λ ($m_\Lambda = 1.115683$ GeV/c^2). In most cases, the misidentification of the daughter particles results in a quite different invariant mass. Therefore, only one of the two mass hypothesis passes the cut, making it possible to differentiate between a Λ and a $\overline{\Lambda}$.

$$M^2_{\text{candidate}}(\Lambda) = (E_{\text{pos.}} + E_{\text{neg.}})^2 - (\mathrm{p}_{\text{pos.}} + \mathrm{p}_{\text{neg.}})^2 \tag{4.1}$$

$$= \left(\sqrt{\mathrm{p}^2_{\text{pos.}} + m^2_{\text{pos.}}} + \sqrt{\mathrm{p}^2_{\text{neg.}} + m^2_{\text{neg.}}}\right)^2 - (\mathrm{p}_{\text{pos.}} + \mathrm{p}_{\text{neg.}})^2 \tag{4.2}$$

$$= \left(\sqrt{\mathrm{p}^2_{\text{pos.}} + m^2_{p^+}} + \sqrt{\mathrm{p}^2_{\text{neg.}} + m^2_{\pi^-}}\right)^2 - (\mathrm{p}_{\text{pos.}} + \mathrm{p}_{\text{neg.}})^2 \tag{4.3}$$

A last step consists in forming a cascade candidate via the association of a candidate Λ (or $\overline{\Lambda}$) with any track labelled as secondary[11] (Fig. 4.3, Casc.a), playing the role of the bachelor particle. The procedure is analogous to what was done to build a V0 candidate: only pairs with a sufficiently small DCA between the reconstructed Λ (or $\overline{\Lambda}$) and the bachelor are considered (Fig. 4.3, Casc.b); primary cascades are set apart from secondary ones by introducing the *pointing angle*. The latter corresponds to the angle defined by the direction of propagation (or pointing direction) of the candidate, and the line joining the primary and secondary vertices. This angle should be small for a primary candidate and, even though the magnetic field is bending their trajectory, the change in direction remains moderate. This selection usually goes through the cosine of the pointing angle, that is constrained to be close to unity in order to validate the cascade as primary (Fig. 4.3, Casc.c).

The V0 candidate is subject to the same cut. Due to its large mass compared to the one of the bachelor, the reconstructed Λ (or $\overline{\Lambda}$) takes up most of the cascade momentum, and so most of the pointing direction. As a consequence, in order to ensure that the V0 actually originates from a $\overset{\scriptscriptstyle(-)}{\Xi}{}^{\pm}$ or $\overset{\scriptscriptstyle(-)}{\Omega}{}^{\pm}$ decay, the cosine of its pointing angle has to be close to unity.

As a final topological selection, the cascade and V0 decay vertices must lie within a certain confidence area, in the transverse plane (Fig. 4.3, Casc.d). Close to the interaction point, at small radii, the combinatorial background is overwhelming due to the high density of tracks. Conversely, at large distance, the probability of finding a $\overset{\scriptscriptstyle(-)}{\Xi}{}^{\pm}$ or $\overset{\scriptscriptstyle(-)}{\Omega}{}^{\pm}$ becomes extremely low. For comparison, the inner wall of the TPC (~ 85 cm) lie at ~ 18 $c.\tau_\Xi$ and ~ 35 $c.\tau_\Omega$. At such distance, the $\overset{\scriptscriptstyle(-)}{\Xi}{}^{\pm}$ and $\overset{\scriptscriptstyle(-)}{\Omega}{}^{\pm}$ survival probabilities are about 2% and 0.001%[12] respectively. Therefore, the decay vertices of both cascade and V0 must be located beyond a radius deemed critical; those decaying too far away with respect to their lifetime are rejected[13].

[10] The width of the mass window depends directly on the ALICE performances in terms of transverse momentum resolution, which sits around a few MeV/c for low- and intermediate-p_{T} tracks.

[11] With the exception of the V0 daughters tracks.

[12] Considering a high-momentum cascade of 5 GeV/c.

[13] Notice that one consists in a selection on the radial position of the decay vertices, the other a cut on their 3D location.

II-B.iii Invariant mass of the cascade candidates

At this stage, the topological reconstruction is over; each triplet of tracks forms a cascade candidate, that can correspond to a $\overset{(-)}{\Xi}{}^{\pm}$, a $\overset{(-)}{\Omega}{}^{\pm}$ or some residual background. The distinction is made based on the invariant mass of each candidate (Eq. 4.5).

$$M^2_{\text{candidate}}(\text{casc.}) = (E_{\text{V0}} + E_{\text{bach.}})^2 - (\mathbf{p}_{\text{V0}} + \mathbf{p}_{\text{bach.}})^2 \tag{4.4}$$

$$= \left(\sqrt{\mathbf{p}^2_{\text{V0}} + m^2_{\Lambda}} + \sqrt{\mathbf{p}^2_{\text{bach.}} + m^2_{\text{bach.}}}\right)^2 - (\mathbf{p}_{\text{V0}} + \mathbf{p}_{\text{bach.}})^2 \tag{4.5}$$

$$M^2_{\text{candidate}}(\overset{(-)}{\Xi}{}^{\pm}) = \left(\sqrt{\mathbf{p}^2_{\text{V0}} + m^2_{\overset{(-)}{\Lambda}}} + \sqrt{\mathbf{p}^2_{\text{bach.}} + m^2_{\pi^{\pm}}}\right)^2 - (\mathbf{p}_{\text{V0}} + \mathbf{p}_{\text{bach.}})^2 \tag{4.6}$$

$$M^2_{\text{candidate}}(\overset{(-)}{\Omega}{}^{\pm}) = \left(\sqrt{\mathbf{p}^2_{\text{V0}} + m^2_{\overset{(-)}{\Lambda}}} + \sqrt{\mathbf{p}^2_{\text{bach.}} + m^2_{\text{K}^{\pm}}}\right)^2 - (\mathbf{p}_{\text{V0}} + \mathbf{p}_{\text{bach.}})^2 \tag{4.7}$$

For each association of three particles, two invariant masses are calculated: one under the hypothesis of a $\overset{(-)}{\Xi}{}^{\pm}$ candidate (Eq. 4.6), the other for a $\overset{(-)}{\Omega}{}^{\pm}$ candidate (Eq. 4.7). Notice that, contrarily to the Λ and $\overline{\Lambda}$ cases, the invariant mass is the same for the particle (Ξ^-, Ω^-) and the anti-particle ($\overline{\Xi}^+$, $\overline{\Omega}^+$). In addition, the masses of the daughter particles involved in Eq. 4.6 and 4.7 correspond, in fact, to the nominal values from the PDG [42]; most importantly, the reconstructed mass of the V0 is not being used here. As long as the latter has been identified as a $\overset{(-)}{\Lambda}$ (*i.e.* its mass fits into a certain tolerance window, Sec. 4|II-B.ii), this choice has the advantage of limiting the deterioration on the cascade invariant mass resolution.

Although the invariant mass allows to distinguish a $\overset{(-)}{\Xi}{}^{\pm}$ from a $\overset{(-)}{\Omega}{}^{\pm}$, there exists a region where this is not possible anymore. The Fig. 4.4 shows the invariant mass distribution of cascade candidates assuming a Ω^- as a function of the same candidate under the hypothesis of a Ξ^-. There are two discernible and perpendicular mass bands, each one corresponding to true population of one of two considered species. At their intersection, the two species become indistinguishables – they compete in some sense –, which results in an increased background in this region: a candidate identified as Ξ^- may, in fact, reveal to be a Ω^- , and vice-versa.

This additional background impacts each kind of cascade in different proportions, though. Since the population of true Ξ^- is much larger than the one of Ω^- [14], the latter constitutes a marginal source of background with respect to the Ξ^-. Conversely, the true Ξ^-– particularly in the low mass region – represent a considerable source of background for the Ω^- . As a consequence, in the context of the reconstruction of $\overset{(-)}{\Omega}{}^{\pm}$ baryons, any candidates also identified as a $\overset{(-)}{\Xi}{}^{\pm}$— that is, with an invariant mass under the assumption of a $\overset{(-)}{\Xi}{}^{\pm}$ within a window of few MeV/c^2 around $m_{\text{PDG}}\Xi$— are rejected.

[14] That is because the Ξ are typically ten times more produced than the Ω [142].

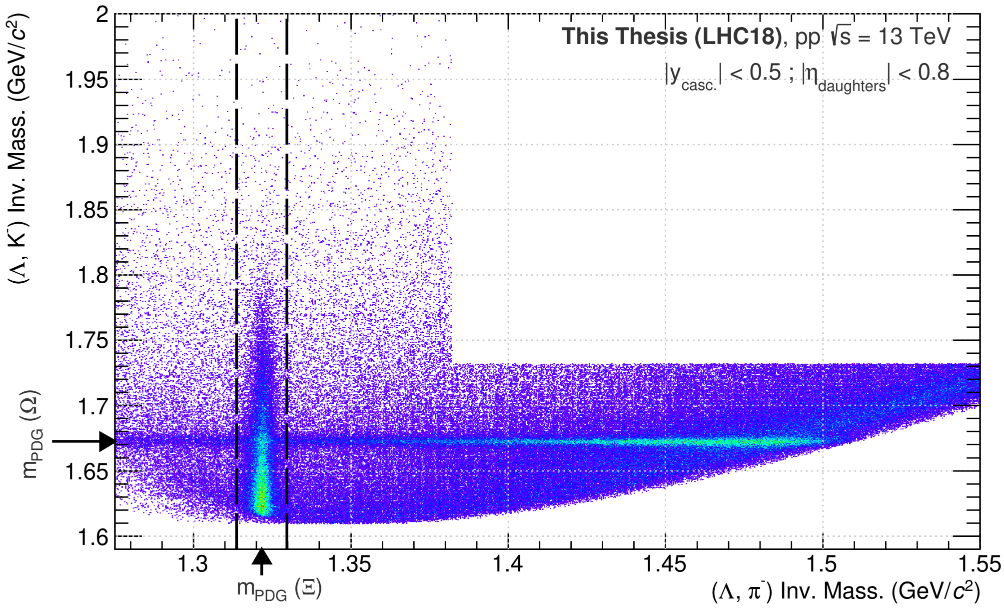

Fig. 4.4: Invariant mass distribution under the Ω^- and Ξ^- mass hypotheses, each cascade candidate can be seen under one hypothesis or the other (Eq. 4.6 and 4.7). The dashed lines show the mass rejection $m_{\rm PDG}\Xi \pm 0.008\text{GeV}/c^2$, applied in the reconstruction of a $\overset{(-)}{\Omega}{}^{\pm}$ candidate.

II-c The context of hyperon reconstruction in ALICE

In view of the characteristics of multi-strange baryons, it appears plainly that their reconstruction require excellent detection capabilities. In that regard, few experiments can compete with the performances of the ALICE detector at mid-rapidity.

As already outlined in Sec. 3|II-B, the high granularity of its inner tracker allows to reconstruct the primary vertex, as well as the secondary vertices from V0 and cascade decays, with a precision better than 100 μm[15]. Thanks to its large lever arm and almost continuous sampling of the particle trajectory, the TPC provides an excellent momentum measurement with a resolution of 0.7%[16] [108], as well as a robust particle identification. Hence, the TPC ensures an efficient reconstruction and identification of the hyperon's decay daughters, and thus of the hyperon itself. Coupled with its extremely low material budget (13% X_0) and moderate magnetic field of 0.5 T, the strange hadron reconstruction can be performed over a wide momentum range and particularly, at low $p_{\rm T}$, where the most important part of the production is.

Furthermore, the experiment benefits from the high-energy collisions delivered by the LHC. At such energies, matter and anti-matter are produced in almost equal proportions, offering the opportunity to study simultaneously hyperons and anti-hyperons. For all these reasons, ALICE stands as a perfectly suited experiment to analyse multi-strange baryons.

[15] Not to mention the resolution on the DCA of the daughter tracks to the primary vertex of about 30 μm [109].

[16] This obviously depends on the track momentum; here this is for $p_{\rm T} = 1$ GeV/c.

It should be emphasised that the cascade reconstruction varies with the track density, that goes from a few charged particles in pp collisions up to 2000 in the most central Pb-Pb collisions at $\sqrt{s_{\mathrm{NN}}}$= 5.02 TeV [105]. In heavy-ion collisions, the enormous amount of tracks means a larger background, but also a larger number of contributor for the primary vertex determination and hence a better resolution on its position. This is in contrast with the pp environment, where the events are less dense but with a poorer quality on the interaction point location. Therefore, the topological selections shall be adapted for each environment, as these differences may lead to various biases on the DCA to the primary vertex, pointing angles, etc.

Also, a compromise has to be made between purity and reconstruction efficiency. In both cases, the key point revolves around the treatement of the background, which depends on the physics analysis. For example, if the background – or more precisely, its shape – is known in advance, the latter becomes tolerable as it can be subtracted later; thus, one may favour a high efficiency (*i.e.* relatively loose selections). In the reverse situation where the background is unknown, it seems preferable to apply tighter cuts in order to keep a signal with a low level of contamination, thus ensuring a high signal purity.

2

Chapter 5 | Mass measurements of multi-strange baryons in pp collisions at $\sqrt{s} = 13$ TeV

1 sur une ligne

The first analysis conducted in this thesis aims at measuring the Ξ^-, $\overline{\Xi}^+$, Ω^- , $\overline{\Omega}^+$ masses and mass differences between particle and anti-particle. This chapter provides a description of the different elements needed for its achievement.

I Introduction

As discussed in Sec. 2|I-A, the Standard Model is built upon a set of symmetries, each being either discrete – such as the combination of the charge conjugation (C), parity (P) and time reversal (T), known as the CPT transformation – or continuous – for example, the Lorentz transformations that includes rotations and boosts. In particular, the Lorentz and CPT symmetries are connected by the so-called CPT theorem which establishes that any unitary, local Lorentz-invariant quantum field theory must be CPT invariant [143]. Consequently, the CPT violation implies the breaking of the Lorentz symmetry, and vice versa[1] [30]. Another implication involves the relation between the properties of matter and antimatter: due to the charge conjugation linking particles to antiparticles, the CPT symmetry imposes that they share the same invariant mass, energy spectra, lifetime, coupling constants, etc [?] 2. Most of the experimental checks of CPT invariance stem from this

[1] In fact, another option exists; to allow for the CPT violation, either the Lorentz symmetry must be broken – as in the case of string theory [144] or the Standard-Model Extension [145] – or some of the other additionnal assumptions of the CPT theorem must be dropped, namely the energy positivity [146], local interactions [147], finite spin [148], etc [149][31].

7

Particle	Quark content	Mass (MeV/c^2)	Relative mass difference	Dominant decay channel	B.R.
$\mathrm{K^0_S}$ ($\overline{\mathrm{K^0_S}}$)	1 $d\bar{s}$ ($\bar{d}s$)	497.611 ± 0.013	$< 6 \times 10^{-19}$	$\pi^+\pi^-$	69.20%
Λ ($\overline{\Lambda}$)	uds ($\bar{u}\bar{d}\bar{s}$)	1115.683 ± 0.006	$(-0.1 \pm 1.1) \times 10^{-5}$	p π^-($\overline{\mathrm{p}}$ π^+)	63.9%
Ξ^- ($\overline{\Xi}^+$)	dss ($\bar{d}\bar{s}\bar{s}$)	1321.71 ± 0.07	$(-2.5 \pm 8.7) \times 10^{-5}$	Λ π^-($\overline{\Lambda}$ π^+)	99.9%
Ω^- ($\overline{\Omega}^+$)	sss ($\bar{s}\bar{s}\bar{s}$)	1672.45 ± 0.23	$(-1.44 \pm 7.98) \times 10^{-5}$	Λ K$^-$ ($\overline{\Lambda}$ K$^+$)	67.8%

Table 5.1: A few characteristics, as of 2023, of the Λ, Ξ, Ω hyperons and the $\mathrm{K^0_S}$ meson: quark content, mass, relative mass difference values with their associated uncertainties and their dominant decay channel as well as the corresponding branching ratio [42].

last point, which imposes several constraints on the anti-particle properties.

The Particle Data Group (PDG) [42] compiles a large variety of CPT tests from many experiments and with different degrees of precision; so far, no CPT violation have been observed. The most stringent test involves the $\mathrm{K^0}$-$\overline{\mathrm{K^0}}$ mixing process, which depends on the mass and lifetime differences of these two states. In this way, assuming no other source of CPT violation in the decay of neutral kaons, these two quantities have been bounded [42][150] to

3 has

2 \rmKzero\ pr ne pas manger l'espace

$$2\frac{|m_{\mathrm{K^0}} - m_{\overline{\mathrm{K^0}}}|}{m_{\mathrm{K^0}} + m_{\overline{\mathrm{K^0}}}} < 6 \times 10^{-19} \quad , \quad 2\frac{|\Gamma_{\mathrm{K^0}} - \Gamma_{\overline{\mathrm{K^0}}}|}{\Gamma_{\mathrm{K^0}} + \Gamma_{\overline{\mathrm{K^0}}}} = (8 \pm 8) \times 10^{-18}. \tag{5.1}$$

These indirect limits are much stronger than the ones extracted from direct tests. For example, in the hyperon sector, the precision on relative mass difference is typically of a few 10^{-5}. In the latter case, it should be mentioned that there is still some room for improvements, and most particularly concerning the mass difference measurements between particle and anti-particle in the multi-strange baryon sector. The only test of this nature dates back to 2006 [151] for the Ξ^- and $\overline{\Xi}^+$, and from 1998 [152] for the Ω^- and $\overline{\Omega}^+$. The former was achieved by exploiting 3.25 million hadronic decays of the $\mathrm{Z^0}$ recorded by the DELPHI detector at LEP-1; the latter was obtained on the E756 spectrometer at Fermilab, using an 800-GeV/c proton beam on a beryllium target. However, both studies suffer from low statistics: approximately 2500(2300) reconstructed Ξ^- ($\overline{\Xi}^+$) and about 6323(2607) reconstructed Ω^- ($\overline{\Omega}^+$) were used.

4 \inel

In comparison, all the pp collisions at a centre-of-mass energy of 13 TeV collected by ALICE throughout the LHC Run-2 contains about 2 500 000 Ξ and 133 000 Ω, with little background. Therefore, in this thesis, the measurement of the mass difference of Ξ^- and $\overline{\Xi}^+$, and Ω^- and $\overline{\Omega}^+$ hyperons is performed. It relies on data samples much larger than those exploited previously. These direct measurements of the mass difference offer a test of the CPT invariance to an unprecedented level of precision in the multi-strange baryon sector. The absolute masses are updated as well, with a precision substantially better than the current values listed in the PDG and presented in the Tab. 4.1.

5 (+)

6 "should offer"

7 "Tab. 5.1" (attention ss dte m̃ label ds les 2 cas Tab. 4.1 Tab 5.1 ici → à changer)

10

(1) (+)

Furthermore, concerning the Λ hyperon and K^0_S meson, the PDG quotes a precision of a few keV/c^2 on the mass value, and about 1×10^{-5} on the relative mass difference value[2]. Abundantly produced, these two hadrons also exhibit an irresistible feature in the context of this thesis: both decay into a V0 in their dominant decay channel, and so can be identified in a similar manner as cascades using topological reconstruction. For those two reasons – high precision on the PDG mass values, and similar decay topology as cascade –, the analysis is reproduced on Λ and K^0_S, both being used as a benchmark for the measurement.

(2) \emph{} (3) expliciter avec des mots (les points sur les i)

In the following, the term *mass difference* always refers to the relative one, namely $2\,(m_{\text{PART.}} - m_{\overline{\text{PART.}}})\,/\,(m_{\text{PART.}} + m_{\overline{\text{PART.}}})$, unless indicated otherwise.

(3)

" namely mass \emph{difference} over the mass \emph{average}: "

II Data samples and event selection

II-A The data samples

(4) the latter 1 l. au-dessus, the former ici ... pas clair → " pp coll° "

All the data samples employed for this measurement originates from the second campaign of data taking, the LHC Run-2. The latter comprises different collision systems at various energies, mainly pp collisions at $\sqrt{s}$ = 13 TeV and Pb-Pb collisions at $\sqrt{s_{\text{NN}}}$ = 5.02 TeV. Based on the elements in Sec. 4|II-C, the analysis exploits (4) ~~the former ones~~ as they provide a less dense collision environment, expectedly easier to reconstruct and thus more controllable. All these pp events have been collected during three data taking periods: between April and October 2016, May and November 2017, April and October 2018 (Sec. 3|I-C, Tab. 3.3).

Considering the target precision on the mass and mass(5)-difference values, it is crucial to have a fine comprehension of the data reconstruction to keep it well under control. For that reason, the analysis uses data in ESD format as they contain all the informations related to event building, thus offering the possibility to replay *offline* the V0 and cascade vertexings/formations. As mentioned in Sec. 3|II-E.iii, the first full reconstruction cycle (Sec. 3|II-E.i), performed right after ~~their~~ (6) the recording of the data, produces ESD files labelled as *pass-1*. Since then, other reconstruction cycles have been carried out, each iteration bringing its share of improvements or fixes. The events analysed for this measurement originates from the second reconstruction cycle, the (7) \emph{} pass-2, which offers better tracking performances: same (8) and consistent version of analysis software over all the data taking periods leading to more uniform performances, better SPD and TPC alignments, improved TPC reconstruction and finer description of the distortions within the TPC gas.

(9) (+)

Each period consists in fact of dozens or hundreds of *runs*, corresponding to sequences of events recorded in an uninterrupted manner[3]. The lists of approriated runs for physics analysis are defined by the ALICE Data Preparation Group (DPG). (10) appropriated

[2]This only concerns the relative mass difference between Λ and $\overline{\Lambda}$. As mentioned above, such quantity is much smaller by fourteen orders of magnitude in the case of K^0.

[3]Throughout the data taking, it is more or less frequent to interrupt the data collection, *i.e.* stop the run. This usually occurs when a detector encounters an error, unfixable while collecting data. Broadly speaking, a period regroups a set of runs that have been recorded within the same data taking conditions.

6

As its name suggests, the latter oversees the preparation, reconstruction, quality assurance of both collected and simulated data, as well as the upkeep of the analysis tools including the event and track selections [153]. The list of runs employed in this study follows the DPG's one for an analysis using central barrel detectors and requiring hadron PID. For a run to be in that list, all the detectors related to the tracking and PID must be operational – *i.e.* SPD, SDD, SSD (ITS), TPC, TOF –, as well as those in charge of triggering, that are the V0 and T0. Note that it does not mean that the PID performances are optimal, nor that the full acceptance of each detector is covered.

1 "recommendat°"

2 +

Besides the real data sample, the measurement also relies on simulated data in order to estimate and optimize the performances of the analysis. To each run corresponds its simulated counterpart, anchored on pass-2 data, as described in Sec. 3|II-E.iv. All the exploited MC productions employ Pythia 8 (version 8.2, tune: Monash 2013) as event generator. For the transport and interaction with the material of the ALICE detector, most of them use Geant3; although Geant4 runs faster, describes more accurately hadronic interactions at very low momentum and is better maintained, only a few of simulations rely on it [154].

3 J'avais en tête $G_4 \approx$ slower plutôt ?!

Since both abundant (K^0_S, Λ and to a certain extent, Ξ) and rare species (Ξ and Ω) are being studied, one may resort to two kinds of simulations: general-purpose MC productions for the first ones, and enriched MC productions for the others. Here, the enriched simulations have been obtained by selecting the events that includes, at least, a K^0_S, $\overset{(-)}{\Lambda}$, $\overset{(-)}{\Xi}{}^{\pm}$ or $\overset{(-)}{\Omega}{}^{\pm}$ in $|\eta| < 1.2$. It turns out that most of the studies carried out in the present analysis use on the latter simulations because of i) the enrichment in strangeness, ii) they cover all the periods of the considered LHC Run-2 data, and iii) they use Geant4.

4 Vérif° $y \leftrightarrow \eta$, ok!

5 +

Furthermore, this analysis also makes use of the track references in the simulation. As mentioned in Sec. 3|II-E.iv, these correspond to the MC informations of the considered track at the location where it crosses a given detection plane. Thereby, they allow to compare the reconstructed track informations with the actual/generated ones at any point along the particle trajectory[4]. Although the track references are effectively stored for only 10% of the production[5], this comparison is proving invaluable to control the tracking in ALICE.

In total, the exploited data sample counts about 2.6 billions minimum bias events at $\sqrt{s}$ = 13 TeV, and approximately 600 millions events in the associated MC productions.

6 +

II-B The event selection

As mentioned in Sec. 3|II-C, the analysis focuses on minimum-bias and/or high-multiplicity events. More precisely, the respective trigger configurations correspond to the $\mathrm{MB_{AND}}$ and/or $\mathrm{HM_{VZERO}}$. Not all the events passing these trigger selections

[4] Strictly speaking, this comparison cannot be done at any point since the track reference is only available where the particle traverses a sensitive volume.

[5] This is done in order to spare some disk space.

Impact de l'enrichissem^t sur une plage bornée en η ($\neq y$)

Check " $|\eta| < 1,2$ " pour les enrichissements MC

① Analyse CPT

dans les analyses
$$\begin{cases} K^0_S & 1-5 \text{ GeV}/c \\ \Lambda, \bar{\Lambda} & " \\ \Xi^- \; \Xi^+ & " \\ \Omega^- \; \Omega^+ & " \end{cases}$$

$p_T(K^0_S) = 1$ GeV/c $\longrightarrow$ $\eta = 1,2 \iff y \approx 0,929$ ✓
$p_T(\Lambda) = 1$ GeV/c $\longrightarrow$ $\eta = 1,2 \iff y \approx 0,886$ ✓
$p_T(\Xi^-) = 1$ GeV/c $\longrightarrow$ $\eta = 1,2 \iff y \approx 0,818$ ✓
$p_T(\Omega^-) = 1$ GeV/c $\longrightarrow$ $\eta = 1,2 \iff y \approx 0,712$ ✓

↳ on a toujours $|y| > 0,5$
pour la génération
∃ Safety margins, ok !

② Analyse corrélée

$$\begin{cases} \phi(1020) & 0,4 - 11 \text{ GeV}/c \\ \Xi^-, \Xi^+ & 0,6 - 6,5 \text{ GeV}/c \\ \Omega^-, \Omega^+ & 1,0 - 6,5 \text{ GeV}/c \end{cases}$$

→ ok ! ∉ enrichissem^t MC

(v4 p. 164)

"

$p_T(\Xi^-) = 0,6$ GeV/c $\longrightarrow$ $\eta = 1,2 \iff y \simeq 0,59$ ✓
$p_T(\Xi^-) = 0,8$ GeV/c $\longrightarrow$ $\eta = 1,2 \iff y = 0,720$ ✓
$p_T(\Omega^-) = 0,6$ GeV/c $\longrightarrow$ $\eta = 1,2 \iff y \simeq 0,489$ ∅
$p_T(\Omega^-) = 0,8$ GeV/c $\longrightarrow$ $\eta = 1,2 \iff y \simeq 0,612$ ✓
$p_T(\Omega^-) = 1,0$ GeV/c $\longrightarrow$ $\eta = 1,2 \iff y \simeq 0,712$ ✓

9

(2) Avec les refs multiples, Tu fais un bon usage du ch. 3 ici, lequel a été bien pensé + bien écrit !

are considered; additional cuts are applied in order to filter out only those of "good" quality for a physics analysis.

(1) cannot

During the data acquisition (DAQ), the event-builder proceeds to the event reconstruction based on the sub-events from all contributing detectors. It may happen, however, that the detector's output can not be transmitted due to the associated data channel being closed[6] [119]. The event-builder still reconstructs the event, although it is tagged as "incomplete DAQ" due to the missing informations. Such events are rejected in the present work.

There exists three types of reconstructed primary vertex in ALICE, from the highest to the poorest quality: one estimated using the global ITS-TPC tracks (Sec. 3|II-D.iii), another based on the SPD tracklets (Sec. 3|II-D.i), and the last built from the TPC standalone tracks in a similar way as the former. By default, only the "best" available reconstructed primary vertex is considered.

(3) optional one; (pr ne pas laisser le message (ftnote 7) que c'est un vtx "fallback sol°" si SPD fails

Nevertheless, to ensure that the event has a vertex of a sufficiently good quality, the analysis relies exclusively on the first two aforementioned primary vertices. This boils down to requiring the presence of, at least, the one reconstructed using tracklets[7]. Moreover, the resolution of the latter in the longitudinal direction should not exceed 0.25 cm. In cases when both SPD tracklets and global ITS-TPC track vertices are available, their positions along the beam axis must coincide within a 0.5 cm window.

linet (4)

(5) As a prerequisite for guaranteeing a ~~n~~ uniform reconstruction efficiency, particles must remain within the acceptance of all the central detectors involved in their reconstruction, that is $|\eta| < 0.9$. For particles originating from the interaction point, this condition implies a constraint on the longitudinal position of the primary vertex: the distance between the interaction point and the centre of ALICE should be below 10 cm along the beam axis[8].

(6) absolute

A key element of the event quality concerns the pile-up level. The latter occurs when there are two or more collisions coming from the same bunch crossing – this is the *in-bunch* pile-up – and/or from different bunch crossings occuring within the readout time of the detectors – also called *out-of-bunch* pile-up. One approach to remove both types of pile-up consists in rejecting events with multiple reconstructed primary vertices. This selection depends on the nature of the best primary vertex available.

(9) bonnes explic° pile-up rejectio°

(8) "primary-like"

- If it is the one reconstructed using ITS-TPC tracks, the event selection algorithm checks the presence of another vertex of reasonably good quality

[6]There are different reasons for the data channel to be closed. At the beginning or the end of each run, a specific procedure is performed on all detectors in order to effectively initiate the start or stop of the run. In particular, the "End Of Run" procedure has to close all the data channel connecting the event-builder and the sub-detectors – *i.e.* the GDCs and LDCs respectively (Sec. 3|II-C) –, but this termination can occur sooner in the case of a connection time-out for example.

[7]As mentioned in Sec. 3|II-D.i, the event cannot be built without the primary vertex based on SPD tracklets. Hence, by construction, the presence of such vertex is guaranteed in the event.

[8]Note that there is no selection of such nature concerning the transverse position of the primary vertex, except that it must be located below the beam pipe.

(7) i.e. \emph{}

6

($\chi^2/NDF < 5$, with NDF the number of degree of freedom), formed out of at least five tracks, and separated from the first one by more than 15σ[9]. If such vertex exists, the event is discarded.

- Otherwise, it corresponds to the one built from SPD tracklets. To maximise the selection efficiency, the cuts adapt to the tracklet multiplicity. Hence, if a second vertex is found to be away from the first one by more than 0.8 cm along the beam axis, with at least three, four or five associated tracklets for a total number of reconstructed tracklets ($N_{tracklets}$) inferior to 20, $20 < N_{tracklets} \leq 50$ and $N_{tracklets} > 50$ respectively, then the event is rejected.

Along the same line, the two innermost layers of the ITS can help to identify the remaining beam-induced background – that have not been removed by the $\mathrm{MB_{AND}}$ trigger selection – ~~and~~ with respect to pile-up events. As mentioned in 3|II-D.i, a tracklet is formed out of pair of clusters found in the two SPD layers, separated by an angle of 0.01 rad at most. Therefore, if the number of clusters increases, so does the amount of reconstructed tracklets. However, in the case of beam-gas event, there should be many clusters but only a small number of tracklets could be formed using the previous definition. In pile-up events, only the tracklets associated with the primary vertex are considered; for that reason, the number of clusters should be relatively larger than expected at ~~such~~ a given tracklet multiplicity [155]. In this way, based on this correlation between the number of SPD clusters and tracklets, the remaining events flagged as background or pile-up are rejected.

The Fig. 5.1 provides the fraction of rejected events as a function of the above selections in pp collisions at $\sqrt{s}$ = 13 TeV.

III Analysis of the hyperon masses

III-A Track selections

The identification of V0s and cascades strongly depends on the quality of the daughter tracks, and more precisely on their momentum resolution and trajectory. For that reason, the strange particle reconstruction relies exclusively on ITS-TPC combined tracks, since they offer the best momentum resolution as discussed in Sec. 3|II-D.ii and shown in Fig. 3.14. In order to ensure an excellent momentum resolution as well as a fine estimation of the particle trajectory, various selection criteria are applied on the daughter tracks.

The analysis concentrates exclusively on tracks comprised within the pseudorapidity region $|\eta| < 0.8$. The latter corresponds to the acceptance volume of all the central detectors, which provides a flat reconstruction efficiency. Moreover, any track containing ITS and/or TPC shared clusters is rejected, as they potentially correspond to wrongly assigned clusters that could bias the tracking quality.

[9] Here, σ denotes the uncertainty on the distance between the two vertices.

2 Si tu peux quantifier donner un ou des ordres de grandeur, serait un +

[7]

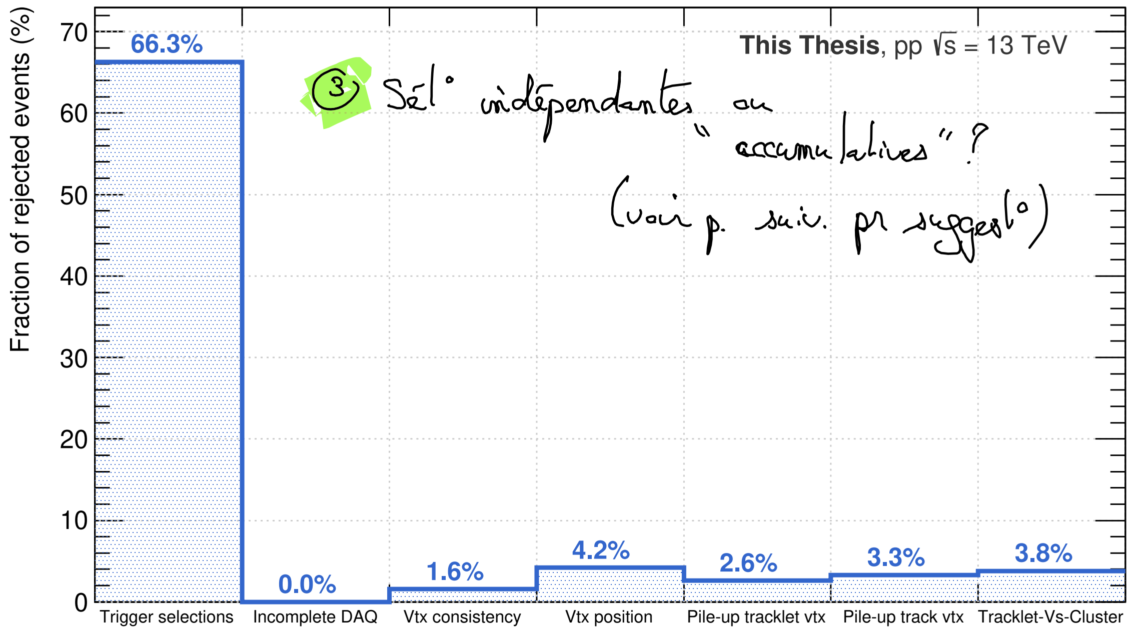

③ Sél° indépendantes ou "accumulatives" ? (voir p. suiv. pr suggest°)

① belle figure ! notamment les données chiffrées au-dessus de chaq bin.

Fig. 5.1: Fraction of rejected events in the present data sample for each event selection: trigger selections ($\mathrm{MB_{AND}}$ and/or $\mathrm{HM_{VZERO}}$), incomplete DAQ, consistency between the global track and SPD tracklet vertices, longitudinal position of the primary vertex ($|\Delta z| <$ 10 cm), pile-up removal for ITS-TPC track and SPD tracklet vertices, correlation between SPD tracklets and clusters.

② inverser l'ordre ? pr suivre l'ordre du TH1

④ Caption préciser le lot de data : 2016+ 2017+ 2018 ?

⑤ pas le meilleur exemple $K^+ \to \pi^0\pi^+ \to \gamma e^+e^- (c\tau_{\pi^0} = 25\,\mathrm{nm})\, \pi^+$

Tracks belonging to a *kink* vertex are discarded from the analysis, as they most certainly do not originate from a cascade decay and thus represent an additional source of combinatorial background. A kink usually happens when a charged particle decays into a neutral and a charged particle, such as ⑤ $\mathrm{K}^{\pm} \to \pi^0\pi^{\pm}$. The former being undetected, they are identified by forming pairs of tracks, that intersect in space with a large angle and share the same electric charge.

⑤ prends $K^+ \to \nu_\mu \mu^+$ (B.R. = 63.6%)

Each track should have passed the final refit in the TPC. This means that its parameters have been estimated successfully in the TPC during the third stage of the tracking, when the track is ⑥ re-propagated inwards to their distance of closest approach to the primary vertex (Sec. 3|II-D.ii). To guarantee a good momentum resolution and a stable particle identification (PID) based on the energy deposit ($\mathrm{d}E/\mathrm{d}x$) in the TPC, the tracks need to be associated to at least 70 readout pad rows in the TPC out of 159 ⑦ possible in total. These selections eliminate the contribution of short tracks and, incidentally, pairs of tracks formed out of the clusters from a single actual particle.

The reconstruction of V0s and cascades presented in Chap. 4 does not resort to any kind of selections on the nature of the daughter particles, apart from their electric charge. This yields *de facto* to an outstanding amount of background candidates. One way of suppressing the latter with a minimal cost in terms of signal candidates consists in using the PID informations provided by the TPC. In practice, the idea is to reject every association that involves tracks inconsistent with the expected identities for either a $\mathrm{K^0_S}$, $\overset{(-)}{\Lambda}$, $\overset{(-)}{\Xi}{}^{\pm}$ or $\overset{(-)}{\Omega}{}^{\pm}$ decay.

③ p. précédente :

- préciser dans le caption si on parle de sél° appliquées indépendamment

(i.e. les evts perdus = 66,3% + 0% + 1,6% + 4,2% ...)

ou plus probablement, si l'on est sur
" a sequence of selections that are applied cumulatively one after the other, from left to right "

(Dans ce 2e cas, cela veut dire en pratique qu'à chaque changement de bin le denominateur, la référence 100%, change)

- \+ Pour rendre la donne claire, peut-être l'illustrer avec un chiffrage
" In the end, the events that are retained will go like:

$(100 - \underline{66{,}3}\%) \times (100 - \underline{0{,}0})\% \times (100 - \underline{1{,}6}\%) \ldots$ "

8

1 As explained in Sec. 3|II-B.ii, a track can be labeled as a pion, proton or kaon by making use the PID estimator in Eq. 3.3, n_σ, which evaluates the difference between the measured dE/dx and the expected one under a given particle mass hypothesis in units of relative resolution. The separation power of such estimator evolves with the particle momentum which, in turn, influences the selection threshold and has some implications in terms of purity and efficiency: the tighter the selection on n_σ, the higher the purity but at the price of a small efficiency (2: er); conversely, a looser cut on n_σ deteriorates the purity in favour of a higher efficiency.

The identification strategy adopted here consists in selecting only the tracks compatible with their expected mass hypothesis within $n_\sigma = \pm 3$ at most. This selection is applied on each (3: \emph{}) decay daughters, irrespective of their momentum or the one of the mother particle. This therefore imposes that:

⑤ Pb ds la logiq de présentation : tu pars sur cas général "($\overline{\Xi}^{\pm}$ ... $\overline{\Omega}^{\pm}$)" puis tu parlers sans prévenir sur un cas particulier, au lieu de le spécifier

- the bachelor track must (4: be) consistent with the $\pi^\pm$ or $\text{K}^\pm$ mass hypothesis, in the case of $\overline{\Xi}^{\pm}$ or $\overline{\Omega}^{\pm}$ respectively,
- the positive (5.1 "baryon") track needs to be compatible with a proton hypothesis, ⑤ ≠ ne marche pas ds le cas général $\Xi^- \to p^+$, $\Xi^+ \to \bar{p}^-$
- and the negative (5.1 "meson") track has to agree with energy loss band of the pion.

~~Note that the last two constraints only allow to identify a Λ and, associated with the bachelor track, a Ξ^- or Ω^-. In order to select their anti-particle, one needs to swap the mass hypothesis of these two items, namely the positive track corresponds to a pion and the negative track, an anti-proton.~~ For the K^0_S, the particle is indistinguishable from the anti-particle in exploited V0 decay channel; both positive and negative tracks should be compatible with the pion hypthesis.

+ 5.1 + 5.2 donne 1 exemple: Ξ^+: bach = ... + $\overline{\Lambda}$ { baryon = ... meson = ...

III-B V0s and cascades selections

III-B.i Topological and kinematic selections

6 lien pointe vers II-B → à fixer

Once the events and tracks have been selected, the topological reconstruction of V0s and cascades comes into play, as explained in Chap. 4. However, not all the candidates are considered in the analysis. As suggested in Sec. 4|II-C, ALICE is well suited for studying hyperons but only at mid-rapidity. This means that the V0s and cascades are reconstructed in the rapidity window $|y| < 0.5$.

The above selections on the track quality in TPC exclude the possibility of studying the particles of interest at low momentum ($p_\text{T} \leq 0.6$ GeV/c). At such values, the V0s and cascades decay into very low momentum tracks, that can only be reconstructed via the ITS standalone tracking. Even when these tracks reach the TPC, they form short tracks and are thus rejected (Sec. 5|III-A). As a matter of fact, in order to secure a reasonably good momentum resolution on the decay daughters, this analysis only considers candidates from 1 to 5 GeV/c. On (7: the) one hand, the Eq. 3.1 indicates that the momentum resolution deteriorates at low momentum ($p_\text{T} \leq 1$ GeV/c) due to their relatively "short" track length, "small" number of clusters and the dominant contribution of multiple scattering. On the other hand, at high p_T ($p_\text{T} \geq 5$ GeV/c), the resolution also decreases as a consequence of less pronunced

8 pronounced

(NB1) Il faudrait voir ds les données TR la résolution σ_{mass} K^0_S et $\sigma_m(\Lambda)$ $\sigma_m(\bar{\Lambda})$ sur 1-5 GeV/c et s'assurer que ∄ signal brut ds $\Delta_m(\Lambda) \pm 5$ MeV, $\Delta_m(K^0_S) \pm 10$ MeV ∀ p_T notamment vers $p_T \approx 5$ GeV/c (σ_m les + larges)

pas une priorité si ∃ effet de contaminat°, cad ss doute plutôt vers $p_T \approx 5$ GeV/c

Candidate variable	Selections $\bar{\Lambda}$	Selections K^0_S
V0 p_T interval (GeV/c)	$1 < p_T < 5$	
V0 rapidity interval	(1) $\lvert y\rvert < 0.5$	
Competing mass rejection (GeV/c^2)	> 0.010	> 0.005
MC association (MC only)	Correct identity assumption	
Track variable	Selections $\bar{\Lambda}$	Selections K^0_S
Pseudo-rapidity interval	$\lvert\eta\rvert < 0.8$	
TPC refit	✔	
Nbr of crossed TPC readout rows	> 70	
n_σ^{TPC}	< 3	
Out-of-bunch pile-up rejection	(2) at least one track with ITS-TOF matching	
Topological variable	Selections $\bar{\Lambda}$	Selections K^0_S
V0 decay radius (cm)	> 0.5	
V0 Lifetime (cm)	$< 3 \times c.\tau$	
V0 cosine of pointing angle	> 0.998	
DCA proton to prim. vtx (cm)	> 0.06	
DCA pion to prim. vtx (cm)	> 0.06	
DCA between V0 daughters (std dev)	< 1	

→ TH_2 $m_{K^0_S}$ vs m_Λ + projo

“ITS ‖ TOF matching” (2) chgmt notations, proposé + elsewhere

(9)

(9) “–” plutôt (≠ veto, = juste, non avenu) tiret

Table 5.2: Summary of the topological and track selections, as well as the associated cut values, used in the reconstruction of $\bar{\Lambda}$ and K^0_S in pp events at $\sqrt{s}$ = 13 TeV. The *competing mass rejection* refers to the removal of the background contamination from other mass hypotheses (Sec. 4|II-B.iii). In the $\bar{\Lambda}$ case, this consists in comparing the invariant mass under the assumption of a $\pi^+\pi^-$and PDG mass of K^0_S, that is the quantity $\lvert m_{inv}\text{hyp. } K^0_S - m_{PDG}K^0_S\rvert$. When reconstructing K^0_S candidates, the selection variable becomes $\lvert m_{inv}\text{hyp. } \Lambda - m_{PDG}\Lambda\rvert$.

(3) ok! clair en fait

NB2 Je garde en tête l'idée à vérifier de faire aussi une exclusion mutuelle Λ vs $\bar{\Lambda}$ (pr le papier, ≠ now) (voir p. 110)

track curvature. (4)

(5) ± 300 ns ↳ ± 12

To further remove the contribution from out-of-bunch pile-up events, it is required for at least one of the daughter tracks to either have a cluster in the innermost ITS layers[10] or match with a hit in the TOF. The former uses the fast readout time of the SPD to limit the pile-up to tracks produced in collisions within ± 300 ns, that is twelve bunch crossings; (6) the latter exploits the highly precise timing information of the TOF to identify the bunch crossing from which the particle originates, with an efficiency of approximately 70 to 80% for intermediate or high p_T particles and drops rapidly for lower momentum due to mismatches [156]. This selection has been thoroughly studied in the context of a strange particle production analysis [157]; it was shown that applying this ITS-TOF matching condition on at least one of the decay daughters is sufficient to eliminate most of the remaining pile-up contamination.

(7) quantifier (i.e. $p_T \geq$ ...)

[10] Technically, it is requested to have passed the final refit in the ITS and to have a hit in one of the two SPD layers. (8)

(6) Footnote: “keep in mind that, in ALICE in Run-2, the average number of collisions per bunch crossing is not 50-50 like for CMS or ATLAS, 1-2 like for LHCb, but ≤ 1-5% i.e. a low trend in terms of pile-up.”

a so-called \emph{offline}

(1) Moreover, the reconstruction procedure presented in the Chap. 4 corresponds to an *offline* reconstruction: V0s and cascades are formed by combining tracks, that have already been reconstructed during the event building (Sec. 3|II-D). However, in the tracking stage, there is no way to know *a priori* that they are, in fact, the decay daughters of a hyperon; they are thus reconstructed as any other track in the event. As a consequence, there is no causality check[11] against assigned ITS clusters anterior to the V0 and/or cascade decays. Due to the possible bias that might be introduced in the invariant mass of the mother particle, all the daughter tracks updated with an ITS cluster (3) \emph below the associated decay point by more than $1\ \sigma_{\mathrm{R}}$[12] are (5) discarded. This requirement applies for both V0 and cascade candidates.

(4) less than ("discarded..." ≠ retained)

In summary, the Tabs. 5.2 and 5.3 provide a list of the track and topological selections employed in the reconstruction of V0s and cascades respectively, as well as the numerical cut values. Note the tight cut on the cosine of pointing angle of the cascade candidate; this is discussed later in Sec. 5|III-C.

(7) "at low masses"

III-B.ii Structure in the invariant-mass spectrum of cascades

(8) texte = clair !

Among the topological selections listed in Tab. 5.3, one of them has not been introduced and discussed in Chap. 4, namely the cut on the pointing angle formed by the bachelor and the positive particles. Contrarily to the other selections, this one is not standard in ALICE; it has been introduced in 2020 by [158]. At that time, a structure in the invariant mass distribution of Ξ and Ω, similar to the one in Figs. 5.2, was observed in Pb-Pb collisions. It turned out that the bump background, between 1.28 and 1.31 GeV/c^2 on Figs. 5.2(a) and 5.2(b), originates from an erroneous track association in the cascade reconstruction.

A V0 decays into a baryon p/$\overline{\mathrm{p}}$ and a π^-/π^+, depending on whether this is a Λ or $\overline{\Lambda}$. In the situation where another negative/positive track in the event passes close by the proton/anti-proton, the reconstruction algorithm may interpret that as a V0 decay; this track plays the role of the negative/positive daughter particle of a $\overset{\scriptscriptstyle(-)}{\Lambda}$, and the proton/anti-proton corresponds to its positive/negative daughter particle. On the other hand, (9) the remaining π^-/π^+ daughter of the actual $\overset{\scriptscriptstyle(-)}{\Lambda}$ is combined to other particles, and most likely to the previously ill-formed V0. In such case, it acts like the bachelor particle of a cascade decay. In other words, while the actual topology is depicted in Fig. 5.3(a), it is reconstructed as a cascade, as illustrated in Fig. 5.3(b).

(10) Schéma = un + !

lame / dummy

The analysis [158] investigated different strategies in order to remove this background contamination. In the end, the best option consists in rejecting candidates (11) with a \emph small pointing angle for (12) the ~~actual~~ V0, *i.e.* the pointing angle ~~between~~ the bachelor and the proton, as shown in Fig. 5.3(c).

(13) formed by the V0 made of

(6) Ptr-ê faire un schéma tel pr le manuscrit final

(2) "downstream"

[11] There is, however, a causality check performed in the cascade reconstruction in order to ensure that the V0 decay point does sit ~~below~~ to the cascade decay position.

[12] σ_{R} refers to the resolution on the radial decay position of the ~~V0 or~~ cascade.

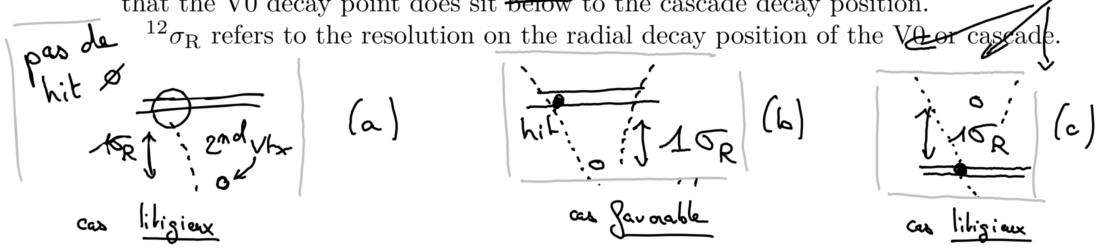

(5) (Pour papier)
On vire cas (c), on garde (a) + (b), si je comprends bien
→ le cas (a) m'interroge

9

① Mettre ce tableau sur une page à part "[!p]"

Candidate variable	Selections $\Xi^{\pm}$	Selections $\Omega^{\pm}$
Cascade p_{T} interval (GeV/c) ②	$1 < p_{\mathrm{T}} < 5$	
Cascade rapidity interval	$\lvert y \rvert < 0.5$	
Competing mass rejection (GeV/c^2)	tiret "–"	> 0.008
MC association (MC only)	Correct identity assumption	
Track variable	**Selections $\Xi^{\pm}$**	**Selections $\Omega^{\pm}$**
Pseudo-rapidity interval	$\lvert \eta \rvert < 0.8$	
TPC refit	✔	
Nbr of crossed TPC readout rows	> 70	
$n_{\sigma}^{\mathrm{TPC}}$	< 3	
Out-of-bunch pile-up rejection	at least one track with ITS-TOF matching ③ "ITS ‖ TOF"	
Anterior ITS cluster rejection	$> 1\ \sigma_{\mathrm{R}}$	
Topological variable	**Selections $\Xi^{\pm}$**	**Selections $\Omega^{\pm}$**
V0		
V0 decay radius (cm)	> 1.2	> 1.1
V0 cosine of pointing angle	> 0.97	
$\lvert m(V0)$ - $m_{\mathrm{PDG}}\Lambda \rvert$ (GeV/c^2)	< 0.008	
DCA proton to prim. vtx (cm)	> 0.03	
DCA pion to prim. vtx (cm)	> 0.04	
DCA V0 to prim. vtx (cm)	> 0.06	
DCA between V0 daughters (std dev)	< 1.5	
Cascade		
Cascade decay radius (cm)	> 0.6	> 0.5
Cascade Lifetime (cm)	$< 3 \times c.\tau$	
DCA bachelor to prim. vtx (cm)	> 0.04	
DCA between cascade daughters (std dev)	< 1.3	
Cascade cosine of pointing angle	> 0.998	
Bachelor-proton pointing angle (rad)	> 0.04 ✓ ④	

Table 5.3: Summary of the topological and track selections, as well as the associated cut values, used in the reconstruction of $\Xi^{\pm}$ and $\Omega^{\pm}$ in pp events at $\sqrt{s} = 13$ TeV. The *competing mass rejection* refers to the removal of the background contamination from other ~~mass~~ hypothese~~s~~ (Sec. 4|II-B.iii) hypothesis [(singulier) ici (?)] ⑥ " in mass " ⑦
⑤ cascade

III-c Mass measurement

III-c.i Principles of mass extraction

Out of all the candidates passing the above selection criteria, there contain~~s~~ ⑧ true V0s/cascades – depending on the particle of interest – and background candidates. Taken individually, they are undistinguishable. The separation of these two can only be achieved statistically, based on the analysis of the invariant mass spectrum. ⑨ +

The invariant mass of each candidate is calculated, as explained in Sec. 4|II-B.ii

$\boxed{7}$

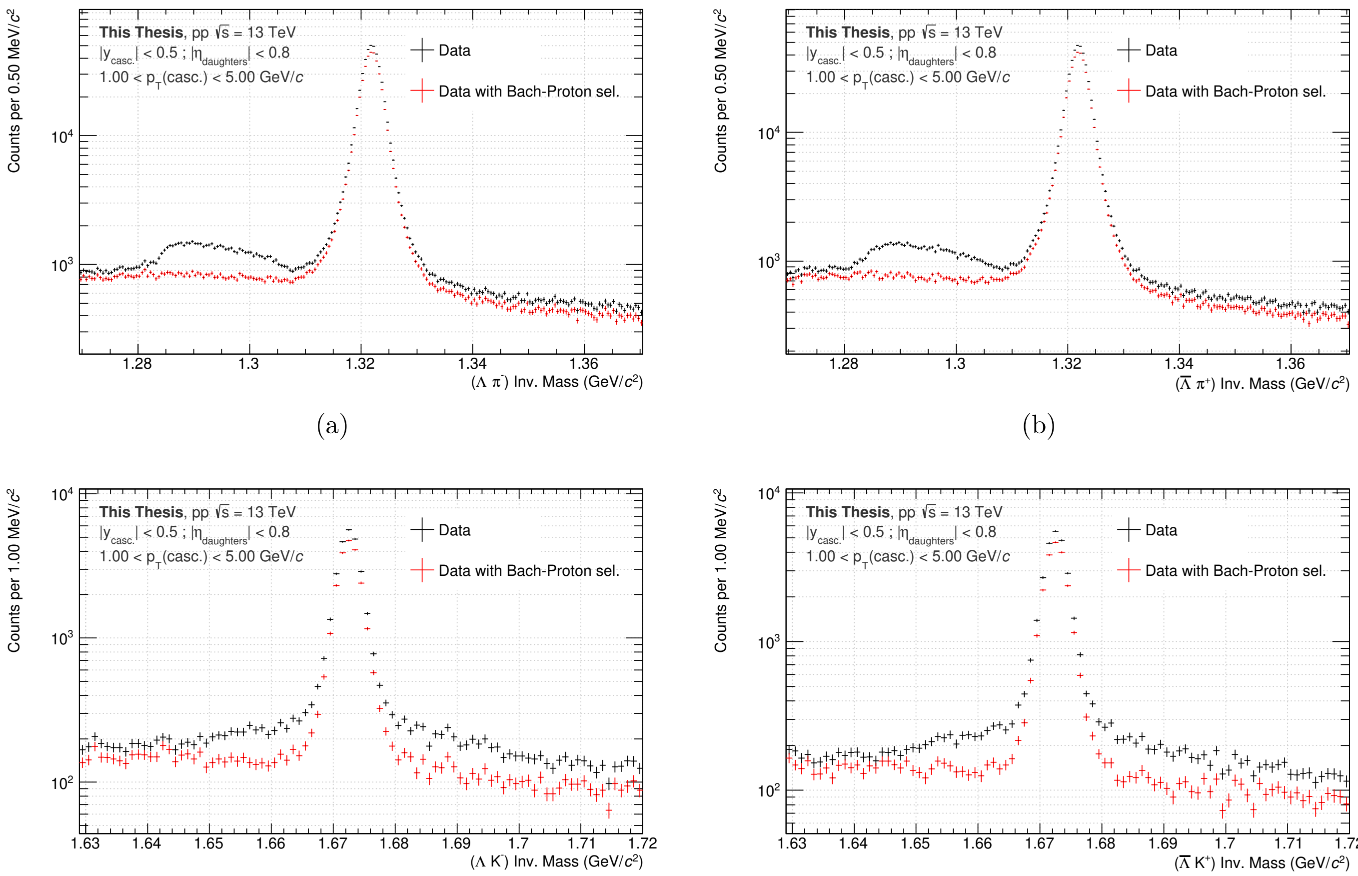

(a) (b) (c) (d)

Fig. 5.2: Invariant mass distribution of Ξ^- (a), $\overline{\Xi}^+$ (b), Ω^- (c) and $\overline{\Omega}^+$ (d) in pp at $\sqrt{s}$ 1 $= 13$ TeV. These have been obtained using the cuts in Tab. 5.3 (red markers), ~~except~~ "and also without..." ~~for~~ the bachelor-proton pointing angle selection ~~in~~ (2 markers) black. This comparison shows the latter selection manages to remove a structure in the invariant mass distribution while preserving the population under the peak. Notice the log-scale on the y-axis, that puts into perspective the signal and background levels. + 3

and Sec. 4|II-B.iii, and sorted according to their electric charge in order to separate the particles from the anti-particles. The V0s being electrically neutral, they follow a different approach: since the K^0_S decays into two particles of the same nature — a $\pi^+$and a π^- — 4 , it is hopeless to try separating particles and anti-particles. This is not the case of Λ and $\overline{\Lambda}$, though. However, it may happen that the same V0 candidate passes the particle and anti-particle selections in Tab. 5.2. To avoid such double-counting, each candidate needs to go through the Λ selections first. If it satisfies all conditions, it is labeled as Λ and we move to the next candidate. Otherwise, it is checked against the requirements for a $\overline{\Lambda}$ baryon.

virgule

5 voir p. 107 + cf. notre discuss° + p. suiv

6 On ~~one~~ the one hand, most of the background candidates originate from a random association of two or three tracks. Those tracks being uncorrelated, the corresponding invariant mass spectrum should be flat or decreasing with the invariant mass value. On the other hand, the invariant mass of true V0s/cascades should be close to the tabulated mass m_{PDG}, such that there emerges an overpopulated region taking the shape of a peak. The Figs. 5.4 show the invariant mass spectra of Ξ and Ω. One + 7

(Pour le papier) [Contamination réciproque Λ Vs $\bar{\Lambda}$]

Effectivement statistiquement, $\exists$ plus de Λ que de $\bar{\Lambda}$

mais la $\neq$ce n'est pas un facteur 10

Donner la préséance au candidat "Λ" sur

l'hyp. "$\bar{\Lambda}$" a du sens

<u>mais</u> selon moi n'est pas "bullet proof"

Le proba de mauvais étiquetage doit rester

~~élevée~~, plausible

la contaminat° mutuelle pt ê un problème

$\boxed{A}$ $\longrightarrow$ (TH_2 $m(\bar{\Lambda})$ Vs $m(\Lambda)$

+ structure q apparaissent dans

les distrib° de masse inv respectives)

$\boxed{B}$ Le proton du Λ ou l'anti-p de l'$\bar{\Lambda}$ récupère statistiquement la plus gr-de part de la qté de mvt de la mère...

a ens il y aura peut-être un truc à exploiter

1. On calcule les 2 masses Λ et $\bar{\Lambda}$
2. repérer l'ordonnancement des $\|\vec{p}\|$ ou p_T
   - Si le p_T le + élevé = trace ⊕

   alors probablement trace ⊕ = proton $\longrightarrow$ label "Λ"
   - Si le p_T le + élevé = trace ⊖

   alors ———— ⊖ = anti-proton $\rightarrow$ label "$\bar{\Lambda}$"
   - Si les p_T = "trop" proches, on vire les 2.

7

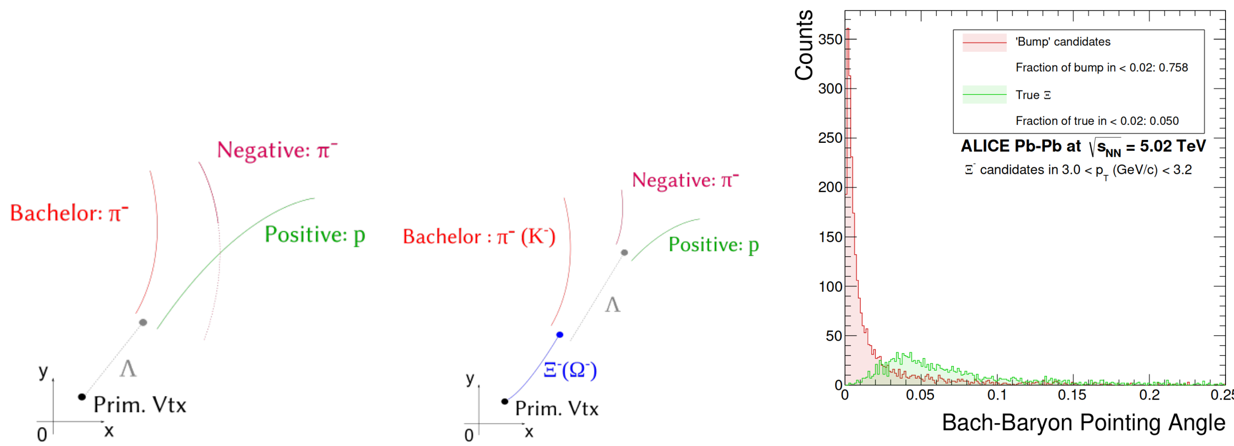

(a) (b) (c)

Fig. 5.3: Invariant mass distribution of Ξ^- (a), $\overline{\Xi}^+$ (b), Ω^- (c) and $\overline{\Omega}^+$ (d) in pp at $\sqrt{s}$ = 13 TeV. These have been obtained using the cuts in Tab. 5.3 (red markers), except for the bachelor-proton pointing angle selection in black. This comparison shows the latter selection manages to remove a structure in the invariant mass distribution while preserving the population under the peak.

can see that the signal for each species sits on top of a small background.

(1) = III-C ii (p. suiv)

(2) + (3) Mettre à jour: triple Gauss + exponentielle

To isolate the signal from the background, a fit of the invariant mass spectra is performed using the sum of two functions: one for modeling the signal peak, the other for describing the background. Several functions can be considered, as discussed in (1) Sec. ??. In Figs. 5.4, the peak is represented by a (2) ~~modified~~ Gaussian [159] and the background by (3) ~~a linear~~ function. Whatever their shape, the fitting procedure is performed with the maximum (log-)likelyhood method.

If the procedure manages to converge, this fit allows to measure the mass of the considered particle: it corresponds to the centre of the invariant mass peak, given by the position of the maximum of the signal function denoted as μ. The width of the peak – the parameter σ – provides an estimation of the mass resolution. (4) The uncertainties on both quantities come from the errors returned by the fitting procedure.

"an estimation of the experimental resolution on the mass"

From these parameters, two regions of interest can be delimited:

(5) within

- the peak region, containing all the signal[13] and some background, is defined in $[\mu-5\sigma;\mu+5\sigma]$;
- the side-band~~s~~ (6) regions (7) (5) solely constituted of background, consists in two bands of the same width[14], surrounding the peak region and covering the range $[\mu-12\sigma;\mu-7\sigma]\cup[\mu+7\sigma;\mu+12\sigma]$.

[13] More precisely, considering the definition of the peak region in this analysis, it should contain approximately 99.99995% (*i.e.* a 5σ significance level) of the true V0s/cascades measured.

[14] As a side note: the two side-bands do not need to be of the same size, but it avoids dealing with a scaling factor when comparing their total area to the one in the peak region. Most often, they have different widths because of an asymmetry in the invariant mass distribution, such as the structure reported in Sec. 5|III-B.ii [142].

6

Hence, the amount of raw signal and background can be evaluated. The peak $(S+B)$ and background (B) populations are estimated by counting the number of candidates in their respective regions. The raw signal (S) in the peak region is obtained by subtracting the background from the peak population, that is $S = (S+B) - B$.

In Figs. 5.4, all the fit are of reasonably good quality[15]. The bottom panels show that the data-model discrepancy does not exceed 5% for the most precise points, i.e. those in the peak region. The mass peak sits on a small background: 1 298 838 ± 1202 Ξ^- (1 229 531 ± 1168 $\overline{\Xi}^+$) and 67 210 ± 265 (284) Ω^- (66 199 ± 281 $\overline{\Omega}^+$) were reconstructed with purities above 90%, as shown in Tab. 5.4.

1 espace

2 erreur de report de valeur

Particle	Ξ^-	$\overline{\Xi}^+$	Ω^-	$\overline{\Omega}^+$
Reduced χ^2	2.474	1.692	1.500	1.826
Raw signal, S	1 298 838	1 229 531	67 210	66 199
Background, B	75209	67 328	6784	6231
S/B	17.3	16.4	9.91	10.63
Purity, $S/(S+B)$	94.5%	94.2%	90.8%	91.4%
Signal significance, $S/\sqrt{S+B}$	1108	1076	247	246

3 + Nice Tab!

Table 5.4: Results from the fit of the invariant mass distributions in Fig. 5.4 concerning the samples of Ξ^-, $\overline{\Xi}^+$, Ω^- and $\overline{\Omega}^+$. Therefore, this table reports the reduced χ^2, raw signal, background, ratio S/B, purity and signal significance.

4 "the overall samples"

III-c.ii Shape of the peak functions

5 +

Since the mass extraction depends on the peak description, it is crucial to identify functional forms that reproduce accurately its shape. Different functions have been studied in MC simulations, based solely on true V0/cascade candidates. Thus, the invariant mass spectra contains no background candidates and follows approximately a quasi-Gaussian distribution centred on the injected mass, which usually corresponds to the PDG mass value. The objective here is to define a list of functions, that describe correctly the shape of the invariant mass peak and are characterised by a resonably good reduced χ^2. Two types of functional forms are considered: symmetric and asymmetric functions.

6 reasonably

Symmetric function: Due to the detector smearing, the core of the invariant mass distribution exhibits a quasi-Gaussian shape; in that respect, one may favour symmetric functions. The tails of the distribution, however, are usually not Gaussian-like, and thus not well described by this class of functions. This is due to the contribution of particles with different transverse momentum; as the p_T resolution varies with the transverse momentum and relates to the width of the invariant

[15] One may argue that, in the case of the Ξ^-, the reduced χ^2 is relatively high. However, the comparison of the bottom panels of the Ξ^- and $\overline{\Xi}^+$ allows to conclude that it certainly comes from a slightly worst description of the background.

3

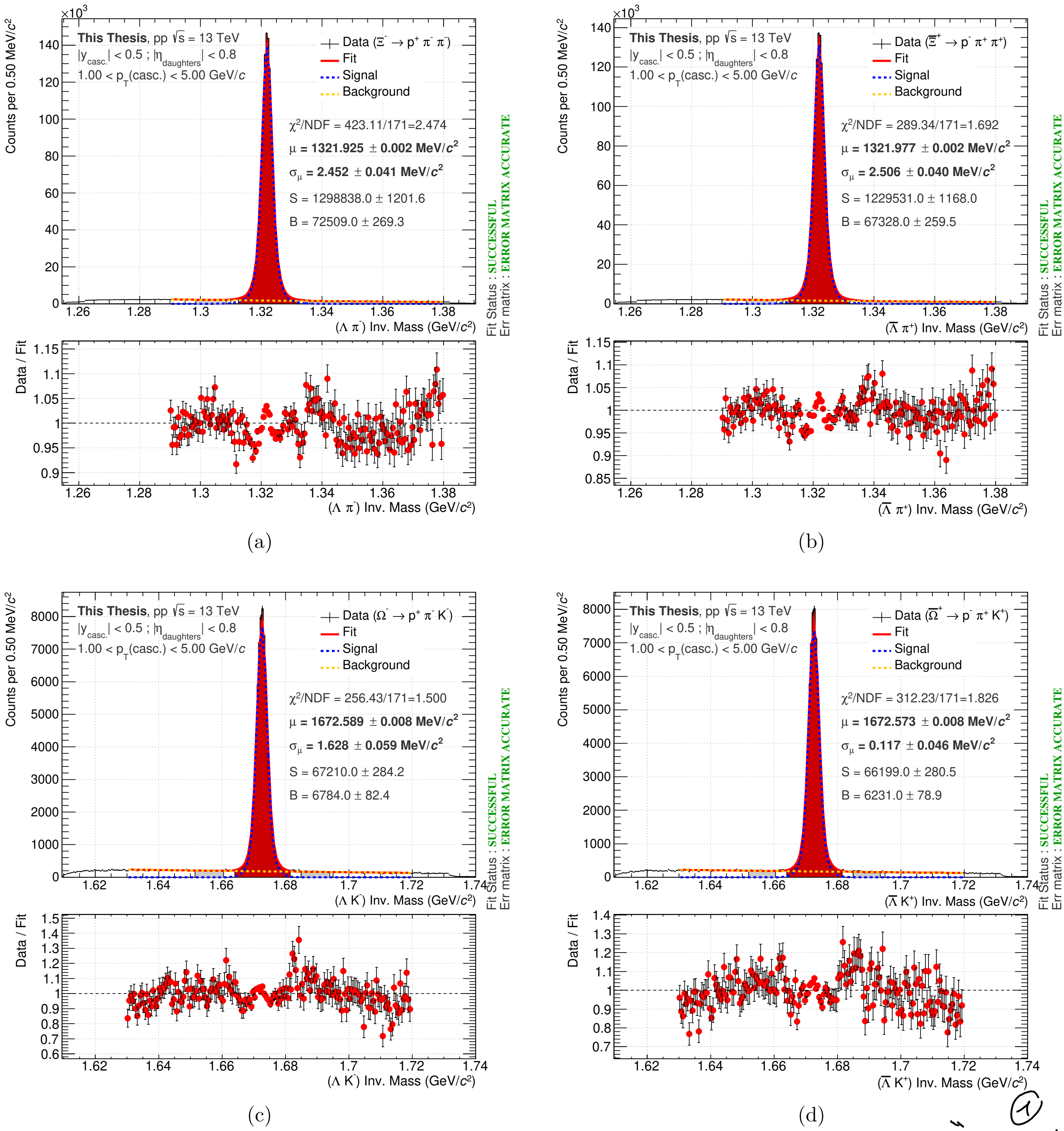

Fig. 5.4: Invariant mass distribution of Ξ^- (a), $\overline{\Xi}^+$ (b), Ω^- (c) and $\overline{\Omega}^+$ (d) hyperons in pp collisions at $\sqrt{s}$ = 13 TeV. Here, the peak is modeled by a triple Gaussian, and the background by an exponential function. Each distribution comes with an additional panel representing the consistency between the data and the fit model, in the form of a ratio. The error bars encompasses the uncertainties on both quantities.

1 "\emph{real}"

2 the

3 "per inv. mass bin"

 4

mass peak, the measured distribution consists in fact in an infinite sum of invariant mass distribution, each with a different width. Always with the aim of employing an symmetric function, the solution thus consists to take an infinite sum of Gaussian with a common mean[16]. In the present analysis, it has been observed that three Gaussians (Eq. 5.2) already offer a resonably reasonably (2) good fit quality. Another option is to resort to slightly modified versions of a Gaussian, such that it provides a better description of the tails of the distribution (Eq. 5|III-C.ii).

- **Triple Gaussian**:

$$\frac{\mathrm{d}N}{\mathrm{d}m_{\mathrm{inv}}} = A_1 \cdot \exp\left[-\frac{(m_{\mathrm{inv}}-\mu)^2}{2\sigma_1^2}\right] + A_2 \cdot \exp\left[-\frac{(m_{\mathrm{inv}}-\mu)^2}{2\sigma_2^2}\right] + A_3 \cdot \exp\left[-\frac{(m_{\mathrm{inv}}-\mu)^2}{2\sigma_3^2}\right] \tag{5.2}$$

  with A_1, A_2, A_3 the amplitudes of the first, second and third Gaussian, μ the common mean value, and σ_1, σ_2, σ_3 the width of the first, second and third Gaussian[17].

- **Modified Gaussian** [?] (4):

$$\frac{\mathrm{d}N}{\mathrm{d}m_{\mathrm{inv}}} = A \cdot \exp\left[-\frac{1}{2} u^{1+\frac{1}{1+0.5u}}\right] \quad ; \quad u = \left|\frac{m_{\mathrm{inv}}-\mu}{\sigma}\right| \tag{5.3}$$

  with A the normalization, μ the mean, and σ the width.

Asymmetric function: Previous functions are all different flavours of Gaussian, and so are all symmetric. However, this is not necessarily the case for the tails of the invariant mass distribution. In such case, an asymmetric function seems more (5) suited for describing the peak. Among those appears the Bukin function [?], that is arXiv: 0711.4449 modified Novosibirsk distribution, constructed from the convolution of a Gaussian and an exponential distributions. It is typically used to fit the invariant mass of J/ψ.

- **Bukin**:

$$\frac{\mathrm{d}N}{\mathrm{d}m_{\mathrm{inv}}} = \begin{cases} A \cdot \exp\left[\rho_{\mathrm{L}} \frac{(u-x_{\mathrm{L}})^2}{(\mu-x_{\mathrm{L}})^2} - \ln(2) + 4 \cdot \ln(2) \frac{(u-x_{\mathrm{L}})}{2\sigma\sqrt{2\ln 2}} \cdot \frac{\xi}{\sqrt{\xi^2+1}+\xi} \frac{\sqrt{\xi^2+1}}{(\sqrt{\xi^2+1}-\xi)^2}\right], & u \leq x_{\mathrm{L}} \\ A \cdot \exp\left[-\ln(2) \cdot \left(\frac{\ln(1+4\xi\sqrt{\xi^2+1}\frac{u-\mu}{2\sigma\sqrt{2\ln 2}})}{\ln(1+2\xi(\xi-\sqrt{\xi^2+1}))}\right)^2\right], & x_{\mathrm{L}} < u < x_{\mathrm{R}} \\ A \cdot \exp\left[\rho_{\mathrm{R}} \frac{(u-x_{\mathrm{R}})^2}{(\mu-x_{\mathrm{R}})^2} - \ln(2) + 4 \cdot \ln(2) \frac{(u-x_{\mathrm{R}})}{2\sigma\sqrt{2\ln 2}} \cdot \frac{\xi}{\sqrt{\xi^2+1}+\xi} \frac{\sqrt{\xi^2+1}}{(\sqrt{\xi^2+1}-\xi)^2}\right], & u \geq x_{\mathrm{R}} \end{cases} \tag{5.4}$$

[16] A more unusual approach would be to consider an infinite sum of Gaussian, each with a different mean. This would be relevant if the mass measurement is biased, in such a way that mass changes with momentum for example. In such case, a non-trivial question arises as of what value to take as a final mass measurement. As of today, there is still no clear answer. (+) (1)

[17] In case of a fit with a triple Gaussian function, it is the weighted width that is considered for the definition of the peak and side-bands regions. The weighting factors for σ_1, σ_2, σ_3 are determined based on the relative contribution of each Gaussian in the fit, *i.e.* $\sigma^2 = \frac{A_1}{A_1+A_2+A_3}\sigma_1^2 + \frac{A_2}{A_1+A_2+A_3}\sigma_2^2 + \frac{A_3}{A_1+A_2+A_3}\sigma_3^2$ (+) (3)

with

$$x_{\mathrm{L,R}} = \mu + \sigma\sqrt{2\ln 2}\left(\frac{\xi}{\sqrt{\xi^2+1}} \mp 1\right) \quad (5.5)$$

where u coincides with m_{inv}, A is the normalization parameter, μ and σ are the mean and the width of the peak, ξ is an asymmetry parameter, ρ_{L} and ρ_R are left and right exponential tail coefficients [?]. (1) To be fixed

- **Double Sided Crystal Ball** [160]:

$$\frac{\mathrm{d}N}{\mathrm{d}m_{\mathrm{inv}}} = \begin{cases} A\cdot\left(\frac{n_{\mathrm{L}}}{\alpha_{\mathrm{L}}(n_{\mathrm{L}}-\alpha_{\mathrm{L}}^2-u\alpha_{\mathrm{L}})}\right)^{n_L}\exp\left[-0.5\alpha_{\mathrm{L}}^2\right], & u < -\alpha_{\mathrm{L}} \\ A\cdot\exp\left[-0.5u^2\right], & -\alpha_{\mathrm{L}} \leq u \leq \alpha_{\mathrm{R}} \\ A\cdot\left(\frac{n_{\mathrm{R}}}{\alpha_{\mathrm{R}}(n_{\mathrm{R}}-\alpha_{\mathrm{R}}^2+u\alpha_{\mathrm{R}})}\right)^{n_R}\exp\left[-0.5\alpha_{\mathrm{R}}^2\right], & u < \alpha_{\mathrm{R}} \end{cases} \quad (5.6)$$

with u equals $(m_{\mathrm{inv}}-\mu)/\sigma_L$ for $m_{\mathrm{inv}}-\mu<0$ and $(m_{\mathrm{inv}}-\mu)/\sigma_R$ for $m_{\mathrm{inv}}-\mu>0$, A is the normalization parameter, μ is the peak position, σ_{L} and σ_{R} parametrise the position where the peak starts to follow a power law towards the low and high mass values respectively, of exponents n_{L} and n_{R}.

To each particle should be associated, at least, two functional forms for the modelisation of the peak: a symmetric and an asymmetric functions. Therefore, after several tests, it turns out that the functions offering the best description of the invariant mass peak are the triple Gaussian and the Bukin. (2) ok!

III-c.iii Shape of the background functions

The origin of the data sample purity has to be found in the (very) tight cut on the cosine of pointing angle of the cascade candidate in Tab. 5.3. As a matter of fact, this selection has been tuned to reach such level of purity. Contrarily to the peak shape, the form of background is *a priori* lesser known. For that reason, it is essential to control the level of background, and most particularly its profile, such that it can be modeled by one of the expected functional form. (3) (+)

For the background, different functional forms are considered :

- **Constant**: one may suspect the combinatorial background to be *a priori* unstructured. In such case, it should follow a~~n~~ uniform distribution, and thus can be approximated by a constant function. (4)
- **Linear**: The previous description can be refined by considering that the number of tracks decreases with momentum. Consequently, the misassociation of low momentum tracks should dominate the combinatorial background at the low invariant mass values, whereas the high values originate from tracks with higher momentum. Hence, the background reduces with the invariant mass value. This decrease may be parametrised, at first order, by a linear function.

8

- **Exponential**: Alternatively, the background can also be decreased by an exponential function.

- **Second order polynomial**: In case the background turns out not to be purely combinatorial, but has a physics origin like, for instance particles produced from the interaction with the detector material. In such scenario, the background may have a specific structure, that needs to be described by more parameters than in the above functions. To that end, a second order polynomial is also considered for modeling the background.

Since the exploited simulations contain only pure samples of strange hadrons, the study of the most appropriate background shapes for each of the considered particles has to be performed on the data[18]. To obtain an invariant mass distribution consisting only of background candidates, the peak is removed by cutting out all the entries falling in an invariant mass region of $m_{\mathrm{PDG}} \pm 10$ MeV/c^2. The obtained invariant mass spectra is then fitted with each of the above functional forms, in order to identify those describing accurately the background.

For $\mathrm{K^0_S}$, Λ, Ξ and Ω, the best parametrisations of the background turn out to be a linear and an exponential functions. Thereby, only these forms will be considered in the following.

2 ok, noted

3 trop tôt dans la logiq de section pour parler MC (Fig 5.4 = data !R)

III-C.iv Correction on the extracted mass

"(See Tab 5.1)", p. 100 4

Although the functions in Sec. 5|III-C.ii describe well the invariant mass peak, the extracted mass does not agree with ~~the injected mass~~ the PDG mass as shown in Figs. 5.4. This seemingly bias may stem from several elements. It can be due to the way data are processed, that might overestimate the reconstructed mass in a systematic manner. The analysis, and particularly the employed selections, may introduce a distortion in the invariant mass distribution, resulting in a different mass than the expected one. The fit procedure could also be the origin of such inconsistency; for instance, one of the tails may pre-dominate the procedure and drive the parameters in a certain direction.

6 "which is always set to the corresponding PDG mass in our sim."

Anyhow, in order to correct for any bias due to the data processing, the analysis or the fit procedure, an offset 5 stated is applied on the extracted mass in simulated events such that it coincides with the injected value. It follows that this correction is then reported on the measured mass in real data. However, such a correction assumes a good agreement between the data and MC. To ensure that "as better as possible" 7 the simulation is re-weighted to match the 8 p_{T} spectra from the data.

8 "the (raw) pT" spectra

This re-weighting procedure starts off by extracting the raw p_{T} spectra in the data. Similarly to the estimation of the amount of raw signal in Sec. 5|III-C.i, the latter is given by subtracting the p_{T} spectrum in the side-bands region from the one in the peak region. It is then compared to the injected transverse momentum distribution of true V0/cascade candidates; the ratio of the p_{T} spectra in the data and MC provides the weighting factors.

[18] As a matter of fact, even if the exploited MC simulations would contain some background, there is no guarantee that they provide the same background as in the real data. (+) 1

[4]

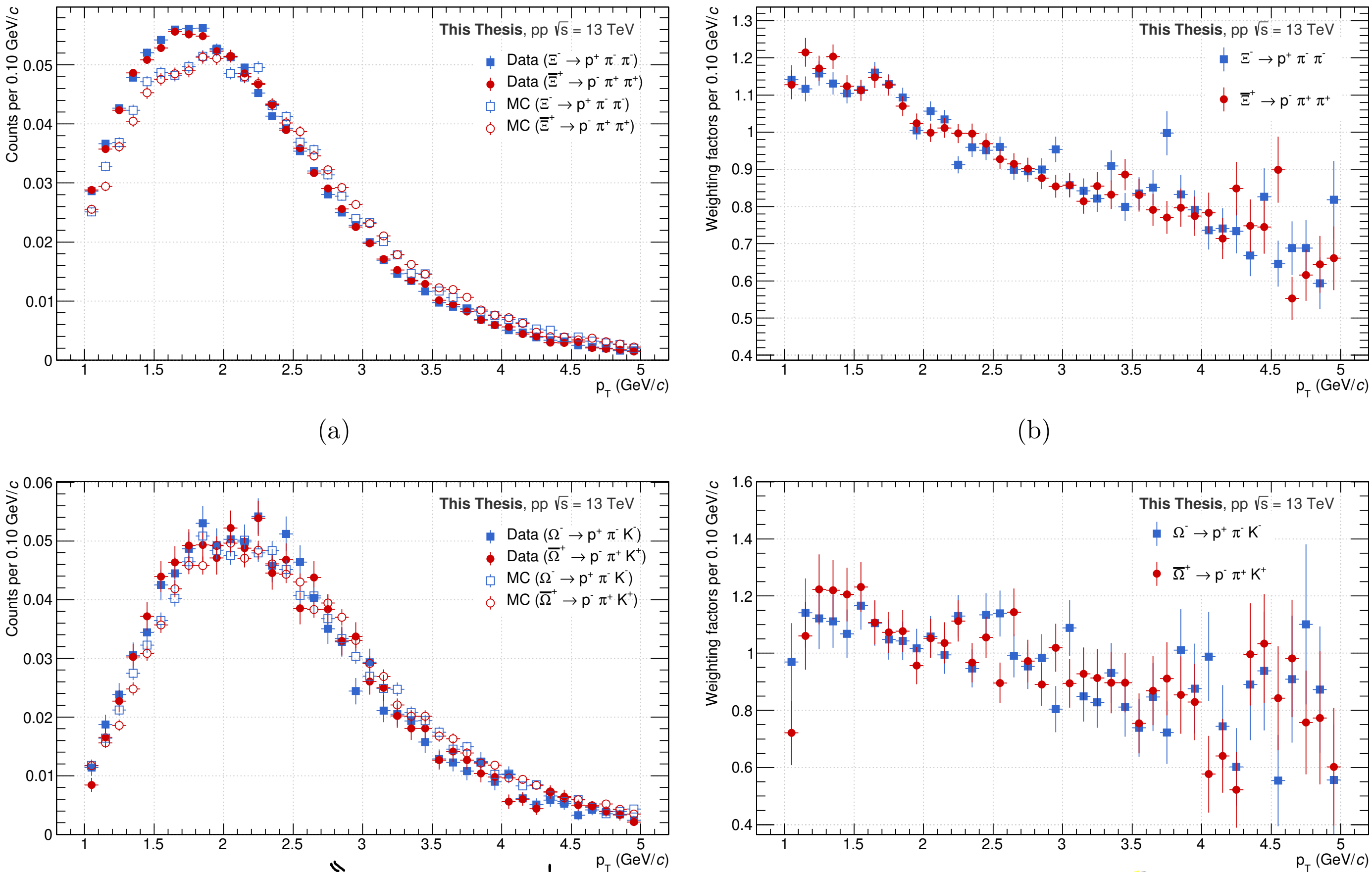

(a) (b)

(c) "raw pT spectra" (d)

1 à mettre à jour ds caption ou bien "mod. G + 1st order"?

Fig. 5.5: Invariant mass distribution of Ξ^- (a), $\overline{\Xi}^+$ (b), Ω^- (c) and $\overline{\Omega}^+$ (d) hyperons in pp collisions at $\sqrt{s}$ = 13 TeV. Here, the peak is modeled by a modified Gaussian, and the background by a first order polynomial. Each distribution comes with an additional panel representing consistency between the data and ~~the fit model~~ the MC 2, in the form of a ratio. The error bars encompasses the uncertainties on both quantities.

ratio "data/MC" 3

↓ for note: "why not triple Gauss? for sake of computing time, ∃ a certain legitimacy to resort to mod Gauss See Sect. IV-D. "mass extract""

Once the simulated data have been re-weighted, the mass offset observed in MC with respect to the injected mass is assessed, corrected and taken into account in the mass measurement in real data. The Tab. 5.5 presents these corrections as well as the corrected mass values. From these derive the (relative) mass difference between particle and anti-particle, given by

4 je suis perdu(e) on est resté dans le MC ici au final?

$$\frac{\Delta\mu}{\mu} = 2 \cdot \frac{\mu_{\text{PART.}} - \mu_{\overline{\text{PART.}}}}{\mu_{\text{PART.}} + \mu_{\overline{\text{PART.}}}}. \tag{5.7}$$

ou

(b) corrected mass values = "chiffres de la Fig 5.4, actualisés" = R data

je crois (b) non?

Its (statistical) uncertainty is obtained via propagation of the ones on the mass values, assuming there is no correlation between the particle and anti-particle measurements – *a priori* correct, since $\mu_{\text{PART.}}$ and $\mu_{\overline{\text{PART.}}}$ have been extracted indepen-

(a) ou (b), il faut le clarifier.

→ Peut-on utiliser des mots en + comme "initial offset in MC", "post pT-reweighting offset in MC, in data"?

(2) Caption préciser si offset = (reco - PDG) ou (PDG - reco) 6

(1) Quelle unité de masse ? préciser MeV/c^2 (1 ligne avec que ça "(all in MeV/c^2)")

Particle	Ξ^-	$\overline{\Xi}^+$	Ω^-	$\overline{\Omega}^+$
(1) Offset in data	0.004 ± 0.004	0.055 ± 0.004	0.090 ± 0.014	0.066 ± 0.014
Offset in MC	-0.127 ± 0.003	-0.125 ± 0.003	-0.023 ± 0.004	-0.005 ± 0.004
Corrected mass	1321.841 ± 0.005	1321.890 ± 0.005	1672.517 ± 0.015	1672.511 ± 0.015

Table 5.5: Measurements of the mass offset (2) with respect to the PDG value (coinciding with the injected mass in MC) in the data and MC, as well as the final masses of Ξ^-, $\overline{\Xi}^+$, Ω^-, $\overline{\Omega}^+$ after correction of that offset in MC. The uncertainties on the mass values correspond only to the statistical one. These measurements have been obtained using the selections in Tab. 5.3, a modified Gaussian for the peak modelisation and a linear function for the background (in the data only).

(3) pour la lisibilité = ajouter une ligne avec les m_{PDG} + voir p. suiv.

Particle	Ξ	Ω
Mass difference offset in data ($\times 10^{-5}$)	0.004 ± 0.004	0.004 ± 0.004
Mass difference offset in MC ($\times 10^{-5}$)	0.004 ± 0.004	0.004 ± 0.004
Corrected mass difference ($\times 10^{-5}$)	0.004 ± 0.004	0.004 ± 0.004

Table 5.6: Measurements of the mass difference in the data and MC, as well as the final mass difference for $\Xi^\pm$ and $\Omega^\pm$ using the corrected mass values in Tab. 5.5. The uncertainties on the mass differences correspond only to the statistical one. These measurements have been obtained using the selections in Tab. 5.3, a modified Gaussian for the peak modelisation and a linear function for the background (in the data only).

dently[19]–,

$$\sigma_{\Delta\mu/\mu} = 4 \cdot \sqrt{\left(\frac{-\mu_{\overline{\text{PART.}}}}{(\mu_{\text{PART.}} + \mu_{\overline{\text{PART.}}})^2}\right)^2 \sigma^2_{\mu_{\text{PART.}}} + \left(\frac{\mu_{\text{PART.}}}{(\mu_{\text{PART.}} + \mu_{\overline{\text{PART.}}})^2}\right)^2 \sigma^2_{\mu_{\overline{\text{PART.}}}}}. \quad (5.8)$$

The Tab. 5.6 shows mass difference for Ξ and Ω, in the data and MC, as well as the corrected value.

IV Study of the systematic effects

(4) effects

A study of the systematic effets – also called *systematic study* in the particle physicist's jargon – consists in reviewing an analysis via the test of its different elements. As its name suggests, it involves identifying the source of systematic uncertainties that might affect the values of the extracted mass and their corresponding uncertainties. Usually, this is achieved by repeating the analysis with a few "minor" changes, hoping that no effect will be observed. In such case, meaning that the obtained values are consistent, then one could argue that the analysis is free of systematic effect and under control: no additional measure are requested. On the contrary, a (5) ~~large~~ deviation in the values indicates the presence of a systematic effect, that should be treated seriously.

(+) (6)

[19]The facts that i) the particle and anti-particle do not share the same data sample (Sec. 5|III-C.i), and ii) the fitting procedure is run separately guarantee the independence of the mass measurements.

(4) ok.

"significant" (me semble plus scientifique, tout en véhiculant le m̂ sens)

③

Si j'essaie de faire du reverse engineering pour comprendre la logique.

(le jury sera tenté de le faire, il faut lui faciliter la tâche)

$$\boxed{m_{PDG}(\Xi^-) = 1321,71 \ \mathrm{MeV}/c^2}$$

Ξ^+ $\quad 1321,71 - (-0,125) + 0,055 = 1321,890 \ \mathrm{MeV}/c^2$

= le ch. de la dern. ligne ! ✓

Ξ^- $\quad 1321,71 - (-0,127) + 0,004 = 1321,841$

$$\boxed{m_{PDG}(\Omega^-) = 1672,45 \ \mathrm{MeV}/c^2}$$

En appliquant la m̂ logique, je n'arrive pas à retomber sur mes pieds pour les Ω^- et les Ω^+

3 footnote: " the formula given here corresponds in fact to the case where the 2 measurements are done of a set and a subset of same dataset, which is typically the case here, unless specified otherwise."

2 practice

In pratice, one needs to define what "small" and "large" deviations mean. If an analysis is performed in two different ways: the first approach gives the result a_1 with an uncertainty σ_1 ; the second a_2 with an uncertainty σ_2. The difference between the results is given by $\Delta = a_1 - a_2$ and the error on the difference by $\sigma_\Delta = \sqrt{|\sigma_1^2 - \sigma_2^2|}$. 3 If the ratio Δ/σ_Δ is greater than a certain threshold value – denoted σ_{Barlow} and to be defined by the analyser –, this points out a systematic effect that requires further investigation. This approach is known as the *Barlow criterion*. 4 espace

5 here ... (+)

As in cooking, what separates the good systematic study from the lesser good one is the choice of the seasoning, namely the choice of the threshold value. The larger the σ_{Barlow}, the more systematic effects would slip under the radar; conversely, the smaller the threshold, the higher the sensitivity to the systematic effects. Since the targeted precision on the mass and mass difference values is very low, the systematic effects must be well under control. Therefore, in the context of this analysis, the contribution of a potential source of systematics is said to be significant for $\sigma_{Barlow} \simeq 1$.

6 "ultimately"

However, the presence of a systematic effect does not necessarily imply a systematic uncertainty. In fact, there are two possibilites. Either a systematic correction can be applied and the error on that correction will be quoted as the systematic uncertainty, or the correction may be difficult (or impossible) to derive and therefore the systematic uncertainty will have to fully encompass the imprecision induced to the systematic effect.

This treatement of the systematic biases corresponds to the one proposed by Roger Barlow [?][?]. The following section presents the list of systematic sources studied for this analysis, with their estimated uncertainties or corrections.

IV-A Topological and track selections

IV-A.i Influence on the mass extraction

As explained in Sec. 4|II-B, the identification of the charged Ξ and Ω baryons relies on their characteristic cascade decay. The reconstruction of these decay topology revolves around, first, the association of two tracks to form Λ candidates, and then these are matched with the remaining secondary tracks. In order to reduce the induced combinatorial background, various topological and kinematic cuts are being used. The choice of the employed cut values may obviously be the source of a bias. Such a systematic effect can be revealed by observing how a different set of selections affects the mass and its uncertainty. (+) 7

The standard approach consists in varying individually each selection, while keeping the others at their reference value. Although it allows to address the bias induced by a given cut, this does not take into account the possible correlation between topological variables. For instance, a higher cut on cascade decay radius also implies that the Λ daughter decays further away in the detector. To tackle that, one needs to build a matrix containing the correlation factors for each pair of selection variables. (+) 8

" We typically deal here for cascades with 13+4 selections, asking for the determination of a symmetric matrix of 17×17 size..." 10

"would need" 9

7

Track variable	Variation range	Signal variation Ξ^- ($\overline{\Xi}^+$)
Nbr of crossed TPC readout rows	> [70;90]	1% (1%)
n_σ^{TPC}	< [1;3]	60% (60%)
Topological variable	Variation range	Signal variation Ξ^- ($\overline{\Xi}^+$)
V0		
V0 decay radius (cm)	> [1.2;8]	11% (11%)
V0 cosine of pointing angle	> [0.97;0.998]	10% (10%)
$\lvert m(V0)$ - $m_{\mathrm{PDG}}\Lambda \rvert$ (GeV/c^2)	< [0.002;0.007]	18% (18%)
DCA proton to prim. vtx (cm)	> [0.04;0.5]	28% (28%)
DCA pion to prim. vtx (cm)	> [0.04;0.95]	10% (10%)
DCA V0 to prim. vtx (cm)	> [0.06;0.2]	12% (12%)
DCA between V0 daughters (std dev)	< [0.4;1.2]	12% (12%)
Cascade		
Cascade decay radius (cm)	> [0.5;2.5]	11% (11%)
Cascade Lifetime (cm)	< [1.6;3.40] $c.\tau$	40% (40%)
DCA bachelor to prim. vtx (cm)	> [0.04;0.5]	15% (15%)
DCA between the cascade daughters (std dev)	< [0.25;1.2]	12% (12%)
Cascade cosine of pointing angle	> [0.995;0.9995]	14% (14%)
Bachelor-proton pointing angle (rad)	> [0.02;0.05]	11% (11%)

Table 5.7: Summary of the variation ranges on the topological and track selections employed in the Ξ^- and $\overline{\Xi}^+$ reconstruction. The last column indicates the *maximum* induced signal variation; for more details, look at Fig. A.1 and Fig. A.2.

2 footnote (voir p. suiv.)

However, a different approach is followed here. To go over the correlations be- ④ → ③ ~~at~~ tween each variable, the sets of selections are randomly generated according to a ~~x~~ uniform law that spans over a certain variation range. The critical point of this study resides ~~in the~~ choice of the variation range, where a careful balance must be found: it should not be too "severe" at the risk of losing all the signal, or too "gentle" to cause any significant shift. It is considered as satisfactory when the induced signal shift reaches approximately at least 10%[20]. The Tabs. 5.7 and 5.8, list the considered selection variables, with their variation range as well as the induced signal variation for Ξ and Ω respectively. As for the K^0_S and Λ, this is summarised in Tabs. A.1 and A.2.

plural plural

4 Préciser que ces "variations = obtenues by varying each selection indiv, all other sel° being equal"

6 Addit° voir p. suiv.

The analysis is repeated for each randomly generated set of cuts i, as detailed in Sec. 5|III-C, meaning that a mass μ_i and its uncertainty σ_i are extracted from the fit of the corresponding invariant mass distribution in the data and MC. However, only the values passing the following criteria are retained:

- the fitting procedure must have converged;

⑦ "close"

- to ensure a good fit quality, its reduced χ^2 needs to be relatively to the unity,

[20] Note that this condition is applied for each topological cuts. For other selections, it may be difficult to satisfy such criterion as they act on the background rather than the signal. This is the case, for example, with the competing mass rejection that could never reach the 10% signal variation threshold, even with an excessively vast range of variation.

cf. page précédente

(2) Footnote : "an alternative randomisation has also been tried: along the "natural" distribution of each selection observable, rather than the uniform distribution.
In the end, both approaches yield to consistent syst. uncertainties. ($\mathcal{O}$[few keV/c^2]).
The extra complexity and the CPU cost of the alternative way have weighed in; given the fact that the randomisations here are part and parcel of the default analysis flow (see later), and will be resorted to many many times,
the uniform randomisation has been retained as default for all what is coming next."

(5) Addition
" Understand that a set of cuts (i) will be built after \emph{each} selection cut is randomised within the defined ranges.
One set of 15 selections will be based on 15 dedicated random numbers, 1 per selection dimension."

5

Candidate variable	Range	Signal variation Ω^- ($\overline{\Omega}^+$)
Competing mass rejection (GeV/c^2)	> [0.006;0.010]	0.9% (0.9%)
Track variable	Range	Signal variation Ω^- ($\overline{\Omega}^+$)
Nbr of crossed TPC readout rows	> [70;90]	2.5% (2.5%)
n_σ^{TPC}	< [1;3]	60% (60%)
Topological variable	Range	Signal variation Ω^- ($\overline{\Omega}^+$)
V0		
V0 decay radius (cm)	> [1;5.5]	11% (11%)
V0 cosine of pointing angle	> [0.97;0.998]	17% (17%)
$\|m(V0)$ - $m_{\mathrm{PDG}}\Lambda$ $\|$ (GeV/c^2)	< [0.002;0.007]	17% (17%)
DCA proton to prim. vtx (cm)	> [0.04;0.5]	34% (34%)
DCA pion to prim. vtx (cm)	> [0.04;0.75]	10% (10%)
DCA V0 to prim. vtx (cm)	> [0.06;0.2]	14% (14%)
DCA between V0 daughters (std dev)	< [0.4;1.2]	11% (11%)
Cascade		
Cascade decay radius (cm)	> [0.5;1.6]	12% (12%)
Cascade Lifetime (cm)	< [1.6;3.40] $c.\tau$	14% (14%)
DCA bachelor to prim. vtx (cm)	> [0.05;0.2]	13% (13%)
DCA between the cascade daughters (std dev)	< [0.15;1.2]	12% (12%)
Cascade cosine of pointing angle	> [0.995;0.9995]	17% (17%)
Bachelor-proton pointing angle	> [0.02;0.05]	13% (13%)

Table 5.8: Summary of the variation ranges on the topological and track selections employed in the Ω^- and $\overline{\Omega}^+$ reconstruction. The last column indicates the *maximum* induced signal variation; for more details, look at Fig. A.3 and Fig. A.4.

$\chi^2/NDF < 3$;

- the uncertainties on the mass value are expected to be below the MeV/c^2. Since the Ξ and Ω masses are of the order of GeV/c^2, a σ_{μ_i} at the level of 0.1% of μ_i represents an uncertainty greater than 1 MeV/c^2. In order to remove outliers, it is required that $\sigma_{\mu_i}/\mu_i < 0.1\%$. 1 (+)

Under these conditions and over a sufficiently large number of sets of cuts, the ~~2~~ distributions μ_i and σ_{μ_i} can be built. These offer the opportunity to re-qualify the mass and its uncertainties: "i.e. what will become default strategy for this analysis outcome"

- the *measured mass* 3 corresponds to the mean value of the μ_i distribution,

- the *systematic uncertainty* due to the candidate selections is the standard deviation of the μ_i distribution, σ_{μ_i}/μ_i distribution

- and the *statistical uncertainty* is given by the mean value of the σ_{μ_i} distribution.

5 the "relative stat. uncertainty" 4

5 + parler du ratio $\left\langle \frac{\sigma_{\mu_i}}{\mu_i} \right\rangle \neq \frac{\langle \sigma_{\mu_i} \rangle}{\langle \mu_i \rangle}$

4

As opposed to most analyses, this re-definition allows to overcome the dependence on a reference set of cuts, making the analysis *in principle* more robust.

The above quantities being extracted from a finite sample, one could expect them to depend on the number of cut sets, N. The stability of the results with the amount of sets employed has been studied and is shown on Fig. 5.6. At first, the mass value, its statistical and systematic uncertainties fluctuate with the N, until they reach a plateau region ~~at~~ after approximately 5000-6000 different sets of cuts. Such amount should thus suffice to perform the mass measurement. However, in order to a guarantee an excellent stability, 20 000 sets are being used.

(1) ? "nb of cut sets"

(2)

The output results of this procedure are presented in the table 5.9.

(3) "It should be seen as an intermediate important outcome but not yet containing the whole story."

Particle	Measured mass (MeV/c^2)	Uncertainty stat. (MeV/c^2)	Uncertainty syst. (MeV/c^2)	Measured mass difference ($\times 10^{-5}$)	Uncertainty stat. ($\times 10^{-5}$)	Uncertainty syst. ($\times 10^{-5}$)
K^0_S	497.737	0.003	0.010	/	/	/
Λ	1115.618	0.002	0.011	4.78	0.17	0.14
$\overline{\Lambda}$	1115.671	0.002	0.012			
Ξ^-	1321.728	0.004	0.016	3.95	0.37	0.39
$\overline{\Xi}^+$	1321.780	0.004	0.019			
Ω^-	1672.536	0.014	0.015	-1.31	1.14	0.76
$\overline{\Omega}^+$	1672.514	0.014	0.015			

Table 5.9: Measured masses and mass differences of K^0_S, Λ, Ξ and Ω, accompanied by their statistical and systematic (due to the topological and kinematic selections) uncertainties. Here, these measurements have been performed with a triple Gaussian for the signal and a first order polynomial for the background.

IV-A.ii Influence on the mass difference mass

In the Tab. 5.9, the mass difference have been obtained taking the independently measured mass values of the particle and the anti-particle from the above procedure (Sec. 5|IV-A.i), and using Eq. 5.7. The uncertainties are then propagated to obtain the statistical and systematic uncertainties on the mass difference. It does not result directly from the aforementioned procedure. In that sense, the mass difference measurement is *indirect*. It carries the full systematic uncertainties from the particle and anti-particle mass values. By extracting the mass difference in a more *direct* way – similarly to what is done for the mass in Sec. 5|IV-A.i –, part of the uncertainties from the particle and anti-particle masses would cancel out in the difference, resulting in a smaller systematic uncertainty.

(4) (+)

To that end, an additional step needs to be introduced in the previous strategy

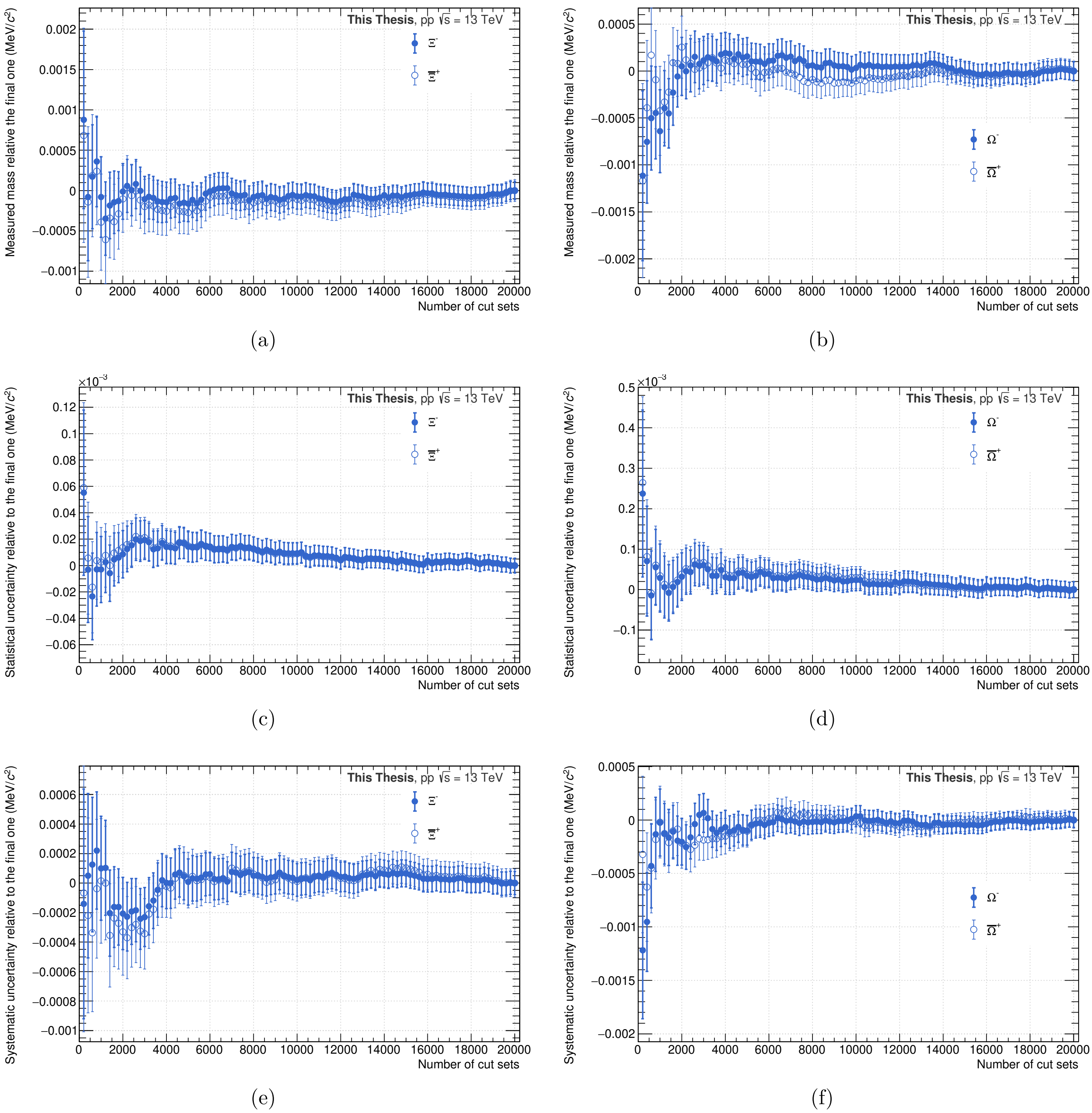

Fig. 5.6: Relative measured mass as well as its statistical and systematic uncertainties in pp collisions at $\sqrt{s}$ = 13 TeV as a function of the number of cut sets, for Ξ in (a), (c), (e) and Ω in (b), (d), (f) respectively. The quantities on the y-axis are relative to the value taken as the final measurement. In this case, it corresponds to the quantity for 20 000 different sets of cuts. Here, the peak is modeled by a modified Gaussian, and the background by a first order polynomial. The error bars represents the uncertainty on the evaluation of the mean or standard deviation.

5

Particle	Mass difference ($\times 10^{-5}$)	Uncertainty statistical ($\times 10^{-5}$)	Uncertainty systematic ($\times 10^{-5}$)
Λ			
Indirect	**4.54**	0.75	1.50
Direct	**4.68**	0.77	0.79
Ξ			
Indirect	**4.54**	0.75	1.50
Direct	**4.68**	0.77	0.79
Ω			
Indirect	**0.48**	1.74	1.57
Direct	**0.53**	1.75	1.19

Table 5.10: Comparison between *direct* and *indirect* mass difference values of Ξ and Ω baryons, with their respective uncertainties (statistical and systematical). The total uncertainty is obtained by summing quadratically the statistical and systematical uncertainties. Here, both direct and indirect measurements have been performed with a modified Gaussian for the peak and a first order polynomial for the side-bands.

in Sec. 5|IV-A.i. For each set of cuts i, both particle and anti-particle masses – $\mu_{i,\text{PART.}}$ and $\mu_{i,\overline{\text{PART.}}}$ – are extracted as well as their uncertainties, $\sigma_{i,\text{PART.}}$ and $\sigma_{i,\overline{\text{PART.}}}$. From these, the computation of the mass difference is performed,

$$\frac{\Delta\mu_i}{\mu_i} = 2 \cdot \frac{\mu_{i,\text{PART.}} - \mu_{i,\overline{\text{PART.}}}}{\mu_{i,\text{PART.}} + \mu_{i,\overline{\text{PART.}}}}, \tag{5.9}$$

and the uncertainties are propagated in order to get the one on the mass difference,

$$\sigma_{\Delta\mu_i/\mu_i} = 4 \cdot \sqrt{\left(\frac{-\mu_{i,\overline{\text{PART.}}}}{\left(\mu_{i,\text{PART.}} + \mu_{i,\overline{\text{PART.}}}\right)^2}\right)^2 \sigma^2_{\mu_{i,\text{PART.}}} + \left(\frac{\mu_{i,\text{PART.}}}{\left(\mu_{i,\text{PART.}} + \mu_{i,\overline{\text{PART.}}}\right)^2}\right)^2 \sigma^2_{\mu_{i,\overline{\text{PART.}}}}}. \tag{5.10}$$

Similarly to the mass extraction, the mass difference and its uncertainties are calculated from the $\Delta\mu_i/\mu_i$ and $\sigma_{\Delta\mu_i/\mu_i}$ distributions over N different set of cuts:

- the *measured mass difference* corresponds to the mean value of the $\Delta\mu_i/\mu_i$ distribution,
- the *systematic uncertainty* due to the candidate selections is the standard deviation of the $\Delta\mu_i/\mu_i$ distribution, va avec (2)
- (2) "relative" (3) and the *statistical uncertainty* is given by the mean value of the $\sigma_{\Delta\mu_i/\mu_i}$ distribution. $\frac{\sigma_{\Delta\mu_i/\mu_i}}{\Delta\mu_i/\mu_i}$

The results on the directly extracted mass difference are presented in Tab. 5.10. Although the values obtained directly are consistent with the indirect ones, the associated systematic uncertainties are smaller by approximately 48% for Ξ and 25% for Ω. Due to this gain in precision, from now on, the mass difference will always be extracted "directly". + (5) clair.

(4)

IV-B Stability of the results

TB intro 1 +

All the elements of the analysis being now introduced, it is essential to control the stability of the results. In other words, it consists to adapt and calibrate the analysis, in order to ensure that the presented measurements can be trusted and do not fluctuate over time, space, momentum, etc. This requires a fine and thorough inspection of what happens throughout the data acquisition and reconstruction. If needed, these shall be tuned in 2 such a way, for instance, that the momentum calibration is satisfactory; or at least, one should identify a region in time, space, momentum, etc, where the latter requirement would be fullfilled.

The measurement of the mass *a priori* relies on a countless number of parameters, some of them being possibly correlated. This analysis focuses on seven possible dependencies on the mass. For the sake of brievety, only figures related to one or two particles will be presented in this manuscript.

IV-B.i Dependence with the data taking periods

As mentioned above, an important check involves the stability of the results over time, that is as a function of the data taking periods. Sec. 5|II-A specifies that all the pp collisions recorded in the 2016, 2017 and 2018 data taking periods are considered. This corresponds to 37 periods collected in different magnetic field configurations for the L3 solenoid magnet[21] ($B = +0.5, -0.5, -0.2$ T), TPC gas composition ($Ne/CO_2/N_2$ for 2016 and 2018; Ar/CO_2 for 2017) and trigger modes ("CENT" or "FAST"). They are designated by a tag made of two numbers – corresponding to the last digits of the data taking year – and a letter, labelling for the period.

3 à changer selon mes correct° faites p.64 ch.3 ALICE TPC

Ar = 2016
Ne = 2017
Ar = 2018

The Figs. 5.7(a) and 5.7(b) show the measured mass of Ξ and Ω hyperons respectively, as a function of the data sample. A striking feature on these figures is the fact that all the values seem to be systematically off by about 250 keV/c^2 for the double strange baryons and 150 keV/c^2 for the triple strange particles. This originates from a momentum miscalibration occuring in the V0 and cascade reconstruction, which is addressed later in Sec. 5|IV-B.ii. Once it is corrected, the mass measurements lie within the PDG uncertainties.

4 + bon commentaire

[21] For almost all the periods, the L3 solenoid and the dipole magnets share the magnetic field polarity, that is (+,+) or (−,−). Each rule has its exception: one data taking periods in 2018 has been collected with the dipole magnet off.

6

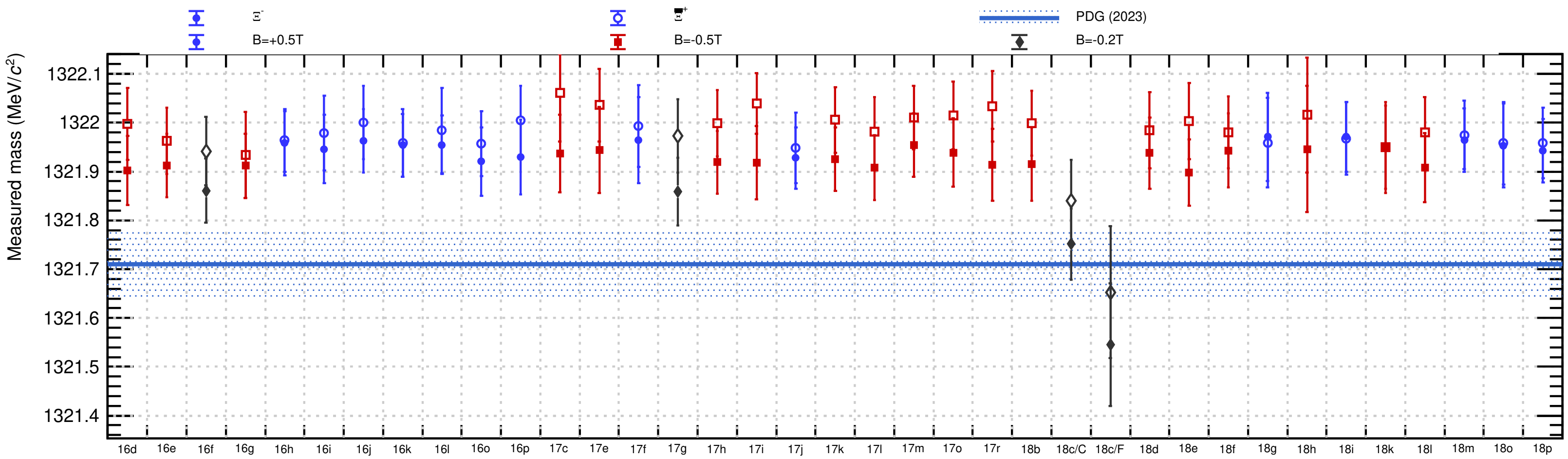

(a)

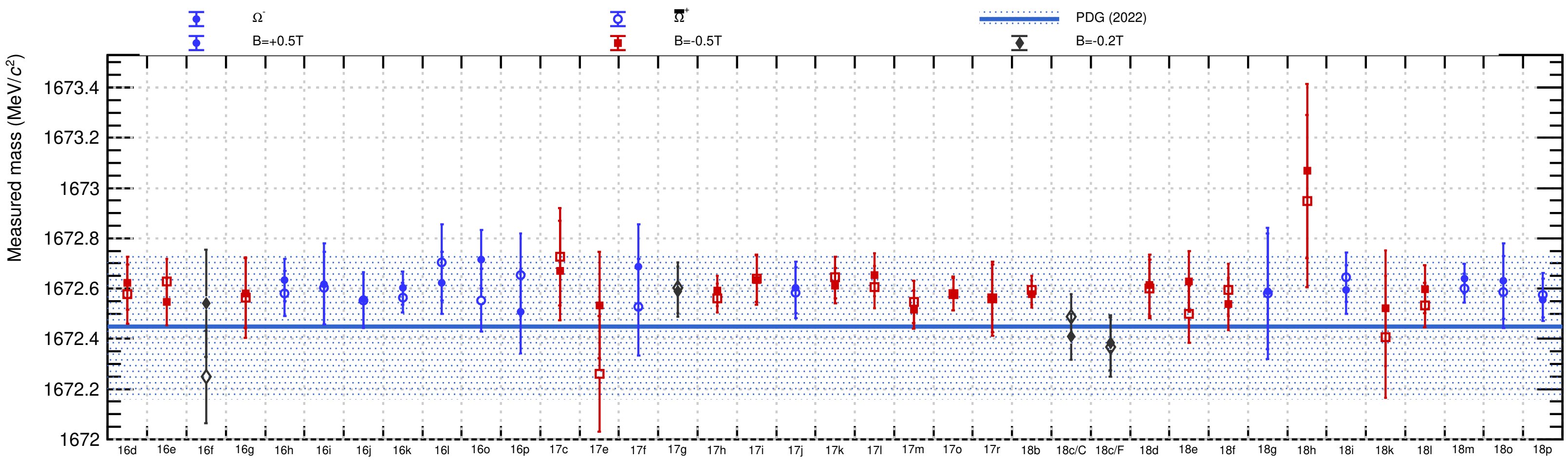

(b)

Fig. 5.7: Measured mass of the Ξ^- and $\overline{\Xi}^+$ (top), and Ω^- and $\overline{\Omega}^+$ baryons (bottom) as a function of the data taking period. These values have been obtained based on 20 000 different sets of selections (Sec. 5|IV-A). Hence, the uncertainties correspond to the quadratic sum of the statistical and systematic uncertainties due to the candidate and track selections. The periods with a magnetic field of $B = +0.5$ T are indicated with blue circles, those with the opposite polarity are shown in red squares, and finally the data sample collected in a configuration of $B = -0.2$ T are represented in black diamonds. Moreover, the "/C" and "/F" tags are here to signify "CENT" and "FAST" trigger modes respectively.

6

The mass measurements in periods collected with $B = -0.2$ T stand out from the rest of the values. This behaviour is attributed to the lower magnetic field, which results in a deterioration of the momentum resolution. The "FAST" configuration – *i.e.* events collected without the two middle layers of the ITS, the SDDs – exhibits a similar pattern. The latter is most certainly due to the missing SDD informations; without these constraints, the probability to incorrectly assigned a cluster to a track increases. As a consequence, the track quality in the ITS, as well as the tracking efficiency, drop but also the track momentum gets biased. This point has been cross-checked by repeating the analysis in pp collisions at $\sqrt{s}$ = 5.02 TeV with $B = \pm 0.5$ T, in "CENT" and "FAST" modes. In the former configuration, the results agreed with those obtained at 13 TeV (for the same magnetic field polarity) whereas, in the latter case, the previous trend was again observed, pointing indeed towards a problem related to the missing SDD informations. Therefore, the data sample taken in a magnetic field of $B = -0.2$ T and/or collected with the "FAST" trigger mode are discarded for the rest of the analysis.

1) espace

2) donner pour info le nb total d'évts $\sqrt{B}$ pr se rendre compte précis° stat pp 5.02 TeV ≈ pp 13 TeV

Finally, concerning the periods with opposite polarities, the results shows a very good agreement. A fit with a constant function (not shown on the figure) displays a χ^2 probability greater than 90%.

3) "A common fit over values mixing the different polarities or separated fits on values per polarity gives compatible results within uncert." displays....

IV-B.ii Dependence with the decay radius

A critical aspect of the analysis is to make sure to have a satisfactory calibration of the momentum. A miscalibration of the latter typically originates either from an imprecision on the magnetic field or imperfect energy loss corrections. The former being addressed in Sec. 5|IV-C.i, this section thus concentrates on the second point.

Miscalculation of the energy losses can arise at two different levels: on one hand, the actual amount of material budget may not be properly accounted for in the detector geometry. In other words, there could be a significant misknowledge on the amount of material budget in the detector. Sec. 5|IV-C.ii is devoted to this aspect. On the other hand, the calculation of the energy loss corrections could be erroneous. A hint of the latter can be found by looking at the dependence of the measured mass on the decay radius, Fig. 5.8.

First of all, the measured mass exhibits an unexpected behaviour with the decay radius: it abruptly drops whenever the particle of interest decays in the vicinity of an ITS layer. Furthermore, this trend is well reproduced in simulated data. The Fig. 5.9 shows the resolution on the cascade decay radius as a function of the radial position. Slighlty above the edge of an ITS detector, this resolution ~~decreases~~ abruptly in such a way that the Ξ and Ω candidates tend to be reconstructed below the detection layer. This underestimation of decay radius leads to a bias in the energy loss corrections and the opening angle (detailed later in Sec. 5|IV-B.iv), thus lowering the measured mass. For that reason, the regions in the ITS corresponding to these dips will be discarded from now on.

4) "degrades"

5) Footnote : rappeler que les coupures à $+1\sigma_R$, $+3\sigma_R$ sont pourtant déjà dedans

Furthermore, whatever the particle of interest, the measured mass in Fig. 5.8 increases significantly with the decay radius, in both data and MC. It turns out that

6) (donner un exemple quantifié "$\Xi^- \to \pm$ 500 keV/c^2")

/ voir sect° III-B.i + donner p. 108

1

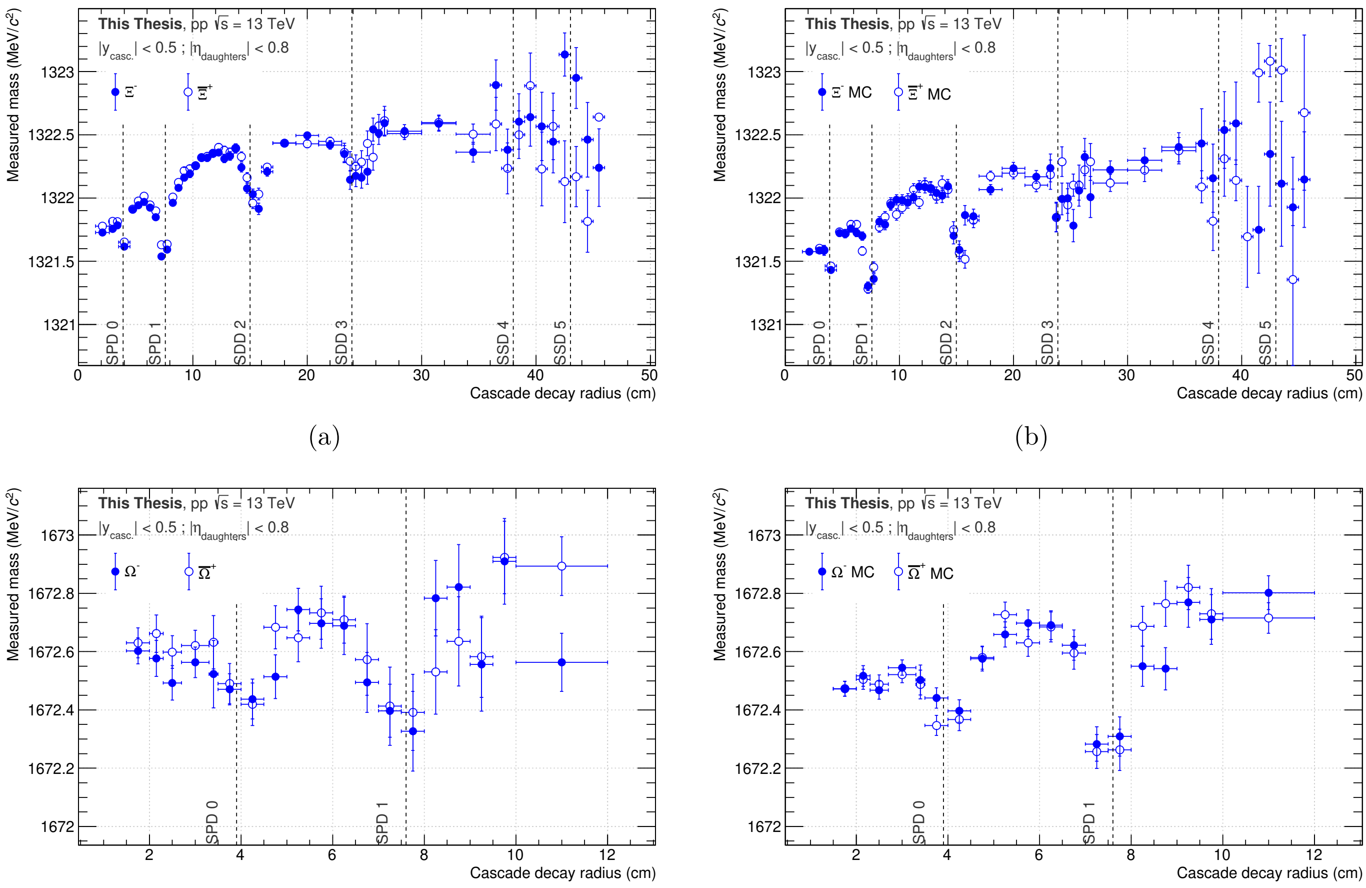

(a) (b)

(c) (d)

Fig. 5.8: Measured mass of the Ξ (top) and Ω baryons (bottom), in the data (left) and in MC (right), as a function of the cascade decay radius. The average radial position for each ITS layer is indicated in dotted line. Note that, for the purpose of the comparison, the MC is *not* re-weighted (Sec. 5|III-C.iv). In both cases, the results have been obtained through a fit with a triple Gaussian function for the invariant mass peak and, only in the data, an exponential function for the background.

this trend results from several approximations in the implementation of the energy loss corrections in the ALICE framework. There are three, classified from the most to the "least" significant. 1 +

1. As explained in Sec. 3|II-D.ii, in the final stage of the tracking, all tracks are propagated inwards to their DCA to the primary vertex, taking into account stochastic processes such as energy losses. While this makes sense for primary tracks, it introduces a bias for secondary ones. Being a decay product, the inward propagation of a secondary track should stop at the decay point, where its parameters are related to the mother particle. Instead, at each propagation step between the secondary and primary vertices, the track receives additional energy from dE/dx-corrections (footnote 27). This excess of energy builds up with the decay point position, biasing further the track parameters the further away the secondary vertex is. Nevertheless, at this stage of the event recon-

[4]

④ TB description de la simulat° + pb.

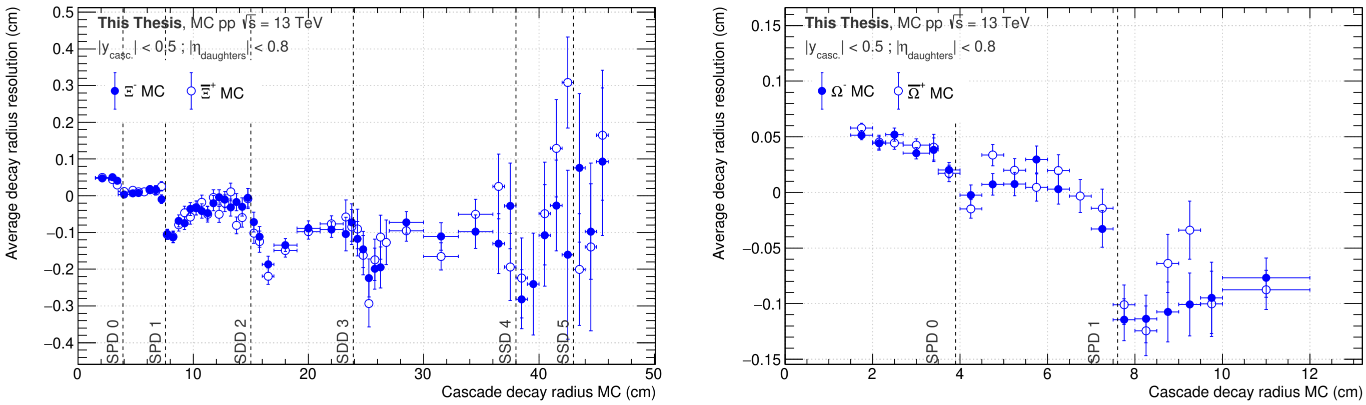

(a) (b)

Fig. 5.9: Resolution on the radial position of the Ξ (top) and Ω (bottom) decay point in MC, as a function of the cascade decay radius. The average radial position for each ITS layer is indicated in dotted line. Here, the MC data have not been *not* re-weighted. In both cases, the results have been obtained through a fit with a triple Gaussian function for the invariant mass peak and an exponential function for the background.

① " the location of (DCA to the prim vtx)" to

struction, there is no way to distinguish a primary from a secondary particle[22]. For that reason, this bias is expected to be removed later, during the V0 and cascade reconstruction. However, as mentioned in Sec. 4|II-B.i (footnote 8), the propagation of daughter tracks from the DCA to the primary vertex to the V0/cascade decay point is performed with no energy loss corrections. This means that the energy previously added during the final inward propagation of the tracking between the secondary and primary vertices, has not been subtracted, leading to additional energy/momentum in the track parameters at the secondary decay position and thus to an offset in the invariant mass.

2. The energy loss calculation relies on the same parametrisation of the Bethe-Bloch formula (Eq. 3.2) as Geant3 and Geant4[23]. For the parameters related to material, they are using the database in [161]. However, as explained in Sec. 3|II-D.ii, the particle energy losses are calculated and corrected assuming that all the materials are made of Si in the ITS volume (including the beam pipe) and Ne in the TPC. This approximation leads inevitably to a systematic misevaluation of the actual energy losses, and thus to bias in the invariant mass.

② ah ça, je ne savais pas. Intéressant... je ne sais pas encore quoi en faire.

③

④ Ss dte secondaire.

[22] Concerning V0 decays, there is indeed no way to identify a secondary particle at this stage of the reconstruction using the so-called *offline* reconstruction, presented Chap. 4. However, there exists another approach, dubbed *on-the-fly*, that performs that track finding, track fitting and V0 vertexing simultaneously. Although it has been checked that on-the-fly V0s do not exhibit the mass dependence on the transverse momentum and radial position of the decay point, they can not be used in the analysis as there exists no on-the-fly cascades.

[23] Although Geant3 and Geant4 are two different version of Geant software series, their treatement of the energy losses of a charged particle in a medium remains the same.

2

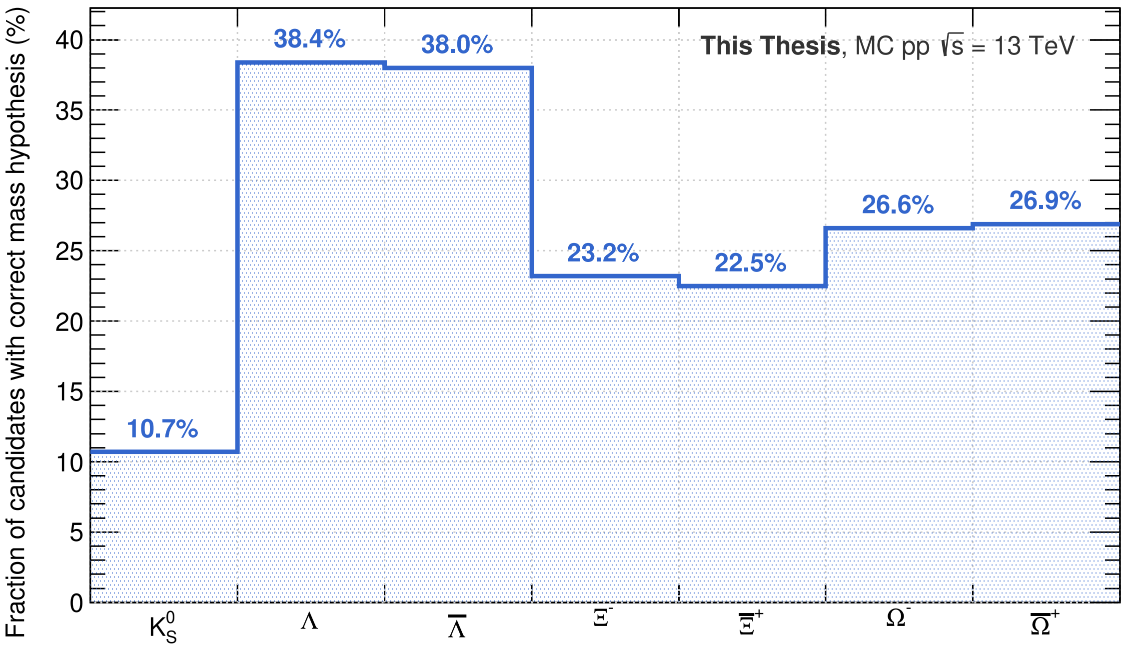

Fig. 5.10: Fraction of V0 and cascade candidates with the correct mass hypothesis for all the associated daughter tracks.

① préciser un peu plus : " during initial track propagation in the event reco "

3. Along the same line, the Bethe-Bloch formula in Eq. 3.2 also depends on the particle traversing the material and, in particular, its charge, momentum and mass. While the Kalman filter provides the first two, the last one comes from the measurement of the energy deposit in the TPC volume, which offers a preliminary particle identification. There is no guarantee, though, that the latter coincides with the expected mass hypothesis for a K^0_S, $\overset{(-)}{\Lambda}$, $\overset{(-)}{\Xi}{}^{\pm}$ or $\overset{(-)}{\Omega}{}^{\pm}$ decay. For instance, Sec. 3|II-D.ii explains that the pion mass is taken as default value. As a matter of fact, only a fraction of the candidates has the correct mass hypothesis for both decay daughters as shown in Fig. 5.10. If the mass hypothesis used in the energy loss calculation turns out to be incorrect, the wrong amount of energy loss correction are applied.

There are different ways to address these issues. The approach followed in this analysis consists in i) replaying the track propagation in order to remove the previous energy loss corrections, and ii) re-applying them with the correct mass hypothesis, appropriate material parameters and stopping at the secondary decay position. The Fig. 5.11 gives a description of this procedure, also called *retro-corrections*.

The procedure starts off with the track parameters at the V0/cascade decay point. They are extrapolated to its point of closest approach to the primary vertex, without accounting for energy losses (Fig. 5.11, 1.). This boils down to undo the track propagation in Sec. 4|II-B.i and recover the track parameters as they were before the V0/cascade reconstruction. From this point, the track is propagated to its position at the TPC inner wall, in the exactly same condition as in the final stage of the tracking (Sec. 3|II-D.ii): same mass hypothesis, same consideration on the detector material. This means that, at each step, the track looses the identical ② +

$\boxed{1}$

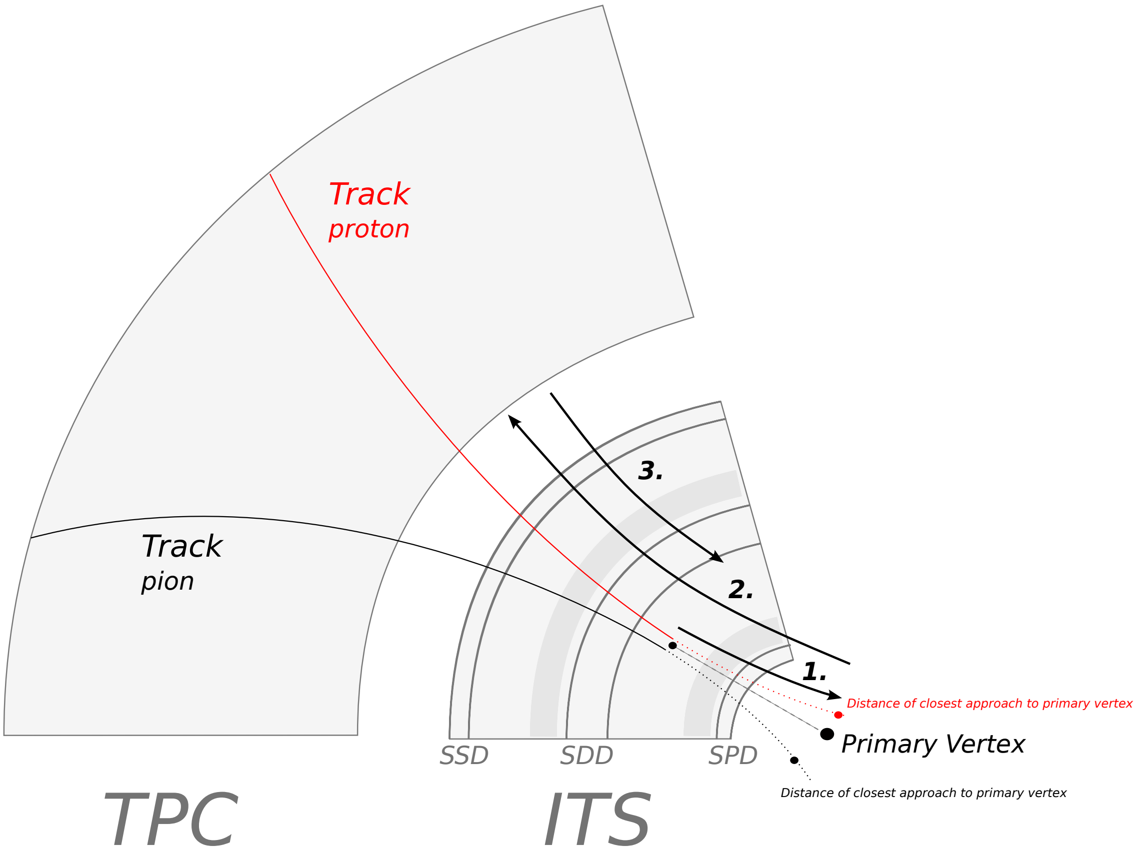

Fig. 5.11: Pictural representation of the fix on the energy loss corrections applied on the proton daughter of a $\overline{\Lambda}$. The general idea breaks off in two stages: removing the previous dE/dx-corrections below the TPC inner wall (1. and 2.), and re-applying them appropriately (3.). The first stage starts with the propagation of the track parameters, initially at the decay position, to its DCA to the primary vertex without accounting for energy loss (1.). Then, the track is propagated to the TPC inner wall (2.) as performed during the final stage of the tracking (Sec. 3|II-D.ii). In the second stage, the energy loss corrections are re-applied with the correct mass hypothesis – here, the proton mass – and stopping at the secondary vertex position (3.). Modified version of the figure from [124].

amount of energy which was previously added. At the TPC inner wall, the aforementioned energy loss corrections *in the ITS* have been fully removed (Fig. 5.11, 2.). As most of the material budget comes from the ITS, the wrong energy loss corrections in the TPC can be ignored in first approximation. This last point was later verified with a propagation up to the TPC outer wall; no significant change could have been observed. 1 +

The second stage takes over with the re-application of the energy loss corrections. From the TPC inner wall, the track parameters are propagated to the secondary vertex position with the appropriate mass hypothesis and the adequate material, in order to correct the right amount of energy losses this time (Fig. 5.11, 3.).

The Fig. 5.12 shows the application of this procedure in the data and MC. The retro-corrections significantly reduces the mass offset with the decay radius. Most importantly, in MC, the trend with the radius seem to have disappeared and now

2

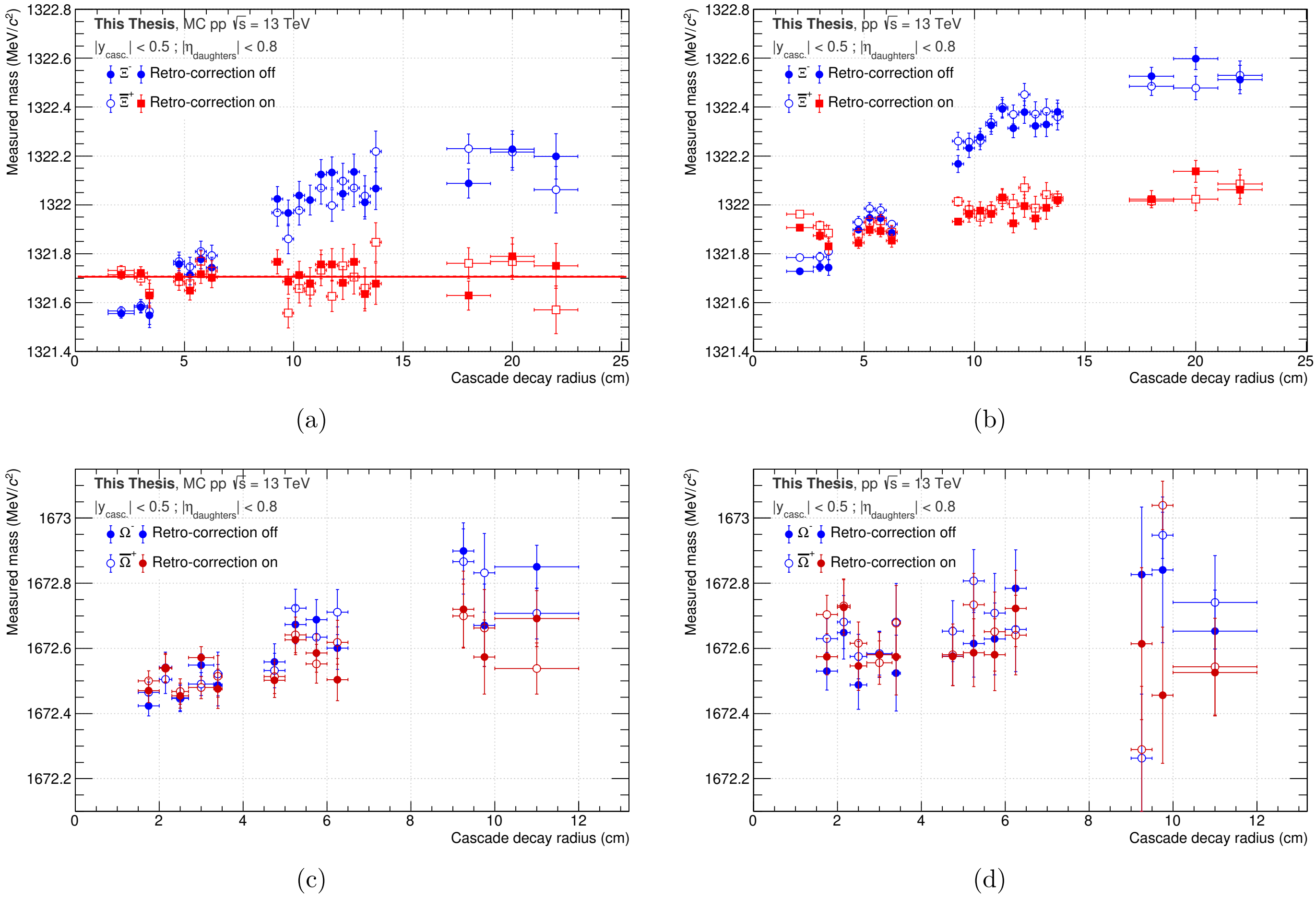

Fig. 5.12: Measured mass of the Ξ (top) and Ω baryons (bottom), in MC (left) and in the data (right), as a function of the cascade decay radius with the retro-corrections on (red) and off (blue). The regions close to ITS layers have been removed, as explained in Sec. 5|IV-B.ii. The solid and dashed lines represent a fit with a constant function. Note that, for the purpose of the comparison, the MC is *not* re-weighted (Sec. 5|III-C.iv). In both cases, the results have been obtained through a fit with a triple Gaussian function for the invariant mass peak and, only in the data, an exponential function for the background.

(À l'occas°, rajouter

1 mass PDG(Ω) = ligne horizontale sur le plot MC (bas gauche)

2 fit sur le plot Ω bas à L ?)

[1]

follows a flat distribution. To quantify it, the measurements have been fitted with a constant function; the latter agrees very well the injected mass of Ξ and displays a χ^2 probability of at least 26%. This validates that the energy losses are properly taken into account. In the data, a slight trend with radius can still be observed. This will flatten in the next sections in such way that, in the end, the residual dependence on the radius can be considered as negligible.

IV-B.iii Dependence with momentum

Although the invariant mass expression in Eq. 4.5 involves only the momentum vector of the decay daughters, it can be re-written to show the *explicit* dependency on the total momentum in Eq. 5.12,

$$\begin{aligned} M^2_{\text{candidate}}(\text{casc.}) &= \left(\sqrt{\mathbf{p}^2_{\text{V0}} + m^2_{\Lambda}} + \sqrt{\mathbf{p}^2_{\text{bach.}} + m^2_{\text{bach.}}}\right)^2 - (\mathbf{p}_{\text{V0}} + \mathbf{p}_{\text{bach.}})^2 && (5.11)\\ &= \left(\sqrt{p^2_{\text{V0}} + m^2_{\Lambda}} + \sqrt{p^2_{\text{bach.}} + m^2_{\text{bach.}}}\right)^2 - \left(p^2_{\text{V0}} + p^2_{\text{bach.}} + 2 \cdot p_{\text{V0}} \cdot p_{\text{bach.}} \cos\theta\right), && (5.12) \end{aligned}$$

and in particular, the *explicit* dependency on the transverse and longitudinal momenta in Eq. 5.13,

$$\begin{aligned} M^2_{\text{candidate}}(\text{casc.}) = &\left(\sqrt{p^2_{\text{T,V0}} + p^2_{\text{z,V0}} + m^2_{\Lambda}} + \sqrt{p^2_{\text{T,bach.}} + p^2_{\text{z,bach.}} + m^2_{\text{bach.}}}\right)^2 \\ &- \left(p^2_{\text{T,V0}} + p^2_{\text{T,bach.}} + 2 \cdot p_{\text{T,V0}} \cdot p_{\text{T,bach.}} \cos\theta_{xy}\right. \\ &\left. + p^2_{\text{z,V0}} + p^2_{\text{z,bach.}} + 2 \cdot p_{\text{z,V0}} \cdot p_{\text{z,bach.}} \cos\theta_z\right), \end{aligned} \tag{5.13}$$

where θ, θ_{xy} and θ_z are the opening angles in 3D, in the transverse plane and in the longitudinal direction, defined in the laboratory frame.

It becomes clear that the invariant mass depends on both momenta and opening angles. Any systematic effect on those variables would immediately bias the invariant mass distributions, and thus the measured mass.

The Fig. 5.13 shows the measurd mass of the Ξ and Ω baryons as a function of the transverse momentum. At low p_{T}, the measured masses scale rapidly with the transverse momentum, due mainly to the impact of multiple scattering. The latter becomes less dominant at intermediate p_{T}, and so this scaling reduces such that a flat dependence is reached at intermediate or high transverse momentum.

In order to avoid the influence of the multiple scattering and ensure stable measurements with p_{T}, the analysis should be performed in this plateau region. Although the K^0_{S} and Λ follows the same V0 decay topology, their decay kinematics are different. This also holds for the Ξ and Ω baryons. Thereby, the position of this stability region has to be identified separately for each particle. For instance, the data points above $p_{\text{T}} > 2$ GeV/c for the Λ in Fig. 5.13(a) and $p_{\text{T}} > 2.4$ GeV/c for the Ξ in Fig. 5.13(b) show little variations with the transverse momentum, and are all contained with a 1σ interval around the final measurement, after accounting for all the other sources of systematic effects. Therefore, in this region, the measurement can be considered as under control.

(2) (+)(+)

2

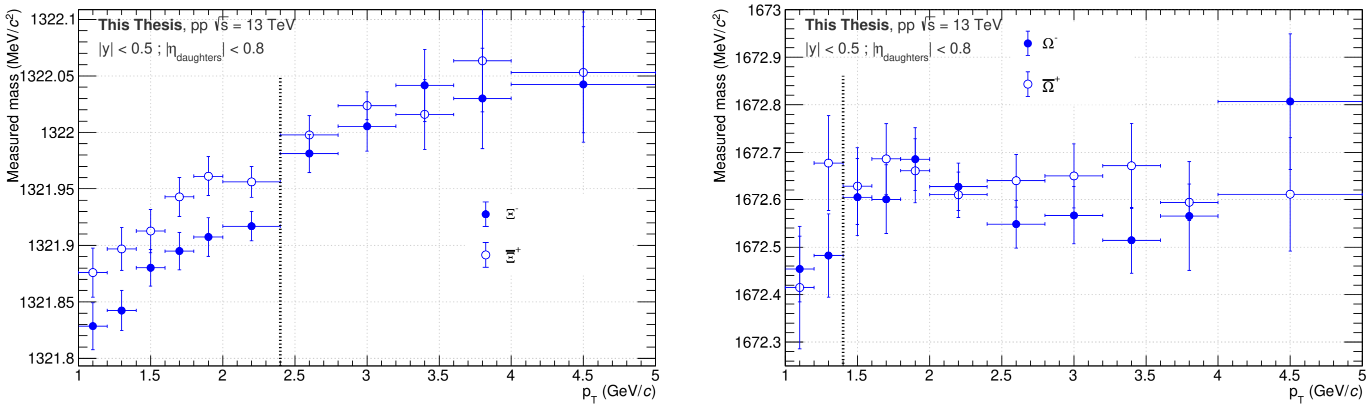

(a) (b)

Fig. 5.13: Measured mass of the Ξ (top) and Ω baryons (bottom) as a function of the transverse momentum. The dashed line represents the transverse momentum threshold, where the mass values can be considered as stable. In both cases, the results have been obtained through a fit with a triple Gaussian function for the invariant mass peak and, only in the data, an exponential function for the background.

5.13 + 5.14 sur une page dédiée [!p]

Along the same line, the influence of the longitudinal momentum on the measured mass has been checked. It is presented in Fig. 5.14. Both in the data and in MC, the dependence remains relatively small, such that it can be considered as negligible.

①

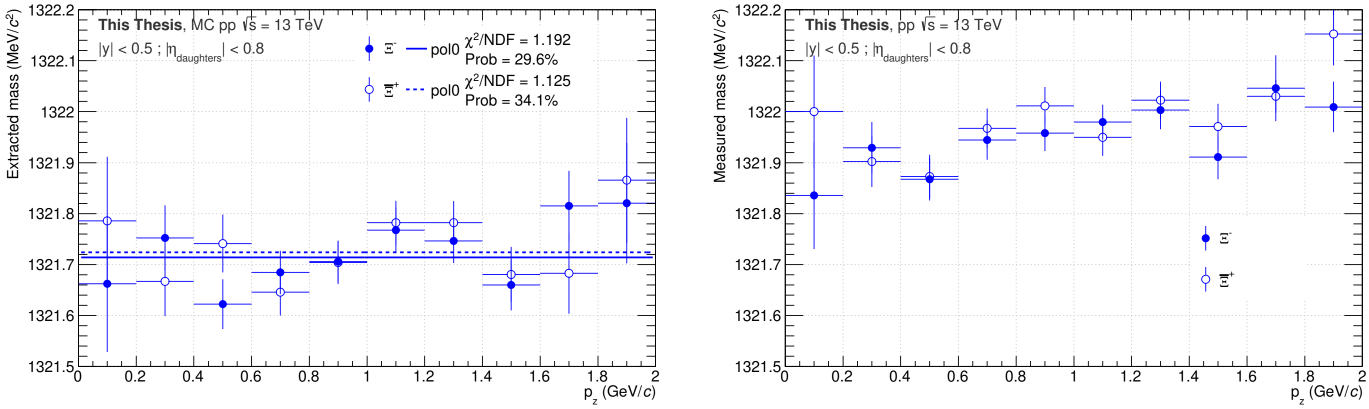

(a) (b)

Fig. 5.14: Measured mass of the Ξ hyperons as a function of the longitudinal momentum. ~~The dashed line represents the transverse momentum threshold, where the mass values can be considered as stable.~~ In both cases, the results have been obtained through a fit with a triple Gaussian function for the invariant mass peak and, only in the data, an exponential function for the background.

② dashed lines = fit, non?

3

IV-B.iv Dependence with the opening angles

As discussed above, the invariant mass depends on the opening angle between the decay products. Due to the multiple scattering, the latter may increase or decrease, thus biasing the estimation of the decay vertex position (as observed in Fig. 5.8) and the measured mass.

Therefore, different opening angles in the laboratory frame are being considered: 1

Stop lecture (15/07/23) ch. 4.

- **the opening angle in 3 dimensions**, also called *3D opening angle*.
  There are two ways to compute this quantity, depending on whether the value must be signed or unsigned. Here, it has been decided that value of the opening angle would be unsigned. It can be calculated from the momentum vectors of the positive and negative decay daughters:

2

$$\mathbf{p}_{\text{pos.}} \cdot \mathbf{p}_{\text{neg.}} = p_{\text{pos.}} p_{\text{neg.}} \cos(\theta) \tag{5.14}$$

besoin de définir $\vec{n}$

$$\Rightarrow \qquad \theta = \arccos \frac{(\mathbf{p}_{\text{pos.}} \cdot \mathbf{p}_{\text{neg.}})\ \mathbf{n}}{p_{\text{pos.}}\ p_{\text{neg.}}} \tag{5.15}$$

- **the transverse opening angle**.
  Here, the sign of the opening angle in the transverse plane might be important, as it relates to two vertex configurations, said "cowboy" and "sailor" [162]. When reconstructing a V0, a search for the minimum distance of closest approach between two oppositely charged tracks is performed as illustrated in Fig. 5.15(a). However, this approach reaches its limit in case there are two minima, as in Fig. 5.15(b). In such case, there is an ambiguity on the position of the DCA between the two tracks which, depending on the point taken as V0 decay vertex, may lead to a bias in the momentum and thus in the reconstructed mass[24]. The same argument could be made for cascade decays. 3 virgule

  To obtain a signed angle, one takes the cross product between the momentum vectors of the decay daughters:

$$\mathbf{p}_{\text{pos.}} \times \mathbf{p}_{\text{neg.}} = p_{\text{pos.}} p_{\text{neg.}} \sin(\theta_{xy})\ \mathbf{n} \tag{5.16}$$

$$\Rightarrow \qquad \theta_{xy} = \arcsin \frac{(\mathbf{p}_{\text{pos.}} \times \mathbf{p}_{\text{neg.}}) \cdot \mathbf{n}}{p_{\text{pos.}}\ p_{\text{neg.}}} \tag{5.17}$$

- **the longitudinal opening angle**.
  Finally, the opening angle in the longitudinal direction, θ_z can be deduced directly from the difference of longitudinal angle between the two decay daughters :

$$\theta_z = \theta_{z,\mathbf{pos.}} - \theta_{z,\mathbf{neg.}} \tag{5.18}$$

[24]There actually exists a procedure – used in this analysis – implemented in the V0 and cascade vertexing algorithm to lift this ambiguity. It consists in finding *analytically* the possible positions of the decay vertex in the transverse plane, using them as a starting point to compute the distance of closest approach in 3-dimensions for each vertex candidate and selecting the one providing the minimum DCA [162].

[4]

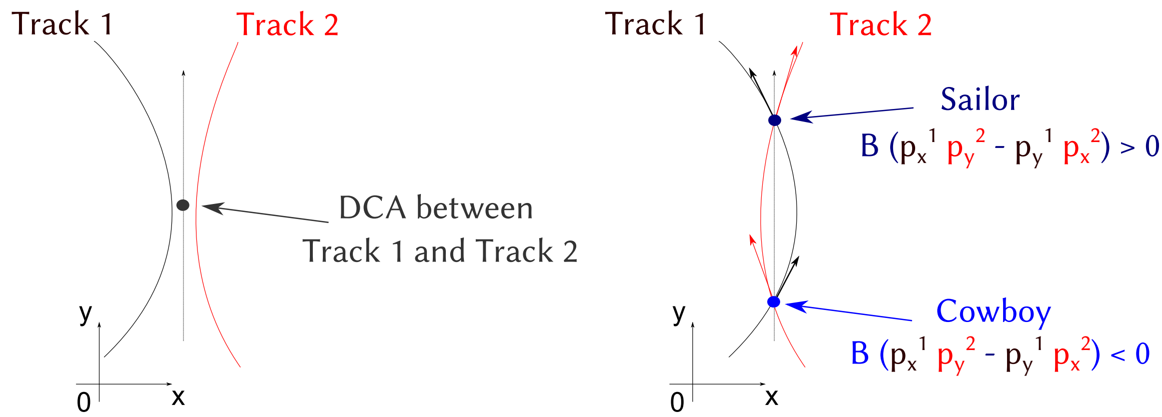

(a) (b)

Sketch

Fig. 5.15: ~~Scheme~~ of the distance of closest approach between two tracks in (a) the most expected case, and in (b) the cowboy and sailor configurations. The reconstructed vertex is said to be in sailor configuration if $B\,(p_{x,\text{pos.}}\;p_{y,\text{neg.}} - p_{x,\text{neg.}}\;p_{y,\text{pos.}}) > 0$, with B being the magnetic field. Conversely, it is in cowboy configuration if $B\,(p_{x,\text{pos.}}\;p_{y,\text{neg.}} - p_{x,\text{neg.}}\;p_{y,\text{pos.}}) < 0$.

① of Λ and $\bar{\Lambda}$

The Fig. 5.16 shows the distributions of the extracted mass as a function of the different opening angles. All display the same trend, namely the measured mass is relatively high for large opening angle values and decreases with the opening angles until reaching a flat region close to the small opening angles. Furthermore, this pattern being well reproduced in the simulations, its origin can be investigated by making use of the MC truth.

② Cap^{ti} Fig 5.17 = "résolution sur le rayon" = à définir

On the Fig. 5.17, the average resolution on the radial position of the decay vertex as a function of the transverse opening angle in MC simulations is shown. At large opening angle, the resolution on the decay vertex is quite poor: it tends to be located at a larger radius. It results in an over-estimation of the momentum of each decay daughters, and so in an increase of the reconstructed mass. As the opening angle becomes narrower, the resolution on the decay vertex ③ improves ~~increases~~ and the momentum bias decreases. The Fig. 5.17 only serves as an example; the same trend is observed for the opening angles in three dimensions and along the z-axis. To tackle that issue, the strategy followed by the present analysis consists to reject candidates with too large opening angles. In this way, one also manages to obtain flat distribution of the measured mass as a function of these variables.

car ici localisat° ≠ résolution sur localisation... i.e. "résol° de 2cm = décalage de 2 cm" ≠ évident a priori

④ ", for K^0_S, Λ, $\bar{\Lambda}$, $\Xi^\pm$, $\Omega^\pm$ "

IV-B.v Dependence with the azimuthal angles

ALICE being a cylindrical detector, any (decay) point can be identified based on its distance from the origin r and its azimuthal angle φ in the transverse plane, as well as its longitudinal position z. The Sec. 5|IV-B.ii investigated how the reconstructed mass varies as a function of the decay radius; along the same line, the dependence with the transverse direction of the decay can also be studied.

Two definitions exist concerning the angle in the transverse plane; there are the *position* and the *momentum* azimuthal angles. The former refers to the spatial coordinate around the z-axis, the latter corresponds to the same coordinate but

1

① À terme (not now) avoir les m̂ échelles L vs R en ordonnées (abscisses = ok)

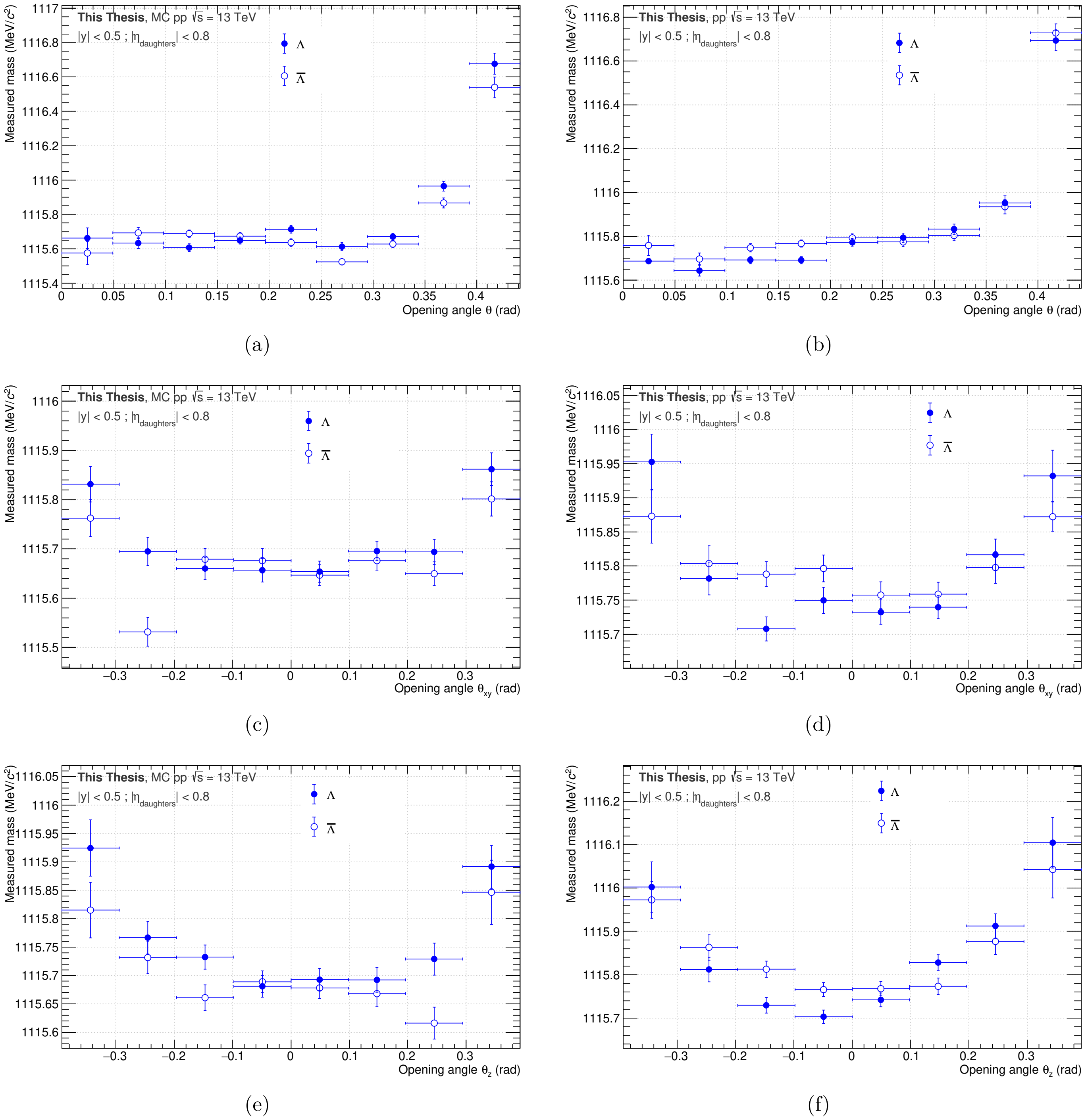

Fig. 5.16: Measured mass of the Λ as a function of the opening angle in three dimensions, in the transverse plane as well as in the longitudinal direction, in MC on the left and in the data on the right. Note that, for the purpose of the comparison, the MC is *not* re-weighted (Sec. 5|III-C.iv). In both cases, the results have been obtained through a fit with a triple Gaussian function for the invariant mass peak and, only in the data, an exponential function for the background.

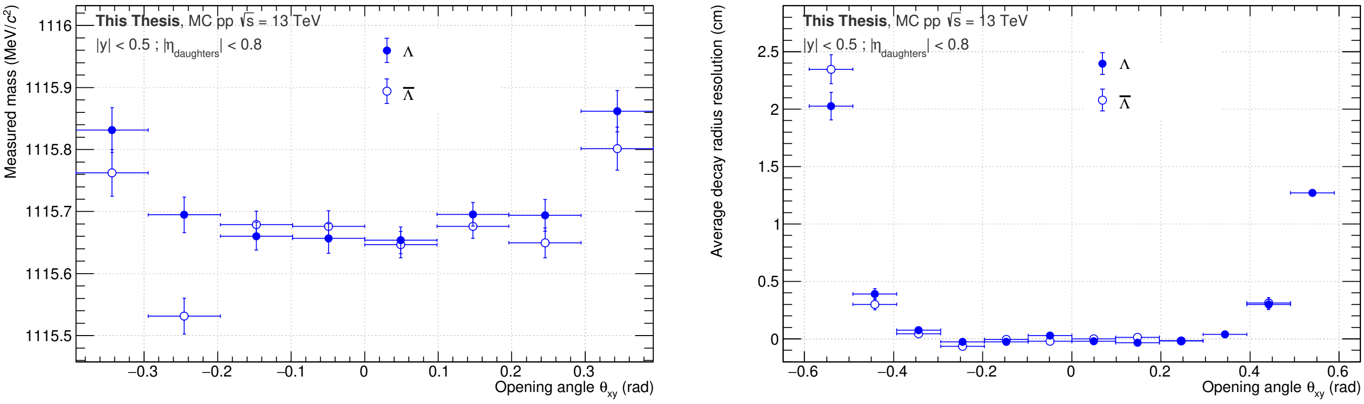

(a) (b)

Fig. 5.17: On the left: the measured mass of Λ hyperons as a function of the transverse opening angle in MC data. On the right: the average resolution on the decay radius as a function of the very same opening angle.

in momentum space. In other words, one can be calculated from the radial decay position, the other using the transverse momenta. For a neutral particle, such as the K^0_S and Λ, these two angles should coincide[25], whereas it should not for charged particles, including the Ξ or Ω. Due to their relatively short flight distance, the difference between these two angles for multi-strange baryons turns out to be negligible. Consequently, the term *azimuthal angle* will be used to designate the momentum one, unless indicated otherwise.

The ALICE volume has been divided into eighteen even azimuthal sectors: nine for the top barrel, and nine for the bottom barrel. This study employs such segmentation as it coincides with the TPC sectors (Fig. 3.6), and thus may help to relate a possible pattern to problematic sectors.

The Figs. 5.20 show the dependence on the momentum azimuthal angle for K^0_S, Λ, Ξ in MC on the left hand-side, and in the data on the right hand-side. The measured masses vary strongly from one angular sector to the next, in the data Figs. 5.18(b),5.18(d),5.18(f). A pattern emerges for all the considered particles: on the edges, the measurement points stay relatively at the same level, and change drastically as they approach $\varphi \simeq \pi$. At such location, the Λ and Ξ masses gain up to 200 keV/c^2, and up to 1.2 MeV/c^2 for the K^0_S. In constrast, the masses extracted in MC simulations exhibit a relatively flat dependence with the azimuthal angle, compatible with a constant function with a χ^2 probability varying between 1% and 86%. The trend observed in real data is not reproduced in the simulations, suggesting that one or several elements of the experiment are not accounted for in the MC productions.

Different leads to identify the possible origins for this "odd" behaviour have been investigated:

1. One possible explanation involves the material distribution within the detector. The Sec. 5|IV-C.ii provides a short explanation on how the material budget is evaluated in ALICE. This section also provides a systematic uncer-

[25] Assuming that the V0 originates from the primary vertex.

tainty on our mass measurement, which proves to be too small to account for the large mass variations in Figs. 5.20. Nevertheless, it is *a priori* possible that some material have not been taken into account in the detector geometry. In particular, an underestimated amount of material budget in the region $\varphi \simeq \pi$ could explain the trend. In such case, this structure is expected to change with the radial position of the decay vertex, as a V0/cascade decaying beyond the region with additional or underestimated material budget should not be affected by it. However, it turns out that the decay radius of the V0 and/or cascade shows no influence on the trend.

2. Another attempt at an explanation concerns the alignement of the ALICE detector, and in particular the ITS. As in the first point with the material distribution, the discrepancy between the data and the MC may be related to residual misalignement. The strategy followed to test this hypothesis is to repeat the whole analysis but using TPC standalone tracks instead of global tracks. The TPC is known to be better calibrated and aligned than the ITS, a change in the azimuthal dependence on the measured mass would point towards an issue related to the alignement. After repeating the analysis with TPC standalone tracks, the shape of the structure changes slightly but a peak still emerges around an azimuthal angle of π.

3. In order to shed light on that issue, the data sample has been divided into two sub-samples according to their magnetic field polarity. Maybe this trend originates only from periods with a specific magnetic field. The Fig. 5.19 shows the distribution of the measured mass as a function of φ. The same trend is observed in both sub-samples though, interestingly, the peaks in the vicinity of $\varphi = \pi$ for the particle and the anti-particle are swapped under an inversion of magnetic field polarity. This tells us that this structure is somehow related to the magnetic field.

4. Similarly, the V0 and cascade candidates have been separated based on whether the longitudinal position of decay and, in particular, whether they locate on the positive or negative z-side. As mentioned in the header of Sec. 3|II-B, these are also referred as A-side and C-side respectively. The comparison of the azimuthal dependence on the measured mass in these two sides is displayed on Fig. 5.20. On the left hand-side panels Figs. 5.20(a),5.20(c),5.20(e) corresponding to the C-side, the dependence is still present. However, it reduces significantly on the A-side (Figs. 5.20(b),5.20(d),5.20(f)), such that it almost follows a flat distribution. Although the K^0_S masses still fluctuate with the azimuthal angle, the magnitude of the variations is smaller on the A-side. Therefore, the origin of such dependence as to be found on the C-side. Amongst its singularities, the most noteworthy are certainly the presence of the muon arm absorber and the dipole magnet. In the past, the former was observed to be the source of many secondary particles, originating from the interaction with absorber material. This can, in turn, distort the background distribution in the invariant mass spectra, leading possibly to a difference in terms of extracted mass. This is rather unlikely in the present conditions of the analysis; the tight selection on the cosine of the pointing angle allows

to reach purities above 95% for the V0s and 90% for the cascades. At such level of background, it would be surprising to find it at the origin of this dependence[26]. On the other hand, the dipole magnet has an influence on the magnetic field within the L3 magnet. The induced distortions have been assessed and accounted for in the detector calibration. However, there may still be some residual distortions that could affect the particle trajectory and ultimately lead to a variation of the reconstructed mass with the TPC sector. On top of that, the magnetic field is supposed to coincide with the z-axis, with the electric field in the TPC cage; if not (due to a distortion induced by the dipole magnet), the so-called $E \times B$ effects can bias the measurement of the particle trajectory, by curling the electrons along their drift to the end plate. This would lead to a systematic displacement of the associated clusters, which later impact the tracking and finally the invariant mass.

In summary, the origin of the azimuthal dependence can not be claimed for sure. It appears clearly, from the Figs. 5.20 that the analysis should focus on the A-side of the detector. The residual variations of the measured mass, those that can not be accounted for by other sources of systematic biases, should be evaluated and encapsulated as a systematic uncertainty.

IV-B.vi Dependence with the rapidity

The dependence with the z position has somehow already been investigated in the Sec. 5|IV-B.v by scrutinising how the measured mass evolves for decays in the A- or C-side. As a cross-check, one can also study the influence of the Lorentz boost along the z-axis, namely the rapidity.

The Fig. 5.21 shows the rapidity dependence on the extracted mass of the Λ hyperon. Following the above discussion (Sec. 5|IV-B.v), the mass is measured on the positive z side of the detector. For that reason, there is no negative rapidity value. The results remain relatively stable over the whole rapidity range; in MC, the data points agree with a flat distribution at 38% for the Λ and 48% for the $\overline{\Lambda}$. Concerning the data, all the fluctuations can be accounted by other systematic uncertainties.

IV-B.vii Dependence with the event multiplicity

Along the same line as Sec. 5|IV-B.i, one may wonder whether the results change or not with the event activity, typically quantified by the event multiplicity. The latter is determined using the VZERO detectors as multiplicity estimator, as described in Sec. 3|II-B.iii. The total charge deposited in each VZERO arrays provides a measurement of the charge particle multiplicity, through the calculation of the average signal amplitude denoted as VZERO-M[27].

[26] As a matter of fact, the level of background as a function of the azimuthal angle has been checked. No correlation with the azimuthal dependence on the measured mass has been seen.

[27] In fact, the VZERO multiplicity estimator corresponds rather to the VZERO-M/⟨VZERO-M⟩. This normalisation allows to account for the ageing of the scintillator arrays, that become less transparent over time leading to a deterioration of the detector performances.

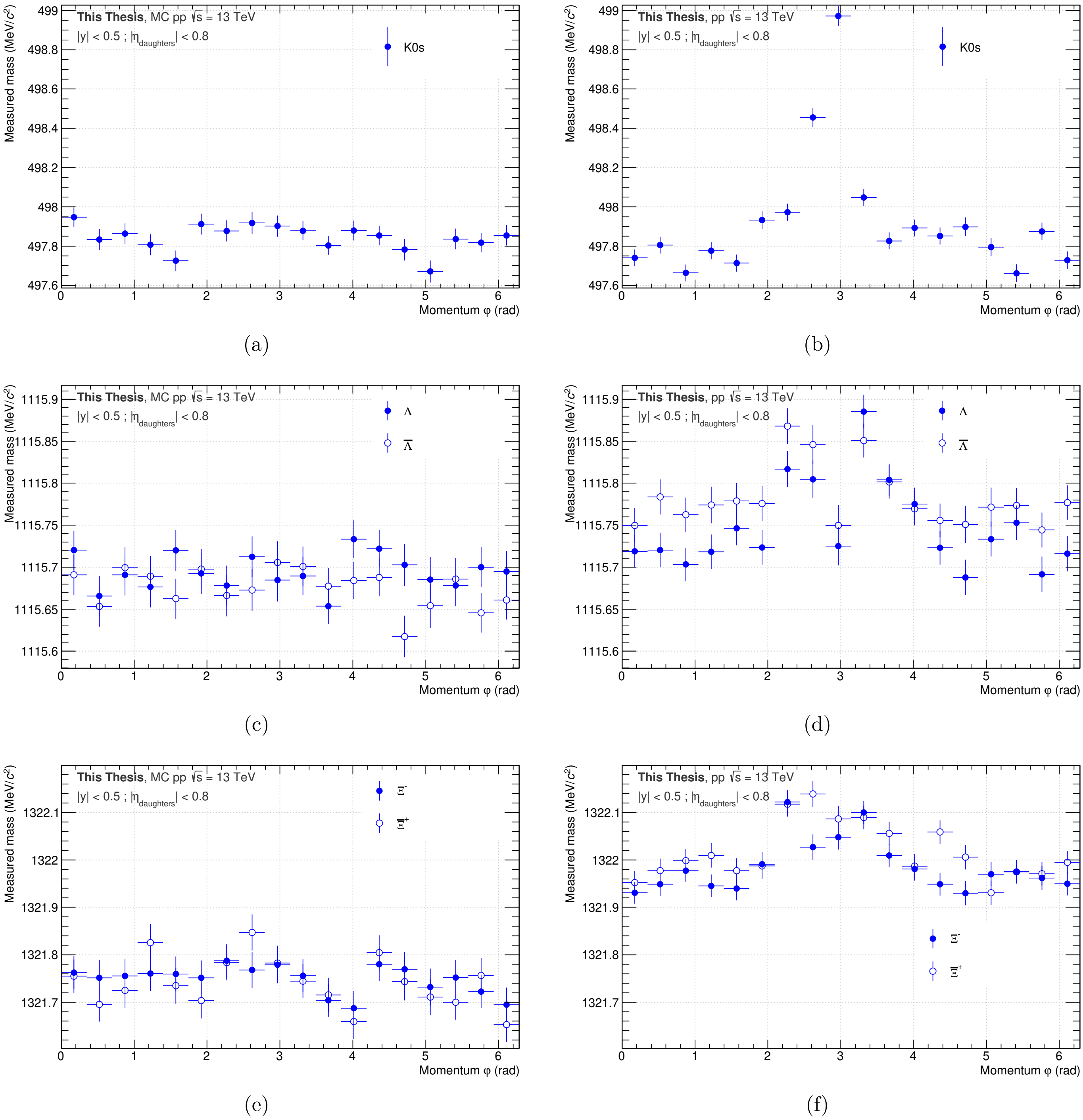

Fig. 5.18: Measured mass in pp collisions at $\sqrt{s} = 13$ TeV as a function of the momentum azimuthal angle. Results in simulated data are presented on the left-hand side, while those in real data can be found on the right-hand side. To each row corresponds a given particle: K^0_S (a) and (b), Λ (c) and (d), Ξ in (e) and (f). The uncertainties comprise only the statistical ones.

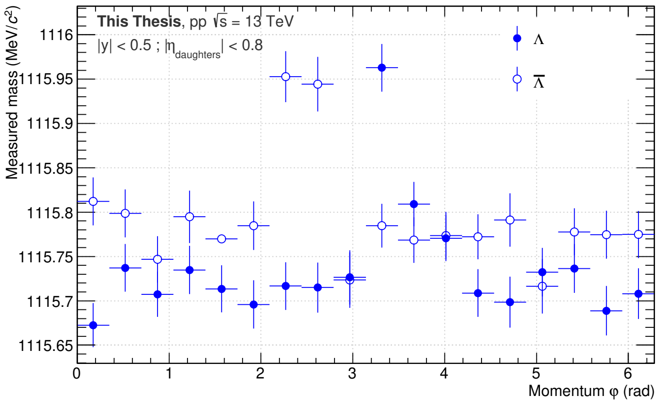

(a)

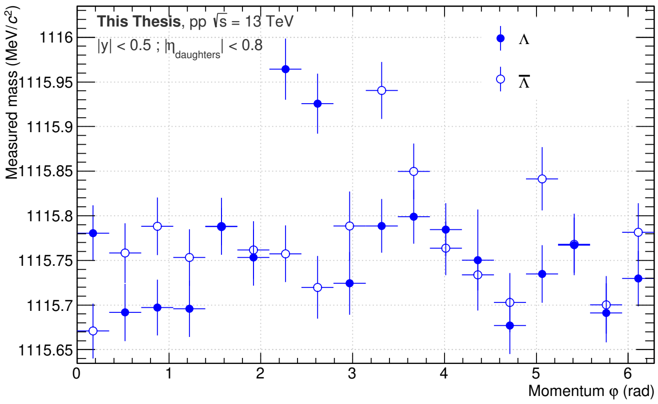

(b)

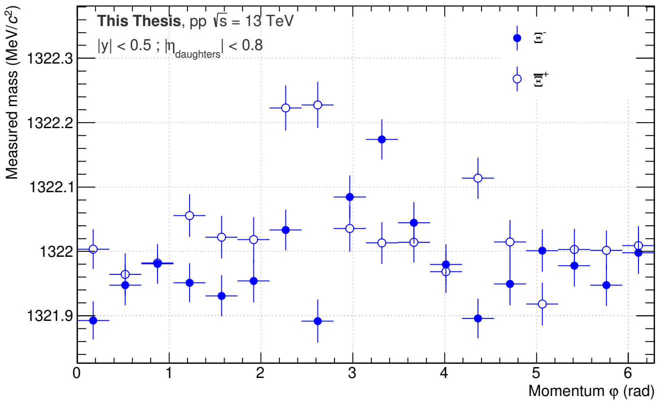

(c)

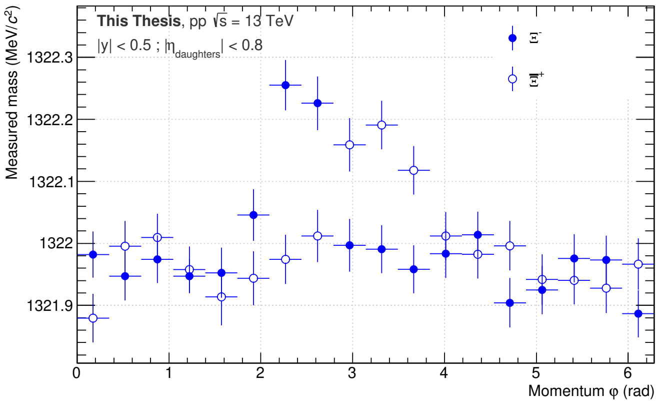

(d)

Fig. 5.19: Measured mass in pp collisions at $\sqrt{s} = 13$ TeV as a function of the momentum azimuthal angle in two opposite magnetic field polarities: $B = -0.5$ T on the left, and $B = +0.5$ T on the right. To each row corresponds a given particle: Λ (a) and (b), Ξ in (c) and (d). The uncertainties comprise only the statistical ones.

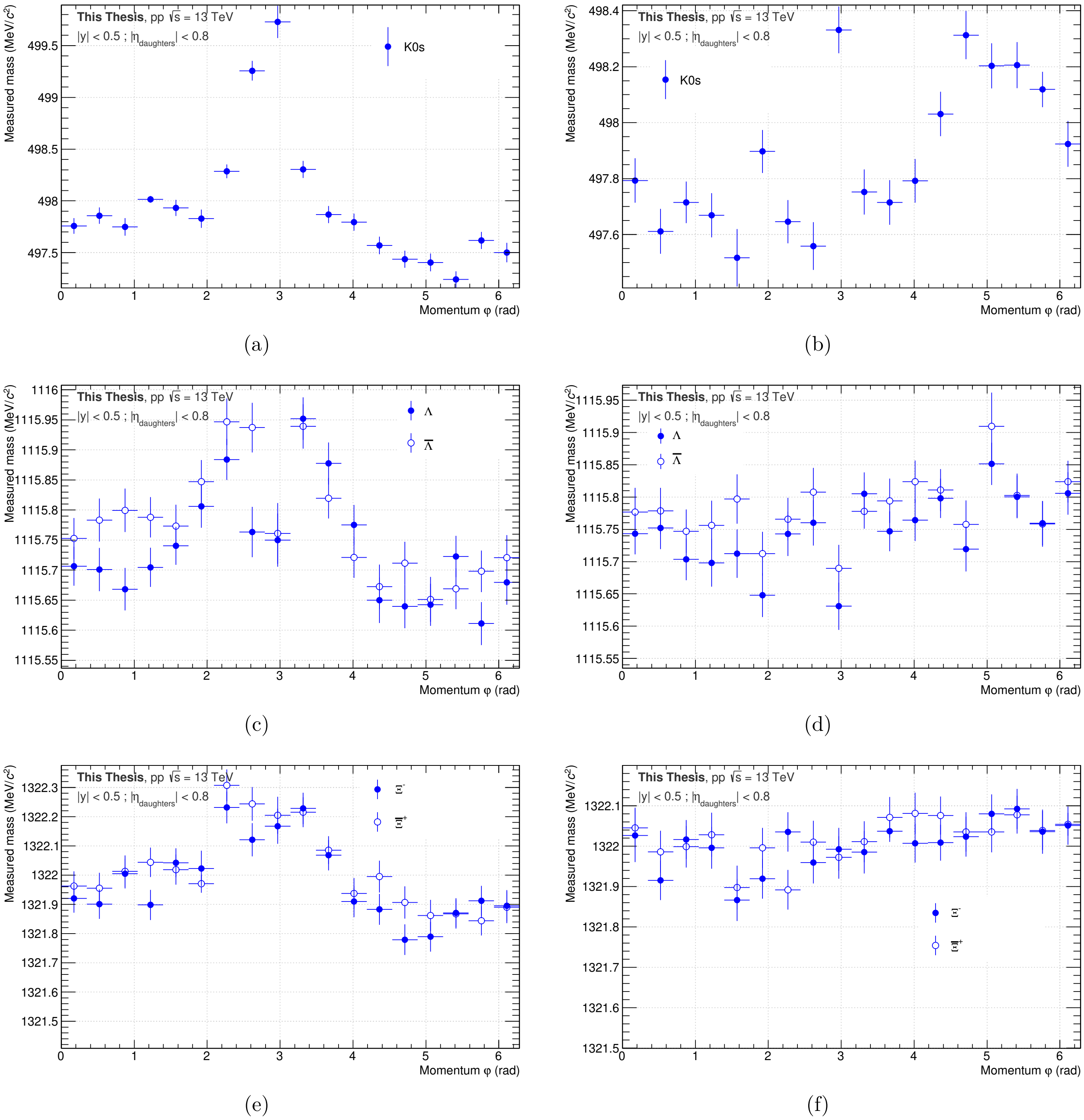

Fig. 5.20: Measured mass in pp collisions at $\sqrt{s} = 13$ TeV as a function of the momentum azimuthal angle in C-side (left) and A-side (right) of the ALICE detector. To each row corresponds a given particle: K^0_S (a) and (b), Λ (c) and (d), Ξ in (e) and (f). The uncertainties comprise only the statistical ones.

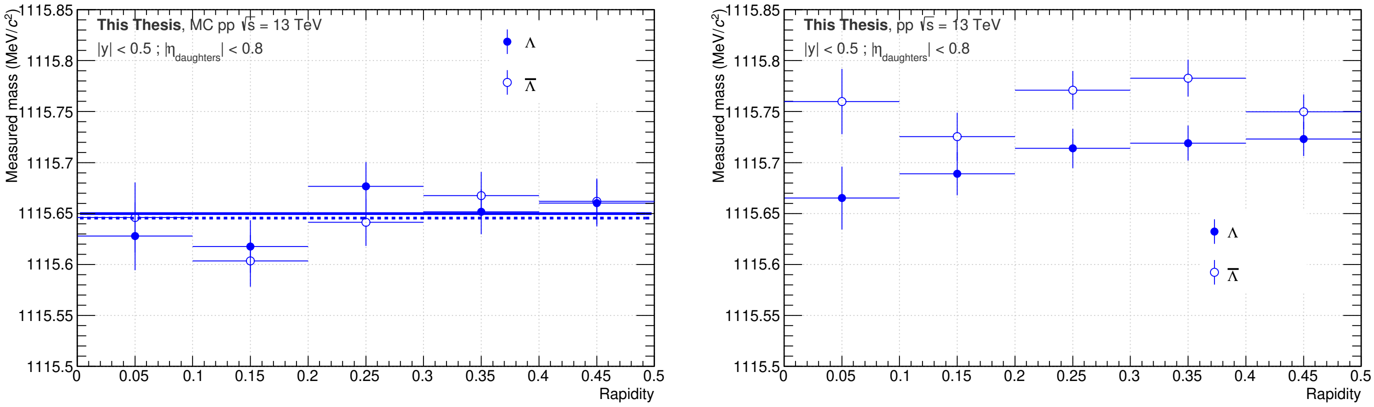

(a) (b)

Fig. 5.21: Measured mass in pp collisions at $\sqrt{s}$ = 13 TeV as a function of the rapidity of the Λ in MC on the left, and in data on the right. The solid and dashed lines on the left figure represent fits with a constant for the particle and the anti-particle respectively, with a χ^2 probability of 38% and 48%. The uncertainties comprise only the statistical ones.

Multiplicity Class	I	II	III	IV	V
$\sigma\ /\sigma_{\mathrm{INEL}>0}$	0-0.95%	0.95-4.7%	4.7-9.5%	9.5-14%	14-19%
$\langle \mathrm{d}N_{\mathrm{ch}}/\mathrm{d}\eta \rangle$	21.3 ± 0.6	16.5 ± 0.5	13.5 ± 0.4	11.5 ± 0.3	10.1 ± 0.3
Multiplicity Class	VI	VII	VIII	IX	X
$\sigma\ /\sigma_{\mathrm{INEL}>0}$	19-28%	28-38%	38-48%	48-68%	68-100%
$\langle \mathrm{d}N_{\mathrm{ch}}/\mathrm{d}\eta \rangle$	8.45 ± 0.25	6.72 ± 0.21	5.40 ± 0.17	3.90 ± 0.14	2.26 ± 0.12

Table 5.11: Event multiplicity classes, with the corresponding fraction of the total inelastic cross section INEL > 0 ($\sigma\ /\sigma_{\mathrm{INEL}>0}$) and average charged particle multiplicity at mid-rapidity in pp at $\sqrt{s}$ = 7 TeV, $\langle \mathrm{d}N_{\mathrm{ch}}/\mathrm{d}\eta \rangle$. Table taken from [163].

The events are divided into ten multiplicity classes, as indicated in Tab. 5.11. The Fig. 5.22 shows the dependence of the measured mass of the Λ as a function of the multiplicity. Both in MC and in the data, the measured mass shows little dependence on the event multiplicity, such that it can reasonably considered as stable with the event activity.

IV-c Momentum scale calibration

The dominant source of systematic uncertainty comes from the momentum scale calibration. This can originate from the uncertainty on the value of the magnetic field (Sec. 5|IV-C.i) or imperfect energy loss corrections (Sec. 5|IV-C.ii)

IV-c.i Imprecision on the magnetic field

As mentioned in Sec. 5|IV-B.i, the data sample has been collected with two opposite magnetic field polarities, $B = \pm 0.5$ T. The stability of the measured masses

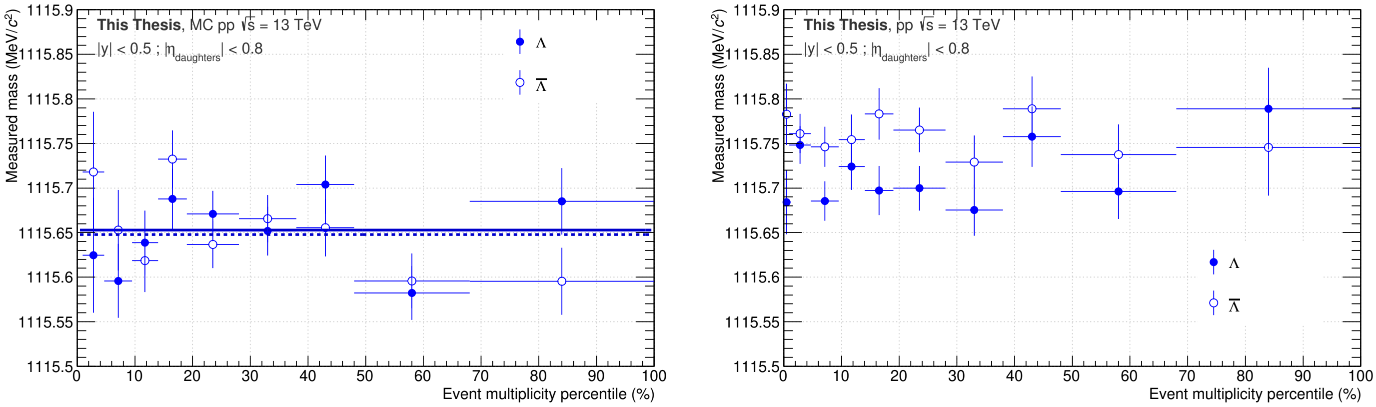

(a) (b)

Fig. 5.22: Measured mass in pp collisions at $\sqrt{s}$ = 13 TeV as a function of the event multiplicity percentile for Λ in MC on the left, and in data on the right. The solid and dashed lines on the left figure represent fits with a constant for the particle and the anti-particle respectively, with a χ^2 probability of 8% and 14%. The uncertainties comprise only the statistical ones.

and mass differences has been checked, and the results in different magnetic field configuration has been found to be in good agreement. However, this only guarantee that the calibrations of the ALICE detector between periods of opposite polarities are compatible; nothing can be claimed concerning the precision of such calibrations, and in particular, its influence on the presented results.

The measurement of the magnetic field in the L3 magnet has been performed in 2007 and is reported in [164]. It uses 31 Hall probes, calibrated to a precision of 1 Gauss and distributed over two arms, that could rotate around the beam axis and translate along the very same axis. Based on a set of 480 measurement points, the field were interpolated in order to build the full magnetic field map within the L3 volume. Concerning the precision of the latter, the analysis [164] concludes the following:

> *[...] the difference between the corrected data and the obtained parameterization which gives an estimate of the uncertainty for the latter (on top of the mentioned constant transverse field): within the TPC volume the differences are contained in 2 Gauss range although on the periphery of the scanned region there are points with difference reaching 5-6 Gauss (these points constitute less than 1 % of all data).*

Since the daughter tracks are required to cross at least 70 readout rows in the TPC, likely distributed over different sectors, the contribution of the points located in the periphery of the scanned region (1 % of all data) can reasonably be considered as negligible. Therefore, for the whole L3 volume, a 2 Gauss uncertainty on the magnetic field is retained.

An uncertainty on the magnetic field translates into a shift of the transverse momentum components of the decay daughters. Transverse momentum is related to magnetic field B_0 and the track curvature R through the relation $p_{\mathrm{T}0} = qB_0R$. If the magnetic field B is smaller or greater than its nominal value, B_0, by 2 Gauss, the transverse momentum would respectively be scaled down or up by a factor B/B_0 :

$$p_{\mathrm{T}0} = qB_0R \qquad \Rightarrow \qquad p_{\mathrm{T}} = \frac{B}{B_0}p_{\mathrm{T}0} \tag{5.19}$$

Here is the strategy adopted to evaluate the impact of the magnetic field imprecision : the transverse components of all the decay daughters will be scaled up or down by B/B_0 – with B being equal to B_0 plus or minus 2 Gauss –, the mass will then be extracted as explained in Sec. 5|III-C and the maximum deviation with respect to the measured mass with the nominal value of the magnetic field will be quoted as our uncertainty due to the B-field imprecision. The numerical value of the latter can be found in Tab. 5.12 for $\mathrm{K^0_S}$, Λ, Ξ and Ω.

Particle	Uncertainty on the mass (MeV/c^2)	Uncertainty on the mass difference ($\times 10^{-5}$)
$\mathrm{K^0_S}$	0.080	/
Λ	0.013	negligible
$\overline{\Lambda}$	0.013	negligible
Ξ^-	0.023	negligible
$\overline{\Xi}^+$	0.028	negligible
Ω^-	0.026	negligible
$\overline{\Omega}^+$	0.027	negligible

Table 5.12: Systematic uncertainties on the mass (second row) and mass difference (third row) due to the imprecision on the magnetic field value for $\mathrm{K^0}$, Λ, Ξ and Ω.

As expected, the magnetic field has no influence on the mass difference. Affecting both particles and anti-particles in the same way – either a scale up or down –, the effect should cancel out in the difference, yielding to a negligible impact on the mass difference measurement.

IV-C.ii Energy loss corrections

Imperfect energy loss corrections only arise from their miscalculation. An example of such miscalculation has already been addressed in Sec. 5|IV-B.ii. Another source of systematic effect related to the energy loss corrections comes from the limited knowledge on the material budget in the detector. If there is a discrepancy between the amount of *known* crossed material and the actual one, the estimation of the energy loss will be directly impacted.

The material budget of the ALICE detector has been estimated experimentally by reconstructing pairs of electron-position originating from photons converted in the detectors. The photon conversion probability being sensitive to the geometry, the composition of detector or the material budget, it provides a precise description of the material distribution. In the LHC Run-2, the material budget in the central barrel of the ALICE detector is known with a precision of about 4.5% [109][165][28].

By varying the material budget, the impact of the misknowledge on the actual material budget can be estimated. This kind of investigation is typically carried out on simulated data. The idea consists in running two simulations: one with an increased/decreased material density[29], and another with the nominal one. In both cases, the event reconstruction uses the standard detector geometry, *i.e.* with the standard amount of material budget. The comparison of the results from these two simulations allows to determine the systematic effect due to an uncertainty of 4.5% on the material budget.

In an ideal scenario, this study should rely on three MC productions: one with nominal material density serving as reference, another with a 4.5% increase of the density with respect to the standard value, and a last one with a decrease by the same amount. In this way, the effect of a increase or decrease of the material budget can be fully assessed.

It turns out that there are no such MC productions in pp collisions at $\sqrt{s}$ = 13 TeV. Instead, there exist only simulations with material budget increased 30%. Here, the approach is slightly different: the goal is to change excessively the material density to guarantee the observation of a systematic effect. The latter is then scaled down to the actual precision on the material budget. In other words, by estimating the variation of the results induced by a 30% increase of the material budget and by assuming linearity, the effect of increase of 4.5% of the material density can derived. It is given by:

$$\begin{bmatrix} \text{Variation of the results due to} \\ \text{4.5\% extra material budget} \end{bmatrix} = \frac{4.5\%}{30\%} \times \begin{bmatrix} \text{Variation of the results due to} \\ \text{30\% extra material budget} \end{bmatrix} \tag{5.20}$$

The aforementioned simulations are enriched[30] MC productions, that uses GEANT4 for the transport and the interaction with the detector material. It may be interesting to compare it to one employing GEANT3. However, most of the simulations in ALICE are general-purpose MC productions which, as mentioned in Sec. 5|II-A, uses the GEANT3 as propagator by default. As a consequence, it is possible to make a comparison between GEANT3 and GEANT4, but certainly not with the Ξ and Ω baryons due to the lack of statistics.

---

[28]As a matter of fact, at the time of the writing of this manuscript, another photon conversion analysis [166] has been performed, that quotes an uncertainty on the material budget of 2.5%. However, not only the precision has changed, but also the amount of material budget. However, as of 2023, there have been no re-processing of the data nor production of MC simulations using this updated version of the material distribution. For that reason, the latter will not be used in this work.

[29]There could be two ways to increase/decrease the material budget. One could increase the thickness of the detectors, but this option is rather disfavoured since it may introduce clipping, overlapping of detector volumes. An alternative is to vary the material density, such as changing the Si density by ± 4.5%. This offers the same results as the first possibility without affecting the detector geometry.

[30]The enriched MC production has been obtained by filtering events containing the expected signal, as explained in Sec. 5|II-A. In our case, it is an enrichement in strange hadrons: K^0_S, Λ, Ξ, Ω.

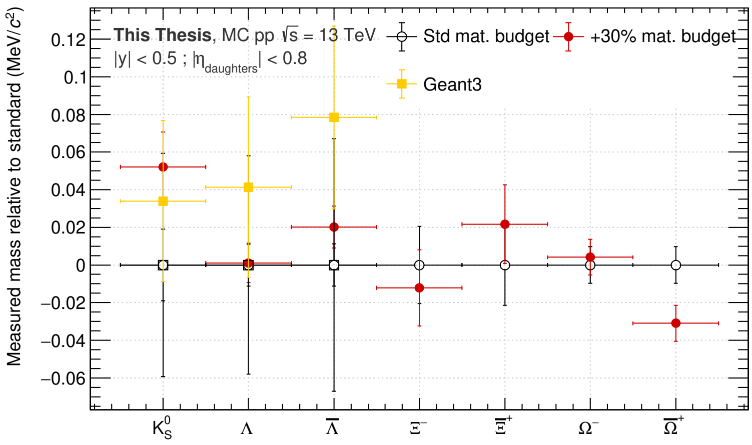

(a)

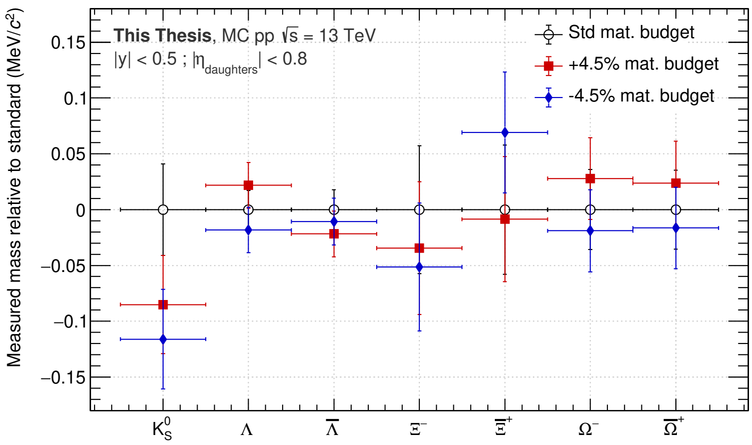

(b)

Fig. 5.23: Measured mass with an excess and/or a lack of material budget relative the one obtained with the standard amount of material budget. The top figure shows the results with MC productions anchored on pp collisions at $\sqrt{s}$ = 13 TeV. The bottom figure presents the measured masses obtained using simulations in Pb-Pb collisions at $\sqrt{s_{\rm NN}}$= 5.02 TeV. The uncertainties comprise only the statistical ones.

However, there also exist simulations with an increase/decrease of the material density by 4.5%, but in Pb-Pb collisions at $\sqrt{s_{\rm NN}}$= 5.02 TeV. Although the collision systems are different, they are *in principle* still usable for this study, since the systematic uncertainty is derived from the deviation with respect to a reference with the nominal amount of material budget. An alternative could be to evaluate this uncertainty using exclusively the simulations with a modified material density. As one would expect that the measured mass should scale with amount of material, the mass deviation should be approximately the same in both cases[31]. Hence, the systematic uncertainty could simply be taken as the deviation between the results divided by two. Whatever the considered approach, in this study, the results ob-

[31] Assuming that the material density is increased and decreased by the same amount in both MC simulations, as it is the case for those in Pb-Pb at $\sqrt{s_{\rm NN}}$= 5.02 TeV.

tained with these MC productions are compared to those derived above, *i.e.* using simulations with an excessive amount of additional material in pp at $\sqrt{s} = 13$ TeV.

The measured mass and mass differences in the different MC simulations are shown in Fig. 5.23. If the actual amount of material turns out to be greater than the one implemented in the detector geometry, the energy loss calculation for a given track would be underestimated, leading to a track with less momentum and consequently a V0/cascade with a lower reconstructed mass. Conversely, a lack of material in the detector with respect to our knowledge would yield to a higher reconstructed mass. Here is what is expected.

However, none of the panels in Fig. 5.23 follows this trend. In fact, the results are "odd". On the Fig. 5.23(a), particle and antiparticle do not go in the same direction. For instance, the $\overline{\Omega}^{+}$ mass decreases in a configuration 30% extra material budget, whereas the Ω^{-} barely moves. Similar abnormalities can be observed in the Fig. 5.23(b): the K^0_S mass decreases in case of additional material budget, but reduces even more if, in fact, there is a lack of material. Therefore, both MC productions in pp and Pb-Pb collisions exhibit unexpected behaviour. Concerning Geant3, it leads to a larger mass shift in the case of the Λ and a smaller one for the K^0_S. Considering the uncertainties, the results provided by Geant3 agree with those obtained in simulations using Geant4.

Finally, it is not clear which uncertainty should be quoted to account for the misknowledge on the material budget. On one hand, the results in Fig. 5.23(b) correspond to those with an increase or a decrease of the material by 4.5%, meaning the actual value of uncertainty on the material budget. However, how to interpret and evaluate a systematic uncertainty when a decrease and an increase of the material budget yields to a diminution of the reconstructed mass. On the other hand, Fig. 5.23(b) highlights the impact of a 30% increase of the material budget. It is not guaranteed that the linearity assumption in Eq. 5.20 remains valid for such an excessive increase of the material density.

Therefore, in order to be conservative, the deviations observed in case of an increase of 30% should be taken as a systematic uncertainty due to the misknowledge of the material budget. The same uncertainty will be attributed to particles and antiparticles.

IV-d Mass extraction

The elements related to the mass extraction are also included in the present study. It covers the considered fit functions for modeling the peak and the background, the fitting range and the bin width of the invariant mass distribution.

IV-d.i Choice of the fit function

By exploiting different peak and background functions for the mass extraction, one can estimate the systematic effect due to the choice of model. The considered functions for each particle have been explained and detailed in Sec. 5|III-C.ii and

5|III-C.iii. In total, four combinations of peak and background models are tested, for which the masses and mass differences, as well as their statistical and systematic uncertainties, are measured using the procedure presented in Sec. 5|IV-A.

As a cross-check, these results are also compared to the mean values extracted directly from the invariant mass distributions. The mean value being sensitive to any outliers or possible asymmetry in the tails of the distribution, a special care should be given to the range of values used for its evaluation. It has to be determined in a well-defined area where the results do not fluctuate significantly with the specified range. This has been investigated, starting with the mean value calculated inside the peak region, that is $[\mu-5\sigma;\mu+5\sigma]$. The latter has been progressively shrunk on both ends, by step of 1σ. It turns out that the results converge for a range of $\mu\pm2\sigma$. In the following, the measured masses and mass differences using the mean value will always be extracted in this range.

IV-D.ii Choice of the fitting range

Let us take two extreme cases : on one hand, if the fitting range is too extended, the fit would become sensitive to some background structures far from the peak such as, for instance, the mis-reconstructed Ξ with a V0 formed from the actual bachelor and the proton daughters in Sec. 5|III-B.ii. On the other hand, if the range is too short, the level of background used in the fit procedure would be too low, leading to fluctuations in the fit results. As a consequence, this aspect has to be investigated and quantified.

This study is performed as follows: similarly as in Sec. 5|IV-A.i, the analysis is repeated 20 000 times. At each round, a different fitting range is being used. The latter is randomly generated according to an uniform distribution on the range indicated in Tab. 5.13. This exercise only makes sense *ceteris paribus*[32]. Therefore, this procedure is carried out by fixing the candidate selections to the values in Tab. 5.2 and 5.3. The standard deviation over the whole set of fitting ranges provides an estimation of the systematic bias induced by the choice of the fit interval.

The results are presented in the two last columns of Tab. 5.13.

IV-D.iii Choice of the binning

As the number of bins increases, the fine structure of the invariant mass distribution becomes more and more apparent, and so the fitting procedure gets more sensitive to it. Therefore, one may suspect that the granularity on the invariant mass distribution may influence the final results.

By default, the binning is set at 0.5 MeV/c^2. To evaluate its impact on the results, the analysis is repeated with a granularity of 1, 0.75 and 0.25 MeV/c^2. In case a significant change in the results is observed, the standard deviation is taken as systematic uncertainty due to the choice of the invariant mass distribution binning.

The results are presented in. This element of the analysis introduces an uncertainty of 0.001 MeV/c^2 on the mass values, and 0.02, 0.06 and 0.13 $\times10^{-5}$ on the

[32] "all other things being equal".

Particle	Randomisation interval (MeV/c^2)		Uncertainty on the measured...	
	Bottom edge	Top edge	...mass (MeV/c^2)	...mass difference ($\times 10^{-5}$)
K^0	[0.460 ; 0.475]	[0.520 ; 0.540]	0.002	/
Λ $\overline{\Lambda}$	[1.098 ; 1.108]	[1.125 ; 1.135]	0.001 0.001	0.02
Ξ^- $\overline{\Xi}^+$	[1.265 ; 1.3]	[1.345 ; 1.38]	0.001 0.001	0.03
Ω^- $\overline{\Omega}^+$	[1.615 ; 1.65]	[1.695 ; 1.73]	0.001 0.001	0.03

Table 5.13: Randomization intervals on the bottom and top edges of the fitting range for K^0, Λ, Ξ and Ω. The adjustement ranges are generated according to an uniform law. The uncertainties due to the choice of the fitting range are indicated in the two last columns.

mass difference values of Λ, Ξ and Ω respectively.

IV-E Pile-up treatment

A contribution to the systematic uncertainty can also originate from the pile-up rejection introduced in Sec. 5|III-B. It is evaluated by varying the rejection requirements.

Pile-up events may induce a bias in the mass measurement due to the association of tracks coming from different collisions, which possibly lead to the formation of a V0 or cascade candidate. Considering the tight selections applied on the candidate variables – and most particularly, on the cosine of the pointing angle to the primary vertex (Tabs. 5.2 and 5.3) –, the probablity of such misassociation is expected to be relatively low. Therefore, the measurement is performed with and without the pile-up rejection cut. If the effect turns out to be statistically significant, the absolute deviation with respect to the standard configuration is taken as systematic uncertainty.

IV-F Correction on the extracted mass

As discussed in Sec. 5|III-C.iv, in order to correct for any remaining bias due to the data processing, the analysis or the fit procedure, the mass measured in data are corrected for the mass offset observed in simulations with respect to the injected mass. This correction can only be as precise as the extracted mass value in MC, which is constrained by the limited size of the simulated data sample. The systematic bias attached to that correction is thus driven by the statistical uncertainty in simulations.

Tab. 5.14 show the systematic uncertainties attached to the MC correction on the measured masses and mass differences. The latter values are obtained via propagation of the uncertainties, using Eq. 5.8.

Particle	**Systematic uncertainty on the...** **...measured mass** (MeV/c^2)	**...measured mass difference** ($\times10^{-5}$)
K^0	0.002	/
Λ	0.001	0.02
$\overline{\Lambda}$	0.001	
Ξ^-	0.001	0.01
$\overline{\Xi}^+$	0.001	
Ω^-	0.001	0.02
$\overline{\Omega}^+$	0.001	

Table 5.14: Summary of the systematic uncertainties due to the MC correction on the extracted mass for K^0_S, Λ, Ξ and Ω.

IV-G Precision on the tabulated masses

The V0 and cascade masses are extracted from their invariant mass distribution, as explained in Sec. 5|III-C. The Eq. 4.3 and 4.5 highlight the quantities entering into the invariant mass calculation of a candidate, *i.e.* the mass and momenta of each daughter particle. In particular, even for the $\overset{(-)}{\Lambda}$ daughter of $\overset{(-)}{\Xi}{}^{\pm}$ or $\overset{(-)}{\Omega}{}^{\pm}$ decay, the former always corresponds to the tabulated mass in the PDG. As presented in Tab. 5.15, the latter has a finite precision. Although the PDG mass values of proton and pion are determined with a high degree of precision ($\sigma_{\rm PDG}$ < 1 keV/c^2), this is not the case of the $K^\pm$ and $\overset{(-)}{\Lambda}$ ($\sigma_{\rm PDG} \sim \mathcal{O}(10)$ keV/c^2). Consequently, they can possibly induce the systematic bias in the invariant mass calculation; all the more so for the cascades, since the latter is one of the products of the Ξ decay, and both the former and the latter are the two decay daughters of the Ω.

Particle	$\pi^\pm$	$K^\pm$	$p^\pm$	$\overset{(-)}{\Lambda}$
$m_{\rm PDG}$(MeV/c^2)	139.57039	497.677	938.27208816	1115.683
$\sigma_{\rm PDG}$ (MeV/c^2)	0.00018	0.016	0.00000029	0.006

Table 5.15: Particle mass ($m_{\rm PDG}$) as well as its uncertainty ($\sigma_{\rm PDG}$) for the decay daughters of K^0_S, Λ, Ξ and Ω, listed into [42], as of 2023.

Similarly as in Sec. 5|IV-A, the mass of each decay daughter is varied randomly 20 000 times, according to a Gaussian distribution centred on the PDG value and with the associated uncertainty $\sigma_{\rm PDG}$ as standard deviation. In case, a systematic effect is observed, the standard deviation of the results over the whole set of generated particle masses is taken as systematic uncertainty.

V Results

V-.i Summary of the systematic uncertainties

The Tabs. 5.16 and Tab. tab:SystMassOmega

Sources	Uncertainties on the measured mass (MeV/c^2)			
	Ξ^-		$\overline{\Xi}^+$	
	Statistical	Systematical	Statistical	Systematical
Topological selections	0.024	0.024	0.024	0.025
Magnetic field	/	0.023	/	0.028
Material budget	/	0.020	/	0.020
Fitting function	/	0.009	/	0.009
Fitting range	/	0.001	/	0.001
Binning	/	0.001	/	0.001
Out-of-bunch pile-up rejection	/	0.004	/	0.004
Precision on the PDG mass	/	0.011	/	0.011
MC mass offset	/	0.008	/	0.009
Total	**0.024**	**0.033**	**0.024**	**0.035**

Table 5.16: Statistical and systematical uncertainties on the mass Ξ^- and $\overline{\Xi}^+$. The total is obtained assuming that there is no correlation between each source of uncertainties.

Sources	Uncertainties on the measured mass (MeV/c^2)			
	Ω^-		$\overline{\Omega}^+$	
	Statistical	Systematical	Statistical	Systematical
Topological selections	0.042	0.034	0.043	0.038
Magnetic field	/	0.026	/	0.027
Material budget	/	0.030	/	0.030
Fitting function	/	0.009	/	0.009
Fitting range	/	0.001	/	0.001
Binning	/	0.001	/	0.001
Out-of-bunch pile-up rejection	/	0.004	/	0.004
Precision on the PDG mass	/	0.018	/	0.018
MC mass offset	/	0.008	/	0.009
Total	**0.004**	**0.033**	**0.004**	**0.035**

Table 5.17: Statistical and systematical uncertainties on the mass Ξ^- and $\overline{\Xi}^+$. The total is obtained assuming that there is no correlation between each source of uncertainties.

Sources	Uncertainties on the measured mass difference ($\times 10^{-5}$) Ξ	
	Statistical	Systematical
Topological selections	0.014 ()	0.015 ()
Out-of-bunch pile-up rejection	/	()
Magnetic field	/	0.028 ()
Material budget	/	0.009 ()
Fitting function	/	0.007 ()
Fitting range	/	0.001 ()
Binning	/	0.001 ()
Precision on the PDG mass	/	0.018 ()
MC mass offset	/	0.012 ()
Total	**0.014 ()**	**0.041 ()**

Table 5.18: Statistical and systematical uncertainties on the mass Ω^- and $\overline{\Omega}^+$. The total is obtained assuming that there is no correlation between each source of uncertainties.

Sources	Uncertainties on the measured mass difference ($\times 10^{-5}$) Ξ	
	Statistical	Systematical
Topological selections	3.07	3.51
Out-of-bunch pile-up rejection	/	negligible
Magnetic field	/	negligible
Material budget	/	0.009
Fitting function	/	0.007
Fitting range	/	0.001
Binning	/	0.001
Precision on the PDG mass	/	0.011
MC mass offset	/	0.012
Total	**0.014 ()**	**0.041 ()**

Table 5.19: Statistical and systematical uncertainties on the mass Ω^- and $\overline{\Omega}^+$. The total is obtained assuming that there is no correlation between each source of uncertainties.

V-.ii Discussion and conclusion

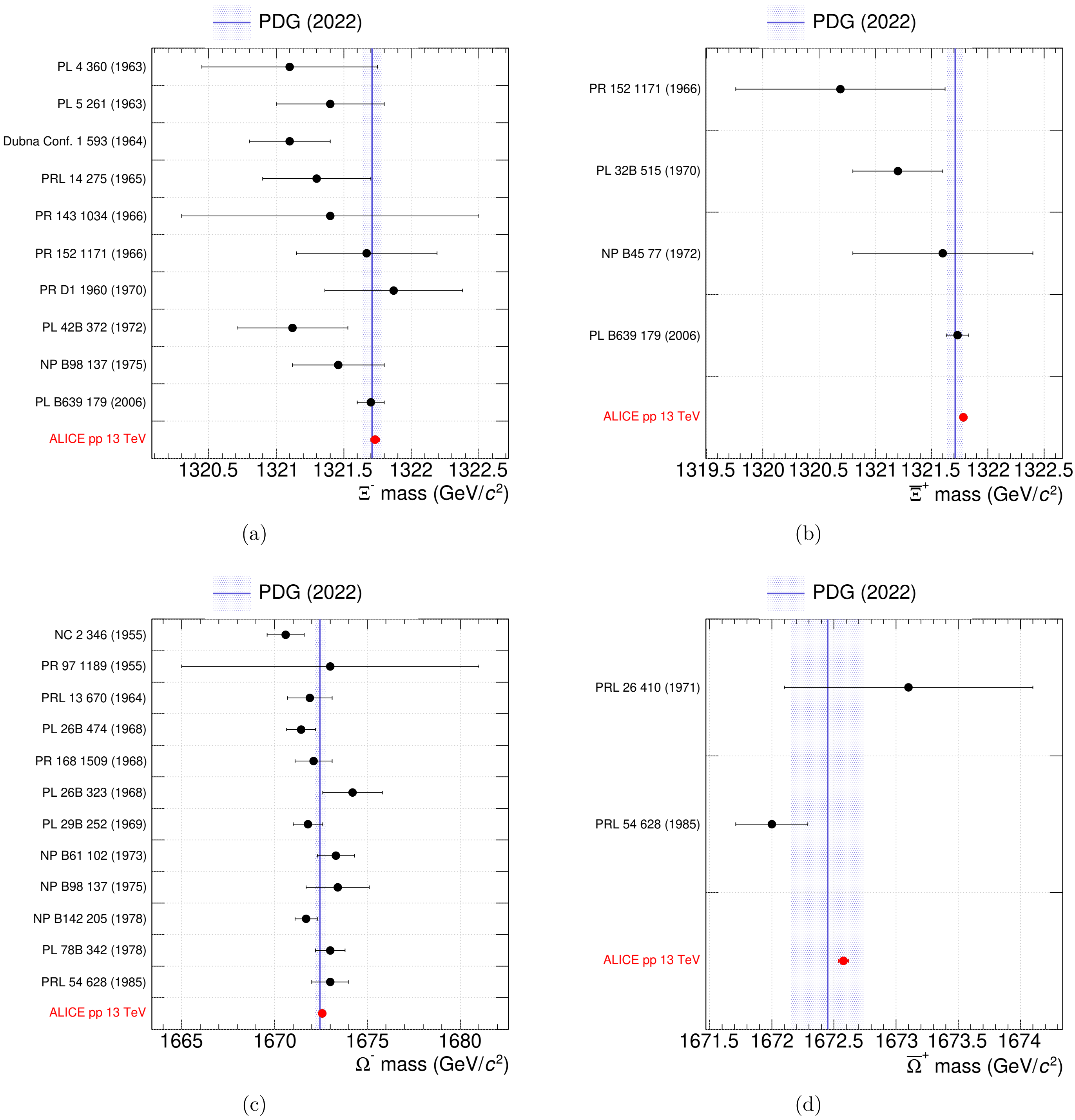

Fig. 5.24: Comparison of our mass values for the Ξ^- (a), $\overline{\Xi}^+$ (b), Ω^- (c) and $\overline{\Omega}^+$ (d) hyperons, to the past measurements quoted in the PDG, as of 2023 [42]. The vertical line and the shaded area represent the PDG average and its associated uncertainty.

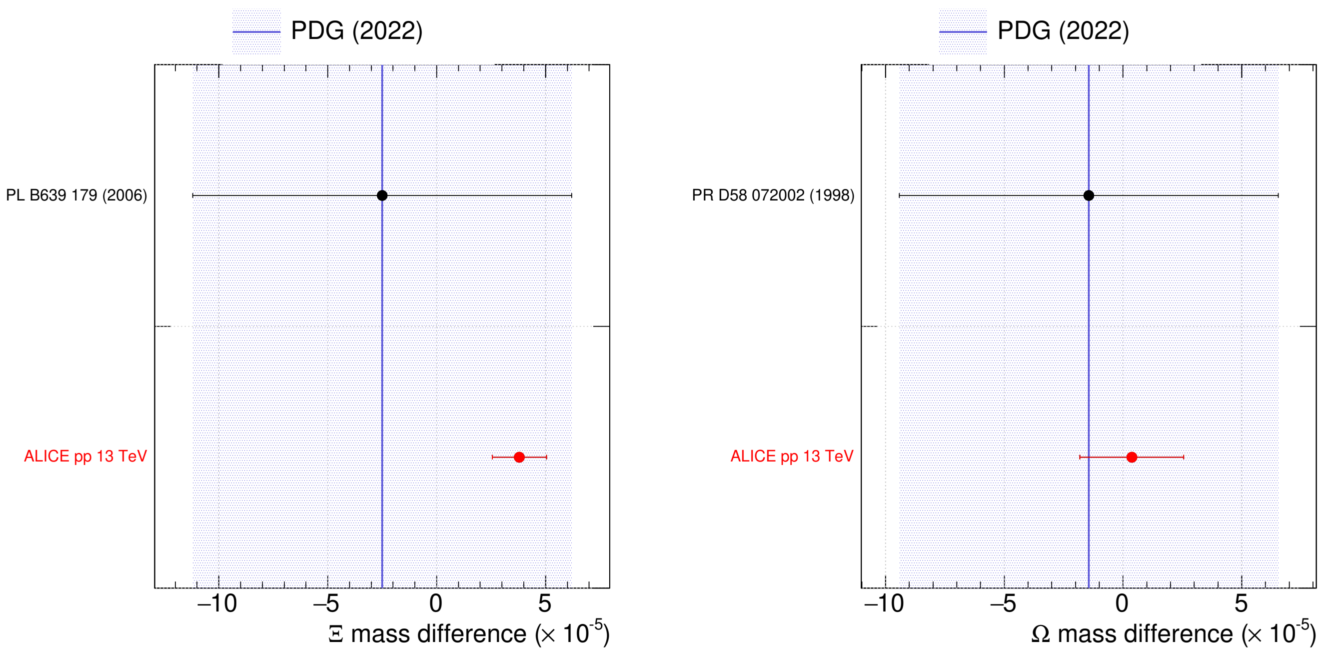

(a) (b)

Fig. 5.25: Comparison of our mass difference values between the Ξ^- and $\overline{\Xi}^+$ (a), and the Ω^- and $\overline{\Omega}^+$, to the past measurements quoted in the PDG, as of 2023 [42]. The vertical line and the shaded area represent the PDG average and its associated uncertainty.

Chapter

6 | Analysis of the correlated production of strange hadrons

Following the mass measurement of multi-strange baryons in Chap. 5, the present work is complemented by a second analysis. Similarly to the first one, the latter pushes the limits of the LHC Run-2. It proposes to correlate the production of hyperons – and most particularly, Ω– and other particles produced in the event.

I Introduction

The Quark Gluon Plasma (QGP) is studied experimentally for more than two decades now, from the first hints of its existence at the SPS in the years 2000's to its fine characterisation at LHC nowadays (Sec. 2|II). It is explored through the study of its signatures and, for a long time, was considered as a well understood medium. Recently, it has been observed that small systems exhibit most of the signs usually attributed to the QGP: long range correlation in the lowest multiplicity pp collisions[167], collective flow [168][169], heavy quarkonia suppression [170][1]. This observation questions the very foundations of the QGP concept: either the QGP physics picture in heavy ion collisions must be re-designed and further rooted on pp collisions, or conversely, the QCD physics in small systems should be extended with new features to introduce collectivity. One way or the other, a better description of

[1] Only the thermal photons and jet quenching signatures have not been observed in small systems (yet), whereas they are present in heavy-ion collisions. The investigation of these two signatures in small systems will be further examined in the LHC Run-3 and Run-4 [171].

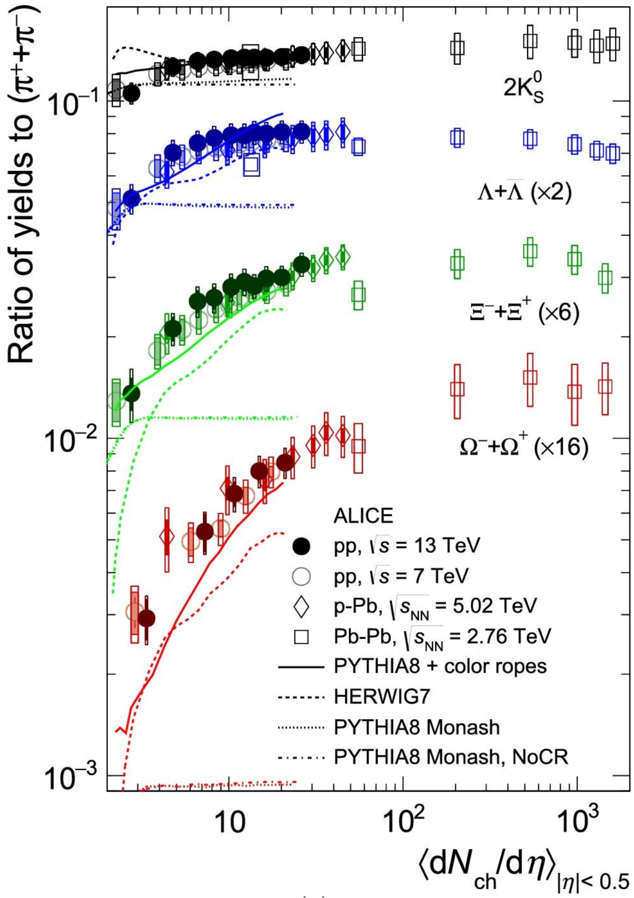

(a)

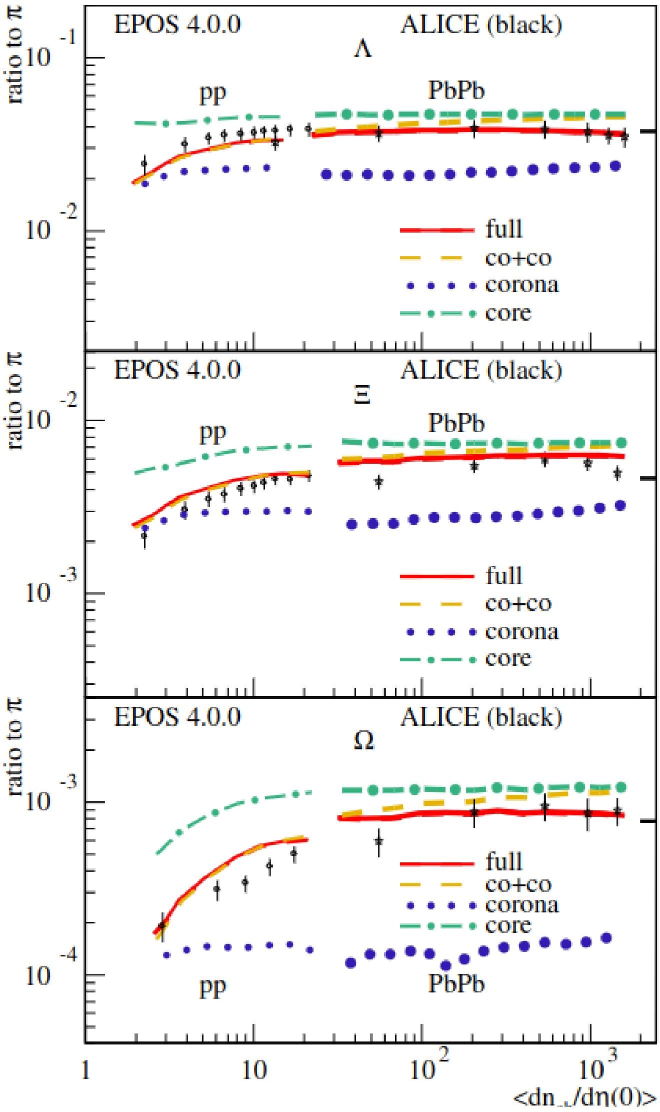

(b)

Fig. 6.1: Integrated strange hadrons-to-pions yield ratio as a function of the average charged particle multiplicity at mid-rapidity in ALICE, compared to different MC predictions. On the left, it is measured in pp at $\sqrt{s}$ = 7 and 13 TeV, p-Pb at $\sqrt{s_{\mathrm{NN}}}$= 5.02 TeV, Pb-Pb collisions at $\sqrt{s_{\mathrm{NN}}}$= 2.76 TeV, and compared to Pythia 8 and Herwig [172]; on the right, these are measurements in pp at $\sqrt{s}$ = 7 TeV and Pb-Pb collisions at $\sqrt{s_{\mathrm{NN}}}$= 2.76 TeV, with different predictions from Epos [173].

the pp and heavy-ion collision dynamics appears as an absolute must, in order to a continuum of physics.

One of the key historical signatures of QGP is the strangeness enhancement which consists in the enhanced yield of multi-strange hadrons in heavy ion collisions with respect to small systems (Sec. 2|II-B). Such yields also scale smoothly with the charged particle multiplicity in pp collisions (Sec. 2|II-C, Fig. 2.15). Different models using fundamentally different mechanisms manage to reproduce qualitatively this trend (Fig. 6.1). On one hand, Pythia models the quark hadronisation using the Lund Strings; these correspond to gluon fields, that break whenever the string ten-

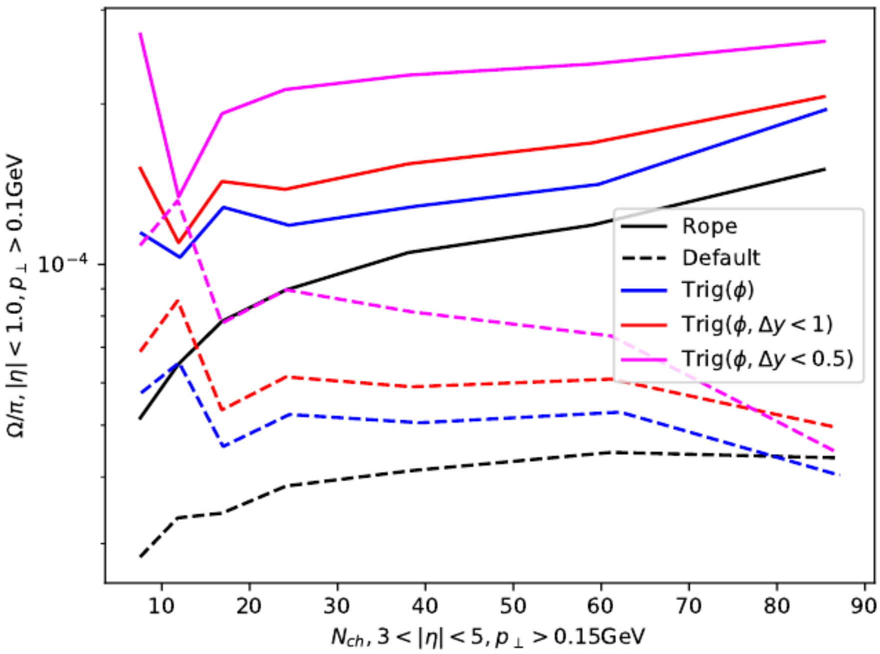

Fig. 6.2: PYTHIA 8 predictions for the Ω-to-$\pi^{\pm}$ yield ratio as a function of the charged particle multiplicity in pp collisions at $\sqrt{s} = 13$ TeV, in presence of a $\phi(1020)$ resonance (colour lines) or not (black line). The default PYTHIA configuration (PYTHIA 8, tune: Monash 2013) is indicated in dashed line, whereas the full curves represent the case with the colour ropes enabled.

sion energy is high enough and thus leading to the formation of hadrons, similarly as in Fig. 2.7. Both pp and heavy-ion collision physics originate from the interaction of these strings, *i.e.* this approach assumes the absence of a QGP. On the other hand, EPOS relies on a core-corona model: a dense core hosting a QGP-like collective medium, surrounded by a hadron gas corona [174]. So far, neither of these approaches has been able to provide an unambiguous explanation on the emergence of collective phenomena in small systems. Further experimental inputs are required in order to distinguish them, and finally identify the hadron production mechanisms.

A way to shed more light on the situation is to perform more multi-differential study, typically of the angular and rapidity correlations between different hadron species. These bring informations on the quark production, and consequently on the hadronisation. Two hadrons produced out of the breaking of a colour string into a quark-antiquark pair, as modeled by PYTHIA, should exhibit a strong local correlations. On the other hand, if the quarks are produced in the early stage of the collision – the so-called "prehadrons" in EPOS framework [173] – and hadronise later, that correlation should vanish.

One example of such measurement comes from the PYTHIA experts; since strangeness is conserved by the strong interaction, the number of strange hadrons is expected to be exactly compensated by the number of anti-strange hadrons, leading to a correlation between these hadrons[2]. In particular, within the standard

[2] As a side note, since all the strange hadrons are correlated, one can control to some extent the strangeness content within an event using a trigger on strange particle, Ξ or Ω for example.

Lund string framework, multi-strange baryons can be produced through a diquark-antidiaquark string breaking. However, the "recent" developments towards heavy-ion collisions – namely the colour reconnection and colour rope [175][176][177] – offer new production mechanisms. As a consequence, it is predicted that i) the Ω abundancy increases in presence of a $\phi(1020)$ in the event, and ii) this enhancement gets more prominent as the gap in rapidity between these two particles decreases.

So far, no such correlation has ever been measured. A similar observable has been studied recently [178], that analyses the angular correlations between the multi-strange baryon $\bar{\Xi}^{\pm}$ and $p^{\pm}$, $\pi^{\pm}$, $K^{\pm}$, $\bar{\Lambda}$, $\bar{\Xi}^{\pm}$ itself. It was not extended to $\phi(1020)$ resonance nor repeated with Ω baryons, though. Therefore, this analysis aims to check this prediction via the measurement of correlated production of Ω and $\phi(1020)$ over all the pp collisions at a centre-of-mass energy of 13 TeV collected throughout the LHC Run-2 by ALICE. In order to reduce as much as possible the background contamination, such measurement requires a trigger with a high purity, and thus good control capabilities over the amount of signal and the background for the trigger. For that reason and contrarily to the PYTHIA's prediction, the trigger is on the Ω particles and not the $\phi(1020)$, the former offering a more governable purity.

Since the Ξ baryon is much more produced than the Ω, two measurements are performed : first, the correlated production of Ξ and $\phi(1020)$, and then the one of Ω and $\phi(1020)$. In this way, the feasibility of such measurement can be checked on the Ξ, and if so, it will be repeated with the Ω.

By design, this kind of analysis relies on two categories of particles: the *trigger particles*, which is then correlated to the particles of interest in the event, the *associated particles*. In the present chapter, the term *trigger particle* designates either a Ξ or a Ω baryon, and the *associated particle* corresponds to the $\phi(1020)$ resonance.

II Data samples and event selection

II-A The data samples

Considering their relatively low yield – about 2×10^{-2} Ξ and $\sim 1.85 \times 10^{-3}$ Ω, and $\sim 3.8 \times 10^{-2}$ $\phi(1020)$ at mid-rapidity [142] – the correlation between these particles requires all the data available. Therefore, this second analysis employs the same real and simulated data samples as in the first one, in Chap. 5. It means that all pp collisions at centre-of-mass energy of 13 TeV collected in 2016, 2017 and 2018 are put to use (Sec. 5|II-A).

Contrarily to the first analysis, this one exploits data in AOD format, as it does not necessitate such a fine control over the data reconstruction. The analysed events also come from the second reconstruction cycle, the pass-2.

II-B The event selection

All the event selections employed in the first analysis (Sec. 5|II-B) are also applied here. These are complemented by an additional requirement on the type of

Multiplicity Class	I	II	III	IV	V
$\sigma\ /\sigma_{\mathrm{INEL}>0}$	0-0.01%	0.01-0.1%	0.1-0.5%	0.5-1%	1-5%
$\langle \mathrm{d}N_{\mathrm{ch}}/\mathrm{d}\eta \rangle$	$35.37^{+0.92}_{-0.86}$	$30.89^{+0.57}_{-0.51}$	$26.96^{+0.37}_{-0.30}$	$24.23^{+0.36}_{-0.30}$	$20.02^{+0.27}_{-0.22}$
Multiplicity Class	VI	VII	VIII	IX	X
$\sigma\ /\sigma_{\mathrm{INEL}>0}$	5-10%	10-15%	15-20%	20-30%	30-40%
$\langle \mathrm{d}N_{\mathrm{ch}}/\mathrm{d}\eta \rangle$	$16.17^{+0.22}_{-0.18}$	$13.77^{+0.19}_{-0.16}$	$12.04^{+0.17}_{-0.14}$	$10.02^{+0.14}_{-0.11}$	$7.95^{+0.11}_{-0.09}$
Multiplicity Class	XI	XII	XIII		
$\sigma\ /\sigma_{\mathrm{INEL}>0}$	40-50%	50-70%	70-100%		
$\langle \mathrm{d}N_{\mathrm{ch}}/\mathrm{d}\eta \rangle$	$6.32^{+0.09}_{-0.07}$	$4.50^{+0.07}_{-0.05}$	$2.55^{+0.04}_{-0.03}$		

Table 6.1: Event multiplicity classes, with the corresponding fraction of the total inelastic cross section INEL > 0 ($\sigma\ /\sigma_{\mathrm{INEL}>0}$) and average charged particle multiplicity at mid-rapidity, $\langle \mathrm{d}N_{\mathrm{ch}}/\mathrm{d}\eta \rangle$. Table taken from [181][182].

event.

The behaviour of the hadronic interactions at high energies is typically described by the Regge theory[179]. There exists two classes of interaction: the elastic collisions – when the initial and final states of the interaction are the same – and inelastic (INEL) collisions, that involve the production of new particles. The latter subdivides into two categories: the diffractive and non-diffractive processes. The former combines single and double diffractive processes. Within the framework of the Regge theory, the diffractive processes occur respectively when either or both incoming protons become an excited system – due to the exchange of Pomerons –, that later decay into stable final-state particles emitted close to the mother direction, *i.e.* close to beam, at very forward rapidity [180].

(1) INEL>0
(NB) = corrigé en A×ε en fait ≠ raw Nch mais corrected Nch

This analysis focuses on hadrons produced in inelastic collisions at mid-rapidity, hence originating *a priori* from non-diffractive processes. Experimentally, this kind of inelastic collisions are selected by requiring, at least, ~~one~~ reconstructed SPD tracklet in $|\eta| < 1$. This condition is commonly refered as INEL > 0[3].

Moreover, two estimators can be considered for the multiplicity determination: the total charge deposited in the VZERO scintillator arrays in $-3.7 < \eta < -1.7$ and $2.8 < \eta < 5.1$ (VZERO-M amplitude, Sec. 5|IV-B.vii); the number of reconstructed SPD tracklets in $|\eta| < 1$ ($N^{|\eta|<1}_{tracklets}$). Although the choice between these two estimators seems innocent/arbitrary, notice that they cover different pseudo-rapidity regions: the former estimates the multiplicity (at mid-rapidity) based on the energy deposited at forward rapidity, while the latter counts the number of tracklets at mid-rapidity. This difference may have some implications. Since the observable is a yield ratio at mid-rapidity, the considered particle and/or its decay products may contribute to the number of reconstructed SPD tracklets, thus self-biasing the multiplicity event. In general, the separation between the region of interest and the

[3]Note that INEL > 0 events do not correspond to the total number of inelastic collisions INEL, due to the acceptance and efficiency of the INEL > 0 condition, the beam-induced background selections, the number of un-reconstructed events (because no preliminary primary vertex ~~could be~~ formed for example, Sec. 3|II-D.i). In fact, for $\mathrm{MB_{AND}}$, the INEL > 0 encompasses about $76.3^{+2.2}_{-0.8}\%$ of the total number of inelastic collisions [153].

je ne suis pas sûr du coup (1) de voir ce que ce chiffre recouvre
MBand = raw // INEL>0 = corrigé...

volume covered by the multiplicity estimator should be as large as possible, in order to avoid or limit this auto-correlation. For that reason, the VZERO-M is taken as default multiplicity estimator.

It follows that the events are divided into thirteen multiplicity classes, presented in Tab. 6.1. The Sec. 6|III will show that the reconstruction of cascade and a $\phi(1020)$ resonance in the same event requires at least five tracks. Therefore, the correlations between these two hadrons are measured for events comprised between the 50% with the lowest multiplicity to the 1% with the highest multiplicity,

III Analysis of the multi-strange baryon-$\phi(1020)$ correlation

III-A The correlation function

The objective is to measure the correlation between a multi-strange baryon, either $\overline{\Xi}^{\pm}$ or $\overline{\Omega}^{\pm}$, and a $\phi(1020)$ meson. Their correlation is evaluated by associating them in pairs, and observing how the pair population is distributed according to a given variable. More precisely, the focus here is on the correlated yield of $\phi(1020)$ meson in events containing, at least, one multi-strange baryon. Therefore, the observable should be the per-trigger yield of the $\phi(1020)$ meson as a function of the difference in p_{T}, rapidity, azimuthal angle between the trigger particle and the associated particles, and the multiplicity of the event,

$$\frac{1}{N_{\mathrm{trigger}}} \cdot \frac{\mathrm{d}N_{\mathrm{pairs}}}{\mathrm{d}y} = \frac{1}{\mathrm{d}N_{\mathrm{cascade}}/\mathrm{d}y} \cdot \frac{\mathrm{d}N_{\mathrm{pairs}}}{\mathrm{d}y} \left(\Delta p_{\mathrm{T}}, \Delta\varphi, \Delta y, \mathrm{multiplicity}\right), \tag{6.1}$$

where the N_{pairs} corresponds to the number of cascade-$\phi(1020)$ pairs.

It will become clear in the next sections that a multi-differential observable such as in Eq. 6.1 cannot be measured currently with the LHC Run-2 data, due to the lack of statistics. Nonetheless, this correlation may still be investigated, although less differentially. Along this line, this analysis proposes to measure the per-trigger yield as a function of one variable at a time, *i.e.*

$$\frac{1}{\mathrm{d}N_{\mathrm{cascade}}/\mathrm{d}y} \cdot \frac{\mathrm{d}^2 N_{\mathrm{pairs}}}{\mathrm{d}y\mathrm{d}\Delta y}, \tag{6.2}$$

$$\frac{1}{\mathrm{d}N_{\mathrm{cascade}}/\mathrm{d}y} \cdot \frac{\mathrm{d}^2 N_{\mathrm{pairs}}}{\mathrm{d}y\mathrm{d}\Delta \varphi}, \tag{6.3}$$

$$\frac{1}{\mathrm{d}N_{\mathrm{cascade}}/\mathrm{d}y} \cdot \frac{\mathrm{d}^2 N_{\mathrm{pairs}}}{\mathrm{d}y\mathrm{d}\Delta p_{\mathrm{T}}}. \tag{6.4}$$

A few words on the analysis strategy before proceeding. Therefore, only events containing a Ξ or Ω candidate are selected; from these, the particles of interest are reconstructed using the selections in Sec. 6|III-C. After calculating the invariant mass of each candidate, they are sorted as a function of their p_{T}[4] and – only for the particles of interest – the difference of rapidity Δy, azimuthal angle $\Delta\varphi$ and transverse momentum Δp_{T} with respect to the trigger particle. The yields of both species are extracted from their respective invariant mass distributions, for each p_{T}, Δp_{T}, Δy and Δp_{T} bins, as presented in Sec. 6|III-D.

In the present measurement, the associated particles comprise solely the $\phi(1020)$. However, the analysis has been designed in view of extending the correlations to other kind of hadrons, namely $\mathrm{p}^{\pm}$, $\pi^{\pm}$, $\mathrm{K}^{\pm}$, K^{*0}, $\mathrm{K}^0_{\mathrm{S}}$, $\bar{\Lambda}$, $\bar{\Xi}^{\pm}$ and $\bar{\Omega}^{\pm}$.

Particle	Quark content	Mass (MeV/c^2)	Lifetime $c.\tau$ (cm) or Width Γ (MeV/c^2)	Dominant decay channel	B.R.
$\phi(1020)$	$s\bar{s}$	1019.461 ± 0.020	$\Gamma = 4.249$	$\mathrm{K}^+\ \mathrm{K}^-$	49.1%
$\Lambda\ (\overline{\Lambda})$	$uds\ (\bar{u}\bar{d}\bar{s})$	1115.683 ± 0.006	$c.\tau = 7.89$	$\mathrm{p}\ \pi^-(\overline{\mathrm{p}}\ \pi^+)$	63.9%
$\Xi^-\ (\overline{\Xi}^+)$	$dss\ (\bar{d}\bar{s}\bar{s})$	1321.71 ± 0.07	$c.\tau = 4.91$	$\Lambda\ \pi^-(\overline{\Lambda}\ \pi^+)$	99.9%
$\Omega^-\ (\overline{\Omega}^+)$	$sss\ (\bar{s}\bar{s}\bar{s})$	1672.45 ± 0.23	$c.\tau = 2.461$	$\Lambda\ \mathrm{K}^-\ (\overline{\Lambda}\ \mathrm{K}^+)$	67.8%

Table 6.2: A few characteristics, as of 2023, of the Λ, Ξ, Ω hyperons and the $\phi(1020)$ meson resonance: quark content, mass, relative mass difference values with their associated uncertainties and their dominant decay channel as well as the corresponding branching ratio [42].

The multi-strange baryons being already introduced in details in Chap. 4 and Chap. 5, we will be concentrating on the $\phi(1020)$ resonance. As presented in Tab. 6.2, it has a mass of 1019.461 MeV and a width of 4.249 MeV, equivalent to a lifetime of approximately 46 fm. It mainly decays via strong interaction into a pair of oppositely charged kaons with a branching ratio of 49.1%, $\phi(1020) \to \mathrm{K}^+\mathrm{K}^-$, as depicted in Fig. 6.3. In the following, the $\phi(1020)$ will be studied in this decay channel.

The $\phi(1020)$ resonance is reconstructed by forming pairs of oppositely charged tracks; similarly to the V0s, the positively charged daughter is called the *positive* particle, the other the *negative* particle. As a consequence of the strong nature of the decay, its short flight distance makes the decay vertex undistinguable from the primary interaction point. Thereby, the misassociated pairs cannot be discarded using geometrical selections – as opposed to the topological reconstruction of V0s and cascades –, leading to a substantial combinatorial background. This is the reason why it was decided to consider the multi-strange baryons as trigger particles, instead of the $\phi(1020)$ resonance meson. This background can be evaluated and subtracted by making use of two techniques here, presented later in Sec. 6|III-C.

[4] This is necessary in order to correct for the detector acceptance and the reconstruction efficiency (Sec. 6|III-F).

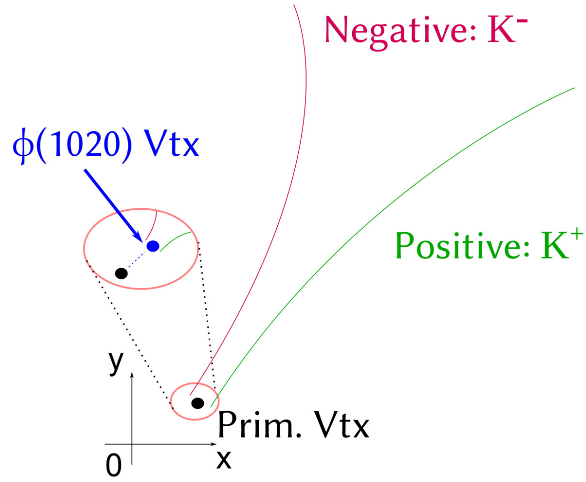

Fig. 6.3: Scheme of the resonance decay of the $\phi(1020)$ meson. Modified version of the original figure [139].

III-B Cascade candidate selections

As in Chap. 5, the identification of multi-strange baryons relies on their characteristic cascade decay channel. Their reconstruction therefore exploits the same topological and kinematic selection variables, Sec. 5|III-A and 5|III-B. These are presented in Tab. 6.3.

There is however one important difference with respect to the first analysis. While the latter measures the mass integrated over all the p_T bins[5], the objective here is to extract the yield of both trigger and associated particles, these being obtained from their p_T-differential production rate.

$$\frac{dN}{dy} = \int_0^{+\infty} \frac{d^2N}{dp_T dy} dp_T \tag{6.5}$$

Thereby, the candidates are sorted as a function of their transverse momentum according to, for $\overset{(-)}{\Xi}{}^{\pm}$ baryons, thirteen p_T intervals:

[0.6; 1.0) GeV/c, [1.0; 1.2) GeV/c, [1.2; 1.4) GeV/c, [1.4; 1.6) GeV/c, [1.6; 1.8) GeV/c, [1.8; 2.0) GeV/c, [2.0; 2.2) GeV/c, [2.2; 2.5) GeV/c, [2.5; 2.9) GeV/c, [2.9; 3.4) GeV/c, [3.4; 4.0) GeV/c, [4.0; 5.0) GeV/c, [5.0; 6.5) GeV/c.

For what concerns the measurement of the $\overset{(-)}{\Omega}{}^{\pm}$ hyperons, due to their lower statistics, six intervals are being used:

[1.0; 1.6) GeV/c, [1.6; 2.2) GeV/c, [2.2; 2.6) GeV/c, [2.6; 3.0) GeV/c, [3.0; 3.8) GeV/c, [3.8; 6.5) GeV/c.

III-C Resonance candidate selections

As explained in the header of this section, the $\phi(1020)$ meson candidates are reconstructed as a pair of K^+ and K^-. Since the decay topology cannot be exploited

[5] There is one exception in Sec. 5|IV-B.iii, where the p_T-differential measurement of the mass is performed in order to check the stability of the results with the transverse momentum.

<table>
<tr><th>Candidate variable</th><th>Selections $\overline{\Xi}^{\pm}$</th><th>Selections $\overline{\Omega}^{\pm}$</th></tr>
<tr><td>Cascade p_{T} interval (GeV/c)</td><td colspan="2">$0.6 < p_{\mathrm{T}} < 6.5$</td></tr>
<tr><td>Cascade rapidity interval</td><td colspan="2">$|y| < 0.5$</td></tr>
<tr><td>Competing mass rejection (GeV/c^2)</td><td>✗</td><td>> 0.008</td></tr>
<tr><td>MC association (MC only)</td><td colspan="2">Correct identity assumption</td></tr>
<tr><th>Track variable</th><th>Selections $\overline{\Xi}^{\pm}$</th><th>Selections $\overline{\Omega}^{\pm}$</th></tr>
<tr><td>Pseudo-rapidity interval</td><td colspan="2">$|\eta| < 0.8$</td></tr>
<tr><td>TPC refit</td><td colspan="2">✓</td></tr>
<tr><td>Nbr of crossed TPC readout rows</td><td colspan="2">> 70</td></tr>
<tr><td>$n_{\sigma}^{\mathrm{TPC}}$</td><td colspan="2">$< 3$</td></tr>
<tr><td>Out-of-bunch pile-up rejection</td><td colspan="2">at least one track with ITS-TOF matching</td></tr>
<tr><th>Topological variable</th><th>Selections $\overline{\Xi}^{\pm}$</th><th>Selections $\overline{\Omega}^{\pm}$</th></tr>
<tr><td>V0</td><td></td><td></td></tr>
<tr><td>V0 decay radius (cm)</td><td>> 1.2</td><td>> 1.1</td></tr>
<tr><td>V0 cosine of pointing angle</td><td colspan="2">> 0.97</td></tr>
<tr><td>$|m(V0)$ - $m_{\mathrm{PDG}}\Lambda$ $|$ (GeV/c^2)</td><td colspan="2">< 0.008</td></tr>
<tr><td>DCA proton to prim. vtx (cm)</td><td colspan="2">> 0.03</td></tr>
<tr><td>DCA pion to prim. vtx (cm)</td><td colspan="2">> 0.04</td></tr>
<tr><td>DCA V0 to prim. vtx (cm)</td><td colspan="2">> 0.06</td></tr>
<tr><td>DCA between V0 daughters (std dev)</td><td colspan="2">< 1.5</td></tr>
<tr><td>Cascade</td><td></td><td></td></tr>
<tr><td>Cascade decay radius (cm)</td><td>> 0.6</td><td>> 0.5</td></tr>
<tr><td>Cascade Lifetime (cm)</td><td colspan="2">$< 3 \times c.\tau$</td></tr>
<tr><td>DCA bachelor to prim. vtx (cm)</td><td colspan="2">> 0.04</td></tr>
<tr><td>DCA between cascade daughters (std dev)</td><td colspan="2">< 1.3</td></tr>
<tr><td>Cascade cosine of pointing angle</td><td colspan="2">> 0.998</td></tr>
<tr><td>Bachelor-proton pointing angle (rad)</td><td colspan="2">> 0.04</td></tr>
</table>

Table 6.3: Summary of the topological and track selections, as well as the associated cut values, used in the reconstruction of $\overline{\Xi}^{\pm}$ and $\overline{\Omega}^{\pm}$ in pp events at $\sqrt{s} = 13$ TeV. The *competing mass rejection* refers to the removal of the background contamination from other mass hypotheses (Sec. 4|II-B.iii)

to reduce the amount of combinatorial background, most of the selection criteria focus on the quality of daughter tracks[6]. These can be found in Tab. 6.4.

Beyond the track selections in common with the hyperons (Sec. 5|III-A), the track quality is improved by requiring a reduced χ^2 up to 36 and 4, for the ITS and TPC standalone tracks respectively[7]. The agreement between the TPC standalone

[6] In this analysis, the focus is on the $\phi(1020)$ yield in presence of a multi-strange baryon. However, note that the same considerations would also apply in the case of the K^{*0} resonance, that decays strongly into a $\mathrm{K}^{\pm}$ and a $\pi^{\pm}$ at ~100%.

[7] The tighter selection on the goodness of the TPC standalone track is related to the fact that TPC is the main tracking device in ALICE and so, contributes the most to the track quality.

Candidate variable	Selection criterion
Resonance rapidity interval	$\|y\| < 0.5$
MC association (MC only)	Correct identity assumption
Track variable	Selection criterion
p_{T} interval (GeV/c)	$0.15 < p_{\mathrm{T}} < 20$
Pseudo-rapidity interval	$\|\eta\| < 0.8$
ITS refit	✔
TPC refit	✔
Kink Topology	✗
n_σ^{TPC}	< 2
n_σ^{TOF} (veto only)	< 3
Nbr of crossed TPC readout rows	> 70
Fraction of crossed TPC readout rows over findable clusters	≥ 0.8
Goodness of the TPC standalone track, $\chi^2_{\mathrm{TPC}}/N_{\mathrm{cluster}}$	< 4
Global and TPC standalone track matching, $\chi^2_{\mathrm{TPC\text{-}CG}}$	< 36
Goodness of the ITS standalone track, $\chi^2_{\mathrm{ITS}}/N_{\mathrm{cluster}}$	< 36
Nbr of associated SPD clusters	≥ 1
DCA to prim. vtx (cm)	$< 0.0105 + 0.035\ p_{\mathrm{T}}\ ^{-1.01}$
DCA to prim. vtx along z (cm)	< 2

Table 6.4: Summary of the track and candidate selections used for the reconstruction of $\phi(1020)$.

track, constrained to the preliminary primary vertex (Sec. 3|II-D), and global track is quantified by the so-called *golden* χ^2; its value should be smaller than 36. Along the same line, each track must have passed the final refit in the ITS, and be associated with at least one hit in the innermost ITS layers, the most granular detector in ALICE. To ensure a good momentum resolution, the fraction of found crossed TPC readout rows over the number of findable clusters must reach at least 80%.

Since the decay point cannot be resolved from the primary vertex, the formation of a resonance candidate uses primary tracks, contrarily to the V0 and cascade reconstruction. These are identified by imposing that their distance of closest approach to the primary vertex is smaller than a critical value. In particular, in the transverse plane, the latter is given by a p_{T}-dependent *ad-hoc* formula in order to be even more selective.

Further combinatorial background is suppressed by applying PID criteria. It is required that each track agrees with a $\mathrm{K}^{\pm}$ mass hypothesis within $n_\sigma^{\mathrm{TPC}} = \pm 3$. Whenever it matches a hit in the TOF detector[8], the time-of-flight informations supplement the selection on the nature of the decay daughter using the PID estimator in Eq. 3.6, n_σ^{TOF}.

[8] Since a substantial amount of particles do not reach the TOF detector or cannot be matched with a hit, the associated hadron identification capabilities can only be used as a veto, in complement to other PID informations; otherwise, this would drastically affect the track reconstruction efficiency.

Finally, any pair of tracks satisfying the above criteria and lying at mid-rapidity, $|y| < 0.5$, is considered as a $\phi(1020)$ meson candidate. Their measurement is performed in the following eight p_{T} intervals:

$[0.4; 0.8)$ GeV/c, $[0.8; 1.2)$ GeV/c, $[1.2; 1.8)$ GeV/c, $[1.8; 2.6)$ GeV/c, $[2.6; 3.4)$ GeV/c, $[3.4; 4.2)$ GeV/c, $[4.2; 5)$ GeV/c, $[5; 11)$ GeV/c.

III-D The raw signal extraction

III-D.i In the case of multi-strange baryons

The raw signal extraction for the trigger particle follows the very same procedure as in the first analysis. Therefore, the invariant mass peak is modeled by a modified Gaussian (Eq. 5|III-C.ii), and the background by a linear function. The amount of raw signal and background are estimated by bin counting, over the same regions as in Sec. 5|III-C.

The Figs. 6.4, 6.5 show the invariant mass distribution in the different p_{T} intervals for Ξ^-, $\overline{\Xi}^+$, Ω^- and $\overline{\Omega}^+$ respectively.

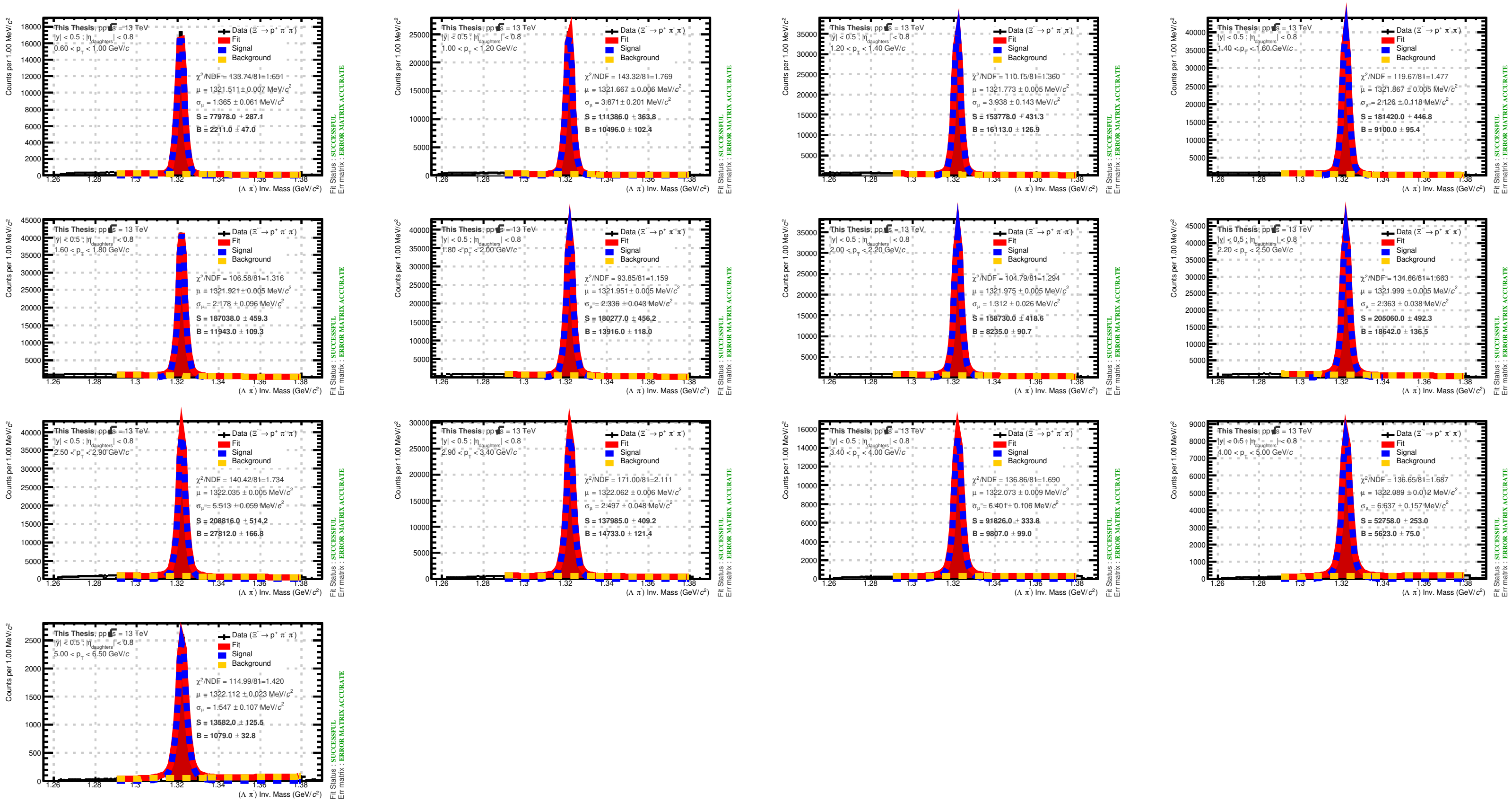

Fig. 6.4: Invariant mass spectra of the Ξ^- candidates in pp collisions at $\sqrt{s} = 13$ TeV, fitted by the combination of three Gaussian functions for the peak and a decreasing exponential function for the background. The amounts of signal and background have been obtained via bin counting in the peak (red area) and side-bands region (gray area).

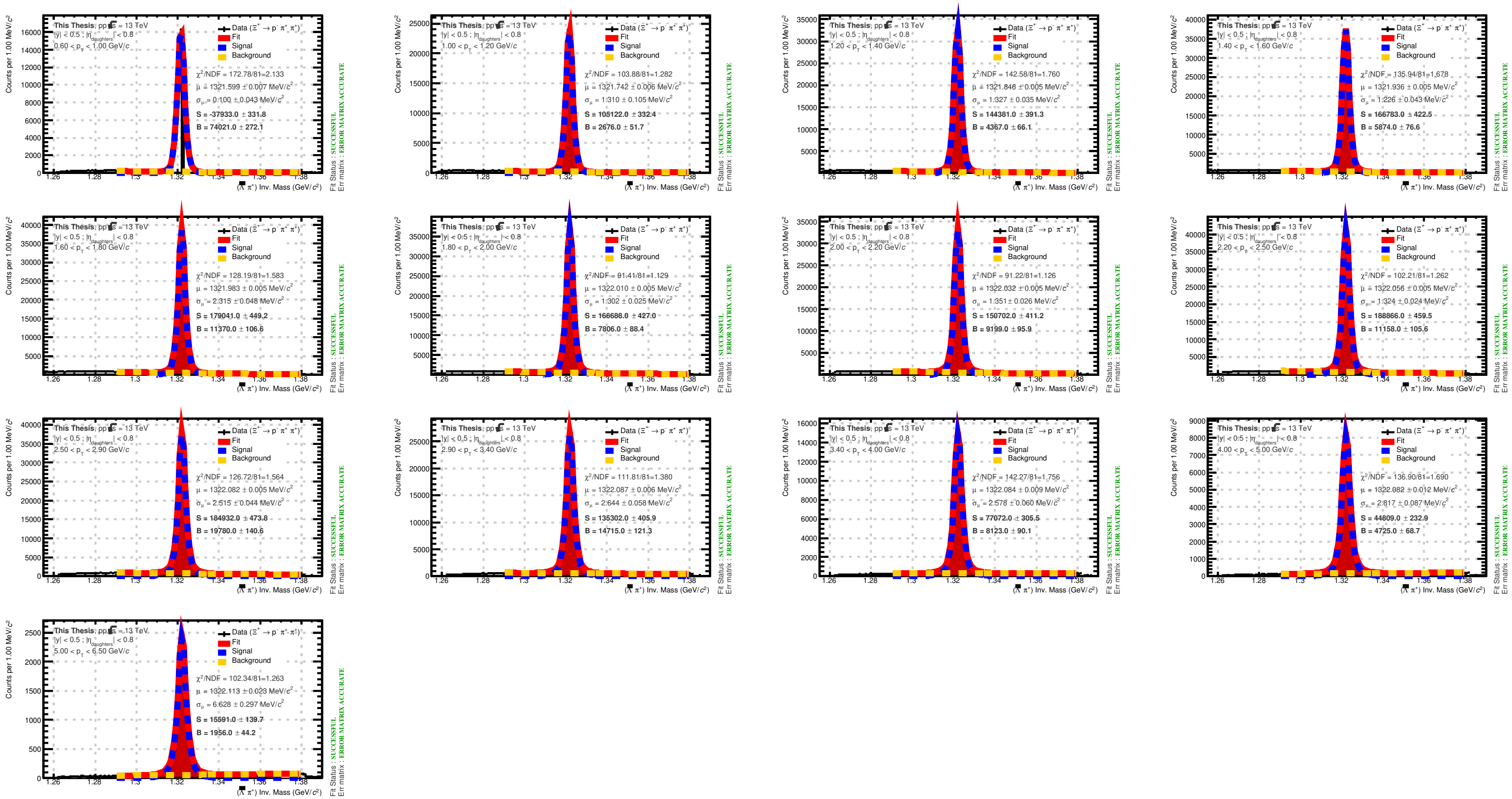

Fig. 6.5: Invariant mass spectra of the $\overline{\Xi}^{+}$ candidates in pp collisions at $\sqrt{s}$ = 13 TeV, fitted by the combination of three Gaussian functions for the peak and a decreasing exponential function for the background. The amounts of signal and background have been obtained via bin counting in the peak (red area) and side-bands region (gray area).

III-D.ii In the case of $\phi(1020)$ meson

The invariant mass of each resonance candidate is calculated using the Eq. 6.8 and making the assumption of a $\mathrm{K}^{\pm}$ mass for both decay daughters. The top left Fig. 6.6 present the invariant mass spectra of the $\phi(1020)$ meson for every p_{T} intervals.

$$M^2_{\text{candidate}}[\phi(1020)] = (E_{\text{pos.}} + E_{\text{neg.}})^2 - (\vec{p}_{\text{pos.}} + \vec{p}_{\text{neg.}})^2 \tag{6.6}$$

$$= \left(\sqrt{\vec{p}^{\,2}_{\text{pos.}} + m^2_{\text{pos.}}} + \sqrt{\vec{p}^{\,2}_{\text{neg.}} + m^2_{\text{neg.}}}\right)^2 - (\vec{p}_{\text{pos.}} + \vec{p}_{\text{neg.}})^2 \tag{6.7}$$

$$= \left(\sqrt{\vec{p}^{\,2}_{\text{pos.}} + m^2_{\mathrm{K}^+}} + \sqrt{\vec{p}^{\,2}_{\text{neg.}} + m^2_{\mathrm{K}^-}}\right)^2 - (\vec{p}_{\text{pos.}} + \vec{p}_{\text{neg.}})^2 \tag{6.8}$$

An excess of counts emerges around the tabulated mass of the $\phi(1020)$, $m_{\mathrm{PDG}} = 1019.461\ \mathrm{MeV}/c^2$, on top of a smooth background. The latter dominates the invariant mass distribution, and derives *a priori* mainly from combinatorics of the tracks. The origin of the background being known, it can thus be removed[9]. The basic idea consists to reproduce the background shape by forming uncorrelated pairs of tracks. There exist two approaches[10]:

- **Event mixing technique:** by definition, particles originating from different events could not have been produced together, and so are uncorrelated. Consequently, the association of tracks from different events should *in principle* result in combinatorial background. This is core concept of event mixing. Therefore, each positively charged track passing the above selections (Sec. 6|III-C) gets paired to a negatively charged track from another event, under the exact same set of cuts, and vice versa. Each event is mixed with five other events at most. In order to estimate correctly the combinatorial background, the mixing has to be performed between events with similar collision kinematics. To ensure that, it is required that i) the longitudinal position of their primary vertex agrees within a range of ± 1 cm, and ii) their difference in terms of event multiplicity should be sufficiently low, such that they belongs to the same multiplicity class. Moreover, since the several events are involved in the mixing, the mixed-event invariant mass distribution needs to be normalised, such that it fits the same-event distribution in certain invariant mass region. This normalisation is usually performed far from the peak, in the side-bands regions purely populated by combinatorial background.

- **Rotating procedure:** the excess of counts in the invariant mass distributions originates from correlated pairs of K^+ and K^- due to the $\phi(1020)$ meson decay. If the correlation of the pair could somehow be broken, the invariant mass

[9] Alternatively, one could try to find a functional form that describes correctly the shape of the background, as it was done in Chap. 5. For instance, here, it could be modeled by a second order polynomial.

[10] In fact, there also exist a third approach. These resonances are formed out of two oppositely charged, *i.e.* unlike-charge, tracks. Particles of the same charge are uncorrelated with respect to the $\phi(1020)$ decay. Hence, by pairing like-charge tracks, $\mathrm{K}^+\ \mathrm{K}^+$ and $\mathrm{K}^-\ \mathrm{K}^-$, the combinatorial background can be estimated. However, this procedure has been implemented in the analysis, and so will not be used.

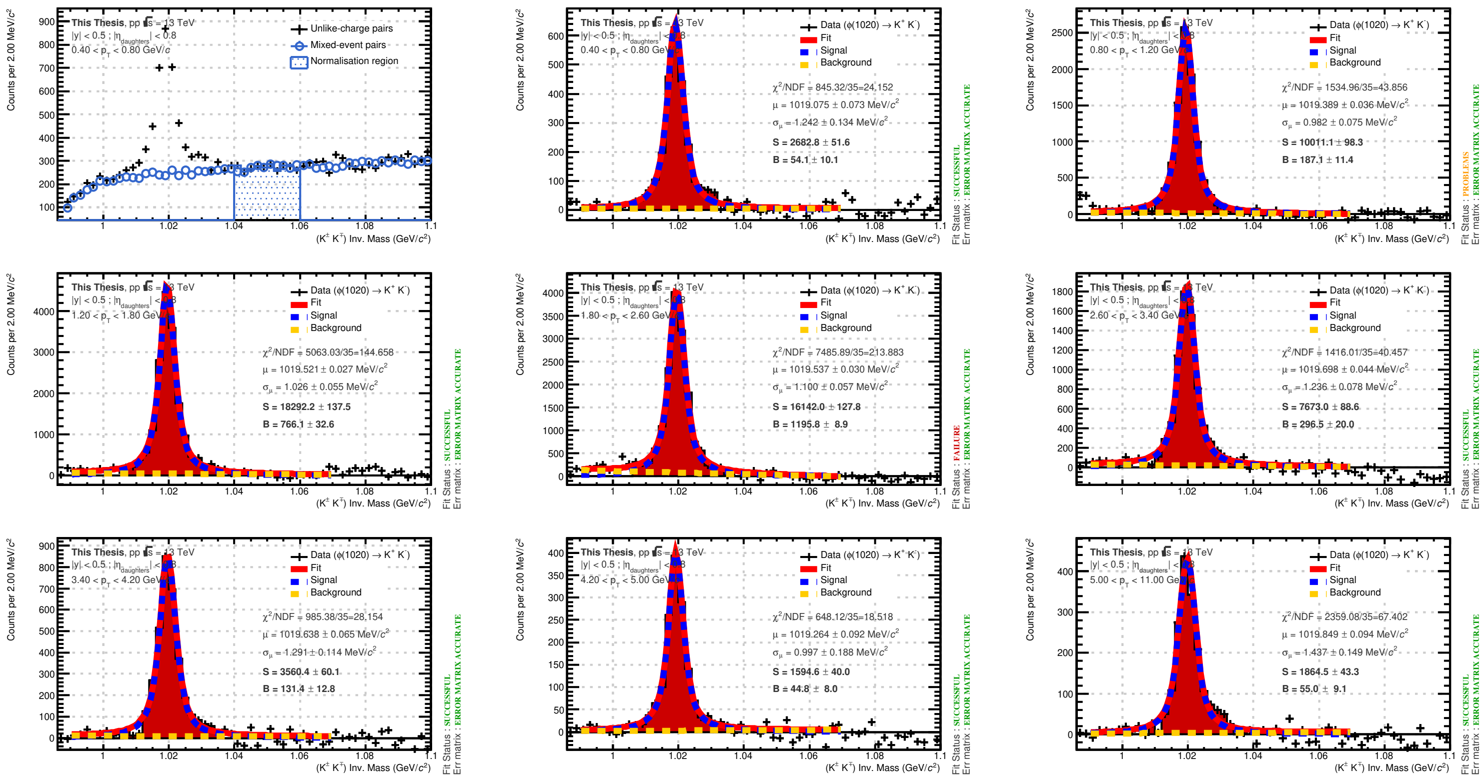

Fig. 6.6: Top left panel: Unlike-charge and mixed-event invariant mass distribution for p_{T} between 0.4 and 0.8 GeV/c. The other panels: Invariant mass spectra of the $\phi(1020)$ meson candidates in pp collisions at $\sqrt{s}$ = 13 TeV, fitted by the sum of a Voigt function for the peak and a linear function for the residual background. The amounts of signal have been obtained as explained in Sec. 6|III-D.ii, while the background has been obtained via bin counting in the region covered by the red area, that is 1.005 and 1.035 GeV/c^2.

spectrum should be populated solely by combinatorial background. This can be achieved by considering the already formed pairs of kaons from the same event and rotating one of track by a significant amount, typically by an angle of 180°.

The event mixing technique is taken as the default option, as it will later facilitate another part of the analysis Sec. 6|III-G. The rotating procedure is going to be used in the systematic study.

Whatever the considered approach, the combinatorial background is subtracted from the invariant distribution, yielding to the Figs. 6.6. The invariant mass now sits on top of a small residual background. The signal is separated from the background through a (log-)likelyhood method.

The ideal signal for a resonance should exhibit a Breit-Wigner shape [183]. However, the invariant mass peak rather corresponds to the convolution of Breit-Wigner and Gaussian – due to the smearing induced by the detectors response – distributions, namely the Voigt profile in Eq. 6|III-D.ii.

$$\frac{\mathrm{d}N}{\mathrm{d}m_{\mathrm{inv}}} = A \cdot \frac{\Gamma}{(2\pi)^{3/2}\sigma} \int_{-\infty}^{\infty} \exp\left[-\frac{(m_{\mathrm{inv}} - m')^2}{2\sigma^2}\right] \frac{1}{(m' - \mu)^2 + \Gamma^2/4} \mathrm{d}m', \qquad (6.9)$$

where:

- A coincides with the integral of the function from 0 to $+\infty$,
- μ corresponds to the centre of the Voigt function,
- Γ is the resonance width,
- and σ describes the width of the Gaussian.

Only this function is considered for the peak description. Here, two types of Voigtian fits are considered: one with the resonance width fixed at the nominal value ($\Gamma = 4.249$ MeV/c^2), the other where it is allowed to vary freely. Concerning the residual background, as in the first analysis, different shapes can be considered: constant, linear, exponential functions, second order polynomial.

If the fitting procedure converges, the signal and background are estimated. As the Voigt function (resonance case) does not decrease as fast as a Gaussian (multi-strange baryon case) with the distance to centre, the amount of raw signal and background have to be evaluated differently. In this context, the peak region is defined in $[1.005; 1.035]$ GeV/c^2, and contains most of the signal and some background. Therefore, the raw signal is obtained by counting the number of candidates in this region and subtracting the background population; the latter is given by the integral of the background function over the same region, hence $S_{\text{counting}} = (S+B)_{\text{counting}} - B_{\text{integral}}$. The rest of the signal population sits outside the peak region, from 0.987354[11] to 1.005 GeV/c^2 and 1.035 to $+\infty$ GeV/c^2. Consequently, the integral of the Voigt function in these two regions provides an estimation of the missing signal population, which is then incorporated in the total raw signal $S = S_{\text{counting}}(1.005; 1.035) + S_{\text{integral}}(0.987354; 1.005) + S_{\text{integral}}(1.035; +\infty)$[12].

III-E Fraction of background cascade

As explained in the header of this section, the correlation between cascade and resonances goes through pairs of particle candidates. Thereby, as illustrated in Tab. 6.5, there exist four types of pairs depending on whether they are signal or background candidates.

In the ideal case, only correlation between a true $\ddot{\Xi}^{\pm}$ or $\ddot{\Omega}^{\pm}$ and an actual $\phi(1020)$ should be observed. As explained in Sec. 6|III-C, the contribution from the background resonances is already removed bin-by-bin first using an event mixing technique, and then the raw signal of $\phi(1020)$ is isolated from the residual background through a fit with a linear function. The only remaining source of correlation with background candidate comes from the multi-strange baryons. Considering the

[11]It corresponds to $2m_{\mathrm{K}^{\pm}} = 0.987354$GeV/$c^2$ with $m_{\mathrm{K}^{\pm}} = 0.493677$GeV/$c^2$ [42]. The population of $\phi(1020)$ cannot be found below this mass value because it is kinematically forbidden.

[12]In the analysis, the peak function is not integrated to + infinity, but rather up to a large mass value with respect to the $\phi(1020)$ mass – that is 5 GeV/c^2– such that most of the missing raw signal has been taken into account.

$\phi(1020)$ / $\Xi^{\pm}$ or $\Omega^{\pm}$	Signal candidate	Background candidate
Signal candidate	Signal-Signal	Signal-Background
Background candidate	Background-Signal	Background-Background

Table 6.5: Four types of cascade-resonance correlation in the analysis, depending on the cascade and resonance candidates. The red cells represent the correlations with a background trigger candidate, that must be removed.

purity of the sample, the contribution of the cascade background candidates could be assumed as negligible. This means that

$$\frac{1}{N_{\text{trigger}}} \cdot \frac{\mathrm{d}^2 N_{\text{pairs}}}{\mathrm{d}y\mathrm{d}X} = \frac{1}{N_{\text{trigger}}(S)} \cdot \frac{\mathrm{d}^2 N_{\phi(1020)}}{\mathrm{d}y\mathrm{d}X}\bigg|_{(S)\text{ trigger}-\ (S)\text{ associated pairs}} \tag{6.10}$$

$$\simeq \frac{1}{N_{\text{trigger}}(S+B)} \cdot \frac{\mathrm{d}^2 N_{\text{pairs}}}{\mathrm{d}y\mathrm{d}X}\bigg|_{(S+B)\text{ trigger}-\ (S)\text{ associated pairs}}, \tag{6.11}$$

where X corresponds to either Δy, $\Delta\varphi$ or Δp_{T}, $(S+B)$ signifies signal and background candidates, and (S) is for pure signal candidates.

An attempt is made to get as precise as possible. To that end, two measurements are performed: one in which cascades in the peak region are correlated to resonance candidates, and another with cascades from the side-bands region instead. Each of them provides a set of invariant mass distributions for the associated particles as a function of their rapidity, azimuthal angle and/or transverse momentum gap with respect to the trigger particle.

$$\frac{1}{N_{\text{trigger}}} \cdot \frac{\mathrm{d}^2 N_{\phi(1020)}}{\mathrm{d}y\mathrm{d}X} = \frac{1}{N_{\text{trigger}}(S)} \cdot \frac{\mathrm{d}^2 N_{\phi(1020)}}{\mathrm{d}y\mathrm{d}X}\bigg|_{(S)\text{ trigger}-\ (S)\text{ associated pairs}} \tag{6.12}$$

$$= \frac{1}{N_{\text{trigger}}(S+B) - N_{\text{trigger}}(B)} \cdot \left[\frac{\mathrm{d}^2 N_{\phi(1020)}}{\mathrm{d}y\mathrm{d}y}\bigg|_{(S+B)\text{ trigger}} - \frac{\mathrm{d}N_{\phi(1020)}}{\mathrm{d}y}\bigg|_{(B)\text{ trigger}} \right]. \tag{6.13}$$

III-F Acceptance and efficiency corrections

The raw signal quantifies the amount of multi-strange baryons or $\phi(1020)$ resonances reconstructed within the acceptance of the ALICE detector, and satisfying the selections in Tabs. 5.3 and 6.4. In fact, this quantity corresponds to a fraction of the total number of particles produced in the fiducial volume $|y| < 0.5$ due to i) the limited acceptance of the detector that prevents the reconstruction of tracks within certain region of the ALICE apparatus (beyond $|\eta| < 0.8$, deadzones), and ii) the finite reconstruction and selection efficiencies of the cascade and resonance decays. This fraction can be estimated using MC simulations.

In principle, the correction on the raw signal breaks down into two terms, one for each of the aforementioned contributions: the *acceptance*, that corresponds to the fraction of reconstructable particles in the fiducial volume among the total number of generated particles within the desired rapidity region ($|y| < 0.5$), and the *efficiency* given by the ratio of the number of reconstructed hadrons over the number of reconstructable ones in the same rapidity interval. The product of these two terms provides the acceptance and efficiency correction factors (Eq. 6.14).

$$\text{Acceptance} \times \text{Efficiency} = \frac{N^{\text{daughter in acc.}}_{\text{generated in } |y|<y_{\text{fid.}}}}{N_{\text{generated in } |y|<0.5}} \times \frac{N_{\text{reconstructed in } |y|<y_{\text{fid.}}}}{N^{\text{daughter in acc.}}_{\text{generated in } |y|<y_{\text{fid.}}}} \tag{6.14}$$

$$= \frac{N_{\text{reconstructed in } |y|<y_{\text{fid.}}}}{N_{\text{generated in } |y|<0.5}} \tag{6.15}$$

For the sake of simplicity, instead of evaluating these correction factors individually, this analysis goes directly for the product of the two (Eq. 6.15). Since the above selections impact differently low-p_{T} and high-p_{T} candidates, these acceptance and efficiency correction factors do depend strongly on the transverse momentum. Therefore, they have to be determined for every p_{T}-bin. Moreover, note that the branching ratio of the considered particle stands as an upper bound for the reconstruction efficiency, and so for the acceptance × efficiency.

These corrections aim to compensate for the un-detected and/or un-reconstructed particles in the analysis. Hence, most of the measurements apply such corrections on both trigger and associated particles. While this makes sense in the latter case, it is more dubious for the former ones: by correcting the cascade raw signal, one increases basically the number of such hadrons in the analysis. Those being used as a trigger, it also amounts to increase the number of triggered events. Depending on whether those additional/corrected events contains a $\phi(1020)$ meson or not, whether they are reconstructed or not, whether they are correlated to the trigger particle or not, this will most certainly affect the estimation of the $\overset{(-)}{\Xi}{}^{\pm}$-$\phi(1020)$ and $\overset{(-)}{\Omega}{}^{\pm}$-$\phi(1020)$ correlations. If, as depicted in the left panel of Fig. 6.7, such correlation in non-triggered event turns out to be small, the previous concerns may reasonably be neglected in first approximation. Conversely, in the configuration shown in the right panel of Fig. 6.7, one should be extremely cautious on how to correct the trigger particle yield.

Due to the non-trivial application of the acceptance × efficiency correction factors on the trigger particle, the present measurement restricts only to correlations in triggered events. This means that the acceptance and efficiency corrections concern solely the associated particles, namely the $\phi(1020)$.

III-G Accounting for the uncorrelated cascade-resonance pairs

As for the $\phi(1020)$ meson reconstruction, there is no way to tell *a priori* which cascade is correlated to a resonance. All the possible combinations have to be exhausted. This inevitably leads to the formation of uncorrelated cascade-$\phi(1020)$ pairs.

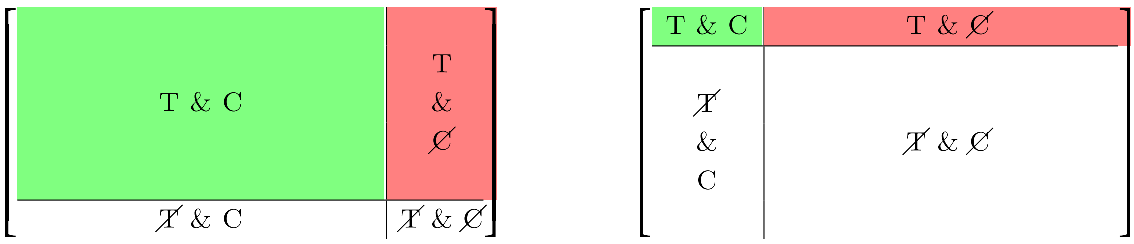

Fig. 6.7: Study of the correlated yield between the trigger and associated particles in two different cases. The area occupied by each cell provides its relative contribution to the correlated production. Four contributions are considered: a trigger particle has been found/detected/reconstructed in the event (T) and it is correlated to at least one associated particle (C); there is no correlation between these particles (T & $\not\mathrm{C}$); a trigger particle is present and correlated to an associated particle, though it is not reconstructed ($\not\mathrm{T}$ & C); the trigger particle is not found and is not correlated to the particle of interest ($\not\mathrm{T}$ & $\not\mathrm{C}$). The green area corresponds to the measurement at stake, while the red zone represents the contribution accounted for in Sec. 6|III-G. The un-coloured areas are not seen in the present analysis.

Such contribution can be removed using the exact same methods as those used for subtracting the combinatorial background of the resonances: either via an event mixing technique or rotating procedure (Sec. 6|III-C). Our choice went on the first option, purely for simplicity. On the practical side, by re-using the same mixed-event list as for the $\phi(1020)$, the longest part of procedure is already done, making the implementation of the event mixing technique straighforward.

The whole analysis chain needs to be repeated, including the previous elements Sec. 6|III-E and 6|III-F.

IV Study of the systematic uncertainties

IV-A Topological and track selections

Selections inspired from the first analysis and [157].

IV-A.i Multi-strange baryon identification

IV-A.ii $\phi(1020)$ meson identification

[184]

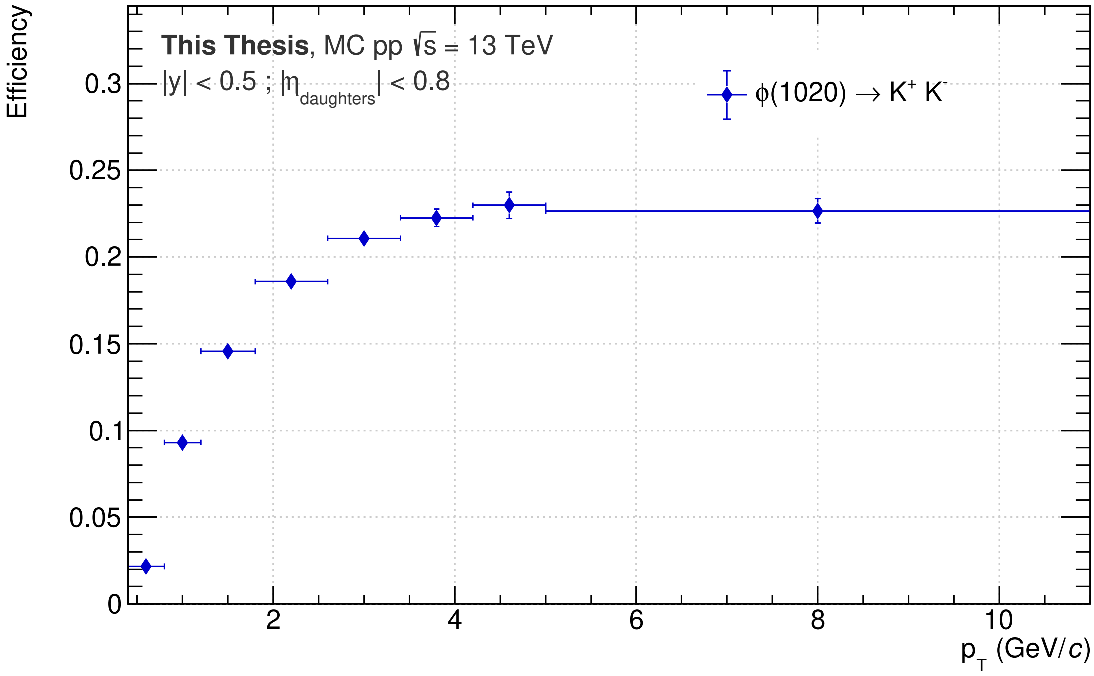

Fig. 6.8: Top left panel: Unlike-charge and mixed-event invariant mass distribution for p_{T} between 0.4 and 0.8 GeV/c. The other panels: Invariant mass spectra of the $\phi(1020)$ meson candidates in pp collisions at $\sqrt{s}$ = 13 TeV, fitted by the sum of a Voigt function for the peak and a linear function for the residual background. The amounts of signal have been obtained as explained in Sec. 6|III-D.ii, while the background has been obtained via bin counting in the region covered by the red area, that is 1.005 and 1.035 GeV/c^2.

Track variable	Very loose	Loose	Default	Tight	Very tight
Nbr of crossed TPC readout rows			> 70	> 80	> 90
$n_{\sigma}^{\mathrm{TPC}}$	< 5	< 4	< 3	< 2.5	< 2
Topological variable					
V0					
V0 decay radius (cm)	> 1	> 1.1	> 1.2	> 3	> 5
V0 cosine of pointing angle			> 0.97	> 0.98	> 0.99
$\lvert m(V0)$ - $m_{\mathrm{PDG}}\Lambda \rvert$ (GeV/c^2)	< 0.010	< 0.009	< 0.008	< 0.007	< 0.006
DCA proton to prim. vtx (cm)			> 0.03	> 0.07	> 0.1
DCA pion to prim. vtx (cm)		> 0.03	> 0.04	> 0.15	> 0.3
DCA V0 to prim. vtx (cm)			> 0.06	> 0.1	> 0.13
DCA between V0 daughters (std dev)	< 2	< 1.8	< 1.5	< 1.2	< 1.0
Cascade					
Cascade decay radius (cm)	> 0.4	> 0.5	> 0.6	> 0.8	> 1
Cascade Lifetime (cm)	$< 5\ c.\tau$	$< 4\ c.\tau$	$< 3\ c.\tau$	$< 2.5\ c.\tau$	
DCA bachelor to prim. vtx (cm)		> 0.03	> 0.04	> 0.1	> 0.17
DCA between cascade daughters (std dev)	< 2	< 1.6	< 1.3	< 1.0	< 0.8
Cascade cosine of pointing angle	> 0.99	> 0.995	> 0.998	> 0.9985	> 0.999
Bachelor-proton pointing angle (rad)	> 0.02	> 0.03	> 0.04	> 0.045	> 0.05

Table 6.6: Summary of the five configurations – the default as well as four variants – on the topological and track selections employed in the identification the $\bar{\Xi}^{\pm}$ in pp events at $\sqrt{s}$ = 13 TeV. When a value is missing, the preceding selection is considered. These sets of selections have been determined based on the signal variation study carried out in the first analysis (Sec. 5|IV-A), in conjunction with the ones used in [157].

Candidate variable	Very loose	Loose	Default	Tight	Very tight
Competing mass rejection (GeV/c^2)	> 0.006	> 0.007	> 0.008	> 0.009	> 0.010
Track variable					
Nbr of crossed TPC readout rows			> 70	> 80	> 90
$n_{\sigma}^{\mathrm{TPC}}$	< 5	< 4	< 3	< 2.5	< 2
Topological variable					
V0					
V0 decay radius (cm)		> 1.0	> 1.1	> 2.5	> 3.5
V0 cosine of pointing angle			> 0.97	> 0.98	> 0.99
$\lvert m(V0)$ - $m_{\mathrm{PDG}}\Lambda \rvert$ (GeV/c^2)	< 0.010	< 0.009	< 0.008	< 0.007	< 0.006
DCA proton to prim. vtx (cm)			> 0.03	> 0.07	> 0.1
DCA pion to prim. vtx (cm)		> 0.03	> 0.04	> 0.15	> 0.3
DCA V0 to prim. vtx (cm)			> 0.06	> 0.08	> 0.1
DCA between V0 daughters (std dev)	< 2	< 1.8	< 1.5	< 1.2	< 1.0
Cascade					
Cascade decay radius (cm)	> 0.3	> 0.4	> 0.5	> 0.6	> 0.8
Cascade Lifetime (cm)	$< 5\ c.\tau$	$< 4\ c.\tau$	$< 3\ c.\tau$	$< 2.5\ c.\tau$	
DCA bachelor to prim. vtx (cm)		> 0.03	> 0.04	> 0.08	> 0.1
DCA between cascade daughters (std dev)	< 2	< 1.6	< 1.3	< 1.0	< 0.6
Cascade cosine of pointing angle	> 0.99	> 0.995	> 0.998	> 0.9985	> 0.999
Bachelor-proton pointing angle (rad)	> 0.02	> 0.03	> 0.04	> 0.045	> 0.05

Table 6.7: Summary of the five configurations – the default as well as four variants – on the topological and track selections employed in the identification the $\overline{\Omega}^{\pm}$ in pp events at $\sqrt{s}$ = 13 TeV. When a value is missing, the preceding selection is considered. These sets of selections have been determined based on the signal variation study carried out in the first analysis (Sec. 5|IV-A), in conjunction with those used in [157].

Track variable	Default	Variations			
n_σ^{TPC}	< 3	< 2.5	< 3.5	< 3	< 3
n_σ^{TOF} (veto only)	< 3	< 3	< 3	veto off	< 4
Nbr of crossed TPC readout rows	> 70	> 80	> 90		
Fraction of crossed TPC readout rows over findable clusters	≥ 0.8	≥ 0.9			
Goodness of the TPC standalone track, $\chi^2_{\mathrm{ITS}}/N_{\mathrm{cluster}}$	< 36	< 25	< 4		
Goodness of the TPC standalone track, $\chi^2_{\mathrm{TPC}}/N_{\mathrm{cluster}}$	< 4	< 2.3			
Global and TPC standalone track matching, $\chi^2_{\text{TPC-CG}}$	< 36	< 25			
Nbr of associated SPD clusters	≥ 1	≥ 0			
DCA to prim. vtx (cm)	$< 0.0105 + 0.035\ p_{\mathrm{T}}\ ^{-1.01}$	$< 0.006 + 0.020\ p_{\mathrm{T}}\ ^{-1.01}$			
DCA to prim. vtx along z (cm)	< 2	< 1	< 0.2		

Table 6.8: Summary of the variations for each track candidate selections used for the reconstruction of $\phi(1020)$ resonances. Contrarily to the hyperon case, each variation for a given variable is tested individually, while keeping the other variables fixed at their nominal values. The only exception concerns the PID variables, where a pair of TPC and TOF selections gives one configuration. This set of variation has been taken from [184].

IV-B Other sources of systematic uncertainties

- the choice of the fit function
- the imprecision on the material budget

V Results

V-A Preliminary results

V-A.i The $\overline{\Xi}^{\pm}$– $\phi(1020)$ correlations

V-A.ii The $\overline{\Omega}^{\pm}$– $\phi(1020)$ correlations

V-B Comparison between measurements and models

The model comparison articulates around the two pictures, the two approaches to describe the small and large systems: Pythia and Epos. The former relies its description of the hadronisation processes via the Lund string model, while the other employs a core-corona model. In the next paragraphs, each of these models will be introduced in details, and most particularly the hadronisation mechanisms used in the model comparison to the results.

V-B.i Pythia

Pythia's hadronisation mechanisms are based solely on the Lund string model. The starting point of this framework is the spring-like nature of the QCD interaction between two quarks, supported by lattice QCD studies (Sec. 2|I-C.i, and in particular Eq. 2.4).

The gluon field between two colour charges can be viewed as a colour flux tube, a string of tension $\kappa \simeq 1$ GeV/fm with a potential energy increasing linearly with the distance between the quarks [131]. As the partons move apart, their kinetic energy is progressively converted into potential energy, until it has been fully transfered to the string . At this point, the string reaches its maximal extension, $E/2\kappa$, and the partons move back to their starting point and meet again. The string has completed a full period. This so-called "yo-yo" motion corresponds to a meson, in the Lund string picture. If the partons move further apart than the maximum, the original string breaks up giving rise to a new $q\bar{q}$ pair[13]. It is through this mechanism that mesons are produced. In order to form a baryon, the string must fragment into diquark–anti-diquark pairs[14].

[13]The typical break-up time of a string is about 2 fm/c [131].

[14]Any quark flavour can be obtained in principle, but the heavier the quark, the more suppressed it is. For instance, the production of light flavour quarks is almost inexpensive, while strange and charm quarks have to pay a suppression factor of 0.3 and 10^{-11}. Consequently, the yield of heavy quark flavour can basically be ignored with the string breaking mechanism, they are produced in other processes in the perturbative regime of QCD [185].

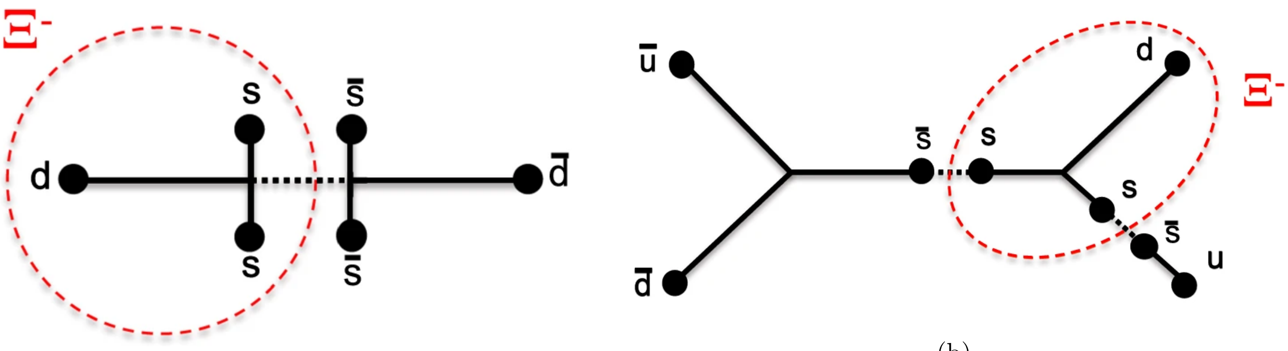

Fig. 6.9: Baryon production mechanism within the PYTHIA framework, in the case of a Ξ^{-} hyperon: (a) the colour string fragments into a diquark–anti-diquark pairs; (b) two strings form a junction, that breaks down into a $s\bar{s}$ pair. Figure taken from [177].

This picture received further developments over the years, amongst the most important: the multiparton interaction (MPI) model and the colour reconnection (CR) mechanism. The former stems from the composite nature of the hadrons, that leads possibly to several parton-parton interactions when colliding two hadrons [186]. MPI model basically comprises all the processes involving multiple partons. The latter refers to the mechanisms allowing the colour strings, in *causal contact*[15], to re-arrange and form different configuration. An example of colour reconnection is the string junction, which opens the way towards additional mechanisms for baryon production as illustrated in Fig. 6.9 [187].

PYTHIA has historically focused on electroweak and hard QCD processes, parton shower, hadronisation, particularly in small systems where no QGP formation is considered. The discovery of long-range particle correlations in high-multiplicity pp collisions in 2010 [188][189][190], followed by the observation of the strangeness enhancement in small systems in 2017 [181], forced to re-consider the QGP-like effects in pp collisions. The aforementioned models could offer a qualitative description of some of those effects, while being completely off on some other observables like the anisotropic flow. New developments were needed. To that end, additional interactions between the strings have "recently" been implemented, namely the rope hadronisation (or also refered as colour rope) and string shoving [131].

The rope hadronisation follows somehow the same idea as the string junction, namely that strings may form in a cluster of partons. When multiple strings overlap, their colour field acts coherently, forming a stronger field. These cluster of strings can then be viewed as a string with an effective tension $\tilde{\kappa}$ greater than κ, that is a colour rope. This increased string tension leads to an increase[16] of the strangeness production (or equivalently, it decreases its suppression factor), that can subsequently be used to model the strangeness enhancement.

[15] This point is extremely important as the space-time separation between two MPIs is not taken into account by default.

[16] This increase actually depends on the colour configuration of the different strings. Quarks with the same colour charges can form a coherent state, increasing $\tilde{\kappa}$; whereas, with opposite/incoherent colour charges, they combine into an anti-colour, thus reducing $\tilde{\kappa}$.

Another effect of the overlapping of strings is the string shoving. Strings occupying the same volume can interact together. It turns out that they dominantly repel each other, resulting in a shoving pressure. Each hadron later receives its share of the push, which leads ultimately to a flow of hadrons, mimicing the anisotropic flow effects.

key ingredients: i) multiple parton scattering (parton ladders)

V-B.ii Epos

ii) core – corona

Originally designed to reproduce heavy-ion interactions, Epos employs a core-corona model, an unique approach when all the other high-energy physics MC generators (Pythia, Herwig, etc) are corona-like models.

The basic idea behind this framework starts with the observation that a hadron-hadron collision corresponds in fact to many elementary collisions happening simultaneously, that can be modelled via the formation of parton ladders – similar to the MPI concept, describing the multiple parton scatterings – or (cut-)Pomerons[17]. It turns out the parton ladder can be viewed as a colour flux tube, a string like in Lund string model that breaks via the production of a $q\bar{q}$ pair into string segments often referred as "pre-hadrons". These serves as initial conditions for the hadronisation.

Based on these pre-hadrons, the core-corona procedure illustrated in Fig. 6.10 comes into play. In the regions with a high density (above a certain threshold, easily reached in heavy-ion collisions) of string segments, these may overlap and fuse into a fluid. This corresponds to the "core" of the system as opposed to the "corona", usually located in the peripheral regions of the system (by definition), where the string density is lower. The pre-hadrons in the core lose their energy and evolve according to hydrodynamics, until the energy density falls below a critical value. At this stage, the fluid undergoes a collective hadronisation via a micro-canonical procedure[18] at the freeze-out surface (Fig. 6.10), in order to ensure energy, momentum and flavour conservation. The formed hadrons receive a Lorentz boost according to the radial and longitudinal expansions of the fluid core. For what concerns the string segments in the corona part, they hadronise through string fragmentations as in Pythia.

[17] A Pomeron – named after Isaak Pomeranchuk – is a concept incorporated by Vladimir Gribov into the Regge theory, developed by Tullio Regge in 1959 [191]. This theory attempts to describe the total cross section of hadronic collisions at high energies, at a time when the quark model does not exist yet. In this theory, a particle and all its excitations – for instance, the ρ meson spin-1, spin-3, spin-5, etc – lie on the same trajectory, the Regge trajectory. Each resonance contributes to the scattering amplitudes; their combined contribution is viewed as an exchange of an object named Reggeon [192]. Although the Regge theory provides a good description of the total cross section at low energies, it predicts a decreasing trend at high energies while it is in fact flat. The solution to this problem is brought by Gribov, who introduces a new Reggeon: the Pomeron. In modern particle physics, the Pomeron corresponds to various processes at high energy, such as a parton ladder. Epos' main theoretical tool is the S-matrix theory, inspired by the Gribov-Regge picture [173]. One can distinguish two sorts of Pomeron: the cut and the uncut version. Basically, the latter corresponds to an elastic contribution to the scattering amplitude, whereas the former represents an inelastic contribution [193].

[18] The string segments constituting the core are gathered in different clusters for each pseudorapidity bin. The hadronisation is performed in each cluster separately using the micro-canonical ensemble formalism [133].

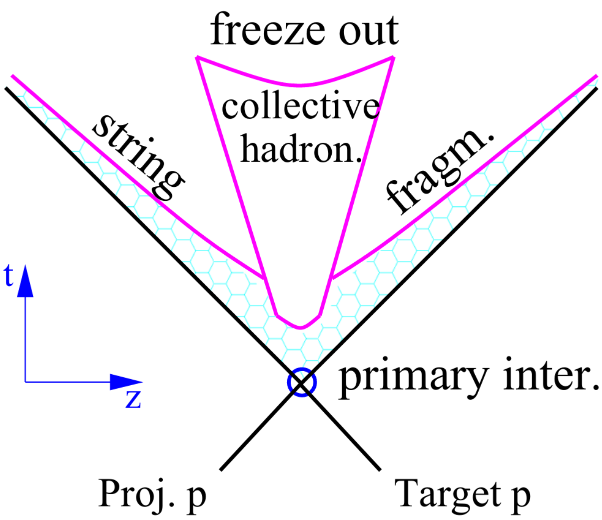

Fig. 6.10: Schematic representation of the space-time evolution of the particle production in a hadron-hadron collision. The central cone represents the core part where the hadrons undergo a collective hadronisation at the freeze-out surface. The hyperbola line encompasses the corona surrounding the core; the string segments in this region hadronise via string fragmentation. Figure taken from [133].

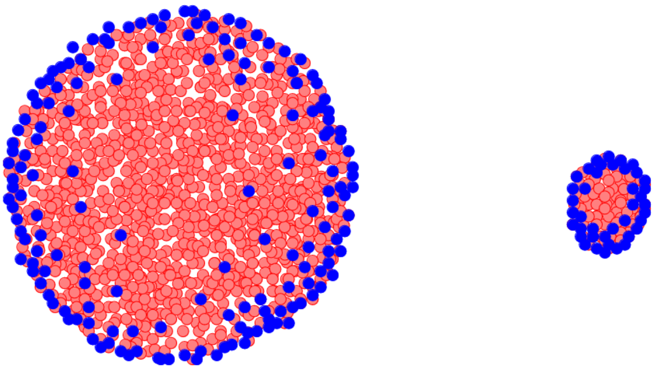

(a) (b)

Fig. 6.11: Schematic representation of the pre-hadrons distributions in a large system such as a Pb-Pb collision (a) and in a small system like a pp collision (b). The red dots represents the pre-hadrons in the core, while the blue ones belong to the corona. Figures taken from [173].

This presentation of Epos corresponds to the current implementation of the model, Epos 4. This procedure is applied for simulating both pp and heavy-ion collisions. Thereby, this model assumes the formation of, at least, a QGP droplet in small systems (Fig. 6.11). There exists also different configurations that considers only "core" or "corona".

V-B.iii Comparison to the model predictions

" A rivet analysis has started. ongoing development by me.
for (PZ Ronash)+(Repe)+(EPOS4)".

Chapter 7 | Discussion and conclusion

7 | Bibliography

[1] P. A. Carruthers, *Quarkium: A Bizarre Fermi Liquid.* 1974. [Cited on page 14.]

[2] B. J. Harrington and A. Yildiz, *High-Density Phase Transitions in Gauge Theories*, *Phys. Rev. Lett.* **33** (July, 1974) 324–327. DOI Link. [Cited on page 14.]

[3] J. C. Collins and M. J. Perry, *Superdense Matter: Neutrons or Asymptotically Free Quarks?*, *Phys. Rev. Lett.* **34** (May, 1975) 1353–1356. DOI Link. [Cited on page 14.]

[4] *New State of Matter created at CERN*, https://home.web.cern.ch/news/press-release/cern/new-state-matter-created-cern, Jan. 2023. [Cited on pages 14 and 38.]

[5] T. Ludlam and S. Aronson, *HUNTING THE QUARK GLUON PLASMA.*, https://digital.library.unt.edu/ark:/67531/metadc1411284/, Apr. 2005. [Cited on pages 14 and 38.]

[6] I. Arsene, *Quark Gluon Plasma an Color Glass Condensate at RHIC? The perspective from the BRAHMS experiment*, *Nuclear Physics A* **757** (Aug., 2005) 1–27, [nucl-ex/0410020]. DOI Link. [Cited on pages 14 and 38.]

[7] B. B. B. et al, *The PHOBOS Perspective on Discoveries at RHIC*, *Nuclear Physics A* **757** (Aug., 2005) 28–101, [nucl-ex/0410022]. DOI Link. [Cited on pages 14 and 38.]

[8] P. Collaboration and K. Adcox, *Formation of dense partonic matter in relativistic nucleus-nucleus collisions at RHIC: Experimental evaluation by the PHENIX collaboration*, *Nuclear Physics A* **757** (Aug., 2005) 184–283, [nucl-ex/0410003]. DOI Link. [Cited on pages 14 and 38.]

[9] S. Collaboration and J. Adams, *Experimental and Theoretical Challenges in the Search for the Quark Gluon Plasma: The STAR Collaboration's Critical Assessment of the Evidence from RHIC Collisions*, *Nuclear Physics A* **757** (Aug., 2005) 102–183, [nucl-ex/0501009]. DOI Link. [Cited on pages 14 and 38.]

[10] *The third run of the Large Hadron Collider has successfully started*, https://home.cern/news/news/cern/third-run-large-hadron-collider-has-successfully-started, Jan. 2023. [Cited on page 14.]

[11] T. A. ALICE Collaboration, *Upgrade of the ALICE Experiment: Letter Of Intent*, *J. Phys. G: Nucl. Part. Phys.* **41** (July, 2014) 087001. DOI Link. [Cited on page 14.]

[12] A. Collaboration, *Characterizing the initial conditions of heavy-ion collisions at the LHC with mean transverse momentum and anisotropic flow correlations*, *Physics Letters B* **834** (Nov., 2022) 137393, [arXiv:2111.06106]. DOI Link. [Cited on page 14.]

[13] R. Schotter, *A multi-differential investigation of strangeness production in pp collisions with ALICE*, Feb. 2023. arXiv:2302.00454. [Cited on pages 14 and 19.]

[14] Schotter, *QCD@LHC2022*, https://indico.cern.ch/event/1150707/contributions/5112603/. [Cited on pages 14 and 46.]

[15] B. Pullman, *The Atom in the History of Human Thought*. New York : Oxford University Press, 1998. [Cited on page 17.]

[16] J. J. Thomson, *XL. Cathode Rays*, *The London, Edinburgh, and Dublin Philosophical Magazine and Journal of Science* **44** (Oct., 1897) 293–316. DOI Link. [Cited on page 17.]

[17] C. M. G. Lattes, H. Muirhead, G. P. S. Occhialini, and C. F. Powell, *Processes Involving Charged Mesons*, *Nature* **159** (May, 1947) 694–697. DOI Link. [Cited on page 17.]

[18] G. D. ROCHESTERDr. and C. C. BUTLERDr., *Evidence for the Existence of New Unstable Elementary Particles*, *Nature* **160** (Dec., 1947) 855–857. DOI Link. [Cited on page 17.]

[19] V. D. Hopper and S. Biswas, *Evidence Concerning the Existence of the New Unstable Elementary Neutral Particle*, *Phys. Rev.* **80** (Dec., 1950) 1099–1100. DOI Link. [Cited on page 17.]

[20] O. Chamberlain, E. Segrè, C. Wiegand, and T. Ypsilantis, *Observation of Antiprotons*, *Phys. Rev.* **100** (Nov., 1955) 947–950. DOI Link. [Cited on page 17.]

[21] F. Reines and C. L. COWANjun., *The Neutrino*, *Nature* **178** (Sept., 1956) 446–449. DOI Link. [Cited on page 17.]

[22] G. Danby, J.-M. Gaillard, K. Goulianos, et al., *Observation of High-Energy Neutrino Reactions and the Existence of Two Kinds of Neutrinos*, *Phys. Rev. Lett.* **9** (July, 1962) 36–44. DOI Link. [Cited on page 17.]

[23] V. E. Barnes, P. L. Connolly, D. J. Crennell, et al., *Observation of a Hyperon with Strangeness Minus Three*, *Phys. Rev. Lett.* **12** (Feb., 1964) 204–206. DOI Link. [Cited on pages 17 and 25.]

[24] R. Serway, C. Moses, and C. Moyer, *Modern Physics*. Cengage Learning, 2004. [Cited on pages 17, 20, and 22.]

[25] V. Koch, *Aspects of Chiral Symmetry*, *Int. J. Mod. Phys. E* **06** (June, 1997) 203–249, [nucl-th/9706075]. DOI Link. [Cited on pages 18 and 33.]

[26] M. E. Peskin, *An Introduction To Quantum Field Theory*. CRC Press, Boca Raton, Jan. 2018. [Cited on pages 18, 26, and 34.]

[27] S. Braibant, G. Giacomelli, and M. Spurio, *Particles and Fundamental Interactions*. Undergraduate Lecture Notes in Physics. Springer Netherlands, Dordrecht, 2012. [Cited on pages 18, 19, 22, and 28.]

[28] E. Noether and M. A. Tavel, *Invariant Variation Problems*, *Transport Theory and Statistical Physics* **1** (Jan., 1971) 186–207, [physics/0503066]. DOI Link. [Cited on page 18.]

[29] *Definition of GAUGE*, https://www.merriam-webster.com/dictionary/gauge, Feb. 2023. [Cited on page 19.]

[30] M. S. Sozzi, *Tests of discrete symmetries*, *J. Phys. G: Nucl. Part. Phys.* **47** (Nov., 2019) 013001. DOI Link. [Cited on pages 19 and 99.]

[31] R. Lehnert, *CPT Symmetry and Its Violation*, *Symmetry* **8** (Nov., 2016) 114. DOI Link. [Cited on pages 19 and 99.]

[32] R. G. Sachs, *The Physics of Time Reversal*. University of Chicago Press, Chicago, IL, Oct. 1987. [Cited on page 19.]

[33] S. Glashow and B. Bova, *Interactions: A Journey Through the Mind of a Particle Physicist and the Matter of This World, Sheldon Glashow with Ben Bova. 1988. Warner Books; New York, NY. 347 pages. ISBN: 0-446-51315-6. $19.95*, *Bulletin of Science, Technology & Society* **10** (Aug., 1990) 241–241. DOI Link. [Cited on pages 20, 25, 28, 29, and 31.]

[34] J. B. Kim, J. H. Kim, and H. K. Lee, *Electron-Neutrino Degeneracy and Primordial Nucleosynthesis*, Jan. 1997. astro-ph/9701011. [Cited on page 20.]

[35] M. Thomson, *Modern Particle Physics:*, *Cambridge University Press*, Sept. 2013. DOI Link. [Cited on pages 21, 22, 24, 28, 31, and 33.]

[36] *Quantum Diaries*, http://www.quantumdiaries.org/2011/06/19/helicity-chirality-mass-and-the-higgs/. [Cited on page 21.]

[37] C. MissMJ, *Standard model of elementary particles – wikimedia*, https://commons.wikimedia.org/wiki/File:Standard_Model_of_Elementary_Particles.svg, Sept. 2019. [Cited on page 21.]

[38] G. Jaeger, *The Elementary Particles of Quantum Fields*, *Entropy* **23** (Nov., 2021) 1416. DOI Link. [Cited on page 22.]

[39] J. Schmidhuber, *Evolution of National Nobel Prize Shares in the 20th Century*, Sept. 2010. arXiv:1009.2634. [Cited on page 22.]

[40] C. S. Wu, E. Ambler, R. W. Hayward, et al., *Experimental Test of Parity Conservation in Beta Decay*, *Physical Review* **105** (Feb., 1957) 1413–1415. DOI Link. [Cited on page 23.]

[41] M. Goldhaber, L. Grodzins, and A. W. Sunyar, *Helicity of Neutrinos*, *Phys. Rev.* **109** (Feb., 1958) 1015–1017. DOI Link. [Cited on page 23.]

[42] P. D. Group, *Review of Particle Physics*, *PTEP* **2022** (2022) 083C01. DOI Link. [Cited on pages 23, 24, 30, 52, 58, 65, 77, 88, 89, 95, 100, 152, 155, 156, 163, and 172.]

[43] CERN, *New results indicate that particle discovered at CERN is a Higgs boson*, https://home.web.cern.ch/news/press-release/cern/new-results-indicate-particle-discovered-cern-higgs-boson, Mar. 2023. [Cited on page 25.]

[44] T. W. B. Kibble, *Englert-Brout-Higgs-Guralnik-Hagen-Kibble mechanism (history)*, *Scholarpedia* **4** (Jan., 2009) 8741. DOI Link. [Cited on page 25.]

[45] S. Sakata, *On a Composite Model for the New Particles*, *Progress of Theoretical Physics* **16** (Dec., 1956) 686–688. DOI Link. [Cited on page 25.]

[46] J. J. Sakurai, *Theory of strong interactions*, *Annals of Physics* **11** (Sept., 1960) 1–48. DOI Link. [Cited on page 25.]

[47] M. Gell-Mann, *THE EIGHTFOLD WAY: A THEORY OF STRONG INTERACTION SYMMETRY*, Tech. Rep. TID-12608; CTSL-20, California Inst. of Tech., Pasadena. Synchrotron Lab., Mar. 1961. [Cited on page 25.]

[48] Y. Ne'eman, *Derivation of strong interactions from a gauge invariance*, *Nuclear Physics* **26** (Aug., 1961) 222–229. DOI Link. [Cited on page 25.]

[49] M. Gell-Mann, *Isotopic Spin and New Unstable Particles*, *Phys. Rev.* **92** (Nov., 1953) 833–834. DOI Link. [Cited on page 25.]

[50] P. Skands, *Introduction to QCD*, in *Searching for New Physics at Small and Large Scales*, pp. 341–420, Nov. 2013, [arXiv:1207.2389]. DOI Link. [Cited on pages 26 and 27.]

[51] O. W. Greenberg, *Spin and Unitary-Spin Independence in a Paraquark Model of Baryons and Mesons*, *Phys. Rev. Lett.* **13** (Nov., 1964) 598–602. DOI Link. [Cited on page 26.]

[52] M. Y. Han and Y. Nambu, *Three-Triplet Model with Double $\mathrm{SU}(3)$ Symmetry*, *Phys. Rev.* **139** (Aug., 1965) B1006–B1010. DOI Link. [Cited on page 26.]

[53] J. Bjorken, *Current Algebra at Small Distances*, Tech. Rep. SLAC-PUB-0338, SLAC National Accelerator Lab., Menlo Park, CA (United States), June 2018. [Cited on page 26.]

[54] R. P. Feynman, *The Behavior of Hadron Collisions at Extreme Energies*, in *Special Relativity and Quantum Theory: A Collection of Papers on the Poincaré Group* (M. E. Noz and Y. S. Kim, eds.), Fundamental Theories of Physics, pp. 289–304. *Springer Netherlands*, Dordrecht, 1988. DOI Link. [Cited on page 26.]

[55] H. Fritzsch, M. Gell-Mann, and H. Leutwyler, *Advantages of the color octet gluon picture*, *Physics Letters B* **47** (Nov., 1973) 365–368. DOI Link. [Cited on page 26.]

[56] J. E. Augustin, A. M. Boyarski, M. Breidenbach, et al., *Discovery of a Narrow Resonance in ${e}\hat{}{+}{e}\hat{}{\ensuremath{-}}$ Annihilation*, *Phys. Rev. Lett.* **33** (Dec., 1974) 1406–1408. DOI Link. [Cited on page 29.]

[57] J. J. Aubert, U. Becker, P. J. Biggs, et al., *Experimental Observation of a Heavy Particle J*, *Phys. Rev. Lett.* **33** (Dec., 1974) 1404–1406. DOI Link. [Cited on page 29.]

[58] H. Harari, *A new quark model for hadrons*, *Physics Letters B* **57** (July, 1975) 265–269. DOI Link. [Cited on page 30.]

[59] S. W. Herb, D. C. Hom, L. M. Lederman, et al., *Observation of a Dimuon Resonance at 9.5 GeV in 400-GeV Proton-Nucleus Collisions*, *Phys. Rev. Lett.* **39** (Aug., 1977) 252–255. DOI Link. [Cited on page 30.]

[60] CDF Collaboration, F. Abe, H. Akimoto, et al., *Observation of Top Quark Production in $\overline{\mathit{p}}\mathit{p}$ Collisions with the Collider Detector at Fermilab*, *Phys. Rev. Lett.* **74** (Apr., 1995) 2626–2631. DOI Link. [Cited on page 30.]

[61] D0 Collaboration, S. Abachi, B. Abbott, et al., *Observation of the Top Quark*, *Phys. Rev. Lett.* **74** (Apr., 1995) 2632–2637. DOI Link. [Cited on page 30.]

[62] B. R. Martin and G. Shaw, *Particle Physics*. John Wiley & Sons, Jan. 2017. [Cited on page 31.]

[63] A. Maire, *Production des baryons multi-étranges au LHC dans les collisions proton-proton avec l'expérience ALICE*. PhD thesis, 2011. [Cited on pages 32, 44, and 45.]

[64] D. J. Gross and F. Wilczek, *Ultraviolet Behavior of Non-Abelian Gauge Theories*, *Phys. Rev. Lett.* **30** (June, 1973) 1343–1346. DOI Link. [Cited on page 31.]

[65] H. David Politzer, *Asymptotic freedom: An approach to strong interactions*, *Physics Reports* **14** (Nov., 1974) 129–180. DOI Link. [Cited on page 31.]

[66] FT2, *English: Explanatory diagram showing how symmetry breaking works. At a high enough energy level, a ball settled in the center (lowest point), and the result has symmetry. At lower energy levels, the center becomes unstable, the ball rolls to a lower point - but in doing so, it settles on an (arbitrary) position and the result is that symmetry is broken - the resulting position is not symmetrical.*, 15 December 2012, 16:53:46. [Cited on page 34.]

[67] Y. Nambu and G. Jona-Lasinio, *Dynamical Model of Elementary Particles Based on an Analogy with Superconductivity. I*, *Phys. Rev.* **122** (Apr., 1961) 345–358. DOI Link. [Cited on page 34.]

[68] S. Muroya, A. Nakamura, C. Nonaka, and T. Takaishi, *Lattice QCD at Finite Density – An introductory review*, *Progress of Theoretical Physics* **110** (Oct., 2003) 615–668, [hep-lat/0306031]. DOI Link. [Cited on page 35.]

[69] W. Weise, *Chiral symmetry in strongly interacting matter*, *Progress of Theoretical Physics Supplement* **186** (Oct., 2010) 390–403, [arXiv:1009.6201]. DOI Link. [Cited on page 35.]

[70] A. Bazavov, T. Bhattacharya, C. DeTar, et al., *The equation of state in (2+1)-flavor QCD*, *Phys. Rev. D* **90** (Nov., 2014) 094503, [arXiv:1407.6387]. DOI Link. [Cited on page 36.]

[71] E. Annala, T. Gorda, A. Kurkela, et al., *Evidence for quark-matter cores in massive neutron stars*, https://arxiv.org/abs/1903.09121v2, Mar. 2019. [Cited on page 36.]

[72] M. Alford, K. Rajagopal, and F. Wilczek, *QCD at Finite Baryon Density: Nucleon Droplets and Color Superconductivity*, *Physics Letters B* **422** (Mar., 1998) 247–256, [hep-ph/9711395]. DOI Link. [Cited on page 36.]

[73] A. Maire, *Phase Diagram of QCD Matter: Quark-Gluon Plasma.* 2015. [Cited on page 37.]

[74] O. Philipsen, *The QCD equation of state from the lattice*, *Progress in Particle and Nuclear Physics* **70** (May, 2013) 55–107, [arXiv:1207.5999]. DOI Link. [Cited on page 36.]

[75] M. A. Stephanov, *QCD phase diagram and the critical point*, *Int. J. Mod. Phys. A* **20** (July, 2005) 4387–4392, [hep-ph/0402115]. DOI Link. [Cited on page 36.]

[76] Rafelski, *Melting Hadrons, Boiling Quarks - From Hagedorn Temperature to Ultra-Relativistic Heavy-Ion Collisions at CERN.* Springer Cham, Apr. 2015. [Cited on page 37.]

[77] J. Rafelski, *Melting Hadrons, Boiling Quarks*, *Eur. Phys. J. A* **51** (Sept., 2015) 114, [arXiv:1508.03260]. DOI Link. [Cited on page 37.]

[78] G. F. Chapline and A. K. Kerman, *On the Possibility of Making Quark Matter in Nuclear Collisions*, . [Cited on page 37.]

[79] S. A. Chin, *Transition to hot quark matter in relativistic heavy-ion collision*, *Physics Letters B* **78** (Oct., 1978) 552–555. DOI Link. [Cited on page 38.]

[80] J. D. Bjorken, *Highly relativistic nucleus-nucleus collisions: The central rapidity region*, *Phys. Rev. D* **27** (Jan., 1983) 140–151. DOI Link. [Cited on pages 38 and 39.]

[81] H. Satz, *The SPS heavy ion programme*, *Physics Reports* **403–404** (Dec., 2004) 33–50. DOI Link. [Cited on page 38.]

[82] J. E. Bernhard, *Bayesian parameter estimation for relativistic heavy-ion collisions*, https://arxiv.org/abs/1804.06469v1, Apr. 2018. [Cited on page 39.]

[83] A. Maire, *Two Views on the Bjorken Scenario for Ultra-Relativistic Heavy-Ion Collisions.* 2011. [Cited on page 40.]

[84] A. Collaboration, *The ALICE experiment – A journey through QCD*, Nov. 2022. arXiv:2211.04384. [Cited on pages 42, 46, 59, 60, 66, 67, and 72.]

[85] A. Collaboration, *Suppression of charged particle production at large transverse momentum in central Pb-Pb collisions at $\sqrt{s_{\rm NN}} = 2.76$ TeV*, *Physics Letters B* **696** (Jan., 2011) 30–39, [arXiv:1012.1004]. DOI Link. [Cited on page 43.]

[86] J. Rafelski, *Strangeness enhancement*, *Eur. Phys. J. Spec. Top.* **155** (Mar., 2008) 139–166. DOI Link. [Cited on page 44.]

[87] J. Rafelski and B. Müller, *Strangeness Production in the Quark-Gluon Plasma*, *Phys. Rev. Lett.* **48** (Apr., 1982) 1066–1069. DOI Link. [Cited on page 44.]

[88] J. Adam, D. Adamová, M. M. Aggarwal, et al., *Centrality dependence of ψ(2S) suppression in p-Pb collisions at $$ {\sqrt{s}}_{\mathrm{NN}}=5.02 $$TeV*, *J. High Energ. Phys.* **2016** (June, 2016) 50. DOI Link. [Cited on page 46.]

[89] *Puzzle: Le Grand collisionneur de hadrons | Visitez le CERN*, https://visit.cern/fr/content/lhc_puzzle. [Cited on page 50.]

[90] F. de Rose, *Paris 1951: The birth of CERN*, *Nature* **455** (Sept., 2008) 174–175. DOI Link. [Cited on page 51.]

[91] CERN council, *Convention for the Establishment of a European Organization for Nuclear Research | CERN Council*, https://council.web.cern.ch/en/content/convention-establishment-european-organization-nuclear-research#7, July 1953. [Cited on page 51.]

[92] CERN, *Our People*, https://home.cern/about/who-we-are/our-people, Feb. 2023. [Cited on page 51.]

[93] *The Future Circular Collider*, https://home.cern/science/accelerators/future-circular-collider, Feb. 2023. [Cited on page 52.]

[94] M. Benedikt, A. Blondel, O. Brunner, et al., *Future Circular Collider - European Strategy Update Documents*. 2019. [Cited on page 52.]

[95] *LHC Guide*. 2017. [Cited on page 52.]

[96] Lopienska, Ewa, *The CERN accelerator complex, layout in 2022*, https://cds.cern.ch/images/CERN-GRAPHICS-2022-001-1, Mar. 2022. [Cited on page 53.]

[97] *The accelerator complex | CERN*, https://home.cern/science/accelerators/accelerator-complex. [Cited on page 54.]

[98] *Greybook*, https://greybook.cern.ch/. [Cited on page 54.]

[99] G. Aad, S. Bentvelsen, G. J. Bobbink, et al., *The ATLAS Experiment at the CERN Large Hadron Collider*. 2008. [Cited on pages 54 and 58.]

[100] C. Collaboration, S. Chatrchyan, G. Hmayakyan, et al., *The CMS experiment at the CERN LHC*, *J. Inst.* **3** (Aug., 2008) S08004. DOI Link. [Cited on pages 54 and 58.]

[101] A. Collaboration, K. Aamodt, A. A. Quintana, et al., *The ALICE experiment at the CERN LHC*, *J. Inst.* **3** (Aug., 2008) S08002–S08002. DOI Link. [Cited on pages 54, 60, 62, 70, and 73.]

[102] L. Collaboration, A. A. A. Jr, L. M. A. Filho, et al., *The LHCb Detector at the LHC*, *J. Inst.* **3** (Aug., 2008) S08005. DOI Link. [Cited on pages 54 and 58.]

[103] *LHC commissioning*, https://lhc-commissioning.web.cern.ch/. [Cited on page 55.]

[104] ALICE Collaboration, *ALICE Collaboration*, https://alice-collaboration.web.cern.ch/general-information. [Cited on page 56.]

[105] ALICE Collaboration, J. Adam, D. Adamová, et al., *Centrality Dependence of the Charged-Particle Multiplicity Density at Midrapidity in Pb-Pb Collisions at $\sqrt{{s}_{NN}}=5.02\text{ }\text{ }\mathrm{TeV}$*, Phys. Rev. Lett. **116** (June, 2016) 222302. DOI Link. [Cited on pages 58 and 97.]

[106] R. L. Gluckstern, *Uncertainties in track momentum and direction, due to multiple scattering and measurement errors*, Nuclear Instruments and Methods **24** (July, 1963) 381–389. DOI Link. [Not cited.]

[107] a. F. Carminati, P. Foka, P. Giubellino, et al., *ALICE: Physics Performance Report, Volume I*, J. Phys. G: Nucl. Part. Phys. **30** (Oct., 2004) 1517. DOI Link. [Cited on pages 60, 62, 75, and 81.]

[108] A. Collaboration, B. Alessandro, F. Antinori, et al., *ALICE: Physics Performance Report, Volume II*, J. Phys. G: Nucl. Part. Phys. **32** (Sept., 2006) 1295–2040. DOI Link. [Cited on pages 60, 91, and 96.]

[109] A. Collaboration, *Performance of the ALICE Experiment at the CERN LHC*, Int. J. Mod. Phys. A **29** (Sept., 2014) 1430044, [arXiv:1402.4476]. DOI Link. [Cited on pages 60, 80, 81, 82, 96, and 147.]

[110] A. Collaboration, *Alignment of the ALICE Inner Tracking System with cosmic-ray tracks*, *arXiv:1001.0502 [hep-ex, physics:physics]* (Sept., 2017) [arXiv:1001.0502]. DOI Link. [Cited on page 61.]

[111] A. Maire and D. Dobrigkeit Chinellato, *ALICE Sub-Detectors Highlighted (LHC Runs 1+2 // Runs 3+4)*. 2017. [Cited on page 61.]

[112] J. Alme, Y. Andres, H. Appelshäuser, et al., *The ALICE TPC, a large 3-dimensional tracking device with fast readout for ultra-high multiplicity events*, Nuclear Instruments and Methods in Physics Research Section A: Accelerators, Spectrometers, Detectors and Associated Equipment **622** (Oct., 2010) 316–367. DOI Link. [Cited on page 64.]

[113] A. Maire, *ALICE TPC Sectors and Pad Rows*. 2011. [Cited on page 64.]

[114] A. Collaboration, *Performance of the ALICE VZERO system*, J. Inst. **8** (Oct., 2013) P10016–P10016, [arXiv:1306.3130]. DOI Link. [Cited on pages 67 and 68.]

[115] A. Akindinov, F. Anselmo, M. Basile, et al., *The multigap resistive plate chamber as a time-of-flight detector*, Nuclear Instruments and Methods in Physics Research Section A: Accelerators, Spectrometers, Detectors and Associated Equipment **456** (Dec., 2000) 16–22. DOI Link. [Cited on page 69.]

[116] A. V. Akindinov, A. Alici, F. Anselmo, et al., *Study of gas mixtures and ageing of the multigap resistive plate chamber used for the Alice TOF*, Nuclear Instruments and Methods in Physics Research Section A: Accelerators, Spectrometers, Detectors and Associated Equipment **533** (Nov., 2004) 93–97. DOI Link. [Cited on page 69.]

[117] A. Collaboration, *Determination of the event collision time with the ALICE detector at the LHC*, Eur. Phys. J. Plus **132** (Feb., 2017) 99, [arXiv:1610.03055]. DOI Link. [Cited on page 71.]

[118] I. J. Bloodworth, G. Di Marzo-Serugendo, D. Evans, et al., *The ALICE Central Trigger Processor*. CERN, 2000. [Cited on page 73.]

[119] ALICE Collaboration, *Trigger, Data Acquisition, High Level Trigger, Control System Technical Design Report*, https://edms.cern.ch/ui/#!master/navigator/document?D:1811711722:1811711722:subDocs. [Cited on pages 73 and 103.]

[120] A. Collaboration, *Charged-particle multiplicity measurement in proton-proton collisions at $\sqrt{s}$ = 0.9 and 2.36 TeV with ALICE at LHC*, Eur. Phys. J. C **68** (July, 2010) 89–108, [arXiv:1004.3034]. DOI Link. [Cited on page 74.]

[121] ALICE Collaboration, *ALICE Trigger Coordination Twiki page*, https://twiki.cern.ch/twiki/bin/viewauth/ALICE/TriggerCoordination, Oct. 2020. [Cited on page 74.]

[122] Caffarri, Davide, *Charm suppression in Pb-Pb collisions at the LHC measured using D0 K-pi+ reconstruction with the ALICE experiment*, https://www.research.unipd.it/handle/11577/3422170?mode=complete, Jan. 2012. [Cited on pages 75 and 81.]

[123] R. Mankel, *Pattern recognition and event reconstruction in particle physics experiments*, *Rep. Prog. Phys.* **67** (Mar., 2004) 553. DOI Link. [Cited on page 77.]

[124] A. Maire, *Track Reconstruction Principle in ALICE for LHC Run I and Run II*. 2011. [Cited on pages 78 and 131.]

[125] V. Karimäki, *Effective Vertex Fitting*. 1997. [Cited on page 81.]

[126] Worldwide LHC Computing Grid, *Worldwide LHC Computing Grid's welcome page*, https://wlcg-public.web.cern.ch/. [Cited on pages 82 and 83.]

[127] Rene Brun and Fons Rademakers, *ROOT - An Object Oriented Data Analysis Framework,*, https://root.cern/. [Cited on page 84.]

[128] ALICE Collaboration, *AliRoot*, https://github.com/alisw/AliRoot. [Cited on page 84.]

[129] ALICE Collaboration, *AliPhysics*, alisw, Feb. 2023. [Cited on page 84.]

[130] V. Blobel and C. Kleinwort, *A New Method for the High-Precision Alignment of Track Detectors*, https://arxiv.org/abs/hep-ex/0208021v1, Aug. 2002. [Cited on page 85.]

[131] C. Bierlich, S. Chakraborty, N. Desai, et al., *A comprehensive guide to the physics and usage of PYTHIA 8.3*, Mar. 2022. arXiv:2203.11601. [Cited on pages 85, 180, and 181.]

[132] M. Bähr, S. Gieseke, M. A. Gigg, et al., *Herwig++ physics and manual*, Eur. Phys. J. C **58** (Dec., 2008) 639–707. DOI Link. [Cited on page 85.]

[133] T. Pierog, Iu. Karpenko, J. M. Katzy, et al., *EPOS LHC: Test of collective hadronization with data measured at the CERN Large Hadron Collider*, Phys. Rev. C **92** (Sept., 2015) 034906. DOI Link. [Cited on pages 85, 182, and 183.]

[134] X.-N. Wang and M. Gyulassy, *HIJING 1.0: A Monte Carlo Program for Parton and Particle Production in High Energy Hadronic and Nuclear Collisions*, *Computer Physics Communications* **83** (Dec., 1994) 307–331, [nucl-th/9502021]. DOI Link. [Cited on page 85.]

[135] R. Brun, F. Bruyant, M. Maire, et al., *GEANT 3: User's guide Geant 3.10, Geant 3.11; rev. version*, tech. rep., CERN, Geneva, 1987. [Cited on page 85.]

[136] Geant4, *Geant4 home page*, https://geant4-userdoc.web.cern.ch/UsersGuides/ForApplicationDeveloper/html/Introduction/introduction.html. [Cited on page 85.]

[137] G. Battistoni, T. Boehlen, F. Cerutti, et al., *Overview of the FLUKA code*, *Annals of Nuclear Energy* **82** (Aug., 2015) 10–18. DOI Link. [Cited on page 85.]

[138] J. Speltz, *Caractérisation d'un état dense de quarks et de gluons grâce aux fonctions d'excitation des hypérons multi-étranges mesurées avec l'expérience STAR au RHIC*. PhD thesis, Université Louis Pasteur - Strasbourg I, Oct. 2006. [Cited on page 88.]

[139] A. Maire, *Four types of cascade decays for multi-strange baryons (charged Xi and Omega)*, 2011. [Cited on pages 90 and 164.]

[140] D. D. Chinellato, *Charm and multi-charm baryon measurements via strangeness tracking with the upgraded ALICE detector*, *EPJ Web Conf.* **259** (2022) 09004, [arXiv:2110.00955]. DOI Link. [Cited on page 91.]

[141] A. Maire, *Topological Selections for V0 (K0s, Lambda) and Cascade (Xi, Omega) Reconstruction in ALICE.* 2011. [Cited on page 93.]

[142] A. Collaboration, *Production of light-flavor hadrons in pp collisions at $\sqrt{s}$ = 7 and $\sqrt{s}$ = 13 TeV*, *arXiv:2005.11120 [hep-ex, physics:nucl-ex]* (May, 2020) [arXiv:2005.11120]. [Cited on pages 95, 111, and 160.]

[143] A. Kostelecky, *The Status of CPT*, Oct. 1998. hep-ph/9810365. [Not cited.]

[144] V. A. Kostelecký and S. Samuel, *Spontaneous breaking of Lorentz symmetry in string theory*, *Phys. Rev. D* **39** (Jan., 1989) 683–685. DOI Link. [Not cited.]

[145] D. Colladay and V. A. Kostelecký, *Lorentz-violating extension of the standard model*, *Phys. Rev. D* **58** (Oct., 1998) 116002. DOI Link. [Not cited.]

[146] E. Abers, I. T. Grodsky, and R. E. Norton, *Diseases of Infinite-Component Field Theories*, *Phys. Rev.* **159** (July, 1967) 1222–1227. DOI Link. [Not cited.]

[147] P. Carruthers, *Isospin symmetry, TCP, and local field theory*, *Physics Letters B* **26** (Jan., 1968) 158–160. DOI Link. [Not cited.]

[148] A. I. Oksak and I. T. Todorov, *Invalidity of TCP-theorem for infinite-component fields*, *Commun.Math. Phys.* **11** (June, 1968) 125–130. DOI Link. [Not cited.]

[149] O. W. Greenberg, *CPT Violation Implies Violation of Lorentz Invariance*, *Phys. Rev. Lett.* **89** (Nov., 2002) 231602, [hep-ph/0201258]. DOI Link. [Not cited.]

[150] A. Angelopoulos, A. Apostolakis, E. Aslanides, et al., *K0–$\bar{K}$0 mass and decay-width differences: CPLEAR evaluation*, *Physics Letters B* **471** (Dec., 1999) 332–338. DOI Link. [Not cited.]

[151] J. Abdallah, P. Abreu, W. Adam, et al., *Masses, lifetimes and production rates of Ξ- and Ξ¯+ at LEP 1*, *Physics Letters B* **639** (Aug., 2006) 179–191. DOI Link. [Not cited.]

[152] A. W. Chan, K. C. Cheng, K. B. Luk, et al., *Measurement of the properties of the ${\overline{\ensuremath{\Omega}}}\hat{+}$ and ${\ensuremath{\Omega}}\hat{\ensuremath{-}}$ hyperons*, *Phys. Rev. D* **58** (Aug., 1998) 072002. DOI Link. [Not cited.]

[153] ALICE Collaboration, *ALICE Data Preparation Group*, https://alice-offline.web.cern.ch/Activities/alice-data-preparation-group, May 2023. [Not cited.]

[154] K. N. Barends, *A Geant4 validation study for the ALICE experiment at the LHC*, 2017. [Not cited.]

[155] ALICE Collaboration, *ALICE Physics Forum - 8 June 2016*, https://indico.cern.ch/event/489470/#4-updates-on-physics-selection, June 2016. [Not cited.]

[156] ALICE Collaboration, *ALICE DPG – Pileup in Run-2 data samples*, https://twiki.cern.ch/twiki/bin/view/ALICE/AliDPGtoolsPileup#Removing_tracks_produced_in_out. [Not cited.]

[157] A. Collaboration, *Multiplicity dependence of (multi-)strange hadron production in proton-proton collisions at $\sqrt{s}$ = 13 TeV*, Eur. Phys. J. C **80** (Feb., 2020) 167, [arXiv:1908.01861]. DOI Link. [Not cited.]

[158] D. Silva De Albuquerque, *Multi-strange hadrons in Pb–Pb collisions at the LHC with ALICE*, https://cds.cern.ch/record/2690627, Sept. 2019. [Not cited.]

[159] A. Collaboration, *Kshort and Lambda production in pp interactions at sqrt(s) = 0.9 and 7 TeV measured with the ATLAS detector at the LHC*, Phys. Rev. D **85** (Jan., 2012) 012001, [arXiv:1111.1297]. DOI Link. [Not cited.]

[160] A. Collaboration, *Search for resonances in diphoton events at $\sqrt{s}$=13 TeV with the ATLAS detector*, https://arxiv.org/abs/1606.03833v2, June 2016. [Not cited.]

[161] Geant4, *Geant4 Material Database*, https://geant4-userdoc.web.cern.ch/UsersGuides/ForApplicationDeveloper/html/Appendix/materialNames.html#simple-materials-elements. [Not cited.]

[162] D. D. Chinellato and I. Belikov, *Two-track DCA calculation in ALICE*, 2018. [Not cited.]

[163] A. Collaboration, *Multiplicity dependence of light-flavor hadron production in pp collisions at $\sqrt{s}$ = 7 TeV*, Phys. Rev. C **99** (Feb., 2019) 024906, [arXiv:1807.11321]. DOI Link. [Not cited.]

[164] R. Shahoyan, *Summary of the L3 magnet field analysis.*, InternalNote/Computing (2007), no. ALICE-INT-2007-012. [Not cited.]

[165] ALICE Collaboration, *Validation of the ALICE material budget between TPC and TOF detectors*, ALICE Publications (Feb., 2022). [Not cited.]

[166] A. Collaboration, *Data-driven precision determination of the material budget in ALICE*, Mar. 2023. arXiv:2303.15317. [Not cited.]

[167] ALICE Collaboration, *ALICE sees "the ridge" in simplest collisions yet | ALICE Collaboration*, https://alice-collaboration.web.cern.ch/Moriond2023_ridge. [Not cited.]

[168] C. Collaboration, *Evidence for collective multi-particle correlations in pPb collisions*, Phys. Rev. Lett. **115** (June, 2015) 012301, [arXiv:1502.05382]. DOI Link. [Not cited.]

[169] A. Collaboration, *Anisotropic flow and flow fluctuations of identified hadrons in Pb$-$Pb collisions at $\sqrt{s_{\mathrm{NN}}}$ = 5.02 TeV*, https://arxiv.org/abs/2206.04587v2, June 2022. [Not cited.]

[170] C. R. Singh, S. Deb, R. Sahoo, and J.-e. Alam, *Charmonium suppression in ultra-relativistic proton–proton collisions at LHC energies: A hint for QGP in small systems*, Eur. Phys. J. C **82** (June, 2022) 542. DOI Link. [Not cited.]

[171] M. Van Leeuwen, *Highlights from ALICE, 59th International School of Subnuclear Physics*, https://agenda.infn.it/event/36701/contributions/203759/. [Not cited.]

[172] S. Acharya, D. Adamová, A. Adler, et al., *Multiplicity dependence of $$\pi $$, K, and p production in pp collisions at $$\sqrt{s} = 13$$ TeV*, Eur. Phys. J. C **80** (Aug., 2020) 693. DOI Link. [Not cited.]

[173] K. Werner, *Core-corona procedure and microcanonical hadronization to understand strangeness enhancement in proton-proton and heavy ion collisions in the EPOS4 framework*, June 2023. arXiv:2306.10277. [Not cited.]

[174] K. Werner, B. Guiot, I. Karpenko, and T. Pierog, *Analysing radial flow features in p-Pb and p-p collisions at several TeV by studying identified particle production in EPOS3*, *Phys. Rev. C* **89** (June, 2014) 064903, [arXiv:1312.1233]. DOI Link. [Not cited.]

[175] J. R. Christiansen and P. Z. Skands, *String Formation Beyond Leading Colour*, https://arxiv.org/abs/1505.01681v2, May 2015. [Not cited.]

[176] C. Bierlich, G. Gustafson, L. Lönnblad, and A. Tarasov, *Effects of Overlapping Strings in pp Collisions*, *arXiv:1412.6259 [hep-ph]* (Feb., 2015) [arXiv:1412.6259]. [Not cited.]

[177] J. Adolfsson, A. Andronic, C. Bierlich, et al., *QCD challenges from pp to A–A collisions*, *Eur. Phys. J. A* **56** (Nov., 2020) 288. DOI Link. [Not cited.]

[178] J. Adolfsson, *Study of Ξ-Hadron Correlations in Pp Collisions at $\sqrt{s}=13$ TeV Using the ALICE Detector*. PhD thesis, Lund University Publications, Lund, Sweden, 2020. [Not cited.]

[179] P. D. B. Collins, *An Introduction to Regge Theory and High Energy Physics*. Cambridge Monographs on Mathematical Physics. Cambridge University Press, Cambridge, 1977. [Not cited.]

[180] A. Collaboration, *Measurement of inelastic, single- and double-diffraction cross sections in proton-proton collisions at the LHC with ALICE*, *Eur. Phys. J. C* **73** (June, 2013) 2456, [arXiv:1208.4968]. DOI Link. [Not cited.]

[181] A. Collaboration, *Enhanced production of multi-strange hadrons in high-multiplicity proton-proton collisions*, *Nature Phys* **13** (June, 2017) 535–539, [arXiv:1606.07424]. DOI Link. [Not cited.]

[182] A. Collaboration, *Pseudorapidity and transverse-momentum distributions of charged particles in proton-proton collisions at $\mathbf{\sqrt{\textit s}}$ = 13 TeV*, *Physics Letters B* **753** (Feb., 2016) 319–329, [arXiv:1509.08734]. DOI Link. [Not cited.]

[183] G. Breit and E. Wigner, *Capture of Slow Neutrons*, *Phys. Rev.* **49** (Apr., 1936) 519–531. DOI Link. [Not cited.]

[184] A. Collaboration, *Multiplicity dependence of K*(892)$\hat{0}$ and ϕ(1020) production in pp collisions at $\sqrt{s}$ = 13 TeV*, *arXiv:1910.14397 [hep-ex, physics:nucl-ex]* (Oct., 2019) [arXiv:1910.14397]. [Not cited.]

[185] T. Sjöstrand, S. Ask, J. R. Christiansen, et al., *An Introduction to PYTHIA 8.2*, *Computer Physics Communications* **191** (June, 2015) 159–177, [arXiv:1410.3012]. DOI Link. [Not cited.]

[186] T. Sjöstrand, *The Development of MPI Modelling in PYTHIA*, June 2017. arXiv:1706.02166. [Not cited.]

[187] I. Helenius, J. R. Christiansen, and C. O. Rasmussen, *Recent Pythia 8 developments: Hard diffraction, Colour reconnection and $\gamma\gamma$ collisions*, Apr. 2016. arXiv:1604.07996. [Not cited.]

[188] C. Collaboration, *Observation of Long-Range Near-Side Angular Correlations in Proton-Proton Collisions at the LHC*, *J. High Energ. Phys.* **2010** (Sept., 2010) 91, [arXiv:1009.4122]. DOI Link. [Not cited.]

[189] S. Chatrchyan, V. Khachatryan, A. M. Sirunyan, et al., *Observation of long-range, near-side angular correlations in pPb collisions at the LHC*, *Physics Letters B* **718** (Jan., 2013) 795–814. DOI Link. [Not cited.]

[190] GUNTHER. ROLAND, *Long-range correlations in high multiplicity pp and pA collisions*, *Pramana - J Phys* **84** (May, 2015) 731–746. DOI Link. [Not cited.]

[191] T. Regge, *Introduction to complex orbital momenta*, *Nuovo Cim* **14** (Dec., 1959) 951–976. DOI Link. [Not cited.]

[192] E. Levin, *Everything about reggeons.Part I:Reggeons in "soft" interaction*, Jan. 1998. hep-ph/9710546. [Not cited.]

[193] K. Werner, *Monte Carlo Event Generators*, 2022. [Not cited.]

Chapter

8 | Complementary materials for the analysis: Mass measurements of multi-strange baryons in pp collisions at $\sqrt{s} = 13$ TeV

I Study of the systematic effects

I-.i Topological and track selections

Candidate variable	Range	Signal variation K^0_S
Competing mass rejection (GeV/c^2)	$>[0.002;0.010]$	1.1%
Track variable	Range	Signal variation K^0_S
Nbr of crossed TPC readout rows	$>[70;90]$	0.5%
n_σ^{TPC}	$<[1;3]\ \sigma$	45%
Topological variable	Range	Signal variation K^0_S
V0 decay radius (cm)	$>[0.4;2.2]$	10%
V0 Lifetime (cm)	$<[1.57;3.43]\ c.\tau$	12%
V0 cosine of pointing angle	$>[0.995;0.9998]$	10%
DCA pion to prim. vtx (cm)	$>[0.04;0.5]$	24%
DCA between V0 daughters (std dev)	$<[0.2;1.5]$	12%

Table A.1: Summary of the range variation on the topological and track selections used for the reconstruction of K^0. The induced signal variation is indicated in the last column ; for more details, look at Fig. A.7.

Candidate variable	Range	Signal variation Λ ($\overline{\Lambda}$)
Competing mass rejection (GeV/c^2)	$>$ [0.005;0.012]	3% (3%)
Track variable	Range	Signal variation Λ ($\overline{\Lambda}$)
Nbr of crossed TPC readout rows	$>$ [70;90]	0.8% (0.8%)
$n_{\sigma}^{\mathrm{TPC}}$	$<$ [1;3] σ	45% (45%)
Topological variable	Range	Signal variation Λ ($\overline{\Lambda}$)
V0 decay radius (cm)	$>$ [0.4;3.5]	11% (11%)
V0 Lifetime (cm)	$<$ [1.53;3.43] $c.\tau$	17% (17%)
V0 cosine of pointing angle	$>$ [0.995;0.9998]	13% (13%)
DCA proton to prim. vtx (cm)	$>$ [0.04;0.15]	17% (17%)
DCA pion to prim. vtx (cm)	$>$ [0.04;0.5]	12% (12%)
DCA between V0 daughters (std dev)	$<$ [0.3;1.5]	12% (12%)

Table A.2: Summary of the range variation on the topological and track selections used for the reconstruction of Λ and $\overline{\Lambda}$. The induced signal variation is indicated in the last column ; for more details, look at Fig. A.5 and Fig. A.6.

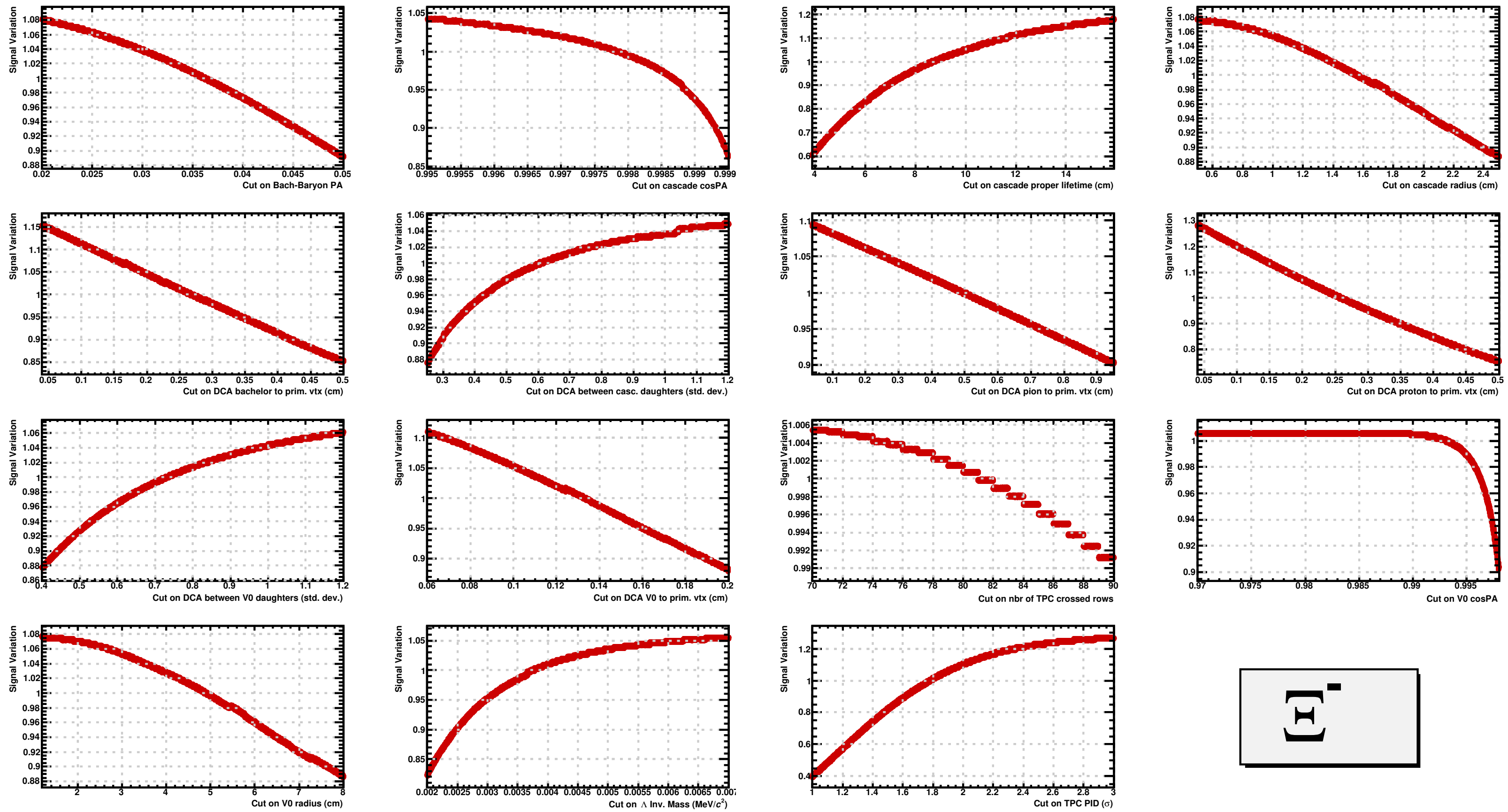

Fig. A.1: Signal variation within the selection range of every topological and track variables used in the Ξ^- analysis. These distributions were obtained by fixing all the cuts to their values in Tab. 5.3 but one ; the aforementioned procedure (section **??**) is then used to vary randomly the latter within its range of selections (see Tab. 5.7). The ratio between the extracted signal and the average signal within the selection range provides the signal variation. Here, the signal was computed based on the fit of the invariant mass using a modified Gaussian for the peak and a first order polynomial for the background.

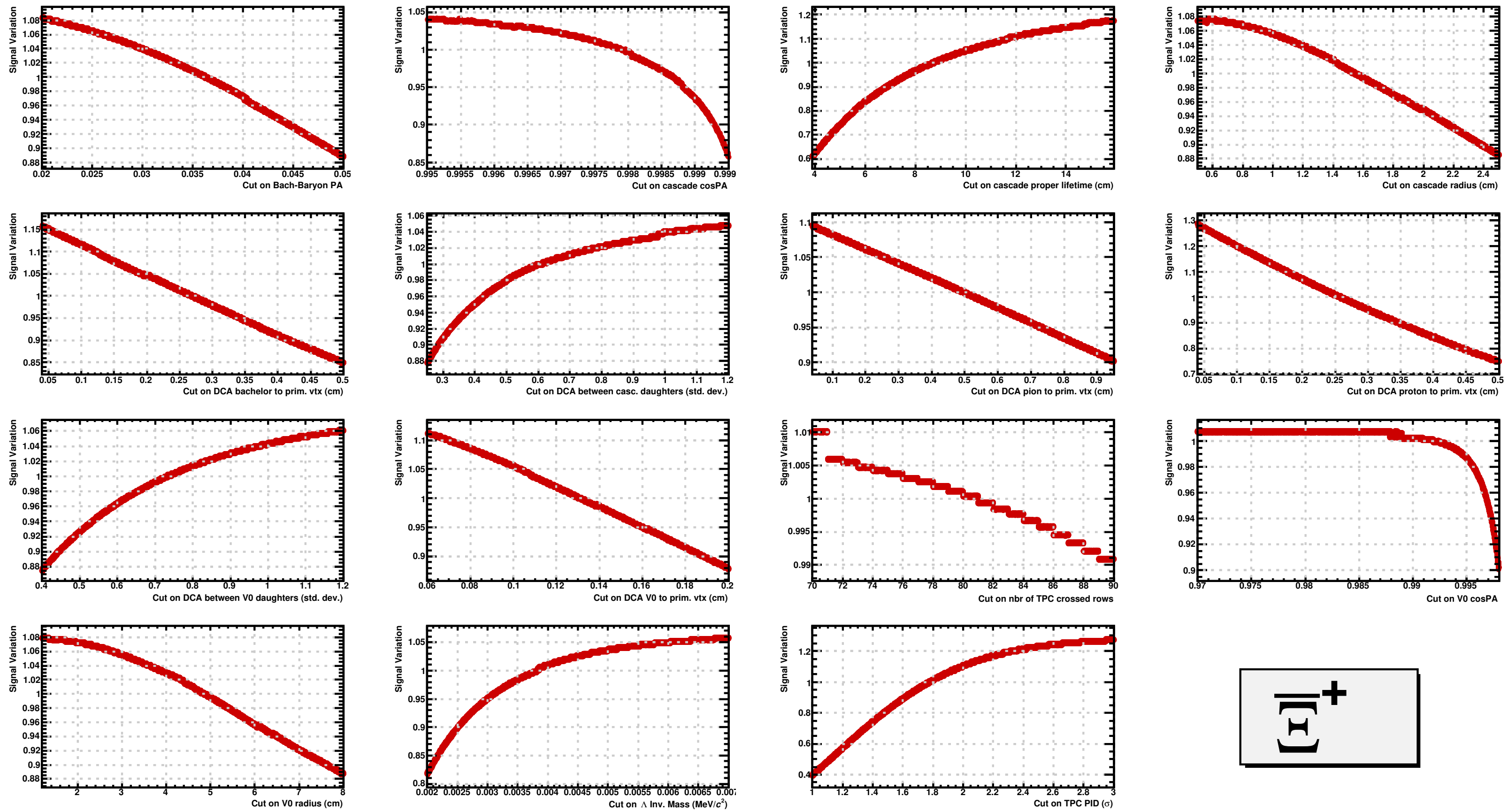

Fig. A.2: Signal variation within the selection range of every topological and track variables used in the $\overline{\Xi}^+$ analysis. These distributions were obtained by fixing all the cuts to their values in Tab. 5.3 but one ; the aforementioned procedure (section **??**) is then used to vary randomly the latter within its range of selections (see Tab. 5.7). The ratio between the extracted signal and the average signal within the selection range provides the signal variation. Here, the signal was computed based on the fit of the invariant mass using a modified Gaussian for the peak and a first order polynomial for the background.

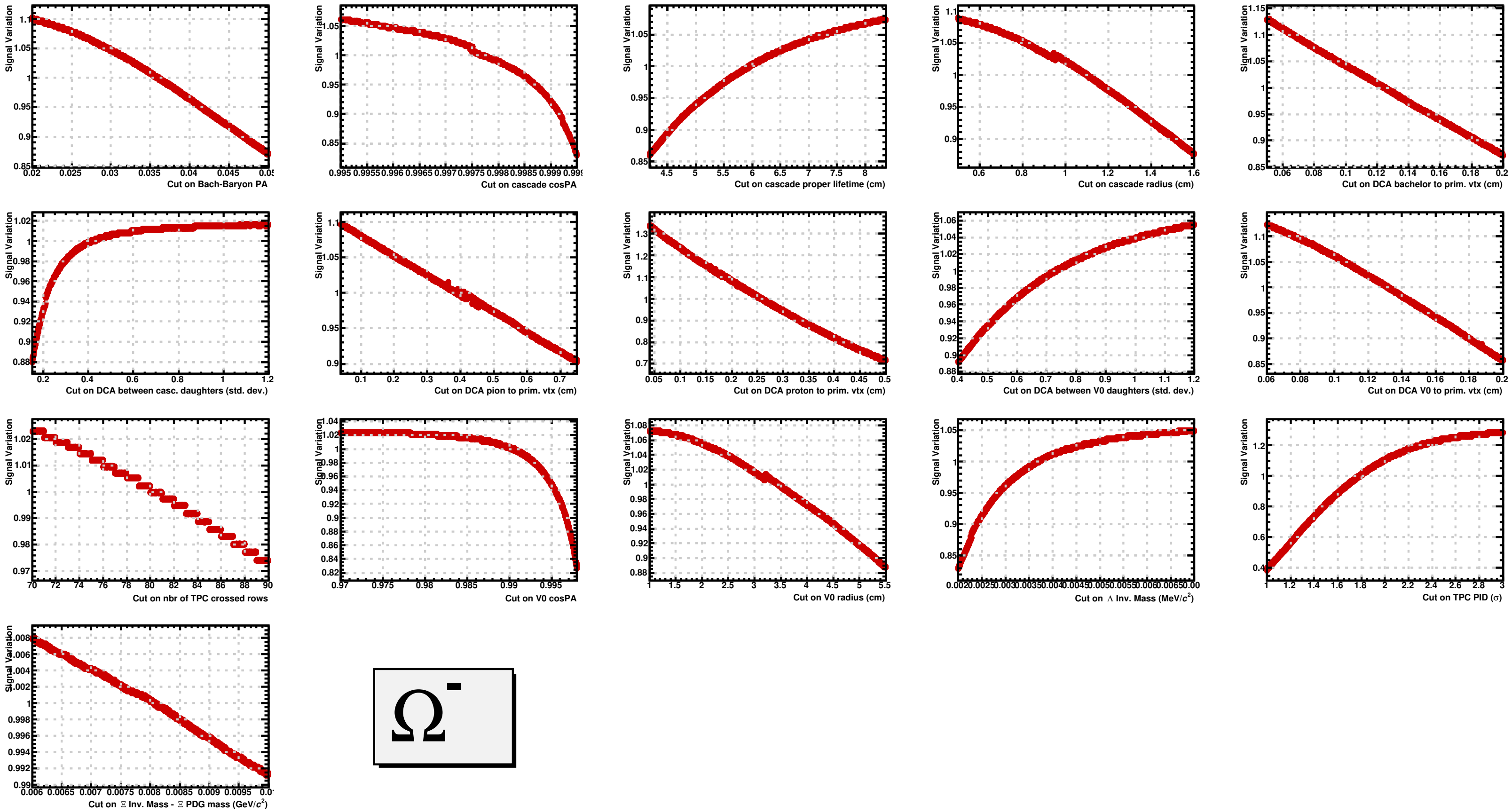

Fig. A.3: Signal variation within the selection range of every topological and track variables used in the Ω^- analysis. These distributions were obtained by fixing all the cuts to their values in Tab. 5.3 but one ; the aforementioned procedure (section **??**) is then used to vary randomly the latter within its range of selections (see Tab. 5.8). The ratio between the extracted signal and the average signal within the selection range provides the signal variation. Here, the signal was computed based on the fit of the invariant mass using a modified Gaussian for the peak and a first order polynomial for the background.

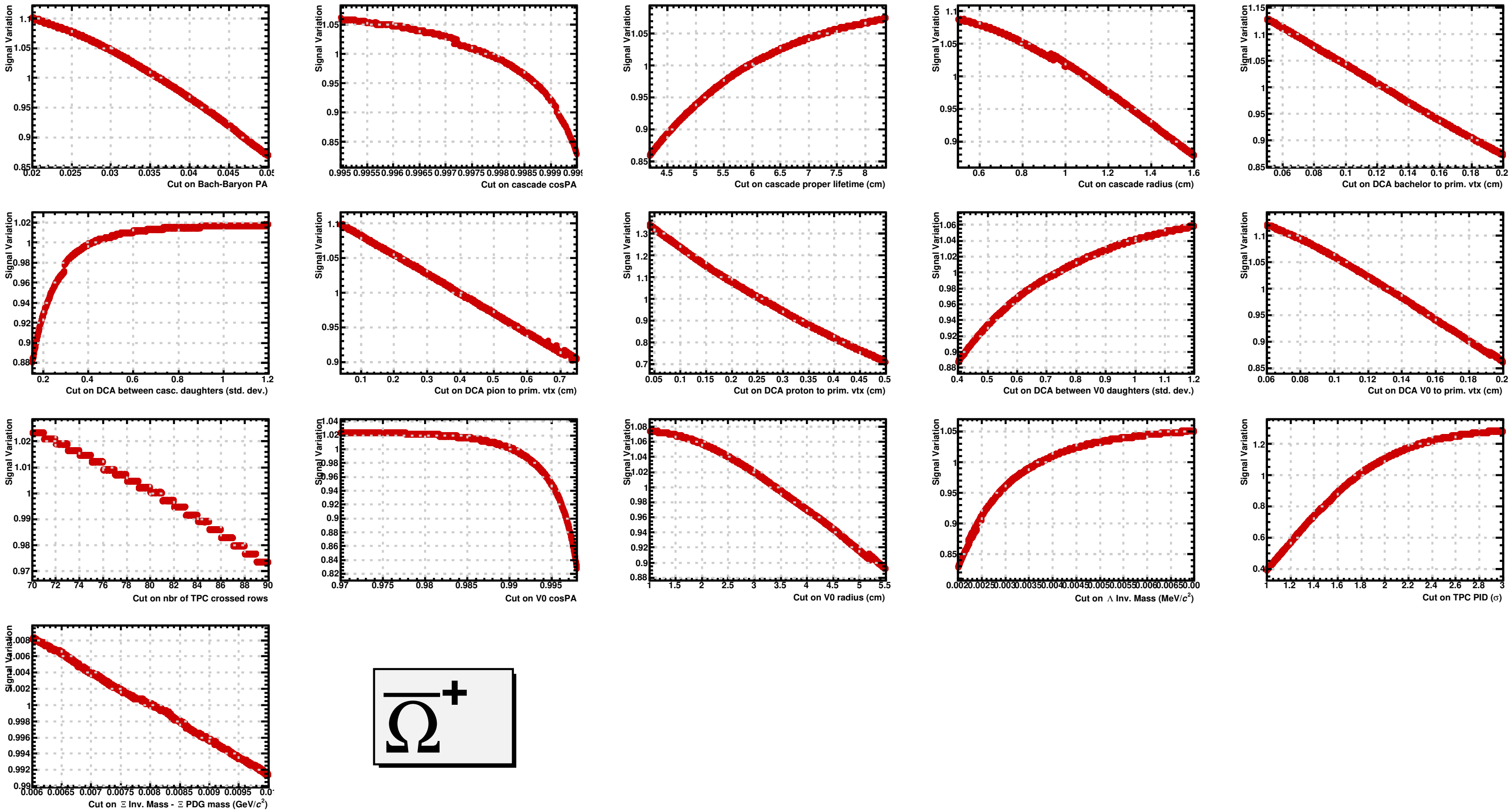

Fig. A.4: Signal variation within the selection range of every topological and track variables used in the $\overline{\Omega}^+$ analysis. These distributions were obtained by fixing all the cuts to their values in Tab. 5.3 but one ; the aforementioned procedure (section **??**) is then used to vary randomly the latter within its range of selections (see Tab. 5.8). The ratio between the extracted signal and the average signal within the selection range provides the signal variation. Here, the signal was computed based on the fit of the invariant mass using a modified Gaussian for the peak and a first order polynomial for the background.

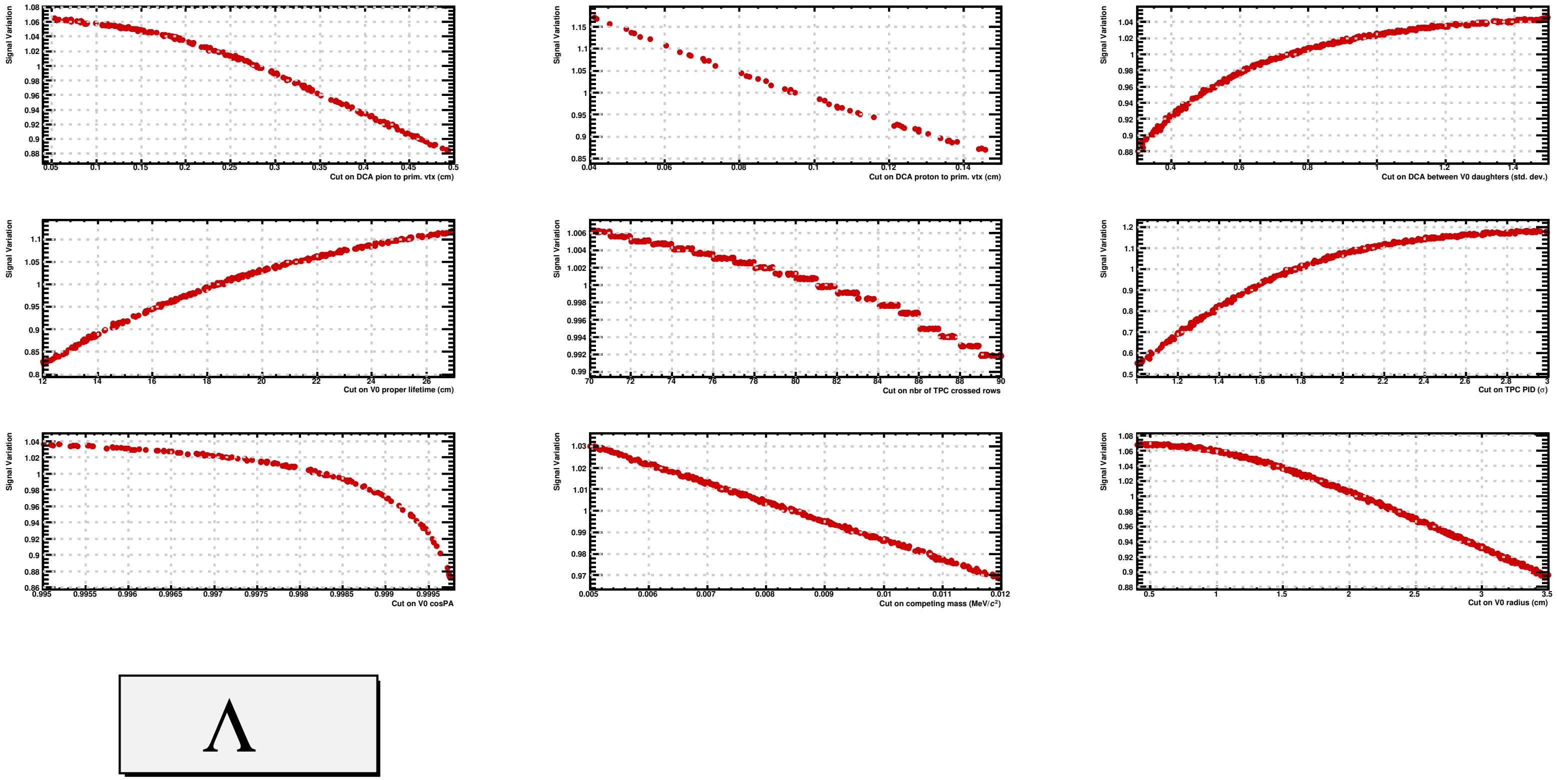

Fig. A.5: Signal variation within the selection range of every topological and track variables used in the Λ analysis. These distributions were obtained by fixing all the cuts to their values in Tab. 5.2 but one ; the aforementioned procedure (section **??**) is then used to vary randomly the latter within its range of selections (see Tab. A.2). The ratio between the extracted signal and the average signal within the selection range provides the signal variation. Here, the signal was computed based on the fit of the invariant mass using a modified Gaussian for the peak and a first order polynomial for the background.

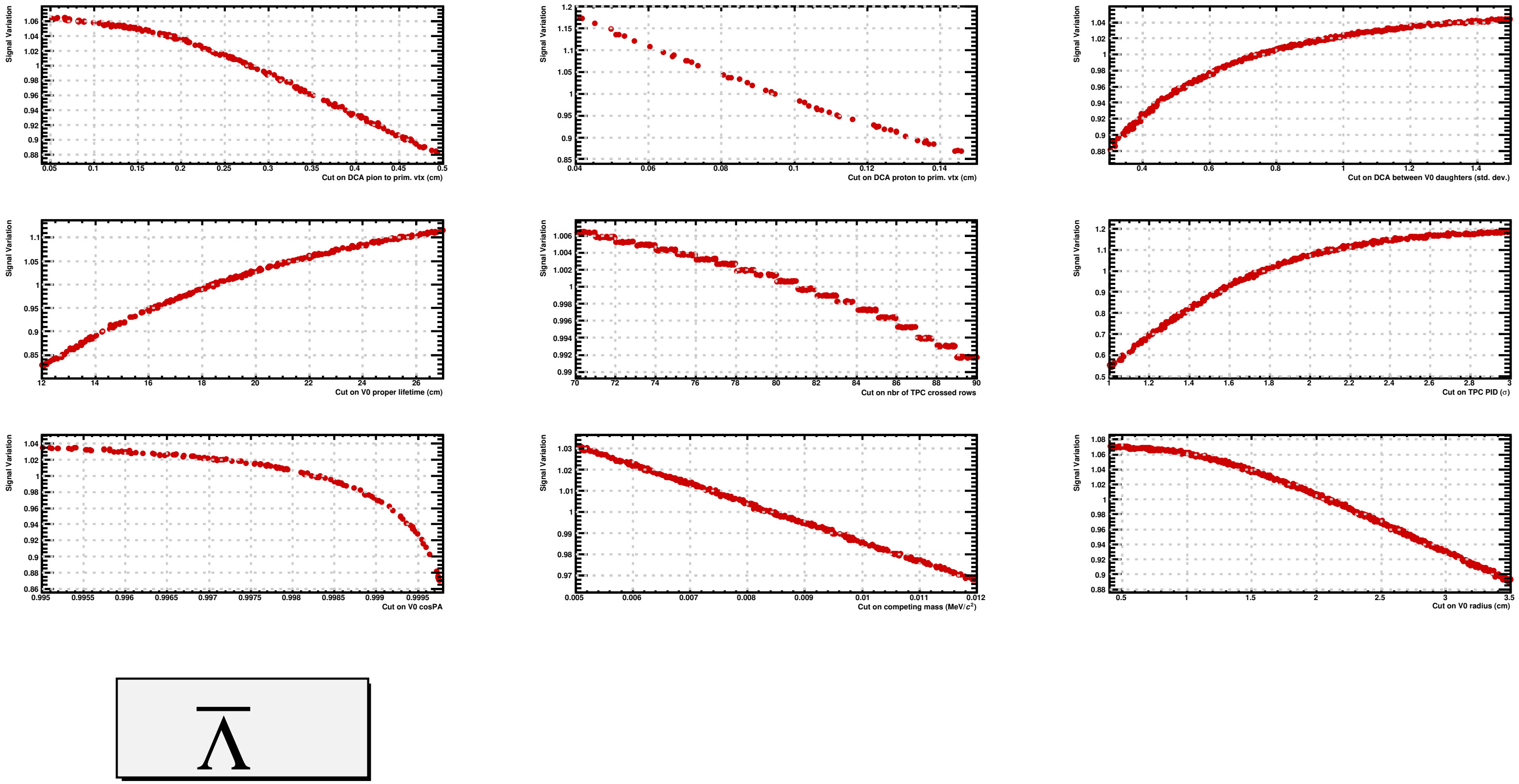

Fig. A.6: Signal variation within the selection range of every topological and track variables used in the $\overline{\Lambda}$ analysis. These distributions were obtained by fixing all the cuts to their values in Tab. 5.2 but one ; the aforementioned procedure (section **??**) is then used to vary randomly the latter within its range of selections (see Tab. A.2). The ratio between the extracted signal and the average signal within the selection range provides the signal variation. Here, the signal was computed based on the fit of the invariant mass using a modified Gaussian for the peak and a first order polynomial for the background.

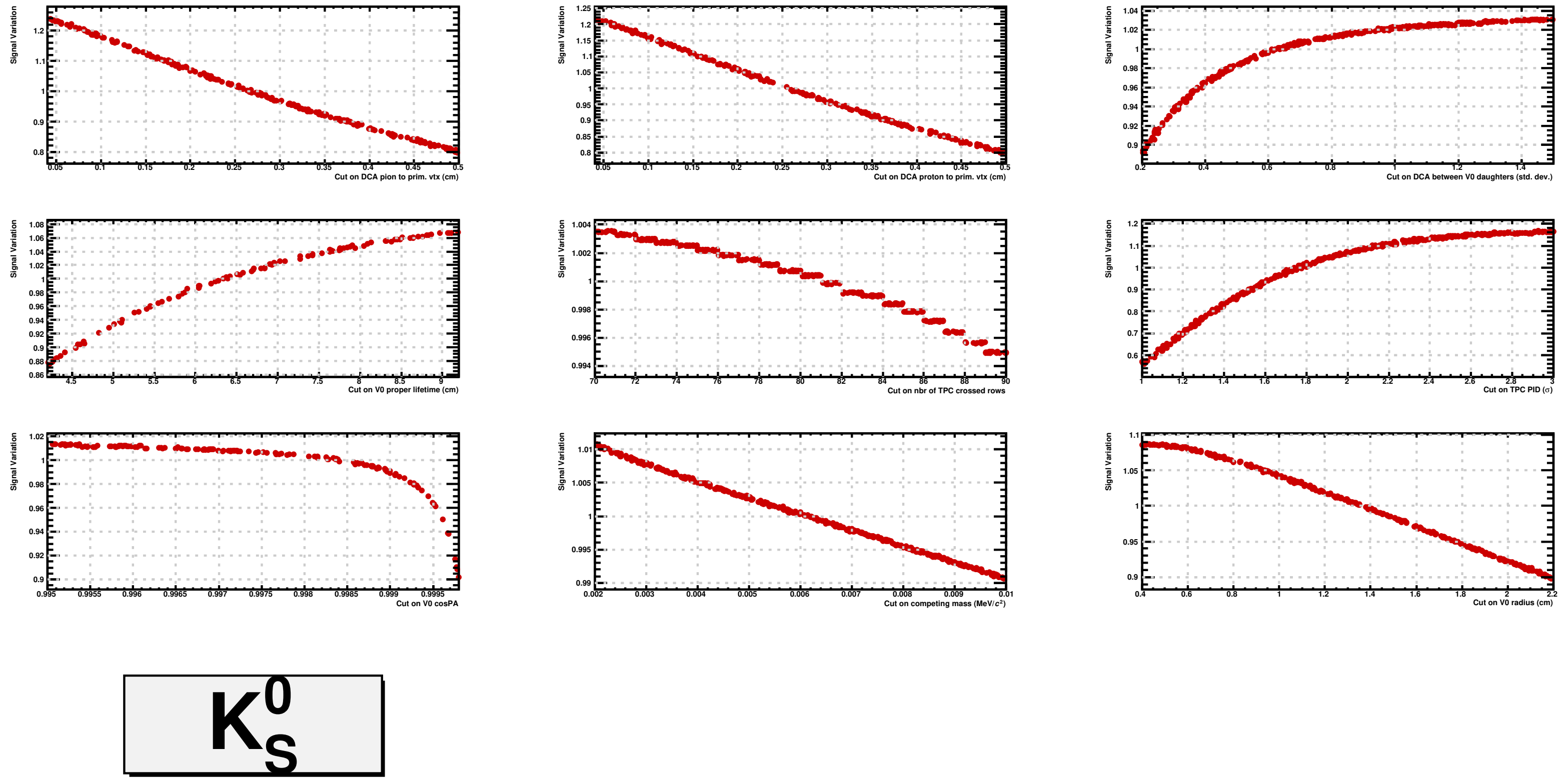

Fig. A.7: Signal variation within the selection range of every topological and track variables used in the K^0analysis. These distributions were obtained by fixing all the cuts to their values in Tab. 5.2 but one ; the aforementioned procedure (section **??**) is then used to vary randomly the latter within its range of selections (see Tab. A.1). The ratio between the extracted signal and the average signal within the selection range provides the signal variation. Here, the signal was computed based on the fit of the invariant mass using a modified Gaussian for the peak and a first order polynomial for the background.

I-A Stability of the results

I-A.i Dependence on the decay radius

I-A.ii Dependence on the transverse momentum

I-A.iii Dependence on the opening angles

I-A.iv Dependence on the azimuthal angles

I-A.v Dependence on the rapidity

I-A.vi Dependence on the event multiplicity

I-B Momentum scale calibration

I-B.i Imprecision on the magnetic field

I-B.ii Energy loss corrections

Chapter 9 | Complementary materials for the analysis: Analysis of the correlated production of strange hadrons

I Epos configuration

```
!--------------------------------------------------------------
!  proton-proton parameterized fluid expansion (mimic hydro)
!    much faster than full hydro
!--------------------------------------------------------------

application hadron !hadron-hadron, hadron-nucleus, or nucleus-nucleus
set laproj 1       !projectile atomic number
set maproj 1       !projectile mass number
set latarg 1       !target atomic number
set matarg 1       !target mass number
set ecms 13000     !sqrt(s)_pp

set istmax 25
```

```
set iranphi 1
ftime on

set ihepmc 1
!set nfull 10           !number of events


!suppressed decays:
nodecays
 110 20 2130 -2130 2230 -2230 1130 -1130 1330 -1330 2330 -2330 3331 -3331
end

set ninicon 1            !number of initial conditions used for hydro evolution
core PFE                 !parameterized fluid expansion (mimic hydro) : PFE, full, of
hydro off                !hydro not activated (hlle, off)
eos off                  !eos not activated (x3ff, off)
hacas full               !hadronic cascade activated  (full, off)

set nfreeze 1            !number of freeze out events per hydro event
set modsho 1             !certain printout every modsho events
set centrality 0         ! 0=min bias

!print * 2                !printout of event to ...check file

!-----put here online analysis part----
!       see expl1,2,3
!--------------------------------------
```

II Pythia 8– Monash 2013 configuration

```
#Beams
Beams:idA = 2212 ! Proton
Beams:idB = 2212

# Min. bias
#SoftQCD:all = on

# Min. bias alternative
SoftQCD:nonDiffractive = on
SoftQCD:singleDiffractive = on
SoftQCD:doubleDiffractive = on

# random seed
Random:setSeed = on
Random:seed = 0
```

```
# Set cuts
# Use this for hard leading-jets in a certain pT window
PhaseSpace:pTHatMin = 0   # min pT
PhaseSpace:pTHatMax = 13000   # max pT

# Use this for hard leading-jets in a certain mHat window
PhaseSpace:mHatMin = 0   # min mHat
PhaseSpace:mHatMax = $SQRTS   # max mHat

# Makes particles with c*tau0 > 10 mm stable: (default value = 10.0 in mm / Here = 10
# See http://home.thep.lu.se/~torbjorn/pythia81html/ParticleDecays.html
# tau0 = seems to deal with particle species by species, i.e. selection based on 'cTa
ParticleDecays:limitTau0 = On
ParticleDecays:tau0Max = 10000.0

# Set tune
Tune:pp=14
```

III Pythia 8 configuration with colour reconnection enabled

```
# Parameter of the MPI model to keep total multiplicity reasonable
MultiPartonInteractions:pT0Ref = 2.15

# Parameters related to Junction formation/QCD based CR
BeamRemnants:remnantMode = 1
BeamRemnants:saturation = 5
ColourReconnection:mode = 1
ColourReconnection:allowDoubleJunRem = off
ColourReconnection:m0 = 0.3
ColourReconnection:allowJunctions = on
ColourReconnection:junctionCorrection = 1.2
ColourReconnection:timeDilationMode = 2
ColourReconnection:timeDilationPar = 0.18

# Enable rope hadronization
Ropewalk:RopeHadronization = on

# Also enable string shoving, but don't actually do anything.
# This is just to allow strings to free stream until hadronization
# where the overlaps between strings are calculated.
Ropewalk:doShoving = on
Ropewalk:tInit = 1.5 # Propagation time
Ropewalk:deltat = 0.05
Ropewalk:tShove = 0.1
```

```
Ropewalk:gAmplitude = 0. # Set shoving strength to 0 explicitly

# Do the ropes.
Ropewalk:doFlavour = on

# Parameters of the rope model
Ropewalk:r0 = 0.5 # in units of fm
Ropewalk:m0 = 0.2 # in units of GeV
Ropewalk:beta = 0.1

# Enabling setting of vertex information is necessary
# to calculate string overlaps.
PartonVertex:setVertex = on
PartonVertex:protonRadius = 0.7
PartonVertex:emissionWidth = 0.1
```